

UC San Diego

UC San Diego Electronic Theses and Dissertations

Title

Topics on In-motion Non-contact Ultrasonic Structural Monitoring of Railroad Tracks

Permalink

<https://escholarship.org/uc/item/0fm9x566>

Author

Datta, Diptojit

Publication Date

2022

Peer reviewed|Thesis/dissertation

UNIVERSITY OF CALIFORNIA SAN DIEGO

**Topics on In-motion Non-contact Ultrasonic Structural Monitoring
of Railroad Tracks**

A dissertation submitted in partial satisfaction of the requirements for the degree

Doctor of Philosophy

in

Structural Engineering

by

Diptojit Datta

Committee in Charge:

Professor Francesco Lanza di Scalea, Chair

Professor William S. Hodgkiss

Professor Hyonny Kim

Professor Thomas T. Liu

Professor Kenneth J. Loh

2022

Copyright

Diptojit Datta, 2022

All rights reserved.

The dissertation of Diptojit Datta is approved, and it is acceptable in quality and form for publication on microfilm and electronically.

University of California San Diego

2022

DEDICATION

To my late grandparents

To my parents, Anindita Datta and Debasish Datta

EPIGRAPH

“Ask the right questions, and nature will open the doors to her secrets”

Chandrasekhara Venkata (C.V.) Raman

TABLE OF CONTENTS

Dissertation Approval Page	iii
Dedication	iv
Epigraph	v
Table of Contents	vi
List of Figures	xi
List of Tables	xviii
Acknowledgements	xix
Vita	xxiii
Abstract of the Dissertation	xxv
Chapter 1. Introduction	1
1.1. Motivation	1
1.2. Scope	1
1.3. Outline of the Dissertation	3
1.4. References	4
Chapter 2. Development of a High-Speed Ultrasonic Rail Inspection Technique	6
2.1. Abstract	6
2.2. Introduction	6
2.3. Theory and Background	9
2.3.1. Transfer Function Extraction (Dual-Output System)	9
2.3.2. Statistical Outlier Analysis	15
2.4. Data Acquisition System	17
2.4.1. Overview	17
2.4.2. Sensor Hardware	18
2.4.3. Positioning System (Distance and Location Tracker)	19

2.4.4. Vision System	20
2.4.5. Data Processing Unit.....	22
2.5. Field Tests	24
2.5.1. Test Setup.....	24
2.5.2. Test Methodology	26
2.6. Acknowledgments.....	28
2.7. References	28
Chapter 3. Influence of Varying Operational Parameters on the Defect Detection Performance of a High-Speed Ultrasonic Rail Inspection System During Field Tests	32
3.1. Introduction.....	32
3.2. Acoustic Signal Strength.....	33
3.3. Receiver Operating Characteristic Curves.....	35
3.3.1. Discretization of Inspected Rail Segments	37
3.3.2. ROC Curves for Different Defect Margins.....	38
3.4. Influence of Operational Parameters on Defect Detection Performance.....	40
3.4.1. Acoustic Signal Strength.....	40
3.4.2. Speed of Test Runs	43
3.4.3. Baseline Distribution Length	44
3.4.4. Signal-to-Noise Ratio of Transfer Functions	48
3.4.5. Redundancies from Multiple Runs	50
3.5. Conclusions.....	55
3.6. Acknowledgements.....	56
3.7. References	56
Chapter 4. Development of an Improved Passive Rail Inspection System with a Controlled Acoustic Source and Modified Transfer Function Reconstruction.....	60
4.1. Introduction.....	60

4.1.1. Need for a Controlled Acoustic Source	61
4.1.2. Need for a Miniature and Ruggedized Sensing Head.....	62
4.2. Laboratory Tests with Controlled Acoustic Source.....	63
4.2.1. Test Setup.....	63
4.2.2. Capacitive Ultrasonic Transducer (VN Instruments CAP-2) as Source	65
4.3. Laboratory Tests with Miniature Electrostatic Transducers	71
4.4. Improved Transfer Function Reconstruction Algorithm	73
4.4.1. Transfer Functions with Simulated Signals	74
4.4.2. Transfer Functions from Experimental Signals	77
4.5. Field Tests	78
4.5.1. Prototype Redesign	78
4.5.2. Test Methodology	79
4.5.3. Results.....	81
4.6. Conclusions.....	85
4.7. Acknowledgements.....	86
4.8. References.....	87
Chapter 5. Ultrasonic Sonar-Based Ranging Technique for Railroad Tie Deflection Measurements (Proof of Concept).....	89
5.1. Abstract	89
5.2. Introduction.....	89
5.3. Theoretical Considerations	93
5.3.1. Sonar Based Ranging Technique	93
5.3.2. Reference-Based Deflection Computation	94
5.3.3. Cross-correlation Operator for Time-of-flight Computation.....	96
5.3.4. Tie Boundary Demarcation.....	98
5.4. Selection of Optimum Transducers	99

5.5. Data Acquisition System and Signal Processing Routines on LabVIEW Real-Time	103
5.5.1. Data Acquisition System.....	103
5.5.2. Implementing Multiple Channels	106
5.5.3. LabVIEW Real-Time Signal Processing Routines	107
5.5.4. Lift-off Distance Resolution Estimation.....	109
5.6. 3-point Bending Test (Proof-of-Concept).....	109
5.6.1. Static Test.....	110
5.6.2. Dynamic Test	113
5.7. Conclusions.....	114
5.8. Acknowledgements.....	116
5.9. References.....	116
Chapter 6. In-motion Full-Field Ultrasonic Tie Deflection Measurements (Rail Defect Testing Facility Tests).....	119
6.1. Introduction.....	119
6.2. Prototype Design.....	120
6.3. Data Acquisition System.....	123
6.3.1. Hardware.....	123
6.3.2. LabVIEW User Interface (Acoustic Signals)	125
6.3.3. LabVIEW User Interface (Image Acquisition).....	126
6.4. Tie Boundary Demarcation.....	127
6.4.1. Signal-Based Demarcation.....	127
6.4.2. Image-Based Demarcation using Machine Learning.....	129
6.4.3. Results.....	133
6.5. Field Tests (Rail Defect Testing Facility).....	137
6.5.1. Test Methodology	137
6.5.2. Test Results.....	138

6.6. Vibration Tolerance Tests.....	143
6.6.1. Vibration Tolerance Test Setup	143
6.6.2. 3D Tie Surface Deflection Profiles (With Coin-Induced Vibrations)	144
6.6.3. Resonance Frequency Identification.....	148
6.7. Conclusions.....	150
6.8. Acknowledgements.....	152
6.9. References.....	153
Chapter 7. In-Motion Full-Field Railroad Crosstie Deflection Measurements (Full-Scale Field Tests).....	155
7.1. Introduction.....	155
7.2. Test Procedure	156
7.3. Bias Removal from Computed Deflections	157
7.4. Image Processing for Spatial Location Along Tie Width and Tie Boundary Demarcation.....	158
7.4.1. Extracting the Travel Distance by Image Analysis.....	158
7.4.2. Machine Learning-Based Tie-Ballast Classification	162
7.5. Results.....	164
7.5.1. 3D Tie Deflection Profiles	164
7.5.2. Displacement Accuracy Verification.....	165
7.6. Statistical Analysis.....	169
7.7. Conclusions.....	170
7.8. Acknowledgements.....	170
7.9. References.....	171
Chapter 8. Conclusions and Future Work	172
8.1. Passive Rail Inspection Technique	172
8.2. Tie Inspection Technique.....	173

LIST OF FIGURES

Figure 2.1 Schematic diagram of passive transfer function reconstruction.....	9
Figure 2.2 A sample transfer function in time domain	15
Figure 2.3 General prototype system diagram.	17
Figure 2.4 Prototype sensing hardware.....	18
Figure 2.5 Prototype laser hardware.	19
Figure 2.6 Novatel GPS receiver (bottom) and antenna (top)	20
Figure 2.7 Vision system diagram.	20
Figure 2.8 Basler ace GigE camera.....	21
Figure 2.9 Smart Vision Over-Drive linear lights.	21
Figure 2.10 National Instruments Real-Time data acquisition unit.....	23
Figure 2.11 Data acquisition and processing unit diagram.....	24
Figure 2.12 Sensor arrangement in prototype with location of alignment lasers.	25
Figure 2.13 Prototype and accessory hardware mounted on the test-car.....	25
Figure 2.14 Data acquisition system (onboard) for the passive inspection system	26
Figure 2.15 Test track layout at TTCI showing the HTL and RTT test tracks.....	27
Figure 3.1 Map of the HTL with regions of high and low signal strengths at 25 mph and 40 mph testing speeds	34
Figure 3.2 ROC curve computation from varying DI thresholds	36
Figure 3.3 Segregating a) pristine and b) defective sections of the rail for computation of PD and PFA in the ROC curves.....	38

Figure 3.4 ROC curves for welds on the HTL track at 40 mph for different defect search tolerance margins.....	39
Figure 3.5 ROC curves for joints on the HTL track at 40 mph for different defect search tolerance margins.....	39
Figure 3.6 ROC curves for joints and welds at 40 mph on the HTL track for different acoustic signal strength regions	41
Figure 3.7 Different locations of the prototype with respect to the locomotive	42
Figure 3.8 Roc curves for joints at 40 mph for different locations of the prototype with respect to the locomotive.....	42
Figure 3.9 ROC curves for joints, welds, and defects at different speeds on the HTL.	44
Figure 3.10 Damage Index trace at 40 mph for baseline length of 30 points (1.75 ft).	45
Figure 3.11 Damage Index trace at 40 mph for baseline length of 240 points (14 ft).	45
Figure 3.12 ROC curves for joints, welds, and defects for different baselines at 40 mph.	46
Figure 3.13 ROC curves for joints & welds for different baselines at 70 mph.	47
Figure 3.14 ROC curves for joints & welds for different baselines at 80 mph.	47
Figure 3.15 Coherent signal and noise floor in the reconstructed transfer function.....	49
Figure 3.16 GPS based map of passive system predictions, ground truth and signal strengths ...	50
Figure 3.17 ROC curves for welds compounding two runs on the HTL track at 40 mph to introduce redundancies	51
Figure 3.18 Redundancy: compounding flagged locations from two independent test runs to reduce the rate of false alarms	52
Figure 3.19 ROC curves for welds at 40mph with redundancies for multiple runs	53
Figure 3.20 ROC curves for joints at 40mph with redundancies for multiple runs.....	54

Figure 4.1 ‘Good’ and ‘bad’ signal strength regions at different speeds (33 mph & 25 mph).....	61
Figure 4.2 Controlled acoustic source laboratory test setup	64
Figure 4.3 Schematic of test setup with function generator and high-voltage amplifier	65
Figure 4.4 Transfer function with 1 CAP2 driven at (a) 30 kHz and (b) 113 kHz	66
Figure 4.5 Frequency spectra with different sources at different driving frequencies	66
Figure 4.6 Test setup with one CAP2 source and different angles of attack	68
Figure 4.7 Transfer function reconstructions at different angles of attack	69
Figure 4.8 Schematic of test setup with one and two sources along with raw acoustic signals ...	69
Figure 4.9 Transfer functions with (a) one source and (b) two sources	70
Figure 4.10 Transfer function from pair 1-7 for different distances from the sources	70
Figure 4.11 Size comparison of SensComp and CAP-2 transducers.....	71
Figure 4.12 Comparison of the signal-to-noise ratio using a) SensComp PID 604142 transducer and b) CAP-2 transducer.....	71
Figure 4.13 Sample transfer function reconstruction using two SensComp transducers	72
Figure 4.14 Gaussian pulse trains generated at two locations with a time delay of 0.1 ms.....	74
Figure 4.15 Transfer functions obtained with different segment lengths (nfft) for a 4096-point gaussian pulse train with added noise	75
Figure 4.16 Transfer functions from TTCI field tests using CAP-2 transducers (Group-1) for different segment lengths.....	76
Figure 4.17 Transfer functions from TTCI field tests using SensComp transducers (Group-2) for different segment lengths.....	77
Figure 4.18 Redesigned prototype with the controlled acoustic source and SensComp transducers (AutoCAD drawing and fabricated product)	78

Figure 4.19 Field test setup with redesigned prototype using active source	79
Figure 4.20 Locations of welds, joints, and transverse defects along the probed rail of the HTL (June 2022 Tests)	80
Figure 4.21 Raw acoustic signal strength classification with source turned on and off.....	80
Figure 4.22 ROC curves for different segment lengths at 40 mph (Group-1 CAP-2) with source on	81
Figure 4.23 ROC curves for source on and off at 40 mph (Group-1 CAP-2).....	82
Figure 4.24 ROC curves at different speeds in the presence of acoustic source	83
Figure 4.25 ROC curves for different transducer type (CAP-2 vs SensComp) at 40 mph with source on.....	84
Figure 4.26 ROC curves compounding data from multiple test runs (6 runs) at different speeds compared to data from 1 test run at 40 mph	85
Figure 5.1 Different deflected shape profiles for good and bad ballast support conditions	90
Figure 5.2 Concept of “tie sonar” for tracking the vertical deflection of a tie.	93
Figure 5.3 Schematic diagram of transducer array and corresponding waveforms for a tie with positive bending	95
Figure 5.4 Difference in time-of-flight of two signals.....	96
Figure 5.5 Cross-correlation operation to compute time-of-flight.....	98
Figure 5.6 Acoustic signal strength-based tie-ballast differentiation	99
Figure 5.7 Array of piezoelectric and capacitive transducers tested at UCSD.....	100
Figure 5.8 Schematic diagram of the setup for data acquisition (1-channel configuration).....	104
Figure 5.9 Tie-sonar experimental setup using one transducer in pulse-echo mode on wood tie	105

Figure 5.10 Front panel of the data acquisition program interface on LabVIEW Real-time.	105
Figure 5.11 Data acquisition setup for two channel acquisition.....	106
Figure 5.12 Drop in signal strength when transducers connected in parallel	107
Figure 5.13 Estimating distance measurement resolution	108
Figure 5.14 Slender wooden beam 3-point bending test setup.....	110
Figure 5.15 Waveforms obtained at the five control points for the loaded and unloaded conditions	111
Figure 5.16 Cross-correlation between the loaded and unloaded waveforms at the five control points.....	112
Figure 5.17 Beam deflections using ultrasonic and visual measurements.....	112
Figure 5.18 dynamic displacements obtained at the five control points as a function of time...	113
Figure 5.19 Dynamic displacement profile at mid-point of the beam	114
Figure 6.1 AutoCAD drawings of the designed prototype mounted on a test-cart.....	121
Figure 6.2 Prototype with transducers and camera.....	122
Figure 6.3 Side view diagram of the prototype mounted on the test car	122
Figure 6.4 The location of the transducers and camera (unit: inch). ‘CH’ denotes the channel number assigned for the transducers.....	123
Figure 6.5 Encoder in contact with the front wheel of the cart in the left side.....	123
Figure 6.6 Schematic diagram of data acquisition setup (1-channel configuration)	124
Figure 6.7 User-interface for data acquisition programmed in LabVIEW Real-Time	125
Figure 6.8 Front panel of the LabVIEW routine for the camera during a test.....	126
Figure 6.9 Acoustic signals at the 6 receiving channels from a tie.....	128
Figure 6.10 Acoustic signals at the 6 receiving channels from ballast.....	128

Figure 6.11 Typical image showing tie and ballast captured by the camera	129
Figure 6.12 KLT tracker to map real displacement to pixel domain.	133
Figure 6.13 Preparing images for analysis.....	134
Figure 6.14 Tie-ballast classification using image-based approach	135
Figure 6.15 Comparison between image-based and signal-based approaches for tie/ballast classification in run #2.	136
Figure 6.16 Test setup with the prototype mounted on a test cart at RDTF	137
Figure 6.17 3D surface deflection profiles for same tie (tie-3) in two different test runs	139
Figure 6.18 3D tie deflection profiles for all 8 ties scanned in one test run	140
Figure 6.19 “Control” wood plank for displacement accuracy verification at tie-6.....	141
Figure 6.20 Tie-width profile at transducer locations 4, 5 & 6.....	142
Figure 6.21 Prototype beam with accelerometers and foam padding.....	143
Figure 6.22 Coins placed on both rails at the beginning of control tie-6.....	144
Figure 6.23 3D surface deflection profiles of control tie-6 with and without the coin-induced vibrations.....	145
Figure 6.24 Surface elevation profiles along the width at sensor locations 5 & 6 with and without the coin-induced vibrations.....	146
Figure 6.25 3D surface deflection profiles of tie-7 with and without the coin-induced vibrations (Top View).....	146
Figure 6.26 3D surface deflection profiles of tie-7 with and without the coin-induced vibrations (Elevation View).....	147
Figure 6.27 Acceleration time-histories from test-run 1 truncated to 8s	147
Figure 6.28 Frequency spectrum of acceleration responses	148

Figure 6.29 Acceleration time-histories from test-run 2 truncated to 1s	149
Figure 6.30 Stabilization plot from stochastic subspace system identification	149
Figure 7.1 Test setup at the BNSF test yard in San Diego	155
Figure 7.2 Bias removal from tie deflection measurements	156
Figure 7.3 Estimation of the tie’s width in the pixel domain.....	159
Figure 7.4 Relative travel distance for test #2. Each data point represents the relative travel distance of the corresponding image count with respect to the previous image count.....	160
Figure 7.5 Image-based reconstructed travel distance and the obtained tie/ballast image classification results for test #1.....	163
Figure 7.6 3D deflection profiles for two different ties in two independent test runs	164
Figure 7.7 3D deflection profiles of 9 ties scanned in a test run	166
Figure 7.8 Longitudinal and transverse deflection profiles of 3 different ties with deflections scaled by 20x.....	167
Figure 7.9 Wood block placed on one of the ties	168
Figure 7.10 3D tie deflection profile with wood block near transducer 1	168
Figure 7.11 Tie width profile at transducer location-1 for control tie with wood block	168
Figure 7.12 Mean tie end deflections of the first 20 ties computed over 4 test runs	169
Figure 7.13 Standard deviation of tie end deflections of the first 20 ties computed over 4 test runs	169

LIST OF TABLES

Table 5.1 Performance Evaluation metrics of Piezoelectric Air-coupled Transducers in Pulse-echo Mode on Wood Tie	102
Table 5.2 Performance Evaluation metrics of Capacitive Air-coupled Transducers in Pulse-echo Mode on Wood Tie	103
Table 5.3 Comparison of Beam deflections using ultrasonic and visual measurements at different control points	113
Table 6.1 Typical 2D FFT and histogram of visual word occurrence for a typical tie and ballast.	132
Table 6.2 Identified natural frequencies and damping ratios.....	150

ACKNOWLEDGEMENTS

This dissertation would not have been possible without the influence of many kind-hearted people in my life. A few pages of text will never be enough to express my gratitude towards these amazing people who have played a key role in supporting me (through thick and thin) on this wonderful journey so far. So, here is my humble attempt to thank them.

First, I would like to express my deepest gratitude to my PhD advisor Professor Francesco Lanza di Scalea. His excellent mentorship, brilliant insight, unparalleled enthusiasm, and caring attitude has made my research experience delightful.

Support from my family has been crucial along this journey. A special note goes to my *Maa* (mother), Anindita Datta, and *Baba* (father), Debasish Datta, for their unwavering love and all the sacrifices they have made to send their only son all the way across to the other side of the world. Their unwavering love, support, and patience was paramount to my success.

I would also like to thank my committee members, Prof. William Hodgkiss, Prof. Kenneth Loh, Prof. Hyonny Kim and Prof. Thomas Liu for their support and suggestions throughout my time at UC San Diego. Fast Fourier Transforms didn't make much sense to me before I took Prof. Hodgkiss' course on digital signal processing. Prof. Loh's course taught me a lot about sensors and data acquisition systems in an experimental and theoretical context. Prof. Kim's course was a wonderful introduction to the world of composites. Prof. Liu's course provided a great insight into the world of biomedical imaging techniques.

My heartfelt gratitude goes to the people at FRA, BNSF, Volpe, TTCI and UCSD Englekirk Center for providing support during numerous field tests. A special note goes to Robert

Wilson, Cameron Stuart, Robert Banister, and Ross Curtright, Ted Sussmann, Brian Lindeman, and Alex Sherman.

A very special shoutout goes to Riya for being that special person in my life showering unconditional love. Thanks for keeping me awake at night and waking me up in the morning.

No journey is memorable without the right companions. I am extremely grateful to my colleagues at the Experimental Mechanics, NDT and SHM Laboratory at UC San Diego. A special mention goes to Ranting Cui, Ali Zare Hosseinzadeh, Albert Liang and Izabela Batista with whom I had the opportunity of collaborating on many research projects. I am also grateful to Chengyang Huang, Guillermo Azuara, Margherita Capriotti, Antonino Spada, Xuan ‘Peter’ Zhu and Stefano Mariani. A special note goes to Simone Sternini who has been like an elder brother to me and provided valuable guidance in times of need. It’s unbelievable how numerous field tests out in the middle of nowhere at freezing cold temperatures (or sometimes scorching heat) were somehow really fun when some of these amazing people were around.

Life outside of work wouldn’t have been the same without all my friends here in the US. A special note goes to Swarvanu Ghosh, Sombuddha Bagchi and Hao-Ping Lin for all the impromptu road trips we did over thousands of miles. I am also grateful to (in random order) Bodhisatwa Goswami, Rupa Goswami, Abhishek Sarkar, Chetna Paras, Brigitta Benitez, Vinod Ramakrishnan, Ananta Sinha, Suborno Jati, Satadeepa Kal, Jeet Chakraborty.

I must also thank all the faculty, students and staff in the Structural Engineering Department at UC San Diego for fostering an atmosphere of learning and care. A special note goes to Yvonne Wollmann, Lindsay Walton, Julie Storing, Kyung Brown, Leslie Verfaillie, Yvette Obando, Anny Tran, Tracy Manfield and Shannon Claridad. I’m also grateful to all the friends I

made in the SE department. I would like to thank Brian West, Adrielly Razzini, Ben Katko, Mike Morano, Sergio Suarez, Karan Taneja, Sumit Gupta, and Mayank Chadha.

Rooting for me from the other side of the planet were my always supportive friends from India. A special note goes to the friends who always asked me when I was going to book my flights for India – Anirban Mandi, Soumya Dey, Sourav Gupta, Souradeep Shome. My heartfelt thanks are also due to (in random order) Sourav Das, Suneet Meena, Amit Das, Souvik Khankari, Subhodeep Kabi, Suraj Pratap Singh, Rohan Dharmadhikari, Sanil Naik, Gitanjali Deka, Jenasree Hazarika, Kaushik Sarkar, Shivani Gupta, Krishna Dutta, Soumya Gorai, Samrat Ray,

I cannot conclude this section without thanking my Master’s thesis advisor Prof. Anjan Dutta who helped me in developing a keen interest in research. I am also grateful to Prof. Sajal Deb, Prof. Arunasis Chakraborty, Prof. Kaustubh Dasgupta, and Prof. Budhaditya Hazra for their invaluable support during my time at IIT Guwahati. A special note goes to my undergraduate professors from NIT Durgapur – Prof. Alope Datta, Prof. Soumya Bhattacharyya.

Portions of this dissertation have been published or are currently being considered or prepared for publication.

Chapter 2, in part, has been published in the following paper: **Datta, D.** and Lanza di Scalea, F. (2022). High-Speed Inspection of Rails by Passive Ultrasonic Monitoring. *Journal of Nondestructive Evaluation, Diagnostics and Prognostics of Engineering Systems*, 5(4). <https://doi.org/10.1115/1.4055382>. The dissertation author was the primary investigator and author of this paper.

Chapter 3, in part, has been submitted for publication of the material as it may appear in the following paper: **Datta, D.** and Lanza di Scalea, F. Influence of Varying Operational Parameters

on the Defect Detection Performance of a High-Speed Ultrasonic Rail Inspection System During Field Tests. Submitted to *Experimental Mechanics*. The dissertation author was the primary investigator and author of this paper.

Chapter 4, in part, is currently being prepared for submission for publication of the material as it may appear in the following paper: **Datta, D.**, Hosseinzadeh, A. Z., Lanza di Scalea, F. Development of an Improved High-Speed Passive Rail Inspection System. The dissertation author was the primary investigator and author of this paper.

Chapter 5, in part, has been submitted for publication of the material as it may appear in the following paper: **Datta, D.**, Cui, R., Hosseinzadeh, A. Z., Lanza di Scalea, F. Non-contact Ultrasonic Sonar-based Ranging Technique for In-motion 3D Railroad Tie Deflection Measurements. Submitted to *Transportation Geotechnics*. The dissertation author was the primary investigator and author of this paper.

Chapter 6, in part, has been published in the following paper: **Datta, D.**, Hosseinzadeh, A. Z., Cui, R., & Lanza di Scalea, F. (2023). High-Speed 3D Railroad Tie Deflection Mapping in Real-Time Using an Array of Air-Coupled Non-contact Transducers. *Lecture Notes in Civil Engineering*, 254 LNCE, 895–904. The dissertation author was the primary investigator and author of this paper.

Chapter 7, in part, is currently being prepared for submission for publication of the material as it may appear in the following paper: **Datta, D.**, Hosseinzadeh, A. Z., Cui, R., Lanza di Scalea, F. In-Motion Ultrasonic Non-contact Full-Field Railroad Crosstie Deflection Measurements During Full-Scale Field Tests. The dissertation author was the primary investigator and author of this paper.

VITA

- 2014 Bachelor of Technology in Civil Engineering (with distinction), National Institute of Technology Durgapur, India.
- 2015 Master of Technology in Structural Engineering, Indian Institute of Technology Guwahati, India.
- 2015-2017 Teaching Assistant, Indian Institute of Technology Guwahati, India.
- 2018 Assistant Professor, Assam Engineering College, Guwahati, India.
- 2018-2022 Graduate Student Researcher, University of California San Diego, USA.
- 2021 & 2022 Associate-in (Course Instructor), University of California San Diego, USA.
- 2022 Doctor of Philosophy in Structural Engineering, University of California San Diego, USA.

PUBLICATIONS

JOURNAL ARTICLES:

1. **Datta, D.** and Lanza di Scalea, F. (2022). High-Speed Inspection of Rails by Passive Ultrasonic Monitoring. *Journal of Nondestructive Evaluation, Diagnostics and Prognostics of Engineering Systems*, 5(4). <https://doi.org/10.1115/1.4055382>
2. Hosseinzadeh, A. Z., **Datta, D.**, Lanza di Scalea, F. (2022). In-Motion Railroad Tie Deflection Measurement via Ultrasonic Airborne Sonar and Computer Vision Techniques. *Research in Nondestructive Evaluation*, 1–21. DOI: 10.1080/09349847.2022.2136808.
3. **Datta, D.** and Lanza di Scalea, F. Influence of Varying Operational Parameters on the Defect Detection Performance of a High-Speed Ultrasonic Rail Inspection System During Field Tests. Submitted to *Experimental Mechanics*.

4. **Datta, D.**, Cui, R., Hosseinzadeh, A. Z., Lanza di Scalea, F. Non-contact Ultrasonic Sonar-based Ranging Technique for In-motion 3D Railroad Tie Deflection Measurements. Submitted to *Transportation Geotechnics*.

SELECT CONFERENCE PROCEEDINGS:

1. **Datta, D.**, Hosseinzadeh, A. Z., Cui, R. and Lanza di Scalea, F., (2022). High-Speed 3D Railroad Tie Deflection Mapping in Real-Time Using an Array of Air-Coupled Non-contact Transducers. *European Workshop on Structural Health Monitoring*, Palermo, Italy. (Awarded 1st place in Best Student Paper Category).
2. Hosseinzadeh, A. Z., **Datta, D.**, and Lanza di Scalea, F., (2022). Railroad Crosstie Deflection Measurement via Ultrasonic Airborne Sonar and Computer Vision Techniques. *ASNT Research Symposium*, USA.
3. Hosseinzadeh, A. Z., **Datta, D.** & Lanza di Scalea, F. (2022). Artificial Intelligence-based Approach to Estimate Relative Deflection of Railroad Ties Using Airborne Ultrasonic Testing. *Health Monitoring of Structural and Biological Systems (SPIE)*, Anaheim, USA. (Awarded Best Student Paper Award)
4. **Datta, D.**, Batista, I., Zare Hosseinzadeh, A., and Lanza di Scalea, F., (2021). High-speed Inspection of Rails by Output-only Ultrasonic Monitoring", *48th Annual Review of Progress in Quantitative Nondestructive Evaluation (QNDE)*, USA. (Awarded best paper in the technical session).
5. **Datta, D.**, Cui, R., and Lanza di Scalea, F. (2021). High-speed Rail Inspection by a Non-contact Passive Ultrasonic Technique. *Transportation Research Board 2021 Annual Meeting*, Washington D.C., USA.
6. **Datta, D.**, Liang, A., Cui, R. and Lanza di Scalea, F., (2020). Defect Detection Performance of a High-Speed Rail Inspection System from Passive Acoustic Identification. *Sensors and Smart Structures Technologies for Civil, Mechanical, and Aerospace Systems (SPIE)*, Anaheim, USA.
7. **Datta, D.**, Cui, R., Batista, I., and Lanza di Scalea, F. (2021). Application of a High-Speed Non-Contact Ultrasonic Technique Coupled with Statistical Data Redundancy for Rail Inspection. *International Workshop on Structural Health Monitoring*, USA.

ABSTRACT OF THE DISSERTATION

**Topics on In-motion Non-contact Ultrasonic Structural Monitoring
of Railroad Tracks**

by

Diptojit Datta

Doctor of Philosophy in Structural Engineering

University of California San Diego, 2022

Professor Francesco Lanza di Scalea, Chair

Internal defects in rails and degrading ballast support conditions in railroad cross-ties (sleepers) are some of the primary causes of train derailments. Current ultrasonic rail inspection techniques can operate up to speeds of 25 mph. Lower testing speeds result in traffic disruptions and are, therefore, not a sustainable inspection solution. Moreover, existing techniques for detecting degraded tie-ballast interface conditions (e.g., center-binding) require transducers mounted on individual ties and do not support in-motion testing. Techniques introduced in this dissertation have the potential of operating at revenue speeds using the concept of a smart train,

with onboard transducers, a data-acquisition system, and real-time data processing, to flag defective rails and crossties during regular service runs.

The first part of this study presents a high-speed non-contact rail inspection technique that utilizes an array of capacitive air-coupled ultrasonic transducers in an output-only mode to extract a transfer function for a rail segment in a passive manner. The passive approach utilizes the ambient excitation of the rail induced by the different mechanisms of rail-wheel interaction. The extracted transfer function is sensitive to the presence of internal rail flaws such as transverse defects. Features from the transfer function are tracked using a statistical outlier analysis with an adaptive baseline to compute a parameter called the Damage Index (DI) that determines if the probed rail segment has a discontinuity. Performance of the system, in terms of receiver operating characteristic curves, are presented from field tests conducted at the Transportation Technology Center Inc. (TTCI) at testing speeds of up to 80 mph.

The second part of this study introduces a non-contact railroad tie inspection system using an ultrasonic sonar-based ranging technique for detecting ties with center-binding support conditions. A transducer array placed parallel to the railroad tie, is used in pulse-echo mode, and full-field tie deflection profiles are computed using a reference-based cross-correlation. Proof-of-concept tests for deflection measurements in a 3-point bending test are presented. In-motion field tests were performed on a replica railroad track at the Rail Defect Testing Facility and a BNSF yard by mounting an inspection prototype on a train car.

Chapter 1. Introduction

1.1. Motivation

Non-Destructive Evaluation (NDE) and Structural Health Monitoring (SHM) techniques are widely being used to ensure safety and reliability during the service life of various structural components in the aerospace, civil and railroad industry. One of the key challenges in the NDE community is the lack of rapid inspection techniques that facilitate frequent and autonomous inspection of structural components. Rapid inspection techniques are of particular interest in the railroad industry which transports more than 10,000 billion freight ton-kilometers and 3000 billion passenger-kilometers every year around the world [1]. Most existing techniques for railroad inspections are contact based [2], require specialized equipment, and result in traffic disruptions. Such techniques, are therefore, not feasible for monitoring thousands of miles of railroad tracks. This dissertation introduces two techniques with the potential of high-speed inspections for rails and railroad ties. The techniques utilize non-contact air-coupled ultrasonic transducers mounted on a regular train, with onboard data processing capabilities, that introduces the potential of inspections during normal service runs at revenue speeds. Non-contact inspections at high speeds also introduces the possibility of compounding data from multiple train passes, thereby introducing redundancies and improving the defect detection performance.

1.2. Scope

The first part of this dissertation introduces the high-speed rail inspection and includes chapters 2, 3, and 4. The rail inspection technique utilizes an array of capacitive air-coupled ultrasonic transducers in continuous recording mode to extract a reconstructed Green's function

(transfer function or impulse response function in time domain) [3-8] for a rail segment in a passive manner. The passive approach utilizes the ambient excitation [9-11] of the rail induced by the wheels of the test car and eliminates the need of a controlled source. A normalized cross correlation operator with modified Welch's periodogram technique is used to extract the transfer function of the rail segment which is independent of the frequency spectrum of the random excitation source (wheels). Presence of discontinuities in the rail reduces the signal-to-noise ratio of the reconstructed transfer function. Features from the transfer function are statistically tracked using an outlier analysis with an adaptive baseline to compute a parameter called the Damage Index (DI) which determines if the probed rail segment has a discontinuity. Full-scale field tests were carried out with a prototype at the Transportation Technology Center Inc (TTCI) in Pueblo, Colorado at testing speeds of up to 80 mph. Discontinuity detection performance in terms of identifying joints, welds and known transverse defects through Receiver Operating Characteristic (ROC) curves were studied for a range of varying operational parameters such as acoustic signal strength, baseline distribution length, prototype location, testing speeds. Data from multiple passes of the train over the same rail segment were compounded to further introduce redundancies and increase the rate of true detections and reduce the rate of false alarms. The use of a non-contact continuously controlled acoustic source, as the input to excite the rail is also introduced to further improve the discontinuity detection performance.

The second part of this dissertation introduces the railroad tie inspection technique for measuring tie deflections and includes chapters 5,6 and 7. The railroad tie inspection technique utilizes an array of capacitive ultrasonic transducers arranged parallel to the length of the railroad tie. The transducer array is used in pulse-echo mode and distances from the transducers to the tie surface are measured by tracking the time-of-flight of the waves reflected from the tie surface. A

reference-based cross-correlation operation is introduced to compute the time-of-flight [12-13], wherein one of the transducers is used as a reference for the distance measurements. The reference-based cross-correlation ensures accurate peak-detection for time-of-flight based differential distance measurements and ensures robustness against variabilities of wave speed in air, elevations of different tie surfaces, etc. An acoustic signal strength-based technique is introduced to differentiate between signals reflected from ties and ballast based on wave scattering phenomenon. Tests were performed as a proof-of-concept on a slender wooden beam to measure deflections in loaded and unloaded conditions. Dynamic tests were also performed to determine the resolution of the system. Field tests on a replica test track with wood ties, at walking speeds, were performed at the Rail Defect Testing Facility at University of California San Diego by mounting the prototype on a test-cart. 3D surface deflection profiles of railroad ties from these tests are presented. Tests were also conducted at a BNSF yard, at walking speeds, by mounting the inspection system on a loaded tank car to simulate real world conditions.

1.3. Outline of the Dissertation

The outline of the dissertation is as follows:

Chapter 2 describes the digital signal processing routines used for the dual-output extraction of the transfer function in a passive only manner. A Damage Index parameter used for tracking the transfer functions through a statistical outlier analysis using Mahalanobis Squared Distance is introduced. The data acquisition system used in the field tests conducted at the Transportation Technology Center Inc. (TTCI) is also described.

Chapter 3 evaluates the performance of the passive rail inspection system in detecting rail discontinuities such as joints, welds, transverse defects for a range of different operational

parameters such as acoustic signal strength, testing speed, length of baseline distribution, location of the inspection prototype and data compounded from multiple test runs. Results from tests conducted at TTCI at speeds of up to 80 mph are presented.

Chapter 4 describes the use of a continuously controlled, non-contact acoustic source used in tandem with the wheel excited signal generation to improve the stability of the reconstructed transfer function. Laboratory tests conducted in selecting the optimum acoustic source are presented. Results from tests conducted at TTCI at speeds of up to 40 mph are also presented with the use of an acoustic source.

Chapter 5 introduces the concept of sonar-based ultrasonic ranging for computing the deflection profiles of railroad tie beams. Results from laboratory tests as a proof-of-concept for evaluating the deflection of a slender wood beam in a 3-point bending test are presented.

Chapter 6 describes presents results from field tests conducted with the tie inspection system at the Rail Defect Testing Facility (RDTF) at UC San Diego.

Chapter 7 presents results from tests conducted, at walking speeds, at a BNSF yard with the inspection system mounted on a loaded train car.

Chapter 8 presents the concluding remarks and possible avenues for future research.

1.4. References

[1] *Statistics | UIC - International union of railways*. (n.d.). Retrieved November 11, 2022, from <https://uic.org/support-activities/statistics/>

[2] Anon, F. (1990). Rail-flaw detection. A science that works. *Railway Track and Structures*, 86(5), 30–32.

- [3] Lobkis, O. I., & Weaver, R. L. (2001). On the emergence of the Green's function in the correlations of a diffuse field. *The Journal of the Acoustical Society of America*, 110(6), 3011. <https://doi.org/10.1121/1.1417528>
- [4] Weaver, R., & Lobkis, O. (2002). On the emergence of the Green's function in the correlations of a diffuse field: pulse-echo using thermal phonons. *Ultrasonics*, 40(1–8), 435–439. [https://doi.org/10.1016/S0041-624X\(02\)00156-7](https://doi.org/10.1016/S0041-624X(02)00156-7)
- [5] Snieder, R. (2004). Extracting the Green's function from the correlation of coda waves: A derivation based on stationary phase. *Physical Review E*, 69(4), 046610. <https://doi.org/10.1103/PhysRevE.69.046610>
- [6] Derode, A., Larose, E., Tanter, M., Rosny, J. de, Tourin, A., Campillo, M., & Fink, M. (2003). Recovering the Green's function from field-field correlations in an open scattering medium (L). *The Journal of the Acoustical Society of America*, 113(6), 2973. <https://doi.org/10.1121/1.1570436>
- [7] Roux, P., & Fink, M. (2003). Green's function estimation using secondary sources in a shallow water environment. *The Journal of the Acoustical Society of America*, 113(3), 1406. <https://doi.org/10.1121/1.1542645>
- [8] Sabra, K. G., Roux, P., & Kuperman, W. A. (2005). Emergence rate of the time-domain Green's function from the ambient noise cross-correlation function. *The Journal of the Acoustical Society of America*, 118(6), 3524. <https://doi.org/10.1121/1.2109059>
- [9] Tippmann, J. D., Zhu, X., & Lanza Di Scalea, F. (2015). Application of damage detection methods using passive reconstruction of impulse response functions. *Philosophical Transactions of the Royal Society A: Mathematical, Physical and Engineering Sciences*, 373(2035). <https://doi.org/10.1098/RSTA.2014.0070>
- [10] Tippmann, J. D., & Lanza Di Scalea, F. (2014). Passive-only damage detection by reciprocity of Green's functions reconstructed from diffuse acoustic fields with application to wind turbine blades. *Journal of Intelligent Material Systems and Structures*, 26(10), 1251–1258. <https://doi.org/10.1177/1045389X14538539>
- [11] Tippmann, J. D., & Lanza di Scalea, F. (2016). Passive-only defect detection and imaging in composites using diffuse fields. *Conference Proceedings of the Society for Experimental Mechanics Series*, 7, 67–72. https://doi.org/10.1007/978-3-319-21762-8_8/COVER
- [12] Queiros, R., Girao, P. S., & Serra, A. C. (2007). Cross-correlation and sine-fitting techniques for high resolution ultrasonic ranging. *IEEE Instrumentation and Measurement Technology Conference Proceedings*, 552–556. <https://doi.org/10.1109/IMTC.2006.328588>
- [13] Khyam, M. O., Ge, S. S., Li, X., & Pickering, M. R. (2017). Highly accurate time-of-flight measurement technique based on phase-correlation for ultrasonic ranging. *IEEE Sensors Journal*, 17(2), 434–443. <https://doi.org/10.1109/JSEN.2016.2631244>

Chapter 2. Development of a High-Speed Ultrasonic Rail Inspection Technique

2.1. Abstract

This chapter presents a novel approach for high-speed inspection of rails with the potential of operating at revenue speeds using a non-contact, passive ultrasonic sensing technique. The technique utilizes air-coupled transducers that pick up the leaky ultrasonic surface waves (leaky waves) generated by the wheels of the train into the rail and does not require a controlled source of excitation. To extract the Green's function between two points on the rail, this technique utilizes the concept of inter-segment and intra-segment averaging, as a modification to the traditional Welch's periodogram method, for computing the auto-power spectrum and cross-power spectrum, respectively. The features from this Green's function are statistically analyzed to determine if a rail segment has existing damage (internal defects) or discontinuities (joints and welds). A prototype with multiple pairs of capacitive ultrasonic transducers was developed to perform the inspection in a non-contact, passive-only, high-speed manner.

2.2. Introduction

Internal defects in rails are a major cause of train derailment related accidents all around the world. In a recent study, the United States Federal Railroad Administration (FRA) reported 4961 train accidents during 2017-2020 out of which 3437 (69.2 %) were caused by derailments due to defects in rails [1]. The four major types of rail defects causing these accidents were identified as: 1. Transverse fissure (TF): a fracture originating in the interiors of the rail-head marked by the presence of a nucleus; 2. Detail fracture (DF): a progressive fracture originating at

or near the surface of the rail head without a nucleus; 3. Vertical split head (VSH) : a crack propagating vertically through or near the middle of the rail-head; 4. Horizontal split head (HSH): a crack developed inside the rail-head and progressing horizontally in all directions [2]. TF and DF are classified as transverse defects (TD) since they progress along the width of the railhead (transverse axis). VSH and HSH are classified as longitudinal type defects since they progress along the rail's longitudinal axis. TDs are the most common type of rail defects and account for the majority of train derailments [3].

Internal rail flaw detection at early stages of initiation can be extremely beneficial for the sustainable long-term maintenance of rails. Non-destructive evaluation (NDE) based rail flaw detection has been an active area of research in the past few decades [4]. Ultrasonic based techniques have been the most popular among various NDE techniques [5]. An existing and most widely used technology for internal rail flaw detection is based on ultrasonic tests performed by piezoelectric transducers hosted in fluid-filled wheels [6], known as Rolling Search Units (RSU). The downside of these RSUs is that they operate at speeds (~25 mph) much lower than the revenue speeds (~ 60 mph) of railroad tracks and result in traffic disruptions and temporary closures for maintenance. To increase the testing speeds, various researchers started working on high-speed rail inspection techniques. Wooh et al. [7] proposed a high-speed rail inspection technique based on the Doppler effect for frequency shifts at high-speeds between a train-mounted transducer and the rail surface. Their technique, however, was limited to detecting rail surface irregularities. Mandriota et al. [8] introduced a filter-based image processing technique for detecting defects in rails. Their technique, again, was limited to surface defects visible to the camera. Ho et al. [9] introduced the concept of monitoring rail-wheel interactions using Fiber Bragg Grating (FBG) transducers attached to the rail. A major downside of this technique is the non-feasibility of

attaching large number of FBG transducers along thousands of miles of railroad track. Another investigation on a non-contact inspection technique was based on electromagnetic acoustic transducers (EMATs) [10-13]. This technique suffered from the drawback of requiring low lift-off distances from the rail surface and the need for hefty magnets to reach the required sensitivity. Ultrasonic non-contact techniques have been also studied utilizing either hybrid laser/air-coupled approaches [14-15] or completely air-coupled approaches [16]. These systems remained limited by the requirement for an active “pulsed” ultrasonic excitation.

More recently, UCSD researchers [17-20] have investigated the possibility for non-contact rail inspection without using an active ultrasonic source, but rather exploiting the natural acoustic excitations imparted by the rolling wheels of a travelling train. This is therefore a case of “passive” or “output-only” inspection that utilizes solely ultrasonic receivers. These receivers are air-coupled transducers that stay above the rail clearance envelope (3 in) for non-contact probing. The sensors are installed on a travelling train car enabling a new concept of “smart train.” If successfully developed, this capability would (a) enable rail inspections at regular (revenue) speeds without traffic disruptions, and (b) maximize the Probability of Detection (POD) while minimizing the Probability of False Alarms (PFA) by exploiting the redundancy afforded by the multiple train passes over the same section of rail. This technology uses concepts of passive reconstruction of a system’s Green’s function (or transfer function) that have been developed in various fields, including seismology [21-22], underwater acoustics [23-25], and also structural inspections [26-30]. Examples include ambient vibrations in bridges induced by traffic [31-32], aerodynamic

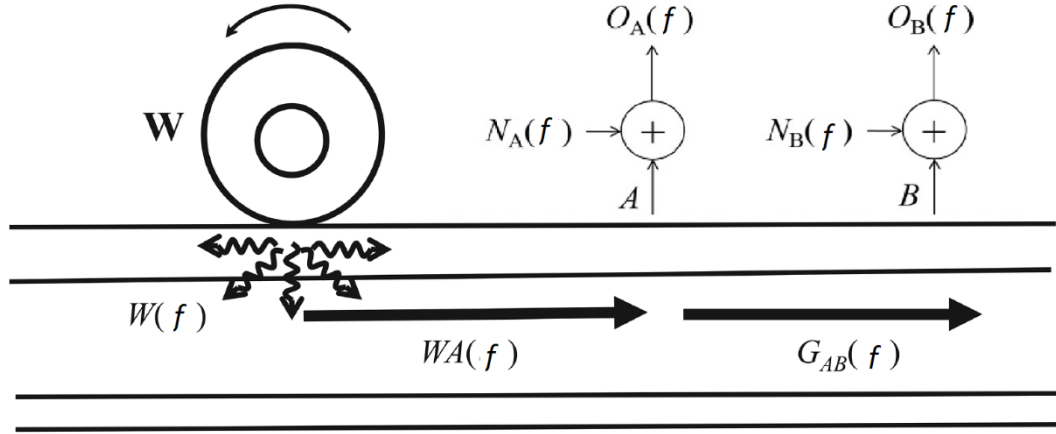


Figure 2.1 Schematic diagram of passive transfer function reconstruction

vibration signatures from aircraft wings and wind-turbine blades [33], wind-induced vibrations in high-rise buildings [34], among others.

2.3. Theory and Background

2.3.1. Transfer Function Extraction (Dual-Output System)

Consider the schematic in Fig. 2.1, showing a rail track dynamically excited by a rolling wheel W , and the acoustic responses are measured by two air-coupled ultrasonic receivers at locations A and B . Assume that both receivers are only sensitive to waves propagating unidirectionally from left to right. The aim is to isolate the transfer function of the test structure (rail) between location A and location B which is denoted by $G_{AB}(f)$. The excitation $W(f)$ is unknown, uncontrolled and comes from the wheels, and it is assumed to be piecewise-stationary, meaning that its statistics do not change during the observation time windows of $O_A(f)$ and $O_B(f)$. $WA(f)$ denotes the transfer function between the wheel and location A . Uncorrelated noise components $N_A(f)$ and $N_B(f)$ are also assumed to be present at each of the two outputs. Assuming all systems to be linear, the outputs at locations A and B with added noise can be written as:

$$O_A(f) = W(f) \cdot WA(f) + N_A(f) \quad \text{receiver A} \quad (2.1)$$

$$O_B(f) = W(f) \cdot WA(f) \cdot G_{AB}(f) + N_B(f) \quad \text{receiver B} \quad (2.2)$$

The transfer function $G_{AB}(f)$ can be computed as a ratio of the cross-power spectrum between responses at A and B divided by the auto-power spectrum of the response at A . Both the cross-power spectrum and auto-power spectrum are computed in an ensemble average sense, by dividing the time-series into n segments, with a 50% overlap between segments to avoid loss of information near the ends of each segment. A Hamming window is also applied to each time segment before computing the Fast Fourier Transform (FFT) which is a common practice in the signal processing domain to prevent side-lobe leakage [35]. Intra-segment averaging is used for computing the cross-power spectrum and inter-segment averaging is used to compute the auto-power spectrum for reasons that will be clear subsequently. Let us first compute the intra-segment cross-power spectrum between outputs at A and B as shown below:

$$\begin{aligned} \langle \text{Cross_Power} \rangle_{\text{intra-segment}} &= \langle O_{Ai}^*(f) \cdot O_{Bi}(f) \rangle = \langle |W(f)|^2 \cdot |WA(f)|^2 \cdot G_{AB}(f) \rangle + \\ &\quad \langle W^*(f) \cdot WA^*(f) \cdot N_B(f) \rangle + \langle W(f) \cdot WA(f) \cdot G_{AB}(f) \cdot N_A^*(f) \rangle + \\ &\quad \langle N_A^*(f) \cdot N_B(f) \rangle = |W(f)|^2 \cdot |WA(f)|^2 \cdot G_{AB}(f) \end{aligned} \quad (2.3)$$

where $*$ denotes the complex conjugate, $\langle \quad \rangle$ denotes an ensemble average, $||$ denotes the absolute value, and i is an index for the different segments over which the averaging is done. The terms $\langle W^*(f) \cdot WA^*(f) \cdot N_B(f) \rangle$, $\langle W(f) \cdot WA(f) \cdot G_{AB}(f) \cdot N_A^*(f) \rangle$ and $\langle N_A^*(f) \cdot N_B(f) \rangle$ can be eliminated because the cross-power spectrum of uncorrelated signals (with no DC bias component) tends to zero in an averaged sense. Since the same segment (i) in responses at A and B is used, this averaging is termed as intra-segment averaging. Computation of the ensemble average is

impractical because an infinitely large number of realizations of a random process are required. If the random process, however, is assumed to be ergodic, the ensemble average is equal to the time-average, which can be easily computed. Therefore, assuming the process to be ergodic, we can express the time-averaged cross-power spectrum as follows:

$$\langle \text{Cross_Power} \rangle_{\text{intra-segment}} = \frac{1}{n} \sum_{i=1}^n O_{A,i}^*(f) \cdot O_{B,i}(f) = |W(f)|^2 \cdot |WA(f)|^2 \cdot G_{AB}(f) \quad (2.4)$$

where n is the total number of segments. It is clear that the cross-power spectrum alone does not isolate the transfer function $G_{AB}(f)$ since it is ‘colored’ by the spectrum of the wheel-induced excitation $|W(f)|^2$ and the transfer function $|WA(f)|^2$ between the excitation source and transducer A . The cross-power spectrum is therefore normalized by the auto-power spectrum of the response at A . Let us first compute the auto-power spectrum using the same intra-segment averaging as discussed above. The auto-power spectrum at A can be written as:

$$\begin{aligned} \langle \text{Auto_Power}_A \rangle_{\text{intra-segment}} &= \langle O_{Ai}^*(f) \cdot O_{Ai}(f) \rangle = \langle |W(f)|^2 \cdot |WA(f)|^2 \rangle + \\ &\langle W^*(f) \cdot WA^*(f) \cdot N_A(f) \rangle + \langle W(f) \cdot WA(f) \cdot N_A^*(f) \rangle + \langle N_A^*(f) \cdot N_A(f) \rangle \\ &= |W(f)|^2 \cdot |WA(f)|^2 + |N_A(f)|^2 \end{aligned} \quad (2.5)$$

Again, assuming ergodicity, Eq. (2.5) may be rewritten as a time-average over n segments:

$$\langle \text{Auto_Power} \rangle_{\text{intra-segment}} = \frac{1}{n} \sum_{i=1}^n O_{A,i}^*(f) \cdot O_{A,i}(f) = |W(f)|^2 \cdot |WA(f)|^2 + |N_A(f)|^2 \quad (2.6)$$

The normalized cross-power spectrum can be obtained as:

$$\frac{\langle \text{Cross_Power} \rangle}{\langle \text{Auto_Power} \rangle} = \frac{\frac{1}{\bar{n}} \sum_{i=1}^n O_{A,i}^*(f) \cdot O_{B,i}(f)}{\frac{1}{\bar{n}} \sum_{i=1}^n O_{A,i}^*(f) \cdot O_{A,i}(f)} = \frac{|W(f)|^2 \cdot |WA(f)|^2 \cdot G_{AB}(f)}{|W(f)|^2 \cdot |WA(f)|^2 + |N_A(f)|^2} \quad (2.7)$$

From Eq. (2.7), it is clear that the transfer function $G_{AB}(f)$ cannot be isolated if the noise term $|N_A(f)|^2$ is non-zero. The term $|N_A(f)|^2$ is non-zero because the auto-power spectrum of an uncorrelated signal cannot be eliminated if it is taken over the same time segment. This problem can be resolved by averaging the same time signal over different segments (inter-segment averaging). Doing this eliminates the noise term $|N_A(f)|^2$. The inter-segment auto-power spectrum for response at A is computed as:

$$\langle \text{Auto_Power}_A \rangle_{\text{inter-segment}} = \frac{1}{\bar{n}} \sum_{i=1}^{n-1} \sum_{j=i+1}^n O_{A,i}^*(f) \cdot O_{A,j}(f) \quad (2.8)$$

where i, j are indices for different segments of the same signal and $\bar{n} = {}^n C_2 = \frac{n!}{2(n-2)!}$ is the number of the possible combinations of two different segments for a total of n segments. Substituting $O_A(f)$ from Eq. (2.1) into Eq. (2.8), the auto-power spectrum can be written as:

$$\begin{aligned} & \langle \text{Auto_Power}_A \rangle_{\text{inter-segment}} \\ &= |W(f)|^2 \cdot |WA(f)|^2 + \frac{1}{\bar{n}} \sum_{i,j} N_{A,i}^*(f) \cdot N_{A,j}(f) \\ &= |W(f)|^2 \cdot |WA(f)|^2 \end{aligned} \quad (2.9)$$

The noise term ($N_{A,i}^*(f) \cdot N_{A,j}(f)$) is eliminated because the cross-power spectrum of uncorrelated noise averaged over different segments tends to zero. Inter-segment averaging,

however, introduces another problem. Strictly speaking, Eq. (2.9) is accurate only if the signals $W(f)$ and $WA(f)$ are correlated in both amplitude and phase over the different possible combinations of segments. This assumption is not true since conformity in phase cannot be assured for different segments. A more reasonable assumption would be that $W(f)$ and $WA(f)$ are correlated in amplitude, but not phase, among different segments. This problem is handled by forcing different segments to be in the same phase. Let us rewrite the response at sensor A by separating the output into signal and noise components in Eq. (2.1) as:

$$O_A(f) = W(f) \cdot WA(f) + N_A(f) = S_A(f) + N_A(f) \quad (2.10)$$

where $S_A(f)$ includes the correlated signal at A and $N_A(f)$ is the uncorrelated noise. Assuming $S_A(f)$ to be time-invariant during the observation window, each inter-segment cross-power spectrum will therefore have an amplitude that is consistent and a phase that is random.

Analytically:

$$\begin{aligned} \langle S_A^*(f) \cdot S_A(f) \rangle_{inter-segment} &= \frac{1}{\bar{n}} \sum_{i=1}^{n-1} \sum_{j=i+1}^n S_{A,i}^*(f) \cdot S_{A,j}(f) \\ &= \frac{1}{\bar{n}} \sum_{i,j}^n |S_{A,i}(f)| e^{-i\phi_{A,i}} \cdot |S_{A,j}(f)| e^{i\phi_{A,j}} = \frac{1}{\bar{n}} \sum_{i,j}^n |S_{A,i}(f)| \cdot |S_{A,j}(f)| e^{i\Delta\phi_{A,ij}} \end{aligned} \quad (2.11)$$

The signals in each segment are shifted appropriately in such a way that their phases are aligned in all segments and therefore phase correlation is enforced in addition to amplitude correlation. The appropriate time-lag of shift for each segment pair is determined by the maximum peak of the cross-correlation function between the two segments. This time-lag for each segment pair is computed as:

$$\tau_{ij} = \operatorname{argmax} \left(\int_{-\infty}^{+\infty} O_{A,i}^*(t) \cdot O_{A,j}(t + \tau) dt \right) \quad (2.12)$$

The final expression for the time-shifted, inter-segment averaged auto-power spectrum is written as:

$$\begin{aligned} \langle \text{Auto_Power} \rangle_{\text{inter-segment shifted}} &= \frac{1}{\bar{n}} \sum_{i=1}^{n-1} \sum_{j=i+1}^n O_{A,i}^*(f) \cdot O_{A,j}(f) \cdot e^{-i2\pi f \tau_{ij}} \quad (2.13) \\ &= |S_A(f)|^2 + \frac{1}{\bar{n}} \sum_{i,j} N_{A,i}^*(f) \cdot N_{A,j}(f) = |S_A(f)|^2 = |W(f)|^2 \cdot |WA(f)|^2 \end{aligned}$$

This technique efficiently removes the noise term since $\frac{1}{\bar{n}} \sum_{i,j} N_{A,i}^*(f) \cdot N_{A,j}(f) = 0$ for uncorrelated noise averaged over different segments. The normalized cross-power spectrum computed using this novel inter-segment auto-power spectrum successfully isolates the transfer function $G_{AB}(f)$ of the system as shown below:

$$\begin{aligned} \frac{\langle \text{Cross_Power} \rangle_{\text{intra-segment}}}{\langle \text{Auto_Power} \rangle_{\text{inter-segment shifted}}} &= \frac{\frac{1}{\bar{n}} \sum_{i=1}^n O_{A,i}^*(f) \cdot O_{B,i}(f)}{\frac{1}{\bar{n}} \sum_{i=1}^{n-1} \sum_{j=i+1}^n O_{A,i}^*(f) \cdot O_{A,j}(f) \cdot e^{-i2\pi f \tau_{ij}}} \\ &= \frac{|W(f)|^2 \cdot |WA(f)|^2 \cdot G_{AB}(f)}{|W(f)|^2 \cdot |WA(f)|^2} = G_{AB}(f) \quad (2.14) \end{aligned}$$

The time-domain transfer function (impulse-response function) can be then retrieved from the frequency domain through an inverse Fourier Transform as shown below:

$$G_{AB}(t) = \frac{1}{2\pi} \int_{-\infty}^{+\infty} G_{AB}(f) \cdot e^{ift} df \quad (2.15)$$

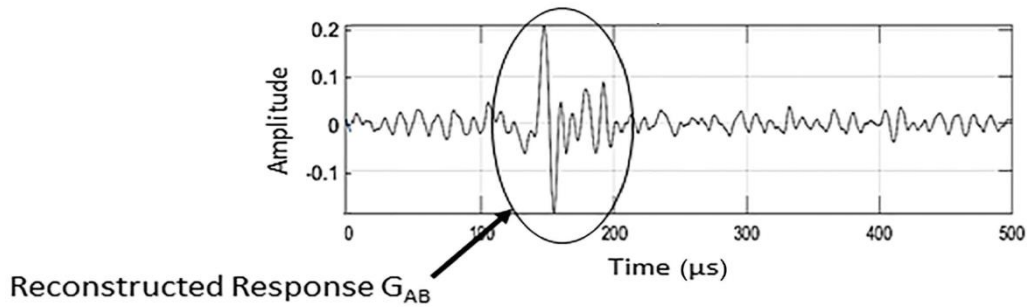


Figure 2.2 A sample transfer function in time domain

Prior to converting the transfer function to time domain, it is filtered in the frequency bands of 20 kHz - 40 kHz and 70 kHz – 120 kHz. These frequency bands were found to reconstruct a stable transfer function and were also most sensitive to rail discontinuities. Fig. 2.2 shows a typical reconstructed transfer function in time domain ($G_{AB}(t)$). The wave packet arrival at $\sim 160 \mu\text{s}$ indicates the time taken by the wave to travel the distance from point A to B (Fig. 2.1) which is around 460 mm (18 inches). The transfer function so obtained defines a system governed by the properties of the rail segment between the two transducers. This transfer function is sensitive to damage or discontinuities present in the rail between the points at which it is extracted. Presence of a discontinuity in the rail impedes the wave propagation resulting in a drop in the amplitude of the transfer function. Features from this impulse response function can be tracked statistically for changes along the length of the track and variations of these features with respect to a baseline distribution of features can be used to indicate whether a given segment of rail is pristine or damaged. The statistical outlier analysis used for tracking changes in the transfer function is discussed briefly in the following section.

2.3.2. Statistical Outlier Analysis

The final step in the data processing is an outlier analysis to compute a statistically robust metric called Damage Index (DI) related to the strength of the reconstructed transfer function. The

DI was calculated as the Mahalanobis Squared Distance [36] of the features of the transfer function from a probed location with respect to a baseline distribution of features. The DI metric is defined below in a multivariate sense:

$$D.I. = (x - \bar{x})^T \cdot Cov^{-1} \cdot (x - \bar{x}) \quad (2.16)$$

where x is the feature vector extracted from the passively reconstructed transfer function, \bar{x} is the mean of the feature vector from the baseline distribution, Cov is the covariance matrix of the baseline distribution, and T represents the matrix transpose operator. The feature vector $\{x\}_{4 \times 1}$ consists of the metric $variance^{-1}$ of the transfer function from four possible combinations of transfer functions from a group of sensors (discussed later). The statistical computation of the DI normalizes the data by the normal (baseline) data variability that occurs during a run. As such, compared to a simple deterministic metric such as the Euclidean distance, the statistical-based DI of Eq. (2.16) significantly improves the detection of anomalous behavior in the data. Moreover, the baseline distribution of the reconstructed signal features was collected adaptively at each position along the rail, by considering the preceding locations before the probed location. Such an adaptive baseline for defect detection eliminated the requirement of pristine training data, thereby improving the operational feasibility of the system. Finally, an “exclusive” version of the baseline was adopted, whereby extreme values of the DI (i.e., values larger than mean + twice the standard deviation) were removed from the baseline computation. This removal ensured that only pristine portions of rail were included in the baseline computation. High values of DI at specific locations of the rail indicate anomalous behavior and possible location of discontinuities such as welds, joints, or defects.

2.4. Data Acquisition System

2.4.1. Overview

A field deployable prototype for passive-only rail inspection was developed to perform rail defect detection at high speeds. The prototype consists of the sensor hardware, positioning equipment, vision equipment, and the data acquisition and processing units. A general diagram of the prototype is provided in Fig. 2.3

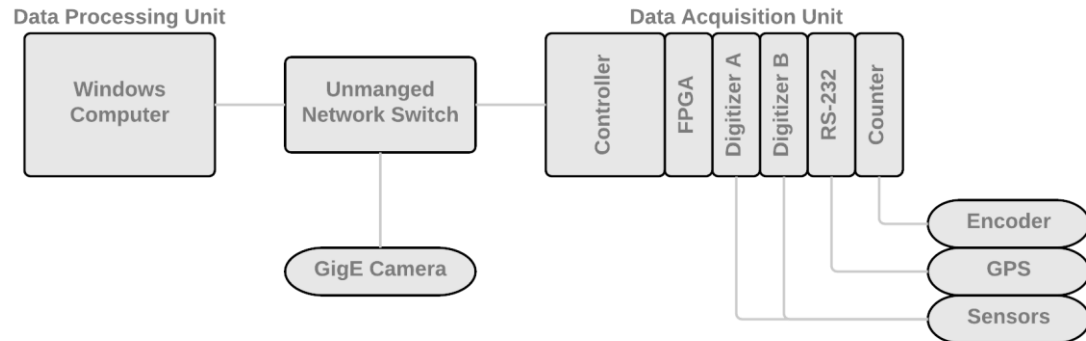


Figure 2.3 General prototype system diagram.

The sensor hardware consists of 12 air-coupled, non-contact, acoustic transducers. Additionally, 2 fore and 2 aft lasers are located on the prototype to provide alignment information between the sensor hardware and the rail. The positioning system includes a GPS receiver capable of position refresh rates of up to 100 Hz with a roof mounted antenna. Data from the GPS receiver is fed directly to the data acquisition unit. A vision system consisting of a GigE camera is connected to the data processing unit through an unmanaged network switch to record the rail for each test run. Lastly, the data acquisition unit consists of a National Instruments (NI) Real Time controller with a Flex-RIO FPGA, NI Digitizer, NI RS-232 Serial, and NI Counter/Timer to

provide real-time signal routing and storage. The data acquisition unit is connected to the data processing unit running LabVIEW Windows through Ethernet.

2.4.2.Sensor Hardware

Two arrays of capacitive air-coupled non-contact sensors are positioned 3 inches off the rail to guarantee noncontact probing of the rail. Additionally, four lasers, two fore and two aft, are mounted to determine alignment with the rail. The 12 capacitive sensors provide an optimal frequency range for rail inspection purposes. The receivers are inclined to provide directional sensing of the acoustic waves generated by the wheels, and to detect the leaky surface wave propagating in the railhead in accordance to Snell's law, as shown in Fig. 2.4. Class 2 photoelectric laser sensors (shown in Fig. 2.5) with PNP logic are used for determining the alignment of the prototype with the rail. A 15 V DC power supplies the required power to operate the sensor and logic. The capacitive and laser sensors signals are routed to Digitizers A and B on the data acquisition unit for further processing.



Figure 2.4 Prototype sensing hardware.



Figure 2.5 Prototype laser hardware.

2.4.3. Positioning System (Distance and Location Tracker)

The positioning system consists of the following: GPS receiver, GPS antenna, and encoder. The encoder was provided by TTCI during the fields test and was able to provide a 2-inch resolution. The GPS unit provided the latitude, longitude, and speed. The GPS receiver is a Novatel FLEX6-G1S-00G-0CN receiver with GPS, L1, SBAS, DGPS, GLIDE capabilities at 100 Hz position refresh rate with communication via RS-232. A GPS antenna, Novatel GNSS-501, receives L1 GPS+GLONASS, BeiDou B1, Galileo E1 signals to determine the location of the prototype. A 12 V DC power supply provides power to the GPS unit in Fig. 2.6. Data from the GPS unit is routed to the data acquisition unit in ASCII format and NMEA protocol. Lastly, the encoder TTL signal routed through a SCB-100 breakout box before connecting to the Counter card on the data acquisition unit.



Figure 2.6 Novatel GPS receiver (bottom) and antenna (top)

2.4.4. Vision System

The vision system (schematic shown in Fig. 2.7) consists of a Basler ace GigE, acA800-200gc color camera at 800 by 600-pixel resolution and 3 Smart Vision Over-Drive ODLW300-WHI-W LED Linear Lights to provide illumination for the camera. A variable focal length LMVZ4411 lens is mounted to the camera with the following specifications: 1/18", 4.4 – 11mm, F1.6 Manual C-Mount. For the tests, the camera was set to record images at 100 frames per second acquisition rate.

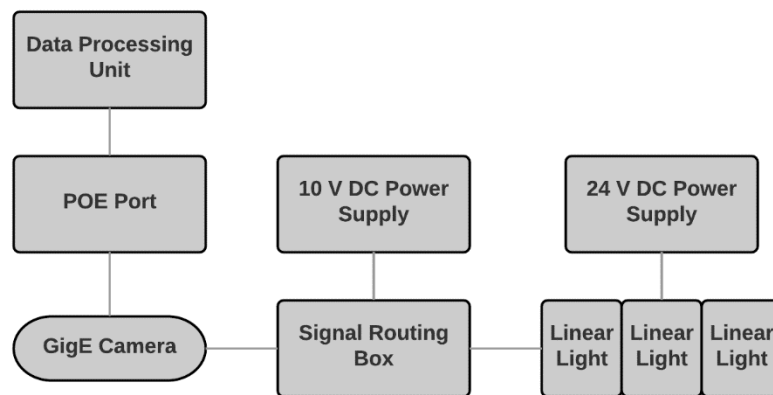


Figure 2.7 Vision system diagram.

The Basler ace camera (shown in Fig. 2.8) controls the Smart Vision strobe lights (shown in Fig. 2.9) through TTL pulses to the linear light PNP input line that correspond to the camera's exposure cycle. The linear lights are powered by an external DC power supply able to provide the 24 V DC at 19 Amps required. A signal routing box takes the I/O cable from the GigE camera and routes it appropriately for the PNP trigger line for the linear lights. A 10 V DC power supply provides the required circuit voltage to trigger the lights. This ensures synchronization between the linear lights and the camera so that during exposure, the lights are on. The Basler ace GigE camera is powered using a Power-Over-Ethernet (POE) Module so a common ethernet cables is used for data transmission and power.



Figure 2.8 Basler ace GigE camera.

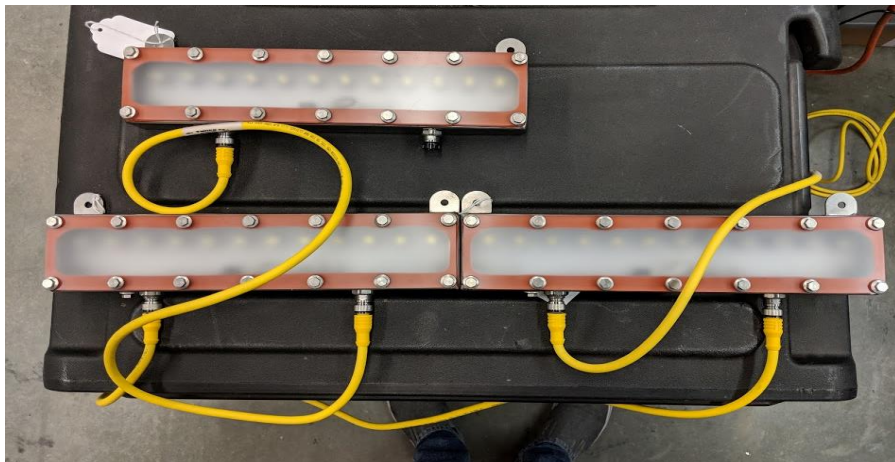


Figure 2.9 Smart Vision Over-Drive linear lights.

2.4.5. Data Processing Unit

The data acquisition and processing unit is composed of two systems. The first system is a National Instruments (NI) PXIe-8880 Real-Time (RT) controller, mounted on a NI PXIe-1082 chassis. The RT controller handles the signal routing for the NI FlexRIO PXIe-7975R FPGA. Data from the sensors is acquired on the NI PXI-5105 Digitizer A and B through SMB connection. GPS position is from the GPS receiver into NI PXI-8432/2 through RS-232., and encoder count is processed from the encoder TTL into NI PXI-6624 Counter/Timer through the SCB-100 breakout box. A frontal view of the data acquisition system is provided in Fig. 2.10. The PXIe-8880 RT controller runs LabVIEW RT 18.0, a 32-bit Pharlap system utilizing 4 GB of Random-Access Memory (RAM) and contains a 700 GB Solid State Drive (SSD) for raw data storage. A real-time operating system was selected to ensure deterministic processing and ensure sustained run-time with reduced computational jitter and instability. The raw data from Digitizer A and B is routed to the NI FlexRIO PXIe-7975R FPGA running LabVIEW FPGA 2018 to be processed. A time domain transfer function is then extracted from the FPGA and routed back to the controller before being sent to the Windows computer via ethernet. At the same time, raw data from Digitizer A and B is tagged with the encoder count, GPS location, GPS speed, and laser Boolean before saving onto the RT controller's internal SSD. Digitizer A contains the front capacitive sensors, 1 through 6, and the front two laser sensors. Digitizer B contains the rear capacitive sensors, 7 through 12, and the rear two laser sensors.

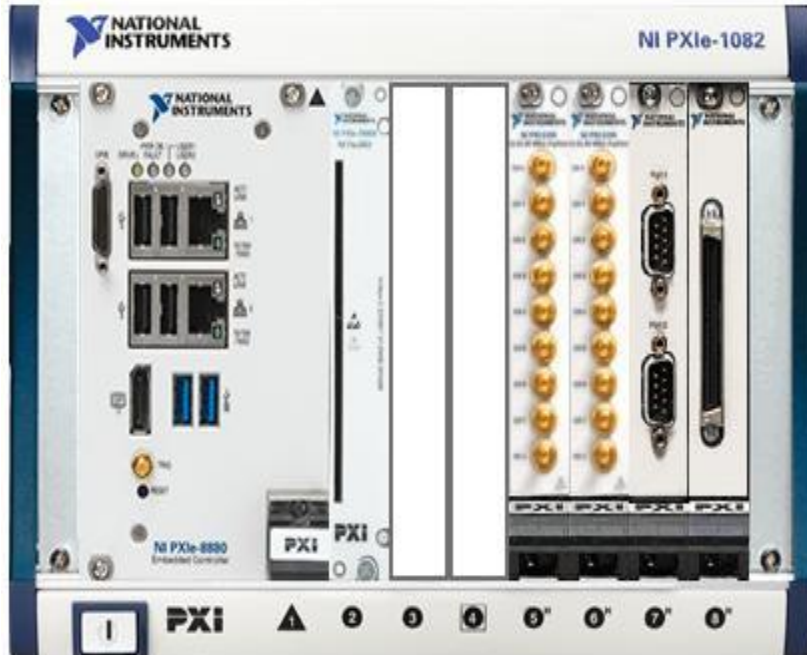


Figure 2.10 National Instruments Real-Time data acquisition unit.

The second system, the data processing unit, is a Windows 64-bit computer running LabVIEW 2018 whose primary purpose is to process the time-domain transfer function into a relevant Damage Index (DI) through a Mahalanobis Squared Distance (MSD) outlier analysis algorithm. The DI is then saved onto the Windows computer SSD with the relevant encoder distance, GPS position, GPS speed, and laser Boolean. Concurrent to the DI calculation, images gathered at 800 by 600-pixel resolution are streamed through ethernet to the data processing unit and tagged with the encoder count and GPS speed before saving on the SSD. A summary of the Data Acquisition and Processing unit is illustrated in Fig. 2.11.

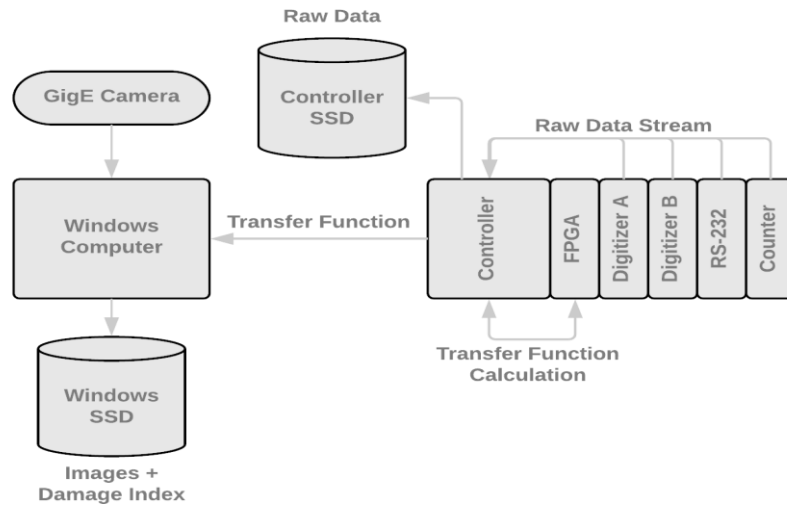


Figure 2.11 Data acquisition and processing unit diagram.

2.5. Field Tests

2.5.1. Test Setup

A set of full-scale field tests were conducted at TTCI, in Pueblo, USA with the passive sensing system mounted on a train. The prototype consisted of 12 ultrasonic capacitive air-coupled transducers (CAP-2 by VN Instruments Inc.) with a central frequency of 120 kHz and arranged as shown in Fig. 2.12. The transducers were arranged in 3 groups with each group having 4 transducers. This configuration resulted in four possible combinations of transfer functions from each group. The transducers were positioned at 3 inches from the rail's top surface at an angle of 6° with the vertical based on Snell's Law [37] to ensure unidirectional reception of the guided waves leaking from the rail into the air. A laser system consisting of two lasers was attached on both ends of the prototype to ensure that the sensor heads were properly aligned with the top surface of the rail. A high-speed camera (up to 100 frames per second) was installed alongside the prototype to continuously capture images of the inspected rail, as the test car moved, to build a

library of the locations of joints, welds, and marked defects on the rail (ground truth). A GPS receiver was mounted on top of the 5229 Test Car which tagged each data point from the transducers and the images captured by the camera to a GPS coordinate on the ground. GPS coordinates were used to assign the signals and ground truth features from the camera to a specific rail section on the track. A light source was also used to illuminate the rail to improve the quality of the images captured by the camera. The arrangement of the test setup, including the transducer prototype, camera, lights and lasers, is shown in Fig. 2.13. Fig. 2.14 shows the data acquisition and processing system placed inside the test car during the field tests at TTCI.

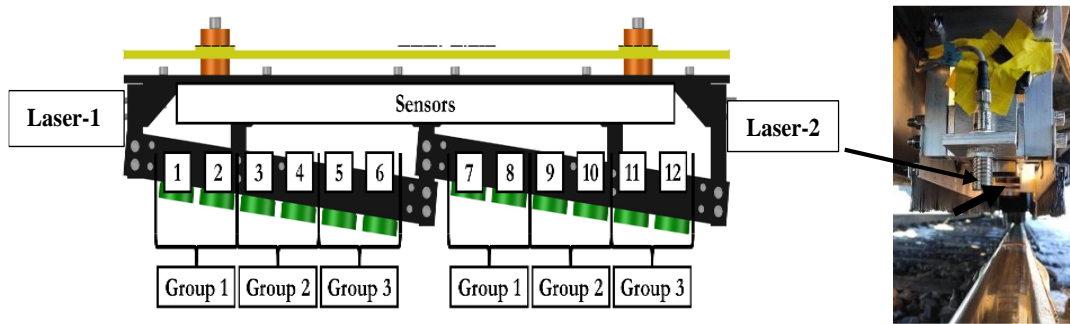


Figure 2.12 Sensor arrangement in prototype with location of alignment lasers.

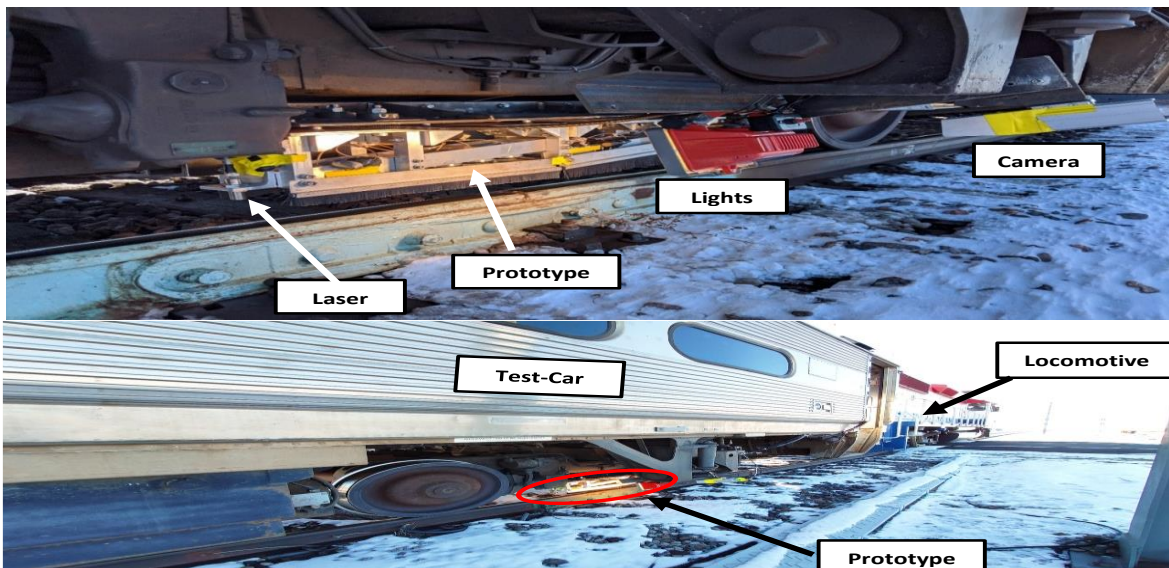


Figure 2.13 Prototype and accessory hardware mounted on the test-car.

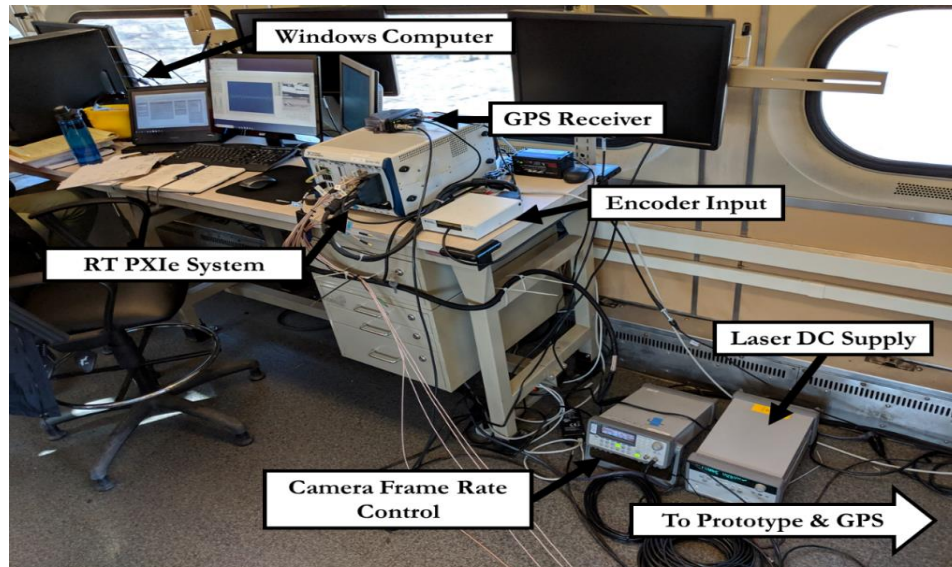


Figure 2.14 Data acquisition system (onboard) for the passive inspection system

2.5.2. Test Methodology

Tests runs were conducted on the High-Tonnage Loop (HTL) track and the Railroad Test Track (RTT) at TTCI by mounting the system on a train. Fig. 2.15 shows a diagram of the HTL and RTT rail tracks where the tests were conducted along with other test tracks present at TTCI. The HTL is a 2.7-mile-long test track that has numerous joints (22) and welds (275) since portions of the track are constantly replaced from damage due to heavy freight cars. The HTL also had three pre-identified defects (TD) that were marked in spray-paint and were picked up by the camera for their precise location. Speeds of 25 mph, 33 mph and 40 mph were tested on the HTL with three runs conducted at each speed. In addition, 12 continuously recorded runs were performed on the HTL at 40 mph and the results were compounded to introduce redundancies which significantly reduced the rate of false alarms in discontinuity detection. Tests were also conducted on the RTT at even higher speeds of 60 mph, 70 mph and 80 mph with 3 runs conducted at each speed. The RTT is a 13.7-mile-long test track with 1801 welds and 45 joints based on the image-based ground truth library. The RTT had no known defects present. In addition to the test runs, a settling run

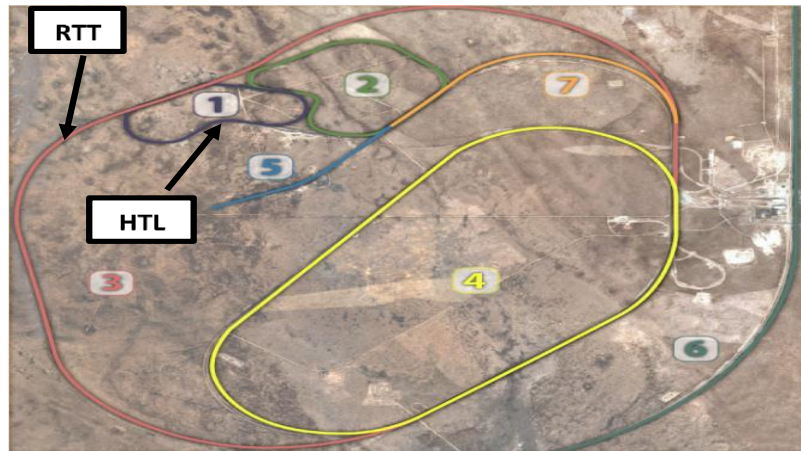


Figure 2.15 Test track layout at TTCI showing the HTL and RTT test tracks

was performed at 5 mph on the HTL and 30 mph on the RTT before the start of the actual testing. Data acquired during the settling runs was not used for analysis since the signal-to-noise ratio was low because of reduced speeds. The images acquired by the camera during the settling runs, however, were used for building the library of the discontinuity locations (ground truth). Since the camera refresh rate (frames captured per second) was kept same for all speeds, the settling runs resulted in greater number of images captured and facilitated the building of an acceptable ground truth. The sensor heads were mounted to probe the inner rail for both the HTL and the RTT and the runs were conducted in a clockwise sense. Data was acquired continuously for the 3 runs at each speed without halting the train. Data recording was stopped at the end of the 3 runs at each speed and the train was brought back to the starting point to begin testing at a different speed. Different speeds were used to test the effects of varying excitation source strengths and their influence on the stability of the reconstructed transfer function. Real-time analysis was performed on a National Instruments FPGA module running on LabVIEW Real-time platform. Extraction of the transfer function and computation of DI was performed in real-time, in tandem with data acquisition, as a quality control check on the acquired data. The first set of field tests was performed in November 2018 on the HTL. Another set of tests were conducted in June 2019 and

December 2019 on the HTL and RTT. The difference between the field tests in 2018 and those in 2019 was that in the latter tests the prototype was placed closer to the locomotive wheels for improved signal strengths. Finally, additional field tests were performed in June 2022 with an improved system consisting of a controlled and continuous acoustic source and is discussed in Chapter 4. Note that the number of joints, welds and known internal defects were different for the tests performed during the different field tests.

2.6. Acknowledgments

This work was funded by the US Federal Railroad Administration under contract 693JJ620C000024 with Dr. Robert Wilson as the Program Manager.

Chapter 2, in part, has been published in the following paper: **Datta, D.** and Lanza di Scalea, F. (2022). High-Speed Inspection of Rails by Passive Ultrasonic Monitoring. *Journal of Nondestructive Evaluation, Diagnostics and Prognostics of Engineering Systems*, 5(4). <https://doi.org/10.1115/1.4055382>. The dissertation author was the primary investigator and author of this paper.

2.7. References

- [1] Federal Railroad Administration (FRA) Office of Safety Analysis (2020). Train Accidents and Rates. Retrieved November 11, 2022, from <https://safetydata.fra.dot.gov/OfficeofSafety/default.aspx>.
- [2] Track Inspector Rail Defect Reference Manual FRA. Retrieved November 11, 2022, from <https://railroads.dot.gov/elibrary/track-inspector-rail-defect-reference-manual>.
- [3] Zakar, F., & Mueller, E. (2016). Investigation of a Columbus, Ohio train derailment caused by fractured rail. *Case Studies in Engineering Failure Analysis*, 7, 41–49. <https://doi.org/10.1016/J.CSEFA.2016.04.001>
- [4] Carlin, B. (1956). Ultrasonic flaw detector. 615, 555. US Patent.

- [5] Berger, H. (1980). Nondestructive testing of railroad rail. *Transportation Research Records*, 744, 22–26.
- [6] Anon, F. (1990). Rail-flaw detection. A science that works. *Railway Track and Structures*, 86(5), 30–32.
- [7] Wooh, S.C., Kim, C. C., & Wei, C. (1999). Real-time processing of continuous doppler signals for high-speed monitoring of rail tracks. *Review of Progress in Quantitative Nondestructive Evaluation*, 2245–2252. https://doi.org/10.1007/978-1-4615-4791-4_287
- [8] Mandriota, C., Nitti, M., Ancona, N., Stella, E., & Distante, A. (2004). Filter-based feature selection for rail defect detection. *Machine Vision and Applications*, 15(4), 179–185. <https://doi.org/10.1007/S00138-004-0148-3>
- [9] Ho, T. K., Liu, S. Y., Ho, Y. T., Ho, K. H., Wong, K. K., Lee, K. Y., Tam, H. Y., & Ho, S. L. (2008). Signature analysis on Wheel-rail interaction for rail defect detection. *IET Seminar Digest*, 2008(12216). <https://doi.org/10.1049/IC:20080342>
- [10] Alers, G. A. (1988). “Railroad rail flaw detection system based on electromagnetic acoustic transducers.” FRA Technical Reports (U.S Dept. of Transportation), OTIFRA/ORD-88/09.
- [11] Alers, G. A., & Manzanares, A. (1990). Use of surface skimming SH waves to measure thermal and residual stresses in installed railroad tracks. *Review of Progress in Quantitative Nondestructive Evaluation*, 1757–1764. https://doi.org/10.1007/978-1-4684-5772-8_226
- [12] Palmer, S. B., Dixon, S., Edwards, R. S., & Jian, X. (2005). Transverse and longitudinal crack detection in the head of rail tracks using Rayleigh wave-like wideband guided ultrasonic waves. *Nondestructive Evaluation and Health Monitoring of Aerospace Materials, Composites, and Civil Infrastructure*, 5767, 70–80. <https://doi.org/10.1117/12.598142>
- [13] Rose, J. L., Lee, C. M., Hay, T. R., Cho, Y., and Park, I. K. (2006). Rail inspection with guided waves. *Proc., 12th Asia-Pacific Conf. on NDT*, Asia-Pacific Federation for Non-Destructive Testing.
- [14] Coccia, S., Bartoli, I., Marzani, A., Lanza Di Scalea, F., Salamone, S., & Fateh, M. (2011). Numerical and experimental study of guided waves for detection of defects in the rail head. *NDT & E International*, 44(1), 93–100. <https://doi.org/10.1016/J.NDTEINT.2010.09.011>
- [15] Rizzo, P., Coccia, S., Bartoli, I., & Scalea, F. L. di. (2008). Noncontact rail monitoring by ultrasonic guided waves. *Encyclopedia of Structural Health Monitoring*. <https://doi.org/10.1002/9780470061626.SHM041>
- [16] Mariani, S., & di Scalea, F. L. (2017). Predictions of defect detection performance of air-coupled ultrasonic rail inspection system. *Structural Health Monitoring*, 17(3), 684–705. <https://doi.org/10.1177/1475921717715429>
- [17] Di Scalea, F. L., Zhu, X., Capriotti, M., Liang, A. Y., Mariani, S., & Sternini, S. (2017). Passive extraction of dynamic transfer function from arbitrary ambient excitations: application to

high-speed rail inspection from wheel-generated waves. *Journal of Computational and Nonlinear Dynamics*, 1(1), 011005–011005–011012. <https://doi.org/10.1115/1.4037517>

[18] Scalea, F. L. di, Sternini, S., & Liang, A. Y. (2018). Robust passive reconstruction of dynamic transfer function in dual-output systems. *The Journal of the Acoustical Society of America*, 143(2), 1019. <https://doi.org/10.1121/1.5024239>

[19] Datta, D., Liang, A., Cui, R., & Scalea, F. L. di. (2020). Defect detection performance of a high-speed rail inspection system from passive acoustic identification. *SPIE*, 11379, 196–204. <https://doi.org/10.1117/12.2558205>

[20] Datta, D., & di Scalea, F. L. (2022). High-speed inspection of rails by passive ultrasonic monitoring. *Journal of Nondestructive Evaluation, Diagnostics and Prognostics of Engineering Systems*, 5(4). <https://doi.org/10.1115/1.4055382>

[21] Chen, J. B., & Cao, J. (2020). Green's function for three-dimensional elastic wave equation with a moving point source on the free surface with applications. *Geophysical Prospecting*, 68(4), 1281–1290. <https://doi.org/10.1111/1365-2478.12928/CITE/REFWORKS>

[22] Wang, S., & Tkalčić, H. (2020). Seismic event coda-correlation's formation: implications for global seismology. *Geophysical Journal International*, 222(2), 1283–1294. <https://doi.org/10.1093/GJI/GGAA259>

[23] Brown, M. G., Godin, O. A., Williams, N. J., Zobotin, N. A., Zobotina, L., & Banker, G. J. (2014). Acoustic Green's function extraction from ambient noise in a coastal ocean environment. *Geophysical Research Letters*, 41(15), 5555–5562. <https://doi.org/10.1002/2014GL060926>

[24] Skarsoulis, E., & Cornuelle, B. (2018). Green's function emergence through cross-correlation of shipping noise. *The Journal of the Acoustical Society of America*, 144(3), 1731. <https://doi.org/10.1121/1.5067677>

[25] Tan, T. W., Godin, O. A., & Shen, Y. (2021). Rapid estimation of empirical Green's functions for passive acoustic characterization of dynamic shallow-water environments. *The Journal of the Acoustical Society of America*, 150(4), A82. <https://doi.org/10.1121/10.0007698>

[26] Tippmann, J. D., & Lanza Di Scalea, F. (2014). Passive-only damage detection by reciprocity of Green's functions reconstructed from diffuse acoustic fields with application to wind turbine blades. [Http://Dx.Doi.Org/10.1177/1045389X14538539](http://Dx.Doi.Org/10.1177/1045389X14538539), 26(10), 1251–1258. <https://doi.org/10.1177/1045389X14538539>

[27] Yang, Y., Xiao, L., Qu, W., & Lu, Y. (2017). Passive detection and localization of fatigue cracking in aluminum plates using Green's function reconstruction from ambient noise. *Ultrasonics*, 81, 187–195. <https://doi.org/10.1016/J.ULTRAS.2017.06.021>

[28] Michaels, J. E., & Michaels, T. E. (2005). Detection of structural damage from the local temporal coherence of diffuse ultrasonic signals. *IEEE Transactions on Ultrasonics, Ferroelectrics, and Frequency Control*, 52(10), 1769–1782. <https://doi.org/10.1109/TUFFC.2005.1561631>

- [29] Chehami, L., Rosny, J. De, Prada, C., Moulin, E., & Assaad, J. (2015). Experimental study of passive defect localization in plates using ambient noise. *IEEE Transactions on Ultrasonics, Ferroelectrics, and Frequency Control*, 62(8), 1544–1553. <https://doi.org/10.1109/TUFFC.2014.006935>
- [30] Sabra, K. G., Winkel, E. S., Bourgoyne, D. A., Elbing, B. R., Ceccio, S. L., Perlin, M., & Dowling, D. R. (2007). Using cross correlations of turbulent flow-induced ambient vibrations to estimate the structural impulse response. Application to structural health monitoring. *The Journal of the Acoustical Society of America*, 121(4), 1987–1995. <https://doi.org/10.1121/1.2710463>
- [31] Salvermoser, J., Hadziioannou, C., & Stähler, S. C. (2015). Structural monitoring of a highway bridge using passive noise recordings from street traffic. *The Journal of the Acoustical Society of America*, 138(6), 3864–3872. <https://doi.org/10.1121/1.4937765>
- [32] Farrar, C. R., & James, G. H. (1997). System identification from ambient vibration measurements on a bridge. *Journal of Sound and Vibration*, 205(1), 1–18. <https://doi.org/10.1006/JSVI.1997.0977>
- [33] Tippmann, J. D., Zhu, X., & Lanza Di Scalea, F. (2015). Application of damage detection methods using passive reconstruction of impulse response functions. *Philosophical Transactions of the Royal Society A: Mathematical, Physical and Engineering Sciences*, 373(2035). <https://doi.org/10.1098/RSTA.2014.0070>
- [34] Ubertini, F., Comanducci, G., & Cavalagli, N. (2016). Vibration-based structural health monitoring of a historic bell-tower using output-only measurements and multivariate statistical analysis. *Structural Health Monitoring*, 15(4), 438–457. <https://doi.org/10.1177/1475921716643948>
- [35] Harris, F. J. (1978). On the use of windows for harmonic analysis with the discrete Fourier transform. *Proceedings of the IEEE*, 66(1), 51–83. <https://doi.org/10.1109/PROC.1978.10837>
- [36] Yeager, M., Gregory, B., Key, C., & Todd, M. (2019). On using robust Mahalanobis distance estimations for feature discrimination in a damage detection scenario. *Structural Health Monitoring*, 18(1), 245–253. <https://doi.org/10.1177/1475921717748878>.
- [37] Drosdoff, D., & Widom, A. (2005). Snell's law from an elementary particle viewpoint. *American Journal of Physics*, 73(10), 973–975. <https://doi.org/10.1119/1.2000974>

Chapter 3. Influence of Varying Operational Parameters on the Defect Detection Performance of a High-Speed Ultrasonic Rail Inspection System During Field Tests

3.1. Introduction

This chapter presents the performance evaluation of a high-speed rail inspection prototype based on this “passive” approach that was tested at the Transportation Technology Center, Inc (TTCI) in Pueblo, CO, USA at speeds up to 80 mph. In particular, the chapter presents Receiver Operating Characteristic (ROC) curves [1-7] that quantify the ability of the system to detect rail discontinuities (welds, joints and TDs) in terms of Probability of Detection (PD) versus Probability of False Alarms (PFA) with varying operational parameters [8-10]. These parameters include: the length of the baseline distribution utilized in the statistical signal processing, the speed of the test run, the type of the wheel-rail interaction, the location of the transducer array with respect to the locomotive, the SNR of the reconstructed transfer function, and the number of test runs (redundancy). These studies build the foundations for future improvements of this system. In this chapter, results from the tests conducted at TTCI during December 2018, June 2019 and December 2019 are presented. The results include:

1. Analysis of the signal strengths at different speeds.
2. Receiver Operating Characteristic (ROC) curves showing the rate of ‘true detections’ vs ‘rate of false alarms’ for varying levels of DI threshold.

3. The effects of changing speeds in the defect detection performance of the system.
4. The effects of changing the length of the baseline distribution on the defect detection performance of the system.
5. Maps of the locations of discontinuities picked up by the camera (ground truth) overlaid on the locations tagged by the passive system for possible discontinuities.
6. Utilization of redundancies introduced by multiple runs on the same track (12 runs on the HTL) for reducing the rate of false positives and improving overall detection performance.
7. A comparison of the results obtained from lower speed tests (up to 40 mph) on the HTL and higher speed tests (up to 80 mph) on the RTT.

3.2. Acoustic Signal Strength

The strength of the raw signals with respect to the noise determines the quality of the data acquired during the tests. When the wheels of the locomotive do not excite the rails sufficiently, the signal in the transducers essentially consist of electronic and environmental noise. This happens when the locomotive is moving at slower speeds such that the energy imparted into the rails is not large enough to leak into the air and be picked up by the transducer array. The variance of the signal (σ_s^2) relative to the variance of the noise (σ_n^2) gives the signal-to-noise ratio (SNR) of the raw data and can be expressed in decibels (dB) as:

$$SNR_{raw}(dB) = 10 \log_{10} \left(\frac{\sigma_s^2}{\sigma_n^2} \right) \quad (3.1)$$

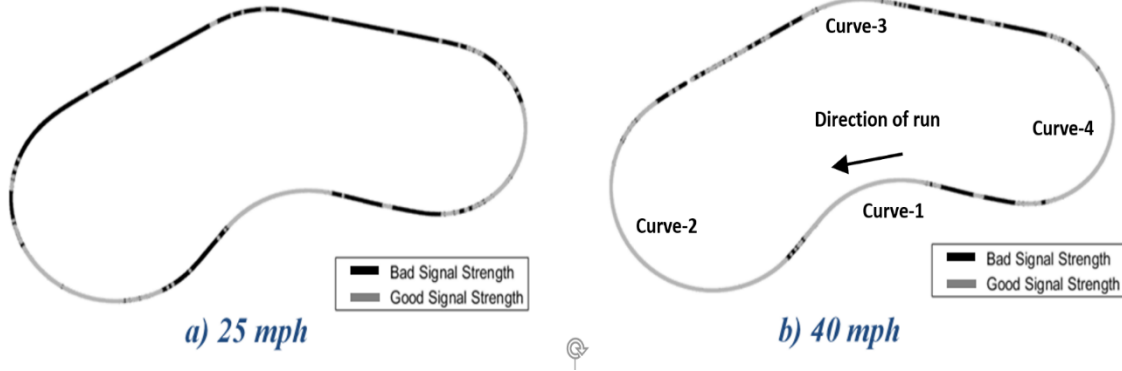


Figure 3.1 Map of the HTL with regions of high and low signal strengths at 25 mph and 40 mph testing speeds

It can be difficult to separate the raw data into signal and noise components because even at higher speeds, the noise component will still be present. Hence, an approximate SNR is calculated based on the assumption that any signal generated at speeds below 5 mph is noise as shown below:

$$SNR_{raw-approx}(dB) = 10 \log_{10} \left(\frac{\sigma_{s>5 mph}^2}{\sigma_{s<5 mph}^2} \right) \quad (3.2)$$

where $\sigma_{s<5 mph}^2$ is the variance of the signal at speeds below 5 mph and $\sigma_{s>5 mph}^2$ is the variance of the signal at speeds above 5 mph. Based on this SNR calculation, a cut-off dB level can be chosen and regions having signals above a threshold dB level can be classified as ‘good’ zones and regions having signals below the threshold dB level can be classified as ‘bad’ zones. Transfer function reconstructions and discontinuity detection performance in the ‘good’ zones would be more reliable compared to those from the ‘bad’ zones and will be shown later. Fig. 3.1 shows the acoustic signal strengths based on a 6 dB SNR threshold for test runs at 40 mph and 25 mph on the HTL. From Fig. 3.1, it is evident that acoustic signal strength increases with increase in the speed of the test runs. Also, signal strengths seem to be consistently good in the curved sections

of the track. Flanging noise induced by the contact between the wheel flange and rail gauge at curved sections of the track [11] could be one of the reasons for this observation. However, since the inner rail of the HTL was probed, wheel flanging would only occur at curve 1 because the wheel on the inner rail at curve 1 has to travel a greater distance. Moreover, at shallow curves and lower speeds, wheel flanging may not occur at curve 1. This does not explain the higher signal strengths at curve 1 for lower speeds (25 mph). Wheel flanging alone, therefore, cannot explain the high signal strengths observed in all the curves. The authors believe curve squeal [12-19] could explain the high signal strengths at curves 2,3 and 4. When a train maneuvers a curve, the axle of the vehicle moves in a transverse direction which leads to a transverse slip between the wheel and the rail (lateral creep). This lateral creep induces a self-excited vibration with a single high-frequency dominant tone which is independent of train speed [20-27]. Curve squeal, therefore, explains the high acoustic signal strengths at curved sections irrespective of train speed.

3.3. Receiver Operating Characteristic Curves

Performance of the passive rail inspection prototype is assessed with the help of ROC curves. A brief explanation of ROC curves is presented in this section (details in [28-29]). An ROC curve is a graphical method of evaluating the performance of a damage detection system (in terms of positive detection and false alarms) as the threshold value of the damage index parameter is varied. The ROC curve consists of a plot between the Probability of Detection (PD) vs Probability of False Alarms (PFA) for different values of the DI threshold level. Calculation of the PD and PFA requires tracking the DI of the test run. The damage indices are relative values which can be attributed to the state of health of the segment of the track they are computed for. A high DI value indicates an outlier and may represent a possible location of some discontinuity/defect. A high

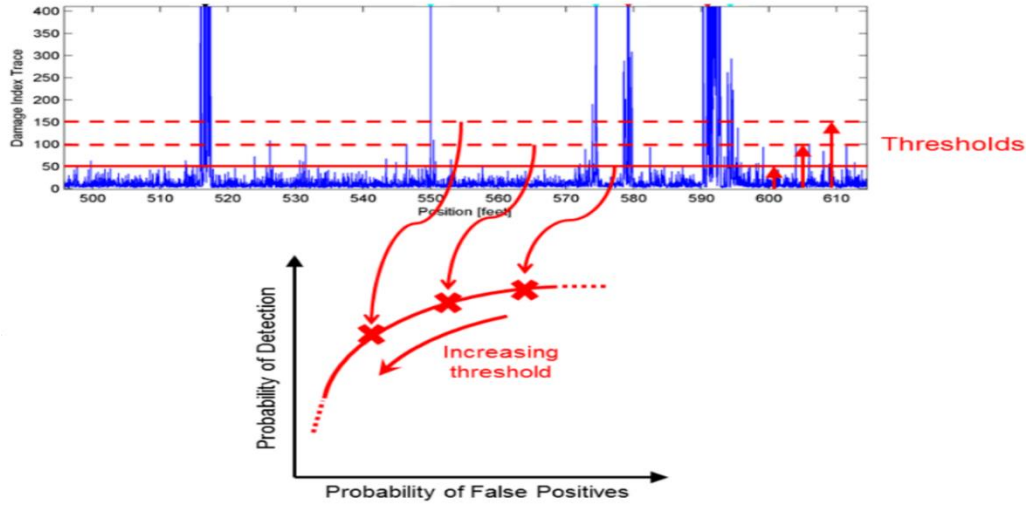


Figure 3.2 ROC curve computation from varying DI thresholds

value of DI in the vicinity of a known discontinuity would mean that the prototype gives a “true positive” result. Similarly, a high value of DI in the vicinity of a pristine segment of track means that the prototype gives a “false positive” result. An ideal scenario is when the number of “true positives” are high and the number of “false positives” are low. Since the number of “true positives” and “false alarms” would be different for different segments of rail scanned, a probabilistic approach is adopted, wherein the probability of these “true positives” or “false positives” are computed. PD gives an estimate of the “true positives” and is calculated by the equation below:

$$PD = \frac{D_i}{D_t} \quad (3.3)$$

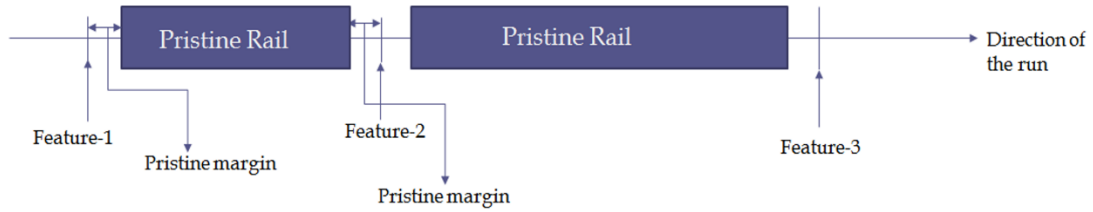
where D_i is the number of discontinuities detected during the test run and D_t is the total number of discontinuities present in the test track. Similarly, PFA gives an estimate of the “false positives” and is computed by the equation:

$$PFA = \frac{D_p}{P_t} \quad (3.4)$$

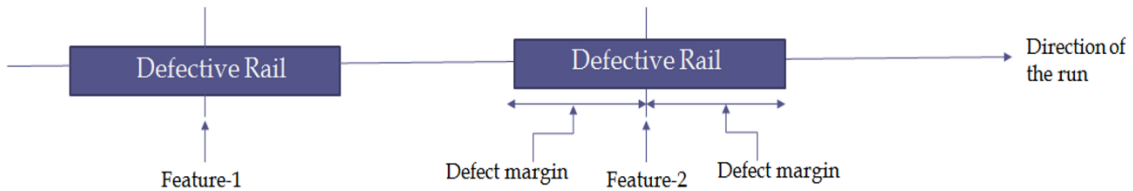
where D_p is the total number of discontinuities spuriously identified in pristine rail segments and P_t is the total number of pristine rail segments scanned. The ROC curves are computed by varying the DI threshold level such that each threshold value corresponds to one point on the curve. A damage detection system having the ROC curve lying towards the top left is the ideal case since it would have a high POD and low PFA for intermediate threshold levels. To ensure robustness of the system, a minimum number of threshold crossings (7) was required within a fixed length of rail segment (18 inch) for a location to be flagged as a possible discontinuity. To compensate for errors in GPS mapping, a defect search range of ± 10 ft was adopted, meaning that any location flagged within the search range of a known location of discontinuity was considered as a true detection. Any defects flagged outside this search range of known discontinuities were considered as false positives. Fig. 3.2 shows a sample DI trace along with the corresponding ROC curve obtained by varying the threshold levels.

3.3.1. Discretization of Inspected Rail Segments

To compute the ROC curves for the test runs, the rail track is first discretized into “pristine” and “defective” portions. The terms “defect” and “feature” are used equivalently with the term “discontinuities” herein. The pristine sections of the track have no discontinuities, while the defective segments have either a joint, a weld or a transverse defect. Since the locations of the discontinuities cannot be ascertained with absolute precision, a portion of the track (called the pristine margin) is eliminated before and after each feature to build the pristine sections of the rail, as shown in Fig. 3.3(a). Similarly, for the defective population, a portion of the track (called the defect margin) is included before and after each feature, as also shown in Fig. 3.3(b). The pristine margin and the defect margin are kept the same for a particular analysis. The ROC curves are computed for each discontinuity by scanning the track from the start of the run until the end of the



a) Segregating pristine segments



b) Segregating defective segments

Figure 3.3 Segregating a) pristine and b) defective sections of the rail for computation of PD and PFA in the ROC curves

run and observing the number of times the DI value from the reconstructed transfer functions crosses a given threshold within the scanning length (gauge length of the prototype of 1.5 ft). If the total count of crossings exceeds the threshold by the Number of Threshold Crossings (NTC) in the defective segment of the track, a “positive detection” is recorded. If, instead, the number of crossings exceeds the NTC threshold in the pristine segment of the track, a “false alarm” is recorded. An NTC value of 7 was found to result in optimum performance and was used in computing all the ROC curves.

3.3.2. ROC Curves for Different Defect Margins

Fig. 3.4 and Fig. 3.5 show the ROC curves for one test run at 40 mph on the HTL track. The curves for welds are shown in Fig. 3.4, and those for joints are shown in Fig. 3.5. The curves were computed for three different defect margins (tolerance ranges): ± 3 ft (0.9 m), ± 5 ft (1.5 m), and ± 10 ft (3 m). A defect search range of ± 10 ft means that if the DI values crossed a threshold for a certain number of times (NTC) in the range of ± 10 ft from the actual location of the defect,

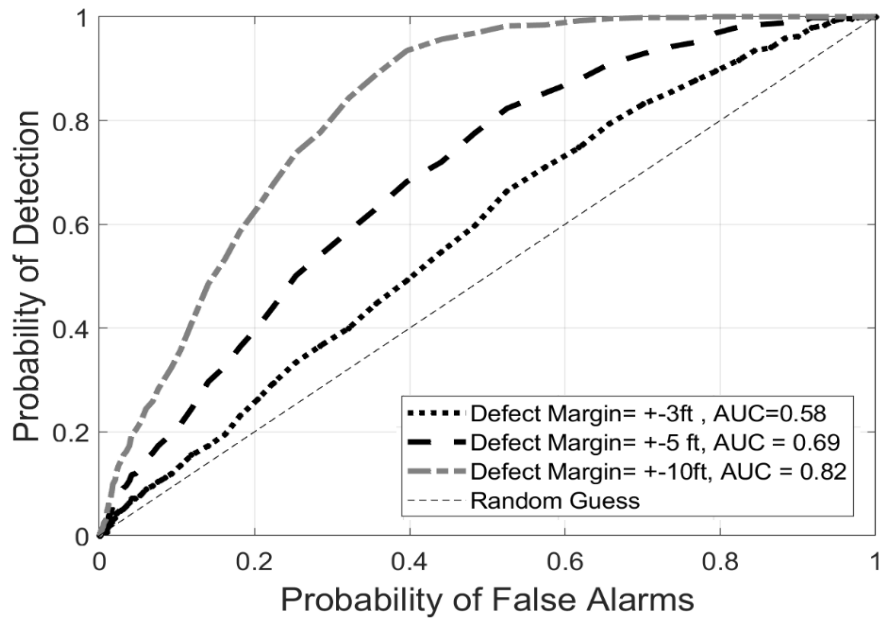


Figure 3.4 ROC curves for welds on the HTL track at 40 mph for different defect search tolerance margins

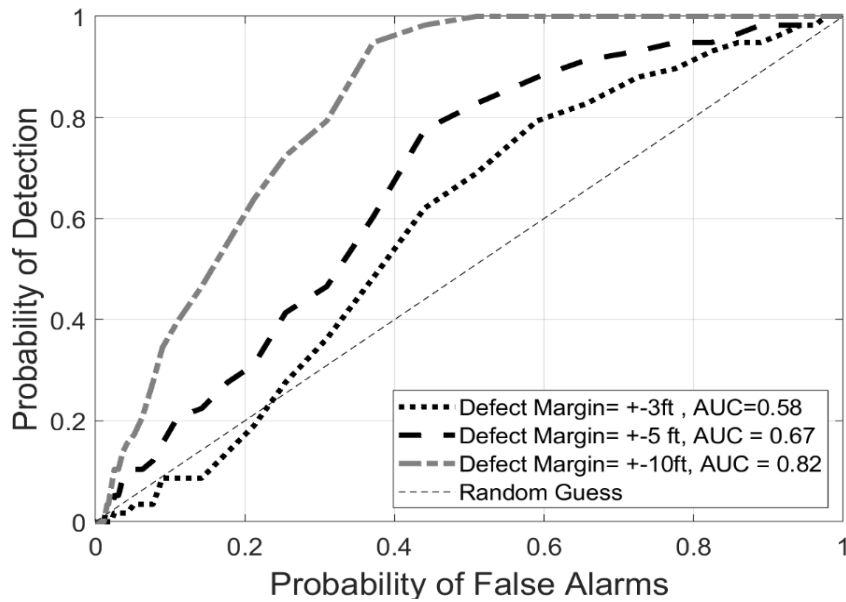


Figure 3.5 ROC curves for joints on the HTL track at 40 mph for different defect search tolerance margins

a true detection is assigned to that location. The plots also show the Area Under the Curve (AUC) metric that indicates the overall damage detection performance of the system for different

threshold levels. A higher AUC represents better performance and visually represents a curve shifted toward the upper-left corner of the ROC graph.

The results in Figs. 3.4 – 3.5 show that as the “defect margin” increases, the curves shift towards the top-left with a corresponding increase in the AUC metric, indicating an increase in overall detection performance (higher PD and lower PFA). This is the case for both weld and joint detections. This result is expected because an increase in the “defect margin” means that the true defect could lie within a larger distance from the identified location and still be considered a positive detection. A defect margin of ± 10 ft seems like a reasonable range given the uncertainties of the location index and the required phase of manual defect verification that follows a detection. Considering this margin, for example, the plots suggest that a PD of 90% for either welds or joints can be achieved at the expense of a PFA of 35%.

3.4. Influence of Operational Parameters on Defect Detection Performance

3.4.1. Acoustic Signal Strength

The first parameter examined was the strength of the raw signals recorded by the air-coupled sensors from the wheel excitations with respect to the recordings’ noise floor. When the train wheels do not acoustically excite the rails sufficiently, the signal in the sensors essentially consist of electronic and environmental noise. Fig. 3.6 (a) shows the ROC curves computed for the “joint” discontinuities at 40 mph comparing the entire run and good signal strength zones only (curves 1-4). The Area Under the Curve (AUC) is a measure of the system’s overall performance for different thresholds, with a higher AUC value indicating better performance. Fig. 3.6 (b) shows the comparison of ROC curves of the “weld” discontinuities for the entire run selected from the

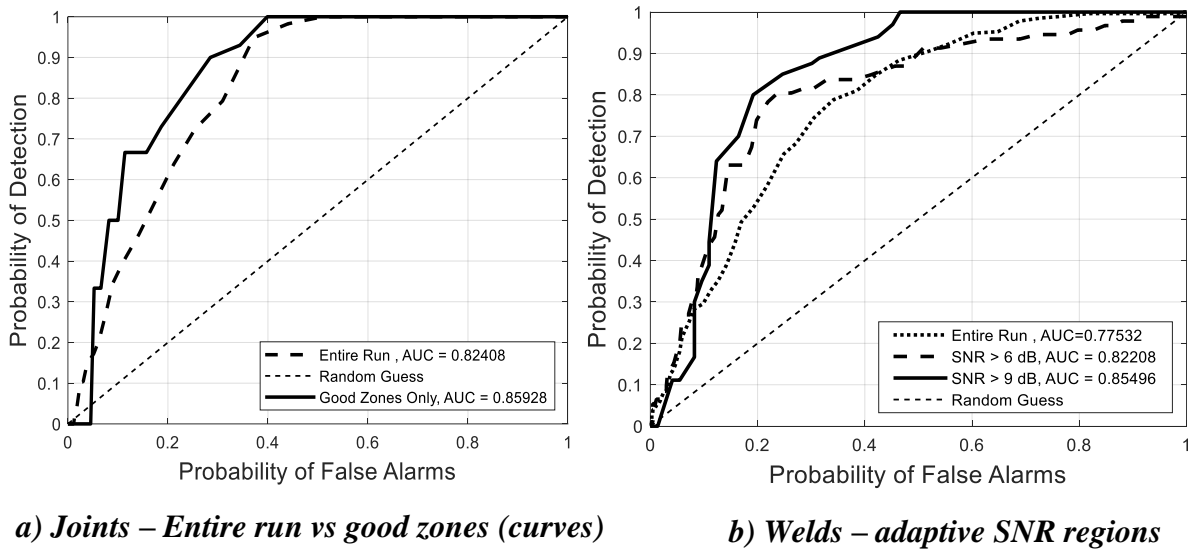


Figure 3.6 ROC curves for joints and welds at 40 mph on the HTL track for different acoustic signal strength regions

SNR of the recordings. Clearly, the joint and weld detection performance of the system improves in regions with higher acoustic signal strengths, as indicated by the shift in the ROC curves towards the top-left and a corresponding increase in the AUC metric. Note that for the entire run considered, the joint detection accuracy is generally better than the weld detection. This is expected since joints are always expected to produce the most severe wave scattering (more pronounced outliers in the DI), whereas weld are expected to produce a limited wave scattering (and no wave scattering at all, at the wave frequencies considered, for a particularly “good” weld).

Location of the prototype with respect to the locomotive also affects the signal-to-noise ratio of the received signals and affects the stability of the transfer function. Tests were conducted with two different locations of the prototype (shown in Fig. 3.7) with respect to the locomotive to evaluate the discontinuity detection performance. Fig. 3.8 shows the ROC curves for joints at 40



Prototype closer to locomotive

Prototype away from locomotive

Figure 3.7 Different locations of the prototype with respect to the locomotive

mph for two different locations of the prototype (sensing array) with respect to the locomotive. It is observed that moving the prototype closer to the locomotive improves the detection performance

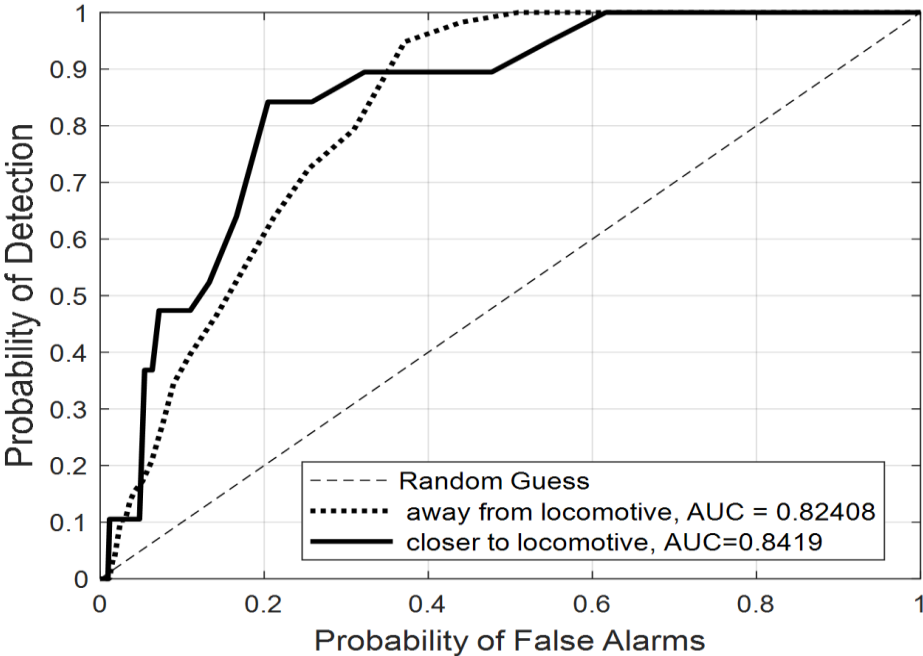


Figure 3.8 ROC curves for joints at 40 mph for different locations of the prototype with respect to the locomotive

of the system because of increased signal-to-noise ratio of the acoustic signals when prototype is closer to the locomotive.

3.4.2. Speed of Test Runs

Another important operational parameter for the prototype is the speed of the test run. Fig. 3.9 shows the ROC curves for welds, joints and defects for tests conducted on the HTL at different speeds. Fig. 3.9 (c) shows the ROC curves for the three TDs present on the HTL track at different speeds. Interestingly, the passive defect detection improves significantly with the increase in speed due to higher acoustic signal strengths at high speeds. Best results were obtained at the speed of 40 mph where a 100 % detection rate (PD) was observed with a 17% possibility of false alarms (PFA). At 33 mph, the rate of detection drops to 67% (POD=67%) for the same rate of false alarms (17%). If the speed is lowered to 25 mph, the rate of detection further drops to 34%. Depending on the allowable rate of false alarms that can be tolerated, the DI threshold level can be selected that optimizes the detection performance of the system for a given set of operational parameters. The staggered nature of the ROC curves was because the PD was calculated with only 3 known location of defects which resulted in only 4 possible values (0, 1/3, 2/3, 1). The fact that speed seems to aid the performance is a comforting result since the objective is enabling inspections at revenue speeds. The sample size of 3 defects makes it difficult to draw any substantial conclusions and further tests need to be conducted on tracks with larger number of known defects to obtain statistically significant inferences. The PFA of 17% (for defects) is still too high for industrial applications and needs further improvements.

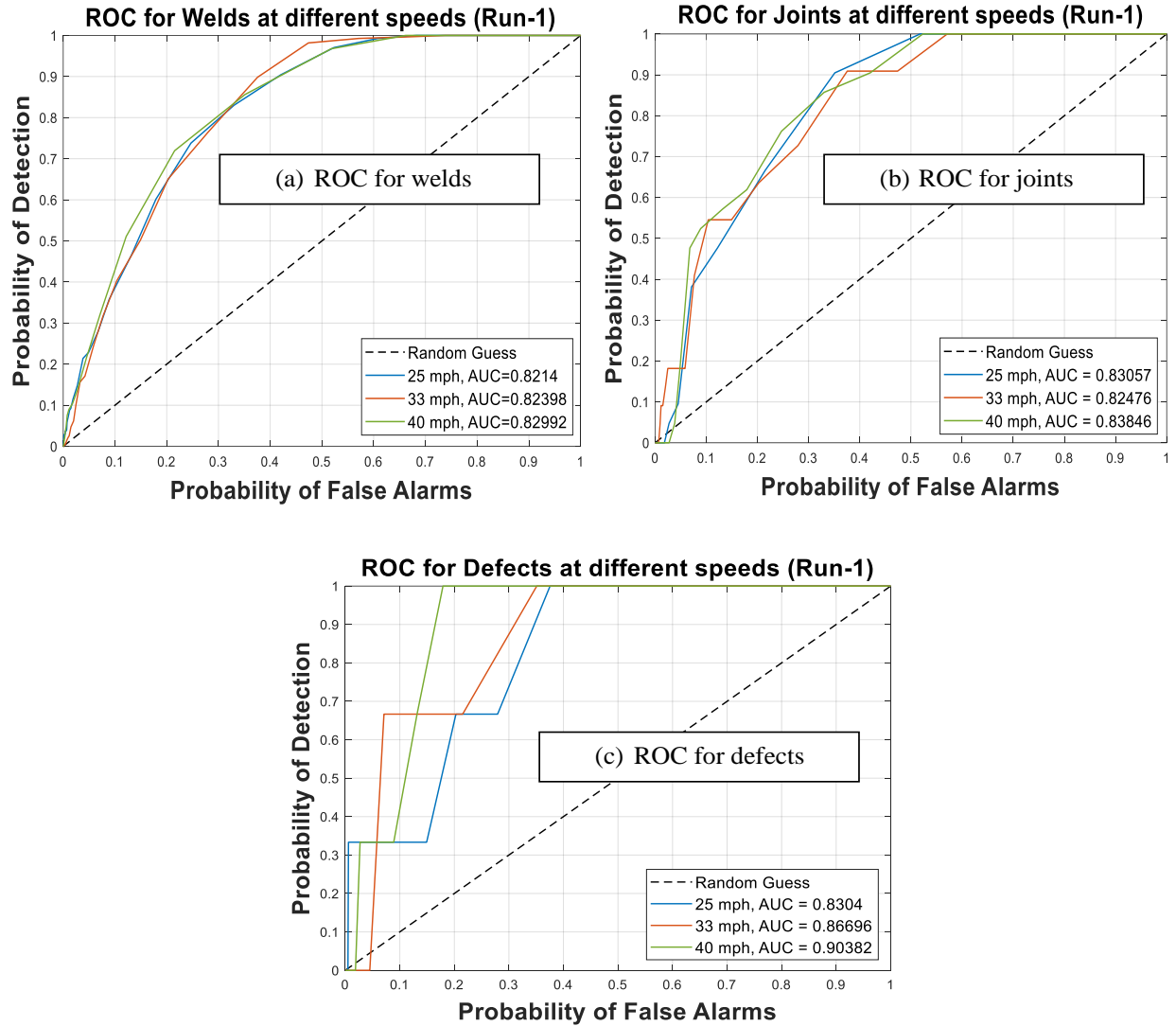


Figure 3.9 ROC curves for joints, welds, and defects at different speeds on the HTL.

3.4.3. Baseline Distribution Length

The length of the baseline plays a key role in the detection of discontinuities in the rails. A longer baseline results in an increased number of points in computing the “normal” distribution which leads to a more averaged statistics of the rail. On the other hand, a shorter baseline results in a lesser number of points in computing the “normal” distribution which leads to a more localized statistics of the rail. Therefore, a longer baseline is expected to result in a reduced sensitivity to

discontinuity detection. A shorter baseline is expected to be more sensitive to discontinuities but can also lead to increased false alarms.

3.4.3.1 HTL Tests

The effects of changing the length of the baseline distribution was analyzed with the help of Receiver Operating Characteristic (ROC) curves. The ROC curves for a given baseline distribution length at different speeds of the test vehicle are plotted for the various discontinuities in the rail such as welds, joints and defects. Test speeds of 40 mph, 33 mph and 25 mph were considered on the HTL and speeds of 70 mph and 80 mph for the RTT. Baseline distribution lengths of 30, 60, 120 and 240 points were analyzed for performance evaluation of the passive rail prototype. The normalized (with respect to maximum values) DI traces for baselines of 30 points and 240 points at 40 mph above 0.2 are shown in Fig. 3.10 and Fig. 3.11 respectively.

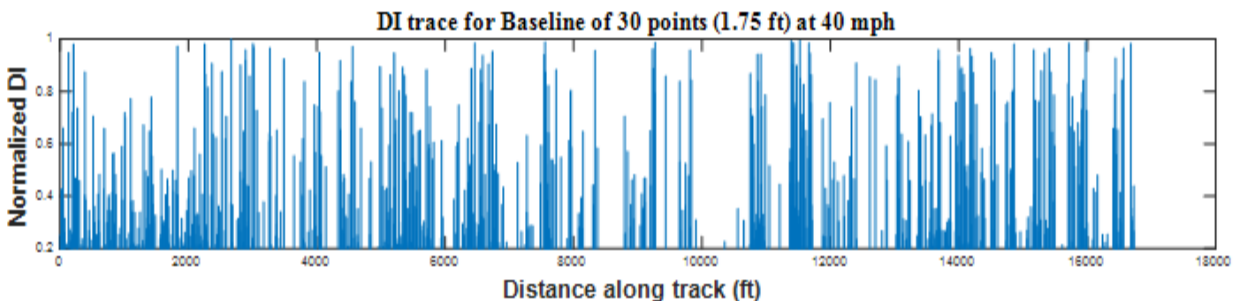


Figure 3.10 Damage Index trace at 40 mph for baseline length of 30 points (1.75 ft).

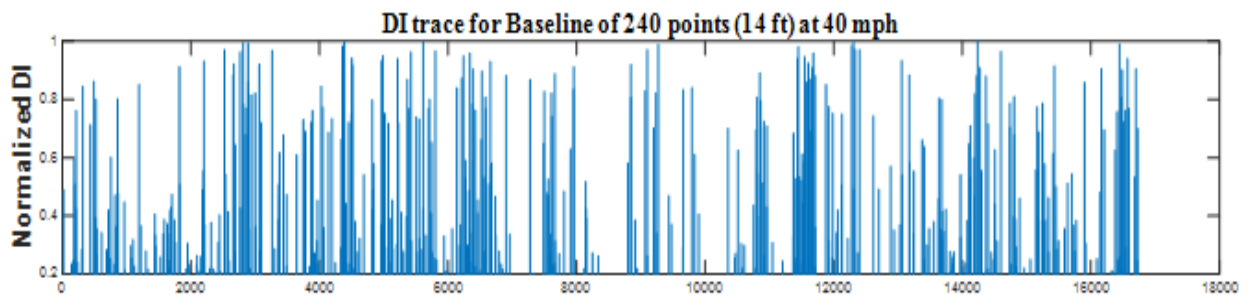


Figure 3.11 Damage Index trace at 40 mph for baseline length of 240 points (14 ft).

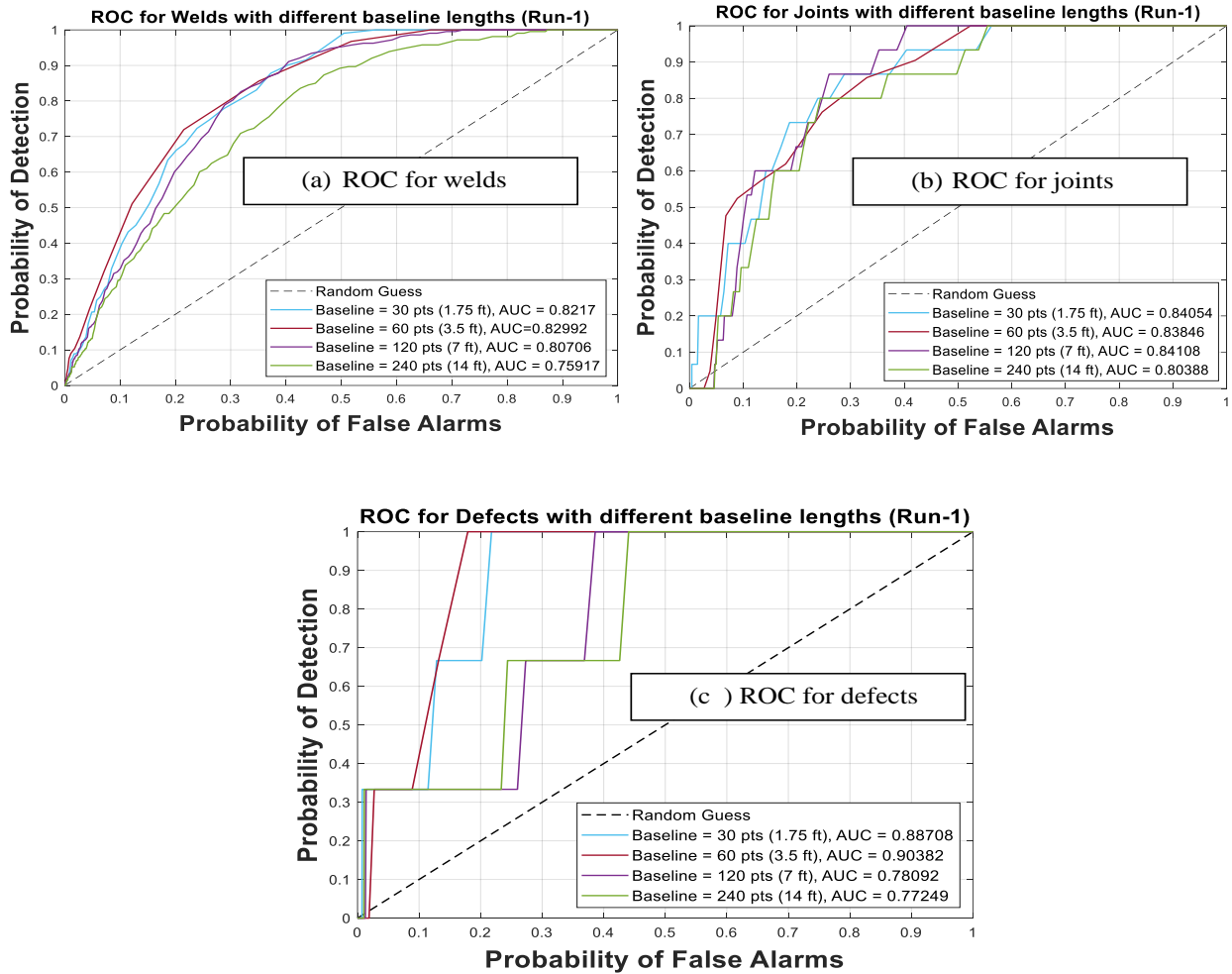


Figure 3.12 ROC curves for joints, welds, and defects for different baselines at 40 mph.

The effects of changing the length of the baseline distribution were analyzed with the help of ROC curves. The ROC curves for welds, joints and defects for the 40-mph run was computed for different baseline distribution lengths. Baseline distribution lengths of 30, 60, 120 and 240 points were analyzed for performance evaluation of the passive rail prototype which correspond to approximately a physical distance of 1.75 ft, 3.5 ft, 7 ft and 14 ft respectively at 40 mph. The ROC curves obtained are shown in Fig. 3.12 (a-c). It is observed from Fig. 3.12 that a reduction in the baseline distribution length increased the sensitivity of the system and improved the ROC

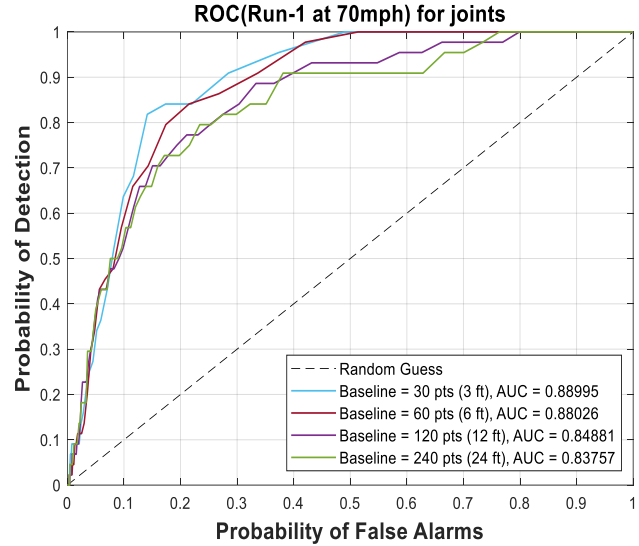
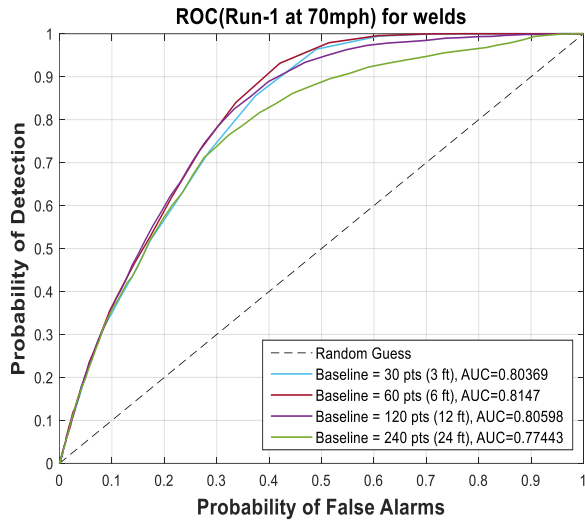


Figure 3.13 ROC curves for joints & welds for different baselines at 70 mph.

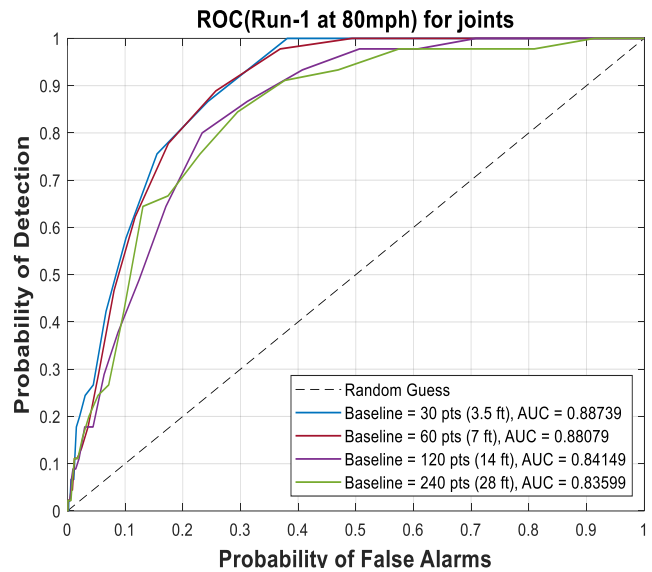
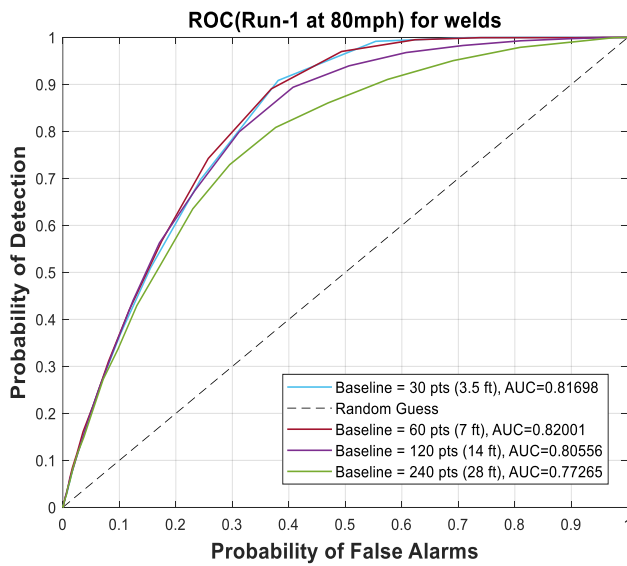


Figure 3.14 ROC curves for joints & welds for different baselines at 80 mph.

curves. Based on the results shown, a baseline distribution length of 60 points (3.5 ft) was found to be the optimum.

3.4.3.2 RTT Tests

Fig. 3.13 shows the ROC curves at 70 mph on the RTT for welds and joints for different baseline distribution lengths. Baseline distribution lengths of 30, 60, 120 and 240 points are

considered. At 80 mph they correspond to 3.5 ft, 7 ft, 14 ft and 28 ft approximately. Fig. 3.14 shows the ROC curves of joints and welds for 80 mph. A reduction of baseline length is observed to improve the discontinuity detection performance which is in agreement with the results observed at lower speeds on the HTL. Also, compared to the ROC curves in Figure 3.12 for the HTL, the ROC curves for RTT show considerable improvements, especially for joints, possibly because of a combination of higher signal strengths on the RTT and improved ground truth maps due to higher camera frame rates used on the RTT.

3.4.4. Signal-to-Noise Ratio of Transfer Functions

The defect detection performance of the passive rail inspection system depends on the quality of the reconstructed transfer function. A distinct wave arrival with minimum noise floor would be an ideal reconstruction. The relative amplitude of the arrival wave with respect to the noise floor is an indication of the quality of the transfer function (Fig. 3.15). The signal-to-noise ratio of the transfer function in dB is calculated as:

$$SNR_{TF}(dB) = 10 \log_{10} \left(\frac{\sigma_t^2}{\sigma_n^2} \right) \quad (3.5)$$

where σ_t^2 is the variance of the transfer function within the arrival window and σ_n^2 is the variance of the noise outside the arrival window as shown in Fig. 3.15. Low SNR of the transfer function would indicate wave attenuation in the presence of discontinuities in the rail segment and can be used to predict defect locations. Fig.3.16 shows the predictions made by the passive inspection system based on a combination of DI values and the SNR of transfer functions from different pairs of group-1 sensors. Black diamonds indicate all four pairs of the transfer functions have SNR less than 3 dB. Red diamonds indicate 3 pairs of transfer functions have SNR less than 3 dB. Yellow diamonds indicate 2 pairs of transfer functions have SNR less than 3 dB and green diamonds

indicate either one or none of the pairs have SNRs less than 3 dB. Black, red, yellow and green diamonds plotted are all above a threshold of 0.02% ($2e-5$) of the maximum DI value in the trace. Blue asterisks, orange triangles, yellow stars are the locations of the welds, joints and defects respectively picked up by the camera and represent the ground truth. Finally, the cyan asterisks represent the regions where the SNR of raw signals falls below 6 dB. Black, red and yellow diamonds represent the locations where the passive system predicts some form of discontinuity (welds, joints or defects). When these diamonds (black, red or yellow) align with any of the plotted ground truth (blue asterisk-welds, orange diamond-joints, yellow star-defects) a true detection can be assigned. When these diamonds occur in regions where there are no known discontinuities, a false alarm is raised. Zoomed views of a region of high signal strength (Zone-A) and a region of low signal strength (Zone-B) are shown in Fig. 3.16. Low signal strength zones have a comparatively higher rate of false alarms compared to the high signal strength zones.

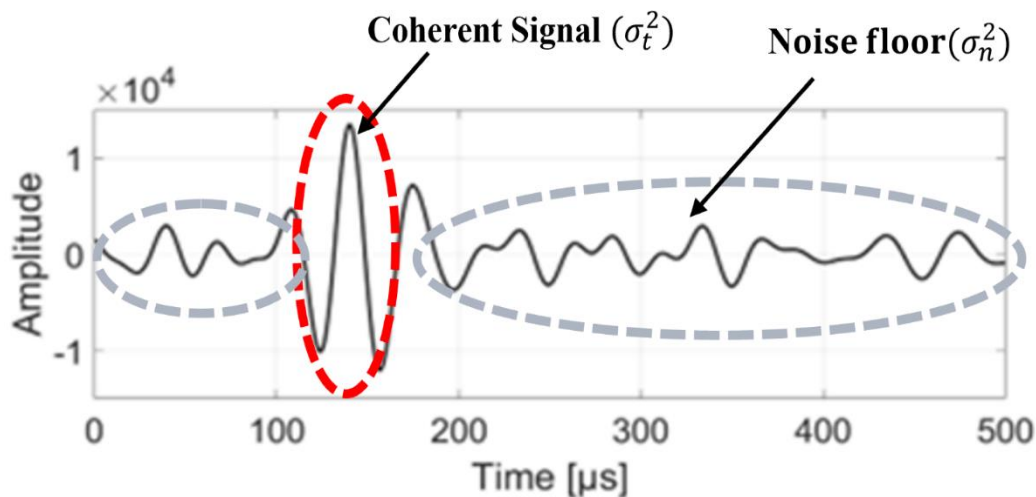


Figure 3.15 Coherent signal and noise floor in the reconstructed transfer function

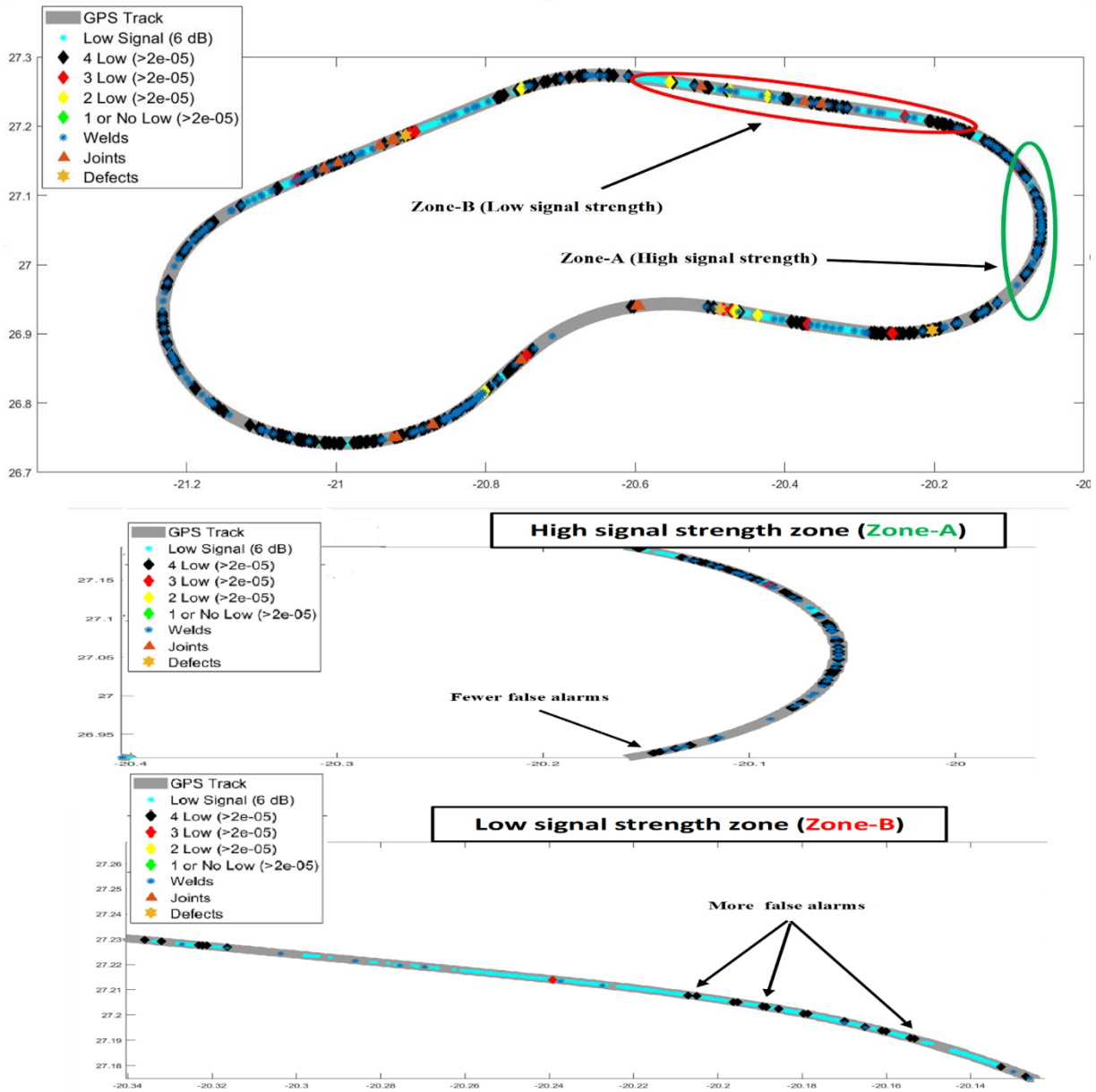


Figure 3.16 GPS based map of passive system predictions, ground truth and signal strengths

3.4.5. Redundancies from Multiple Runs

It was discussed in the Introduction section how an ability for a train to perform rail inspection during normal traffic operations can provide the test redundancy that would result from multiple train passes over the same segment of rail. Such redundancy is expected to improve the

defect detection performance by, for example, reducing the rate of false alarms (PFA) for the same probability of detection (PD). The results discussed so far in this chapter for the discontinuity detection performance of the passive inspection system are only for 1 test run considered at a time. In practical situations, when the prototype will be used for defect detection by mounting it on a revenue train, the same section of the track will be traversed by the train multiple times, resulting in a larger set of observations. Multiple observations on the same track are expected to cause redundancies in the data with consequent reduction of false alarms. This expectation is based on the assumption that false positives will occur at randomly distributed locations along the track, whereas true positives will occur at consistent locations for every run. Locations flagged as possible discontinuities in different runs based on the DI trace can then be overlaid on top of each other and non-coinciding points may be discarded as false positives, whereas coinciding locations could be tagged as true detections.

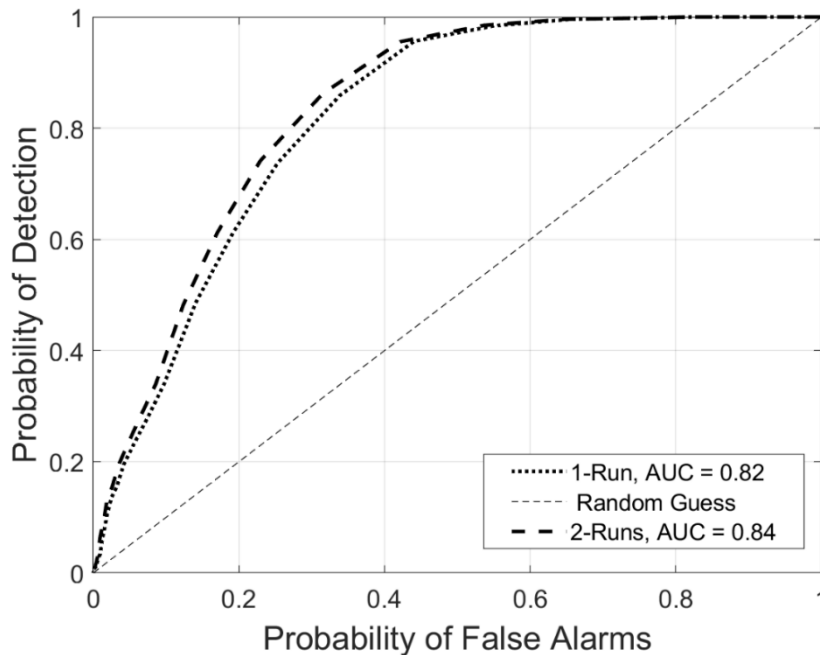


Figure 3.17 ROC curves for welds compounding two runs on the HTL track at 40 mph to introduce redundancies

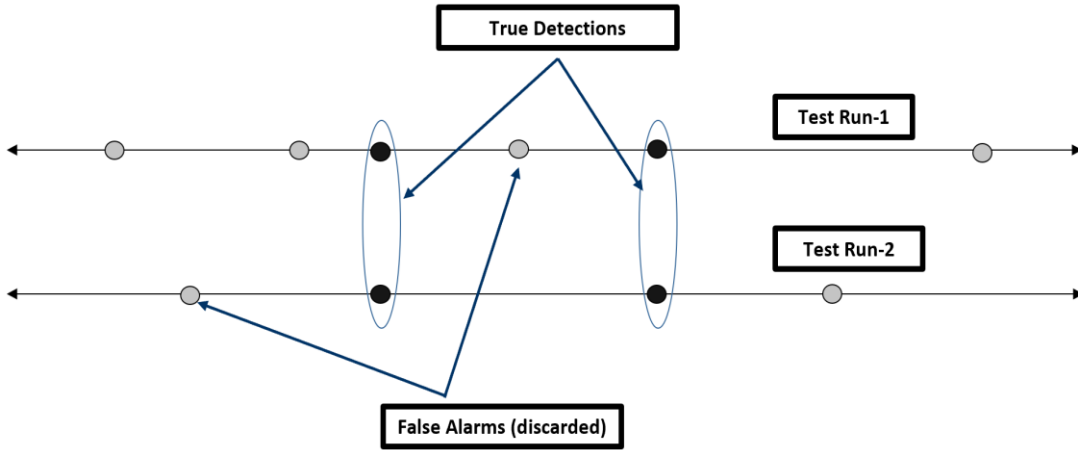


Figure 3.18 Redundancy: compounding flagged locations from two independent test runs to reduce the rate of false alarms

A preliminary analysis on the effect of test redundancy was performed and is shown in Fig. 3.17. The figure presents two ROC curves computed for the weld discontinuities using a single run and two separate runs on the HTL track at a speed of 40 mph. When compounding the two runs, similar locations flagged in both runs are considered “true detections,” whereas different locations flagged in the two runs are discarded as “false alarms” as shown in Fig. 3.18. The ROC curve for the two runs (Fig. 3.17) shows a slight improvement compared to that for the single run. For example, for a PD of 80%, the PFA for the single run is 30% and it decreases to 27% for the two runs. It can be reasonably expected that the advantages of redundancy will increase with increasing number of runs.

Fig. 3.19 shows the results obtained on the 12-run dataset at 40 mph on the HTL for welds. If 33% or more of the number of runs detected a discontinuity at the same location within a search range ($\pm 10 ft$), that location was flagged as a positive detection. Therefore, the number of runs required to assign a positive detection was 1 out of 3 runs, 2 out of 6 runs and 3 out of 12 runs.

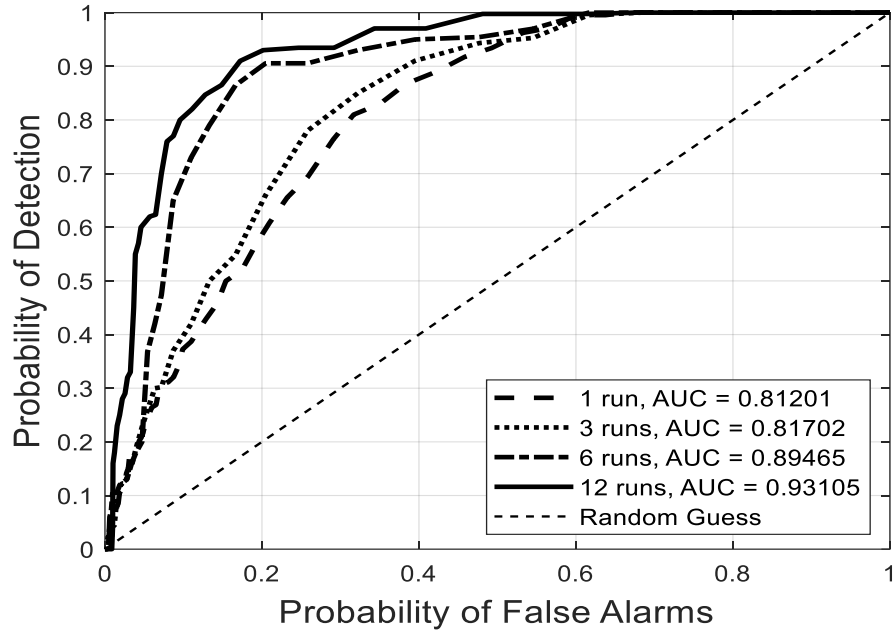


Figure 3.19 ROC curves for welds at 40mph with redundancies for multiple runs

The results obtained for 1-run and 3-run cases do not introduce any redundancies. The 3-run case still performs better than the 1-run case because of the additional odds of detecting the weld in at least 1 out of 3 runs. The 3-run case, however, also increases the rate of false positives simultaneously and therefore a significant improvement is not achieved. The 6-run case improves the performance significantly because now redundancies are introduced, and the false positive detections need to align in at least two of the runs which is more unlikely. In general, it is observed that as the number of runs is increased, the ROC curve shifts towards the top-left indicating the expected reduction in the rate of false alarms. The results also do not improve as much when we compare the 6-run case with the 12-run case (sort of a saturation effect). This suggests that the system's performance tends to a maximum limit as the number of runs are increased. It is also worth noting that not all the false positives are removed by compounding multiple runs. This indicates the system keeps flagging similar locations in multiple runs where possibly unmarked

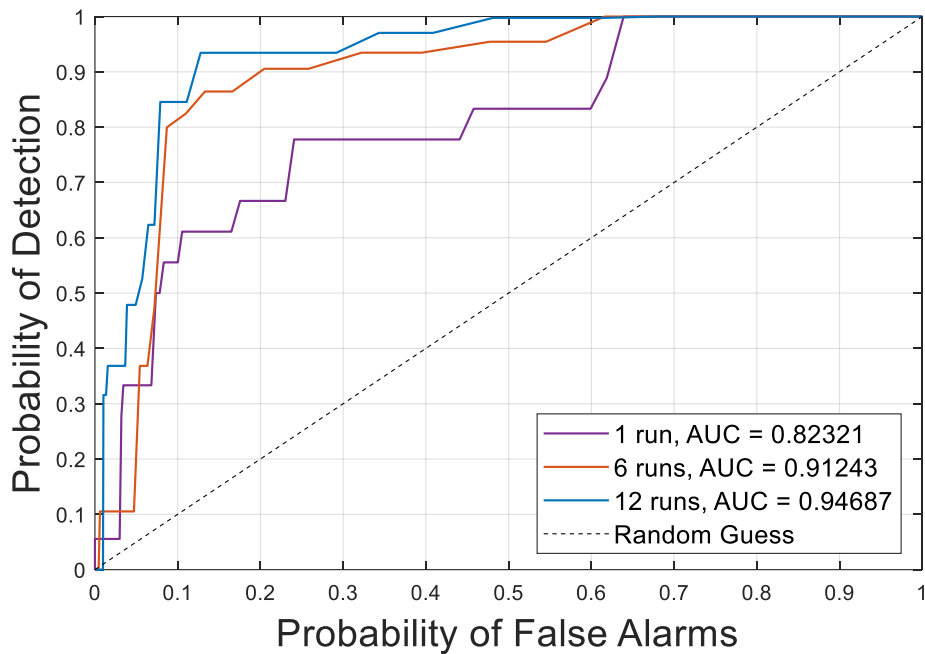


Figure 3.20 ROC curves for joints at 40mph with redundancies for multiple runs

defects or discontinuities are present. A more accurate ground truth is likely to convert many of the false positives to true positives.

Fig. 3.20 shows the results obtained on the 12-run dataset at 40 mph on the HTL for joints. The results obtained for 1-run do not include any redundancies. It is seen that as the number of runs is increased, the ROC curve shifts towards the top-left clearly indicating a reduction in the rate of false alarms. It is also observed that the performance improves considerably when the 1-run case is compared with the 6-run case. The results do not improve as much when we compare the 6-run case with the 12-run case. This is possibly because 6-runs introduce much newer (unique) information when compared to only 1-run. On the other hand, 12-runs do not introduce as much new information when compared to the 6-run case and hence do not improve the results as much.

3.5. Conclusions

This chapter discusses the current state of the high-speed rail inspection system under development at the University of California San Diego on behalf of the Federal Railroad Administration. The system uses a passive ultrasonic sensing approach that utilizes non-contact air-coupled ultrasonic receivers and special signal processing algorithms to flag locations of discontinuities along a rail. The key potential advantages of this technology are: (1) the possibility to inspect the rail at regular train speeds (2) the possibility to enhance the detection performance due to the run redundancies. The field test performance is presented in terms of ROC curves quantifying the trade-off between PD and PFA for various rail discontinuities (joints, welds, defects) and for different operational parameters. The SNR of the raw signal has an obvious effect on the performance, indicating “good” and “bad” portions of rail depending on the rail-wheel interaction conditions. This is a complex problem that needs to be investigated further. and Higher test speeds were found to yield better performance of the system because of the higher energy and higher bandwidth levels introduced into the rail by the wheel excitations, which improved the signal-to-noise ratio of the passively reconstructed ultrasonic transfer function of the rail. Improved performance at higher speeds is very encouraging since one of the primary objectives of this project is enabling rail inspections at regular train speeds (“smart train” concept). The tests also show that the location of the sensors should be as close as possible to the locomotive wheels for enhanced excitation strength. In terms of statistical analysis, it is found that the length of the baseline distribution can affect the performance outcome, with an optimum length resulting in the best performance. Finally, it is found that multiple runs on the same track improve the performance, with the improvement saturating when a certain number of runs is reached (six in our tests).

Although this work has laid strong foundations for this approach, additional research and development efforts are needed to make a successful transition to industry. Further studies need to be conducted to investigate ways of improving signal strengths at lower speeds on straight sections of the track. One possible way to achieve this is to introduce a controlled and broadband excitation source, such as continuous impacts on the rail, using an automatically controlled hammer. Another technique is to use high powered acoustic horns for non-contact excitations. Further research also needs to be conducted to improve and optimize the signal feature vectors used in the outlier analysis with machine learning based techniques.

3.6. Acknowledgements

This work was funded by the US Federal Railroad Administration under contract 693JJ620C000024 with Dr. Robert Wilson as the Program Manager.

Chapter 3, in part, has been submitted for publication of the material as it may appear in the following paper: **Datta, D.** and Lanza di Scalea, F. Influence of Varying Operational Parameters on the Defect Detection Performance of a High-Speed Ultrasonic Rail Inspection System During Field Tests. Submitted to *Experimental Mechanics*. The dissertation author was the primary investigator and author of this paper.

3.7. References

- [1] Mandrekar, J. N. (2010). Receiver operating characteristic curve in diagnostic test assessment. *Journal of Thoracic Oncology*, 5(9), 1315–1316. <https://doi.org/10.1097/JTO.0B013E3181EC173D>
- [2] Kerekes, J. (2008). Receiver operating characteristic curve confidence intervals and regions. *IEEE Geoscience and Remote Sensing Letters*, 5(2), 251–255. <https://doi.org/10.1109/LGRS.2008.915928>

- [3] Pepe, M. S., Cai, T., & Longton, G. (2006). Combining predictors for classification using the area under the receiver operating characteristic curve. *Biometrics*, 62(1), 221–229. <https://doi.org/10.1111/J.1541-0420.2005.00420.X>
- [4] Giglioni, V., García-Macías, E., Venanzi, I., Ierimonti, L., & Ubertini, F. (2021). The use of receiver operating characteristic curves and precision-versus-recall curves as performance metrics in unsupervised structural damage classification under changing environment. *Engineering Structures*, 246, 113029. <https://doi.org/10.1016/J.ENGSTRUCT.2021.113029>
- [5] Liu, C., Dobson, J., & Cawley, P. (2017). Efficient generation of receiver operating characteristics for the evaluation of damage detection in practical structural health monitoring applications. *Proceedings of the Royal Society A: Mathematical, Physical and Engineering Sciences*, 473(2199). <https://doi.org/10.1098/RSPA.2016.0736>
- [6] Bewick, V., Cheek, L., & Ball, J. (2004). Statistics review 13: Receiver operating characteristics curves. *Critical Care*, 8(6), 508–512. <https://doi.org/10.1186/CC3000/TABLES/6>
- [7] Pepe, M. S., Longton, G., & Janes, H. (2009). Estimation and comparison of receiver operating characteristic curves. *The Stata Journal*, 9(1), 1–16. <https://doi.org/10.1177/1536867X09000900101>
- [8] Datta, D., & di Scalea, F. L. (2022). High-speed Inspection of rails by passive ultrasonic monitoring. *Journal of Nondestructive Evaluation, Diagnostics and Prognostics of Engineering Systems*, 5(4). <https://doi.org/10.1115/1.4055382>
- [9] Datta, D., Cui, R., di Scalea, F. L., & Wilson, R. (2021). High-speed rail inspection by a non-contact passive ultrasonic technique. Transportation Research Board 100th Annual Meeting.
- [10] Datta, D., Liang, A., Cui, R., & Scalea, F. L. di. (2020). Defect detection performance of a high-speed rail inspection system from passive acoustic identification. *SPIE*, 11379, 196–204. <https://doi.org/10.1117/12.2558205>
- [11] Kim, J. C., Yun, Y. S., & Noh, H. M. (2019). Analysis of wheel squeal and flanging on curved railway tracks. *International Journal of Precision Engineering and Manufacturing*, 20(12), 2077–2087. <https://doi.org/10.1007/S12541-019-00225-7/FIGURES/18>
- [12] Rudd, M. J. (1976). Wheel/rail nose—part II: Wheel squeal. *Journal of Sound and Vibration*, 46(3), 381–394. [https://doi.org/10.1016/0022-460x\(76\)90862-2](https://doi.org/10.1016/0022-460x(76)90862-2)
- [13] Eadie, D. T., Santoro, M., & Kalousek, J. (2005). Railway noise and the effect of top of rail liquid friction modifiers: Changes in sound and vibration spectral distributions in curves. *Wear*, 258(7–8), 1148–1155. <https://doi.org/10.1016/j.wear.2004.03.061>
- [14] Kim, C., Kwon, Y., & Kim, D. (2018). Analysis of low-frequency squeal in automotive disc brake by optimizing groove and caliper shapes. *International Journal of Precision Engineering and Manufacturing*, 19(4), 505–512. <https://doi.org/10.1007/s12541-018-0061-8>

- [15] Remington, P. J. (1986). Wheel/rail squeal and impact noise: What do we know? What don't we know? Where do we go from here? *Journal of Sound and Vibration*, 116(2), 339–353. [https://doi.org/10.1016/s0022-460x\(87\)81306-8](https://doi.org/10.1016/s0022-460x(87)81306-8)
- [16] Park, S. H., Kim, J. S., & Choi, J. J. (2009). Reference slip ratio generation and adaptive sliding mode control for railway rolling stocks. *International Journal of Precision Engineering and Manufacturing*, 10(2), 39–44. <https://doi.org/10.1007/s12541-009-0025-0>
- [17] Hiensch, M., Larsson, P. O., Nilsson, O., Levy, D., Kapoor, A., Franklin, F., Nielsen, J., Ringsberg, J. W., & Josefson, B. L. (2005). Two-material rail development: Field test results regarding rolling contact fatigue and squeal noise behavior. *Wear*, 258(7–8), 964–972. <https://doi.org/10.1016/j.wear.2004.03.067>
- [18] Anderson, D., & Wheatley, N. (2008). Mitigation of wheel squeal and flanging noise on the Australian rail network. *Notes on Numerical Fluid Mechanics and Multidisciplinary Design*, 99, 399–405. https://doi.org/10.1007/978-3-540-74893-9_56
- [19] Stock, R., Santoro, M., Makowsky, T., Elvidge, D., & Xia, P. (2018). Friction management as a sustainable solution for controlling noise at the wheel-rail interface. *Notes on Numerical Fluid Mechanics and Multidisciplinary Design*, 139, 723–734. https://doi.org/10.1007/978-3-319-73411-8_57
- [20] Thompson, D. J., Squicciarini, G., Ding, B., & Baeza, L. (2018). A state-of-the-art review of curve squeal noise: Phenomena, mechanisms, modelling and mitigation. *Notes on Numerical Fluid Mechanics and Multidisciplinary Design*, 139, 3–41. https://doi.org/10.1007/978-3-319-73411-8_1/COVER
- [21] Shen, Z. Y., Hedrick, J. K., & Elkins, J. A. (1983). A comparison of alternative creep force models for rail vehicle dynamic analysis. *Vehicle System Dynamics*, 12(1–3), 79–83. <https://doi.org/10.1080/00423118308968725>
- [22] Van Ruiten, C. J. M. (1988). Mechanism of squeal noise generated by trams. *Journal of Sound and Vibration*, 120(2), 245–253. [https://doi.org/10.1016/0022-460X\(88\)90432-4](https://doi.org/10.1016/0022-460X(88)90432-4)
- [23] Heckl, M. A., & Abrahams, I. D. (2000). Curve squeal of train wheels, Part 1: mathematical model for its generation. *Journal of Sound and Vibration*, 229(3), 669–693. <https://doi.org/10.1006/JSVI.1999.2510>
- [24] Fingberg, U. (1990). A model of wheel-rail squealing noise. *Journal of Sound and Vibration*, 143(3), 365–377. [https://doi.org/10.1016/0022-460X\(90\)90729-J](https://doi.org/10.1016/0022-460X(90)90729-J)
- [25] Schneider, E., Popp, K., & Irretier, H. (1988). Noise generation in railway wheels due to rail-wheel contact forces. *Journal of Sound and Vibration*, 120(2), 227–244. [https://doi.org/10.1016/0022-460X\(88\)90431-2](https://doi.org/10.1016/0022-460X(88)90431-2)
- [26] Heckl, M. A. (2000). Curve squeal of train wheels, Part 2: which wheel modes are prone to squeal? *Journal of Sound and Vibration*, 229(3), 695–707. <https://doi.org/10.1006/JSVI.1999.2511>

- [27] Hsu, S. S., Huang, Z., Iwnicki, S. D., Thompson, D. J., Jones, C. J. C., Xie, G., & Allen, P. D. (2007). Experimental and theoretical investigation of railway wheel squeal. *Proceedings of the Institution of Mechanical Engineers, Part F: Journal of Rail and Rapid Transit*, 221(1), 59–73. <https://doi.org/10.1243/0954409JRRT85>
- [28] Mariani, S., Nguyen, T., Zhu, X., & Scalea, F. L. di. (2017). Field test performance of noncontact ultrasonic rail inspection system. *Journal of Transportation Engineering, Part A: Systems*, 143(5), 04017007. <https://doi.org/10.1061/JTEPBS.0000026>
- [29] Mariani, S., & di Scalea, F. L. (2017). Predictions of defect detection performance of air-coupled ultrasonic rail inspection system. *Structural Health Monitoring*, 17(3), 684–705. <https://doi.org/10.1177/1475921717715429>

Chapter 4. Development of an Improved Passive Rail Inspection System with a Controlled Acoustic Source and Modified Transfer Function Reconstruction

4.1. Introduction

This chapter introduces improvements to the passive rail inspection system discussed in Chapter 2 and Chapter 3. These changes were aimed at improving the stability of the reconstructed transfer functions through changes in data acquisition hardware and data processing techniques. Another aim was to reduce the size of the sensing head by using miniaturized transducers. Changes were made in the following areas:

- 1) Introducing a non-contact air-coupled acoustic source to act in tandem with the wheel induced excitation.
- 2) Testing miniature electrostatic transducers to reduce the size of the prototype sensing head.
- 3) Changing the transfer function reconstruction algorithm to improve the stability and signal-to-noise ratio.

4.1.1. Need for a Controlled Acoustic Source

Field tests on previous generations of the passive rail inspection system have indicated the importance of rail-wheel interactions in the stability of the reconstructed transfer function [1-3]. The stability of the reconstructed transfer function directly affects the discontinuity detection performance of the developed rail inspection system. Unfortunately, the rail-wheel interaction can be highly variable and is affected by different operational parameters such as train speed, rail morphology, flanging vs non-flanging of the wheels, acceleration and braking actions, rail lubrication, rain, etc. Although the developed signal processing technique tends to mitigate these variabilities during the transfer function reconstruction, some of these variabilities end up affecting the stability of the transfer function. Rail-wheel interaction has been found to be the maximum in curved sections of the track due to a combination of curve squeal and wheel flanging. This, in turn, results in higher acoustic signal strengths in the curved sections of the tested rail compared to the tangent sections. For example, Fig. 4.1 shows the raw acoustic signal strengths in different sections of the High Tonnage Loop (HTL) test track at two different speeds of 25 mph and 33 mph. From Fig. 4.1, it is clear that high acoustic signal strengths are achieved at the curved sections of the

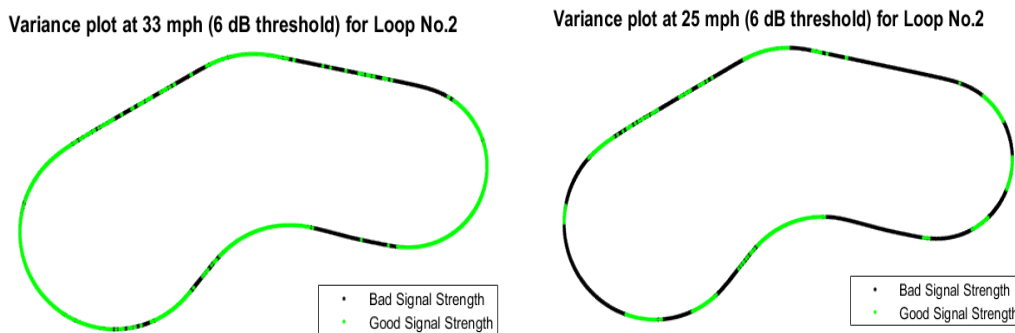


Figure 4.1 'Good' and 'bad' signal strength regions at different speeds (33 mph & 25 mph)

track. Also, higher acoustic signal strengths are obtained when the train speed is increased. In theory, the absolute raw signal strengths should have minimal effect on the reconstructed transfer functions because the normalized cross-power spectrum is computed in the frequency domain. However, the problem starts to occur when the signal-to-noise ratio at the transducers becomes extremely low which leads to the noise affecting the reconstructed transfer function. The intra-segment averaging used to compute the auto-power spectrum tends to minimize the effects of noise. However, the algorithm assumes gaussian and uncorrelated noise at both the receivers. Noise mitigation could adversely be affected if the noise at both receivers is correlated. Therefore, achieving a good signal-to-noise ratio at all the transducer channels is extremely important. To achieve a high acoustic signal strength, several non-contact acoustic sources were studied in the Experimental Mechanics, NDT and SHM laboratory at UC San Diego. The purpose of the controlled acoustic source is to continually excite the rails in addition to the wheel-induced excitation which could potentially be a game changer and improve the stability of the transfer functions and thereby, potentially improving the defect detection performance [4-5].

4.1.2. Need for a Miniature and Ruggedized Sensing Head

Field tests on previous generations of the passive rail inspection system have utilized the VN Instruments CAP-2 air-coupled capacitive ultrasonic transducers for the sensing head on the prototype. The CAP-2 transducers have worked reasonably well in capturing the leaky waves from the wheel-generated excitations in the rail with a relatively low noise-floor and high signal-to-noise ratio. However, the relatively large size of the transducers has resulted in a bulky prototype for the sensing head. Bulky size of the prototype limits the possible locations on the test-car where the prototype can be mounted. Previous tests have indicated that location of the prototype with respect to the locomotive significantly affects the defect detection performance of the passive rail

inspection system. Therefore, it is crucial to have flexibility and convenience in mounting the prototype to ensure optimum location of the sensing head. Reducing the size and weight of the transducers would help in reducing the overall size of the sensing head prototype. Another disadvantage of the CAP-2 transducers is that they have an exposed sensing surface film without any protective covering. Moreover, test runs at high speeds is expected to result in air drafts that can potentially suck pieces of ballast or other debris into the undercarriage of the train and result in damage to the sensing head. An exposed transducer film is expected to undergo more damage in such scenarios than a transducer head that is protected with a cover. Therefore, ruggedizing the sensor head is essential to ensure continuous operation at high speeds with minimal maintenance of the prototype. This chapter delves into a possible alternative transducer with a smaller size, lighter weight and more ruggedized design than the CAP-2 transducer. After careful consideration of various possible options, the SensComp manufactured PID 604142 electrostatic transducer was chosen as an alternative. Another advantage of the SensComp PID 604142 electrostatic transducer over the VN Instruments CAP-2 is the price. The SensComp PID 604142 is priced at USD 24 each while the VN Instruments CAP-2 is priced at USD 650 each. Therefore, if the SensComp PID 604142 is used as an alternative sensing head, it will result in cost savings of up to 96%. Considering the potential of the developed technology being used in multiple trains, this will result in significant cost savings for potential industry partners thereby making the technology more lucrative.

4.2. Laboratory Tests with Controlled Acoustic Source

4.2.1. Test Setup

Several different types of contact-based and non-contact controlled acoustic sources were tested in a laboratory setup to select an optimum excitation source. The test setup is shown in Fig.

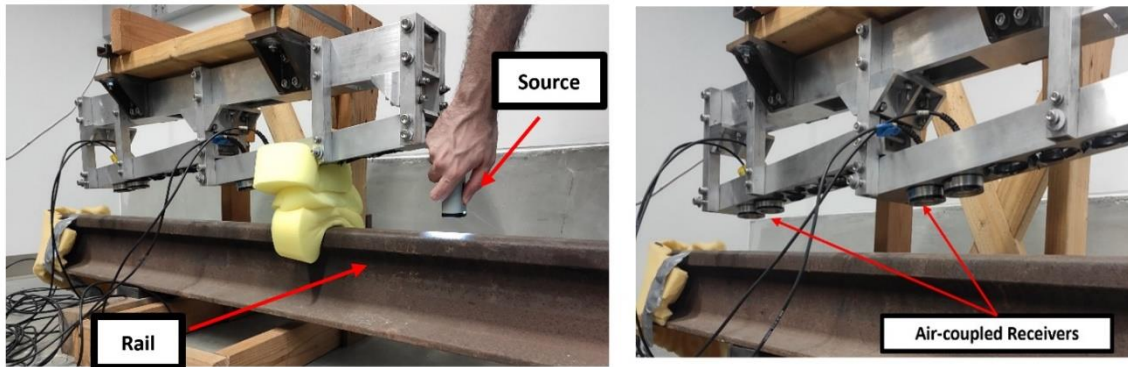


Figure 4.2 Controlled acoustic source laboratory test setup

4.2. The setup consisted of four air-coupled receivers mounted on a prototype (similar to the prototype used in TTCI field tests) above a section of pristine rail. Different sources were mounted near the receivers and were used to excite the rail. Foam padding material was placed between the source and the receivers to minimize the air-shock waves traveling directly through air from the source to the receivers. This is done because we are only interested in the transfer function that captures the ultrasonic waves traveling through the rail from one receiver to the other. The direct wave traveling from the source to the receiver does not represent the rail as the test medium for the transfer function and therefore is not of interest. Data was recorded on all four receiver channels for a duration of 20 seconds at a sampling frequency of 1 MHz. During data processing, the sampling frequency was down-sampled to 500 kHz. Pre-amplifiers were used at each receiver channel with a gain set to 59 dB for all the tests. For continuous excitation when ultrasonic transducers were used a source, a function generator coupled with a high-voltage amplifier was used. The function generator was programmed to generate square waves at different frequencies (for different sources) at ± 1 V peak-to-peak. These square waves were then amplified with the high-voltage amplifier with a gain factor of 200 to convert the ± 1 V square waves to ± 200 V square waves. The reason for this amplification was to ensure that the source imparted sufficient

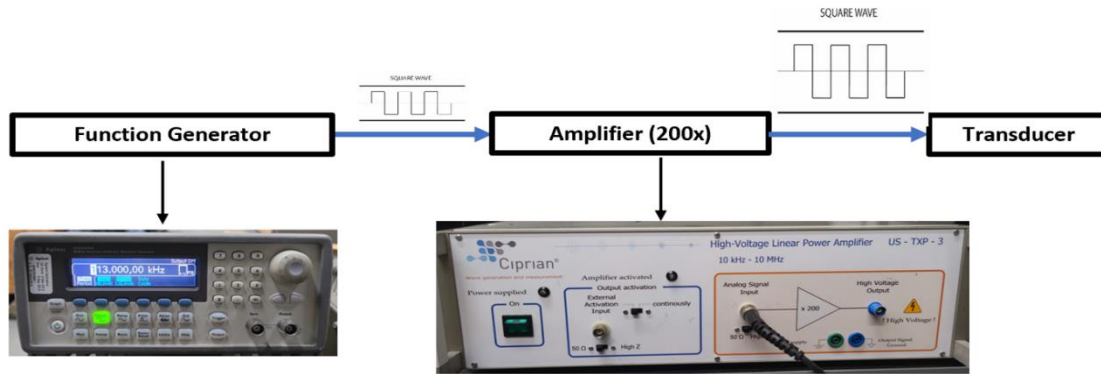


Figure 4.3 Schematic of test setup with function generator and high-voltage amplifier

energy into the rails. A schematic of the test setup with the function generator and the high-voltage amplifier is shown in Fig. 4.3. The amplifier was carefully chosen to ensure a continuous excitation was provided instead of a pulsed excitation which is commonly used in ultrasonic testing. After testing different potential sources, the CAP-2 transducers were chosen for exciting the rails. Section 4.2.2 outlines the results obtained with the CAP-2 transducers as source.

4.2.2. Capacitive Ultrasonic Transducer (VN Instruments CAP-2) as Source

The VN Instruments CAP-2 capacitive ultrasonic transducers were tested as a potential source. These transducers have a central frequency of ~ 113 kHz. Promising results were obtained with these transducers and a number of additional tests were performed with these transducers acting as a source in solo and in multiples. Other parameters such as driving frequency, angle of the transducers and distance from the receivers were also tested to determine the optimum combination. The source is placed approximately 1.5 ft away from the first receiver. The CAP2 transducers also require a 200 V DC bias when operating. The CAP2 transducers are the same type of transducers that were used for the TTCI field tests.

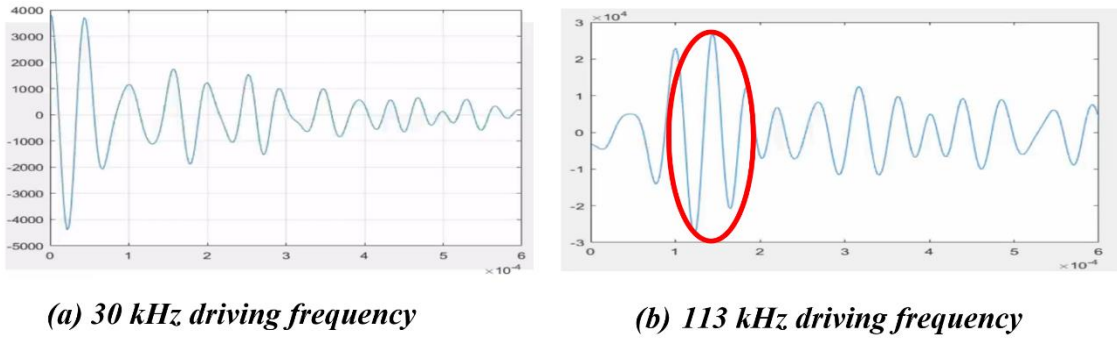


Figure 4.4 Transfer function with 1 CAP2 driven at (a) 30 kHz and (b) 113 kHz

4.2.2.1 One CAP-2 driven at 30 kHz

Fig. 4.4 (a) shows the transfer function reconstruction with 1 CAP 2 transducer as source when driven at 30 kHz driving frequency. In this configuration, the transducer was aimed to launch waves perpendicularly on the rail. No proper reconstructions are achieved with this configuration.

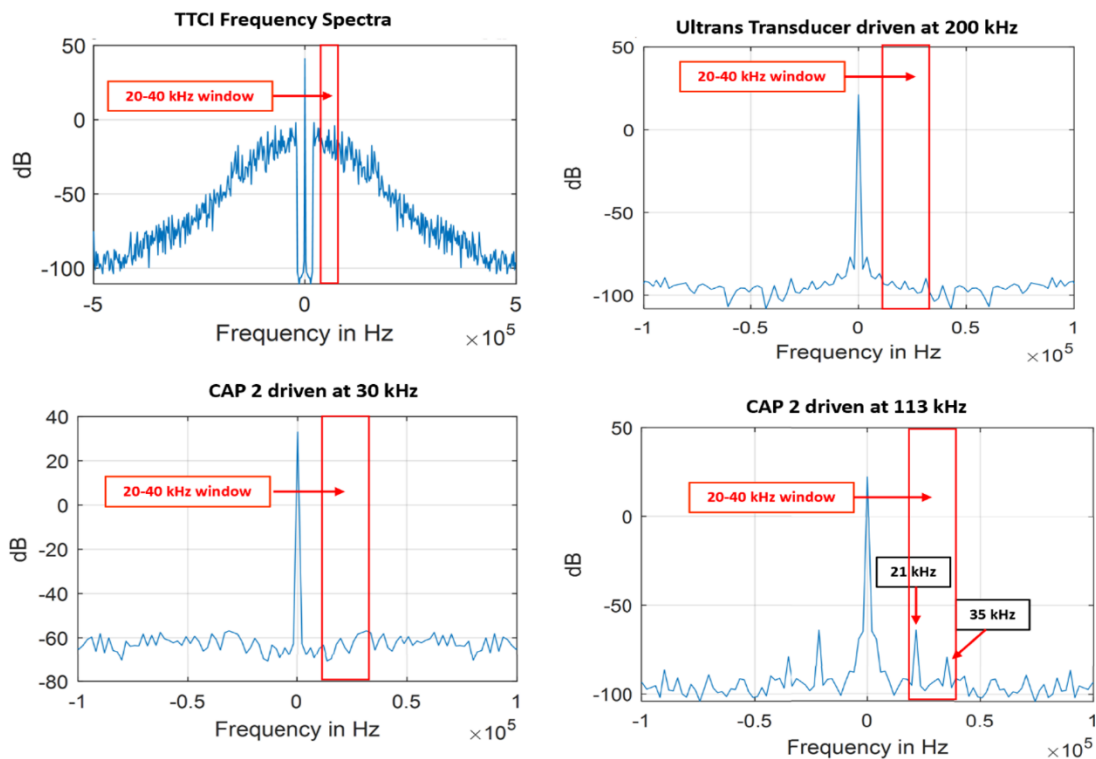


Figure 4.5 Frequency spectra with different sources at different driving frequencies

4.2.2.2 One CAP-2 driven at 113 kHz

Fig. 4.4 (b) shows the transfer function reconstruction with 1 CAP-2 driven at 113 kHz. A proper transfer function reconstruction is achieved with this configuration. It can be determined from these results that the driving frequency for the source transducer also plays an important role. To understand how the driving frequency affects the results, we look at the frequency spectra shown in Fig. 4.5. The transfer function is extracted in the frequency bandwidth of 20 kHz – 40 kHz. From Fig. 4.5 it can be observed that the Ultrason NGC 200 when driven at 200 kHz has no significant energy in the 20 kHz – 40 kHz frequency spectrum. Similarly, the CAP-2 driven at 30 kHz has no significant peaks (energy) in the bandwidth of 20 kHz – 40 kHz. The CAP-2, however, when driven at 113 kHz driving frequency has two resonant peaks at 21 kHz and 35 kHz which lie in the 20 kHz – 40 kHz bandwidth. Therefore, the CAP-2 when driven at 113 kHz yields better transfer function reconstructions compared to a driving frequency of 30 kHz. The TTCI spectrum from wheel generated excitations is, of course, broadband and has significant energy in the 20 kHz- 40 kHz bandwidth.

4.2.2.3 Angles of Attack for the Source

Now that the optimum transducer has been chosen, several tests were performed to determine the best angle of attack for the source transducer. Several different angles of attack were chosen, and the transfer functions were reconstructed at these angles. Fig. 4.6 shows the test setup with different angles of attack for the CAP-2 source. Fig. 4.7 shows the transfer functions obtained at the different angles. Note that 0 degree represents the case when the waves are launched perpendicularly on the rails. The angles are changed with respect to this reference (0 degree) by rotating the sensor in clockwise direction to point towards the receivers which are located to the left of Fig. 4.6. From Fig. 4.7, it can be observed that the transfer function with the best signal-to-

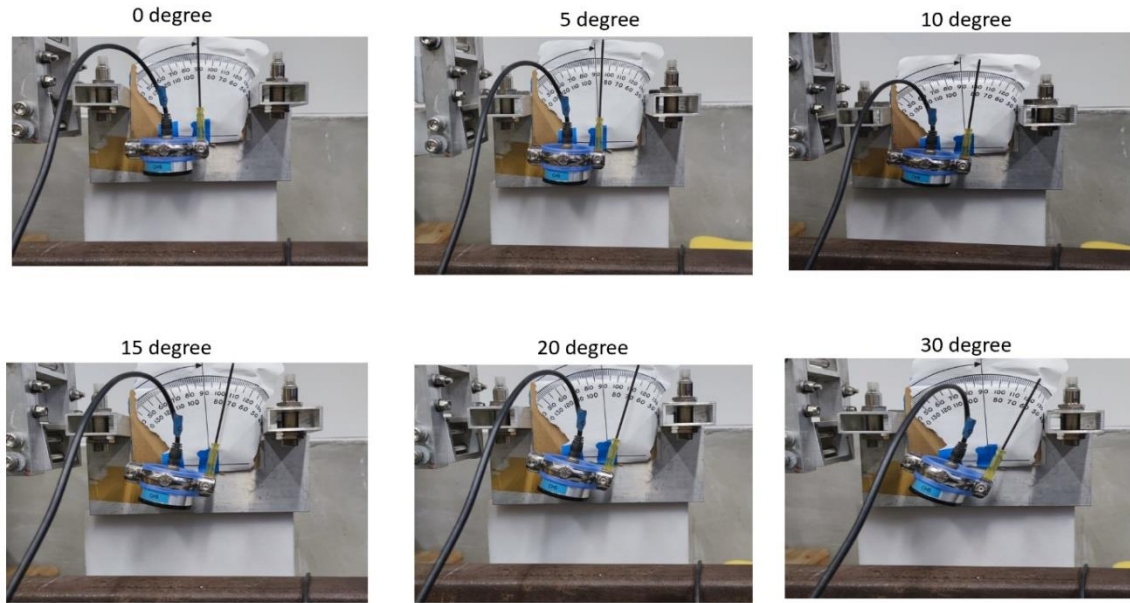


Figure 4.6 Test setup with one CAP2 source and different angles of attack

noise ratio is obtained at an angle of about 5 degrees with respect to the vertical axis. Based on these results, an angle of attack equal to 6 degrees was chosen for the source transducers. The magnitude of the angle is similar to the angle of attack of the receivers for normal incidence of the leaky waves leaking from the rail into the air. The sense of this angle is, however, opposite to the sense in which the receivers are oriented. For example, if the receivers are anticlockwise at 6 degrees with respect to the vertical axis, the source would be clockwise at 6 degrees with respect to the vertical.

4.2.2.4 Number of Source Transducers

To determine if the number of sources affected the transfer functions, tests were performed with one CAP-2 transducer as source and compared to two CAP-2 transducers as source. Fig. 4.8 shows the schematic of the test setup with the raw acoustic signals at the nearest and farthest receiver with one and two CAP-2 sources. There is not a significant difference in the acoustic signal strength with two sources as compared to one. Note that the acoustic signal strength at the

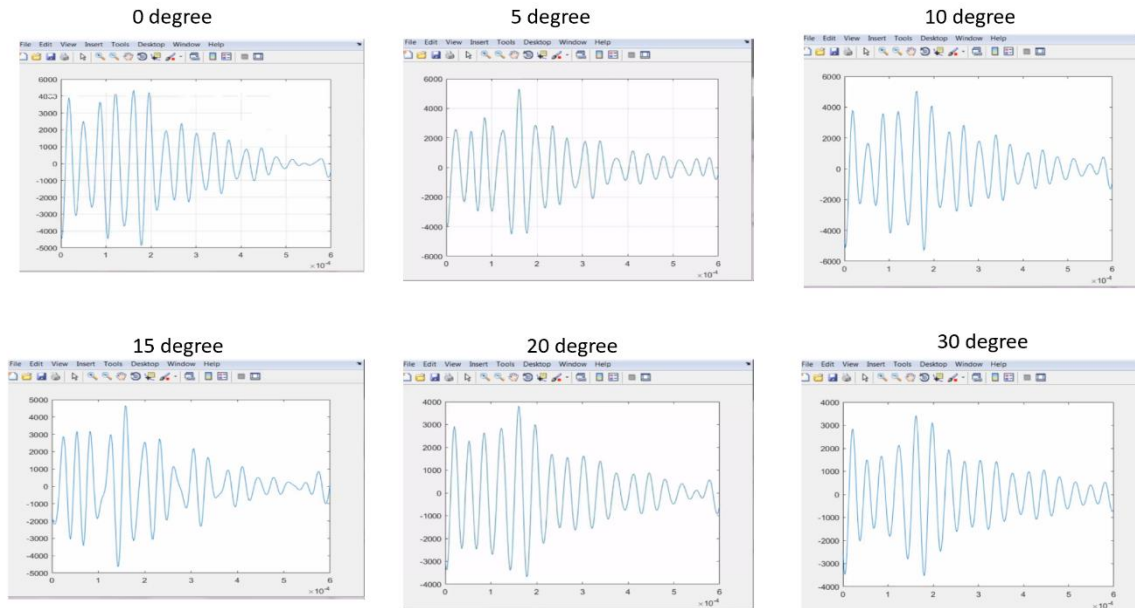


Figure 4.7 Transfer function reconstructions at different angles of attack

nearest receiver is larger than the farthest receiver because of attenuation as the wave travels through the rail. Fig. 4.9 shows the transfer functions with one and two CAP-2 sources. It can be observed that the signal-to-noise ratio of the transfer function is higher when two sources are used as compared to one source. Therefore, two sources were selected as the optimum choice.

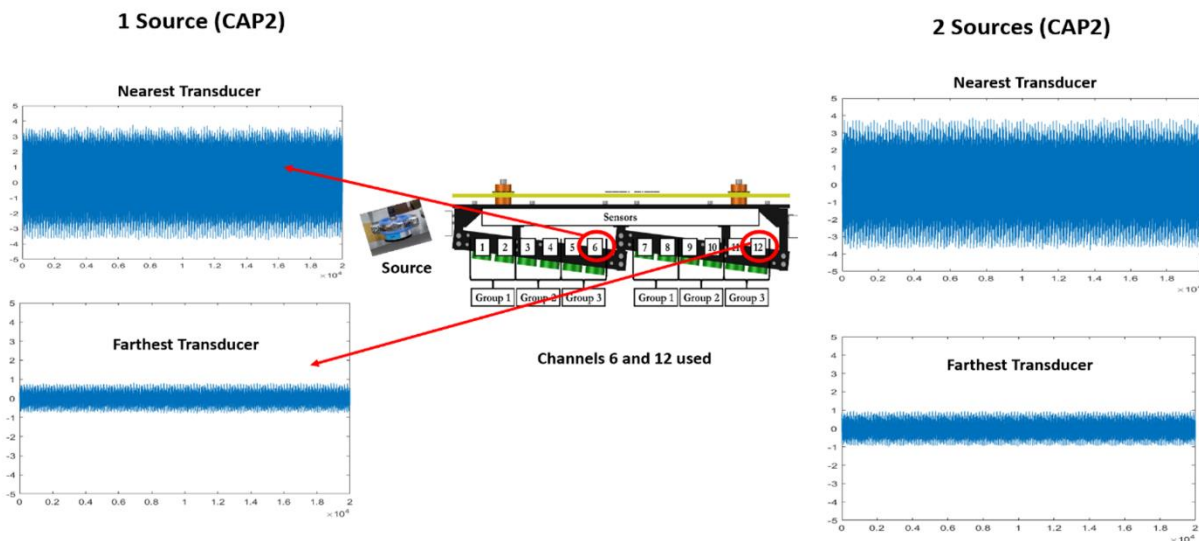
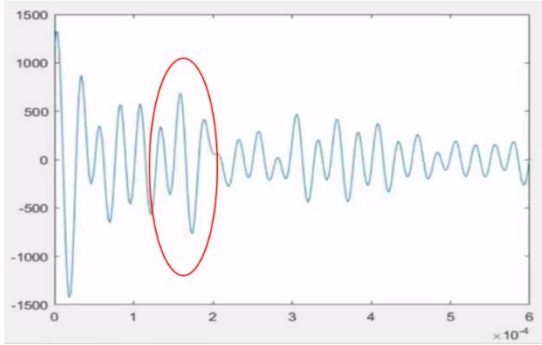
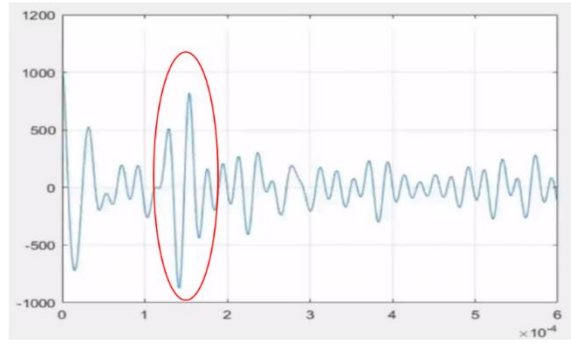


Figure 4.8 Schematic of test setup with one and two sources along with raw acoustic signals



(a) One CAP2 source



(b) Two CAP2 sources

Figure 4.9 Transfer functions with (a) one source and (b) two sources

4.2.2.5 Distance of Source from Receivers

Multiple receivers are used in groups during field tests with the prototype. All the tests discussed so far had the receivers placed quite farther away from the source. To ensure that the distance of the source is enough for receiver group 1, a set of tests were performed by placing the two sources at different distances from the first receiver. One test was performed with the first source placed about 4 inches from the edge of the prototype and another test was performed with the first source at about 6 inches from the prototype edge. Fig. 4.10 shows the transfer functions

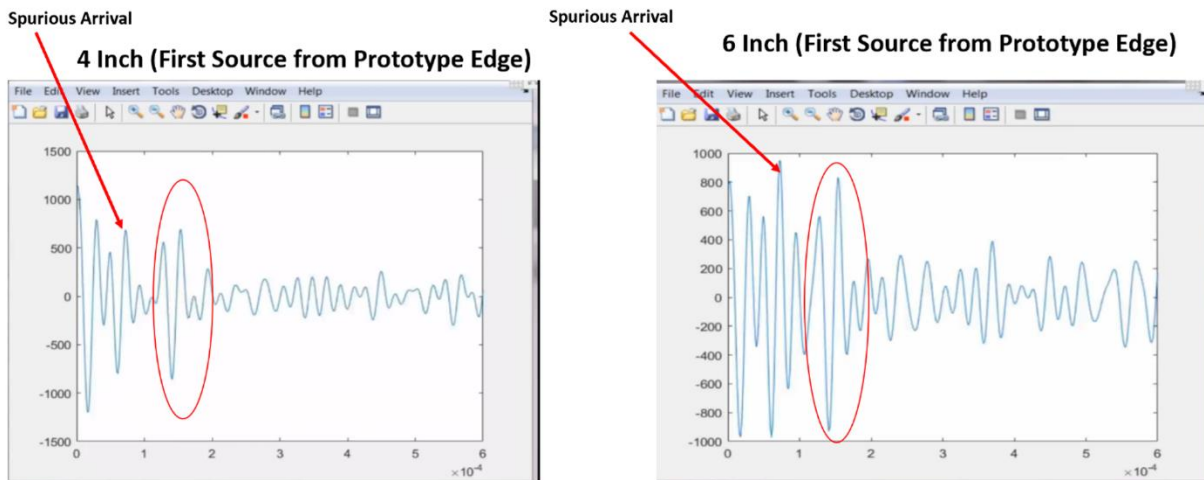


Figure 4.10 Transfer function from pair 1-7 for different distances from the sources

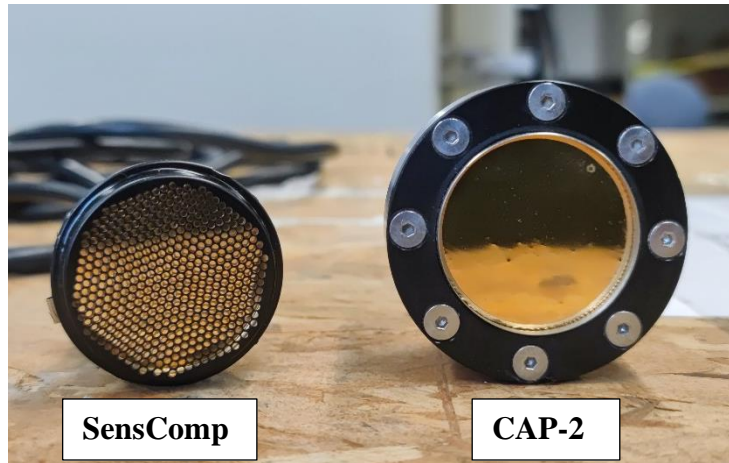


Figure 4.11 Size comparison of SensComp and CAP-2 transducers

obtained from pair 1-7 for distances of 4 inches and 6 inches. Some spurious arrivals can be observed in Fig. 4.10 when the sources are very close to the receivers. These spurious arrivals, however, are not expected to affect the results of defect detection because the arrival wave packet is windowed and that will eliminate these spurious arrivals.

4.3. Laboratory Tests with Miniature Electrostatic Transducers

Tests were performed in a laboratory setting using the SensComp PID 604142 electrostatic transducers and the controlled acoustic source consisting of two CAP-2 transducers. A long piece

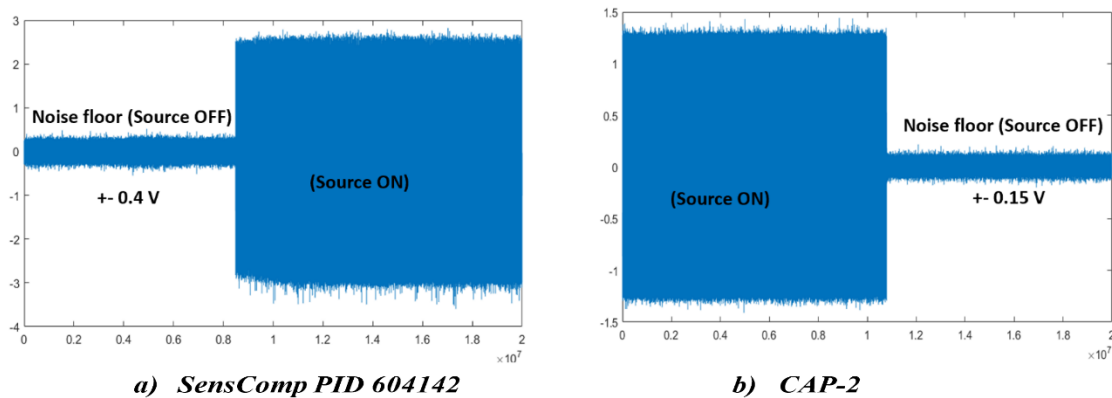


Figure 4.12 Comparison of the signal-to-noise ratio using a) SensComp PID 604142 transducer and b) CAP-2 transducer

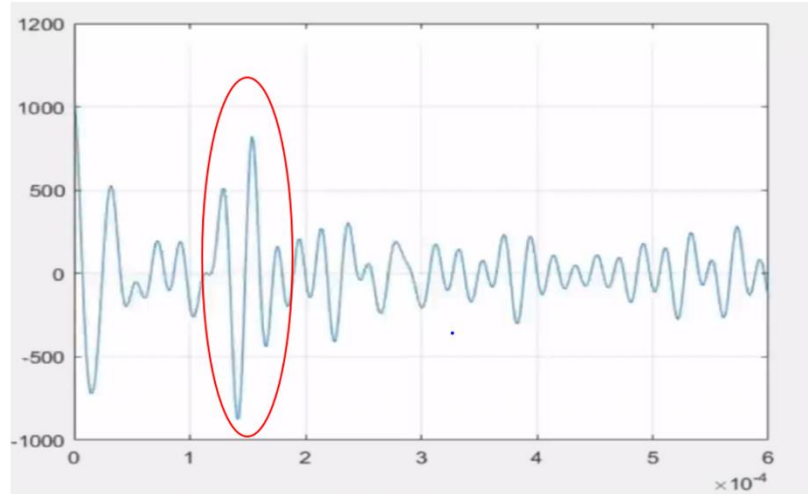


Figure 4.13 Sample transfer function reconstruction using two SensComp transducers

of rail was used for these tests as shown in Fig. 4.2. The source transducers were driven with 400 V square wave using a high-voltage amplifier at a driving frequency of 113 kHz. The electrostatic transducers were used in air-coupled receiving mode. Fig. 4.11 shows a size comparison of the CAP-2 and the electrostatic SensComp PID 604142 transducer. The electrostatic transducers are smaller in size, thickness and weight as compared to the CAP-2. Fig. 4.12 shows a comparison of the electrostatic transducer (SensComp PID 604142) and the CAP-2 transducer with the source turned on vs source turned off. From Fig. 4.12, it is clear that the CAP-2 transducers have a lower baseline noise floor of ± 0.15 V compared to the baseline noise floor of the SensComp PID 604142 which is ± 0.4 V. However, it is worth noting that the SensComp PID 604142 achieves a stronger acoustic signal strength of ± 5 V compared to the CAP-2 which achieves a signal strength of ± 3 V. Therefore, the effective signal-to-noise ratio for both the transducers is similar. In this specific scenario, the CAP-2 transducer achieves a signal-to-noise ratio of 26 dB whereas the SensComp PID 604142 achieves a signal-to-noise ratio of 22 dB. Fig. 4.13 shows a sample transfer function reconstruction using two SensComp PID 604142 transducers. The arrival wave in Fig. 4.13 is indicated in a red oval shape. The time of arrival of this wave corresponds to the time-of-flight of

the waves travelling through the rail to travel 18 inches. A good transfer function reconstruction is obtained using the miniature electrostatic transducers.

4.4. Improved Transfer Function Reconstruction Algorithm

One of the parameters investigated to improve the transfer function reconstruction was the length (and number) of the segments and the snapshot used for each reconstruction. In general, a longer recording time (snapshot length) is likely to result in better transfer function reconstructions. Unlike underwater acoustic applications [6-10] where the sensor array is generally stationary, the passive rail inspection technique utilizes a transducer array that is mounted on a moving train. A key challenge for recording data using a moving transducer array is to ensure sufficient recording length while also maintaining adequate spatial resolution for each recorded snapshot. As the transducer array is moving, longer snapshots will result in lower spatial resolution. Therefore, a compromise needs to be made with a tradeoff between recording length and spatial resolution. For results discussed in chapters 2 and 3, the length of each snapshot used was 4096 samples. For a 1 MHz sampling rate, 4096 samples (snapshot length) correspond to approximately 3 inches in space. The snapshot with 4096 samples is further divided into segments with 256 samples and a transfer function is obtained by averaging the 256-point segments over the 4096-point snapshot using the modified Welch's periodogram technique [11] discussed in Chapter 2. Such averaging improves the signal-to-noise ratio by minimizing the uncorrelated noise [12]. For a 4096-point snapshot with 256-point segments, a total of 31 averages are obtained when a 50% overlap is used between consecutive segments. Increasing the length of the snapshot while keeping the length of the segments constant increases the total number of averages. On the other hand, keeping the length of the snapshot constant while increasing the length of the segments reduces the total number of

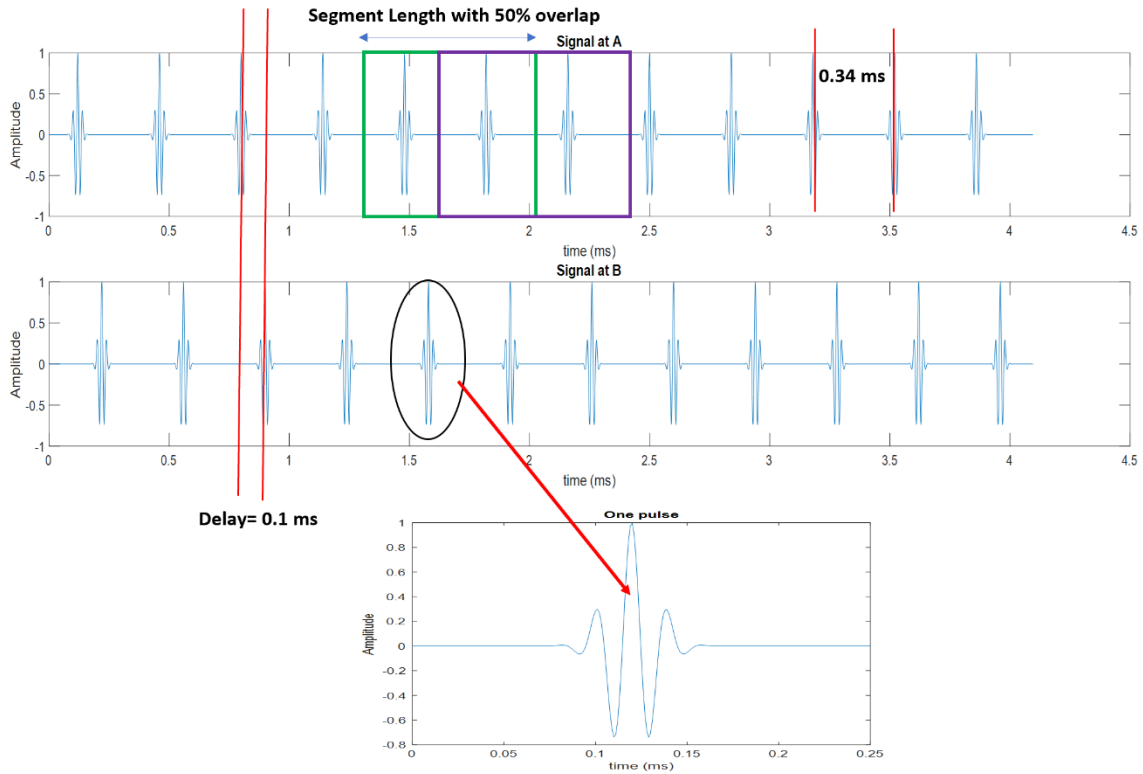


Figure 4.14 Gaussian pulse trains generated at two locations with a time delay of 0.1 ms

averages. In this section, the effect of changing the length of the segments is studied as a possible way of improving the reconstructed transfer functions.

4.4.1. Transfer Functions with Simulated Signals

To understand the effects of different segment lengths on the reconstructed transfer function, a set of simulated signals was used. Fig. 4.14 shows a train of gaussian pulses each having a central frequency of 50 kHz and a bandwidth of 0.6 MHz. These gaussian pulse trains are generated for two different channels (A and B) to simulate the two transducer locations. The signals at location B are shifted with respect to A by 0.1 ms to simulate the delay between time-of-flight at the two locations. The gap between consecutive pulse in both the signals is kept constant at 0.34 ms. A sampling frequency of 1 MHz is used with a total of 4096 samples in each

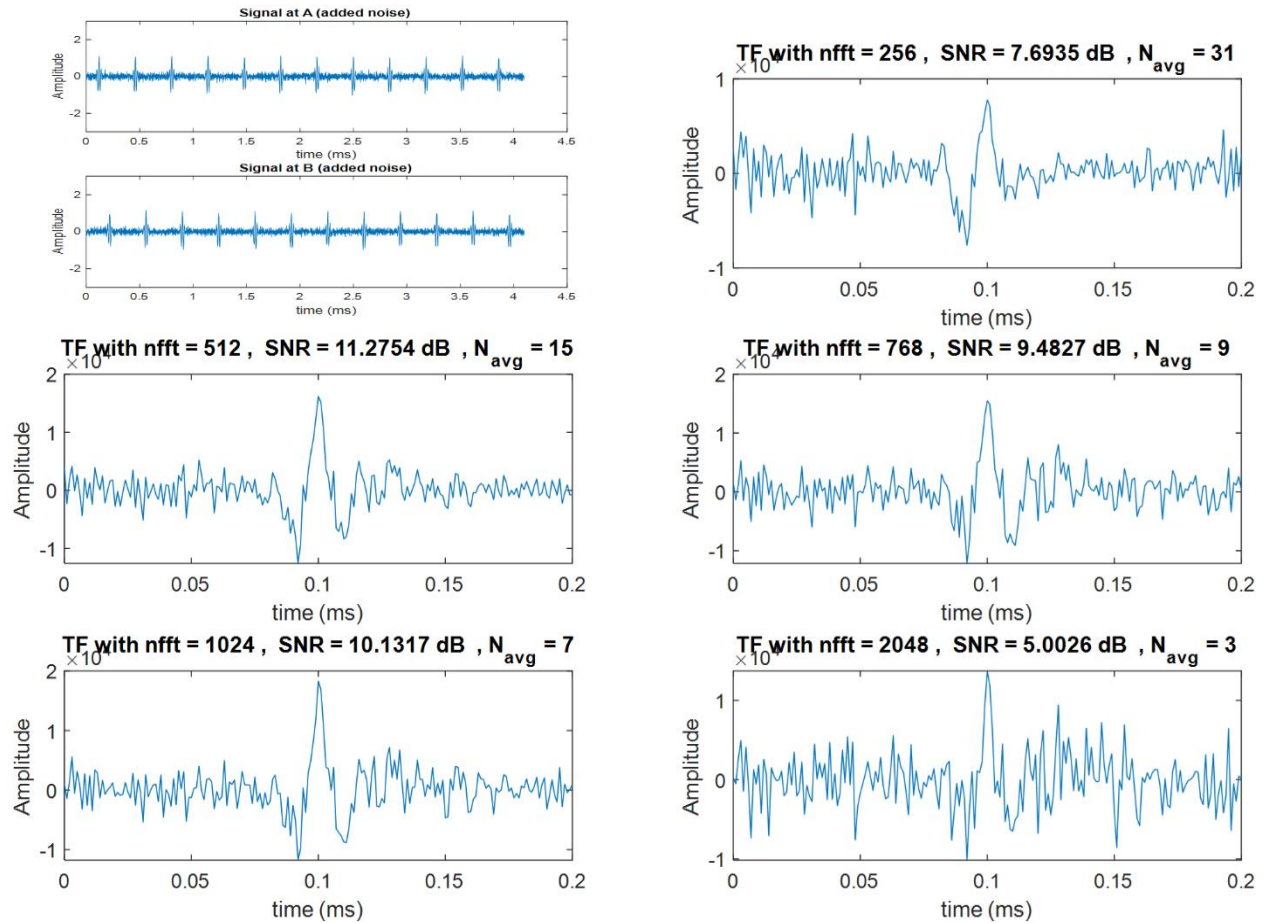


Figure 4.15 Transfer functions obtained with different segment lengths (*nfft*) for a 4096-point gaussian pulse train with added noise

signal at A and B. Uncorrelated white gaussian noise with a signal-to-noise ratio of 20 dB is added to each signal shown in Fig. 4.14 separately. Fig. 4.15 shows the unfiltered (full bandwidth) transfer functions obtained for different segment lengths with 50% overlap. In Fig. 4.15, ‘*nfft*’ is the number of points in the Fast Fourier Transform for each segment. The value of ‘*nfft*’ is taken equal to the length of the segment in each case. Note that as the length of the segment (also *nfft*) increases, the number of averages (N_{avg}) reduces. For example, with a 256-point segment, 31 averages are obtained for the 4096-point snapshot whereas only 15 averages are obtained with a 512-point segment. The arrival wave packet in the transfer functions have a peak at 0.1 ms which is the time-delay between the signals at channels A and B. The signal-to-noise ratio (SNR) is 11.28

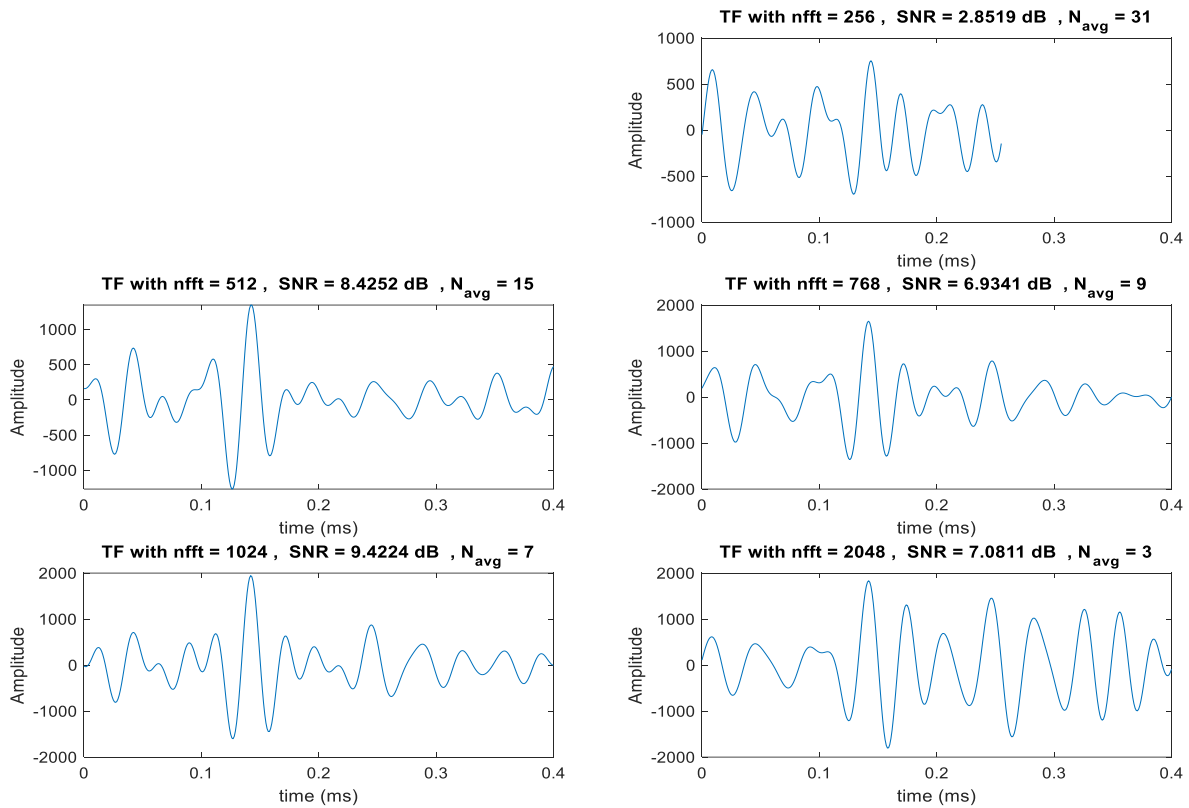


Figure 4.16 Transfer functions from TTCI field tests using CAP-2 transducers (Group-1) for different segment lengths

dB with a 512-point segment and 7.69 dB with a 256-point segment. Higher SNR signifies an improved transfer function reconstruction. From Fig. 4.15, a segment length of 512 points yields the highest SNR. Longer segment lengths include higher number of pulses and therefore, a cross-correlation (cross power spectrum in frequency domain) amplifies the coherent signals, thereby improving the SNR. Averaging (using Welch’s periodogram technique) also produces a similar effect of improving the SNR. Since a 512-point segment (with 15 averages) yields better SNR (of the transfer function) than the 256-point segment (with 31 averages), the effect of a longer segment seems to outweigh the effect of averaging in this case. The SNR drops to 5 dB with a 2048-point

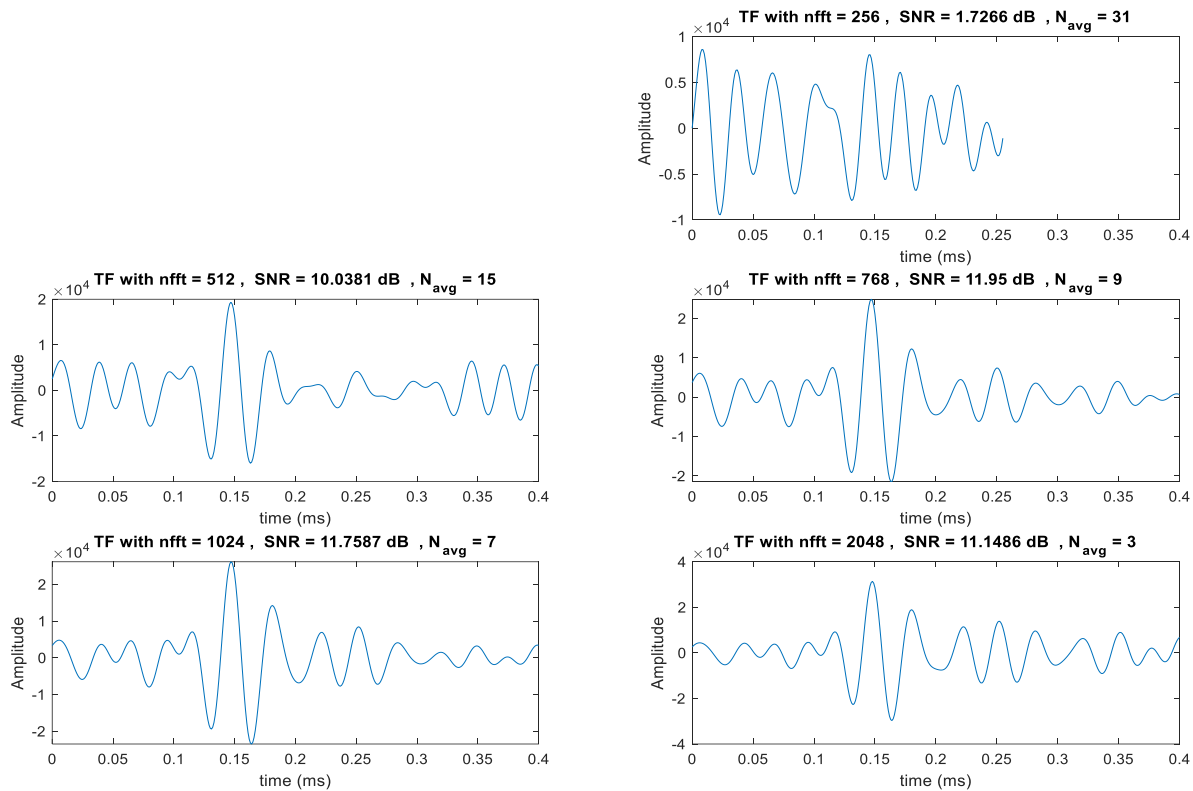


Figure 4.17 Transfer functions from TTCI field tests using SensComp transducers (Group-2) for different segment lengths

segment length which has only 3 averages. Therefore, a combination of segment length and number of averages needs to be considered when selecting the optimum parameters.

4.4.2. Transfer Functions from Experimental Signals

Another set of field tests were carried out at TTCI using the controlled acoustic source and SensComp transducers as discussed in section 4.5. Some sample transfer function reconstructions from these field tests are presented here. Fig. 4.16 and Fig. 4.17 show the filtered transfer functions (20 kHz – 40 kHz) for different segment lengths obtained with the CAP-2 and SensComp transducers respectively. Note that the transfer functions reconstructions with the CAP-2 and SensComp transducers are similar. Clearly, the transfer functions obtained with the of 512-point

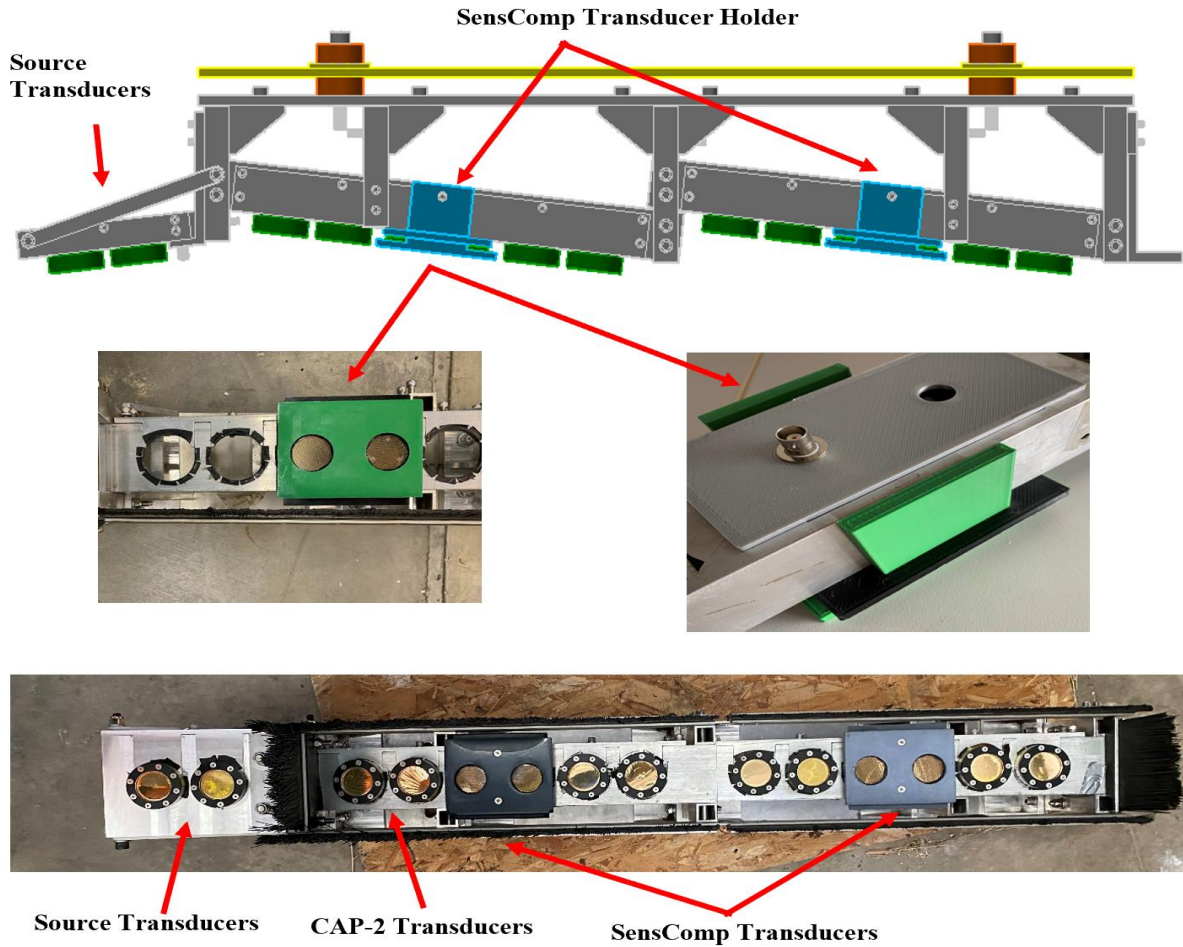


Figure 4.18 Redesigned prototype with the controlled acoustic source and SensComp transducers (AutoCAD drawing and fabricated product)

segments yield better SNR than the 256-point segments for both CAP-2 and SensComp transducers. The 512-point segment length was adopted to obtain the improved transfer functions and results for discontinuity detection performance are discussed in section 4.5.3.

4.5. Field Tests

4.5.1. Prototype Redesign

The existing prototype was redesigned to accommodate the two CAP2 transducers which served as the controlled acoustic source. A new holder was designed to mount the two source

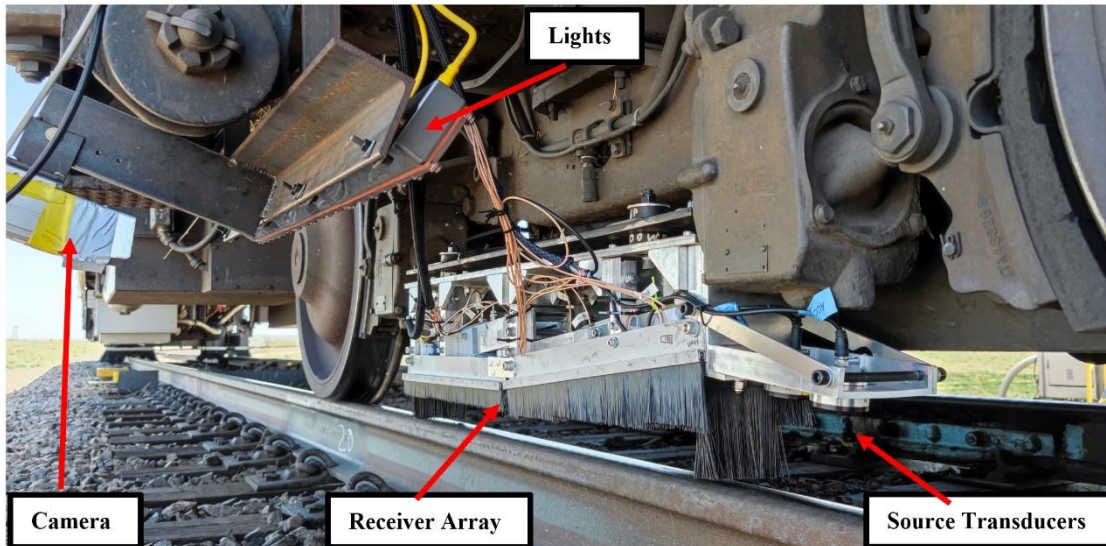


Figure 4.19 Field test setup with redesigned prototype using active source

transducers. The angle of attack of the source transducers was chosen as 6 degrees based on laboratory tests discussed in section 4.2.2.3. Fig. 4.18 shows the redesigned prototype with the holder for the source transducers and SensComp transducers. The source holder was rigidly connected to the main prototype using vertical and horizontal bolts as well as two braces. The four electrostatic SensComp transducers were placed in group-2 of the prototype. Groups 1 and 2 consisted of CAP-2 transducers. This new prototype was used for the field tests at TTCI.

4.5.2. Test Methodology

Tests were conducted at TTCI with the modified prototype incorporating the source transducers and the electrostatic transducers. The test setup is shown in Fig. 4.19. Tests were conducted on the HTL at different speeds. Two test runs were conducted at speeds of 25 mph, 33 mph, 40 mph with the active source turned on. In addition, one test run was conducted at 40 mph with the source turned off to compare the performance in the two different scenarios. Known transverse defects were marked with spray paint to facilitate the camera picking them up. A ground

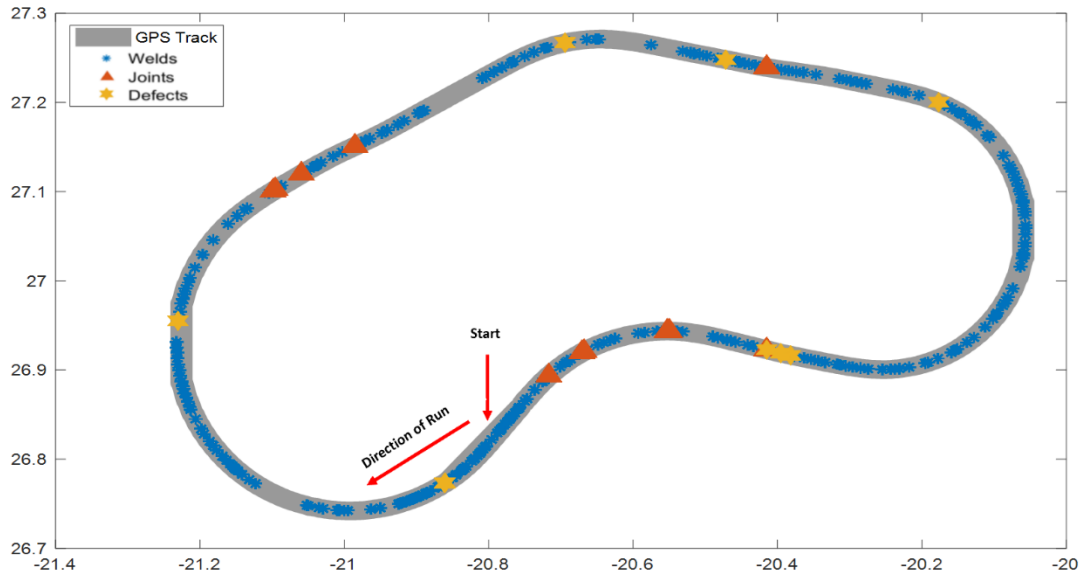


Figure 4.20 Locations of welds, joints, and transverse defects along the probed rail of the HTL (June 2022 Tests)

truth library with GPS coordinates was then built by processing the camera images. Fig. 4.20 shows the locations of welds, joints and defects on the inner rail (inspected) of the HTL. Test runs were performed in an anticlockwise manner probing the inner rail of the HTL. A total of 284 welds, 11 joints, and 9 transverse defects were identified.

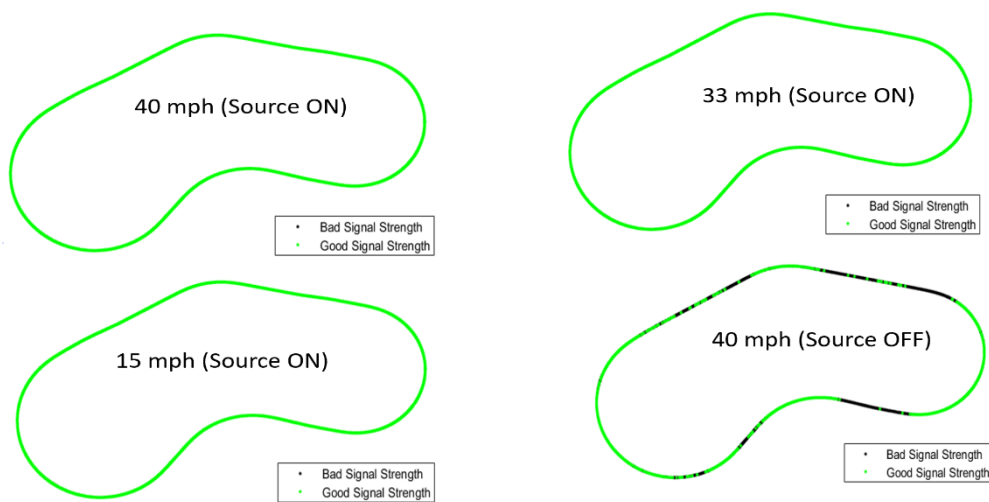


Figure 4.21 Raw acoustic signal strength classification with source turned on and off

4.5.3. Results

4.5.3.1 Acoustic Signal Strengths

Fig. 4.21 shows the acoustic signal strengths at different test speeds with the source on compared to the source turned off. Good signal strengths with the source are obtained even for the tangent sections of the HTL. A comparison of signal strengths with the source turned off indicates the significant improvement in raw acoustic signal strengths.

4.5.3.2 ROC Curves with Improved Transfer Function Reconstruction

The effects of changing the segment lengths used for averaging over the snapshot was discussed in section 4.4. The overall change in discontinuity detection performance was evaluated for segments lengths of 256-points and 512-points. Fig. 4.22 shows the ROC curves with Group-1 (CAP-2) transducers for welds, joints, defects obtained at 40 mph testing speed and the active

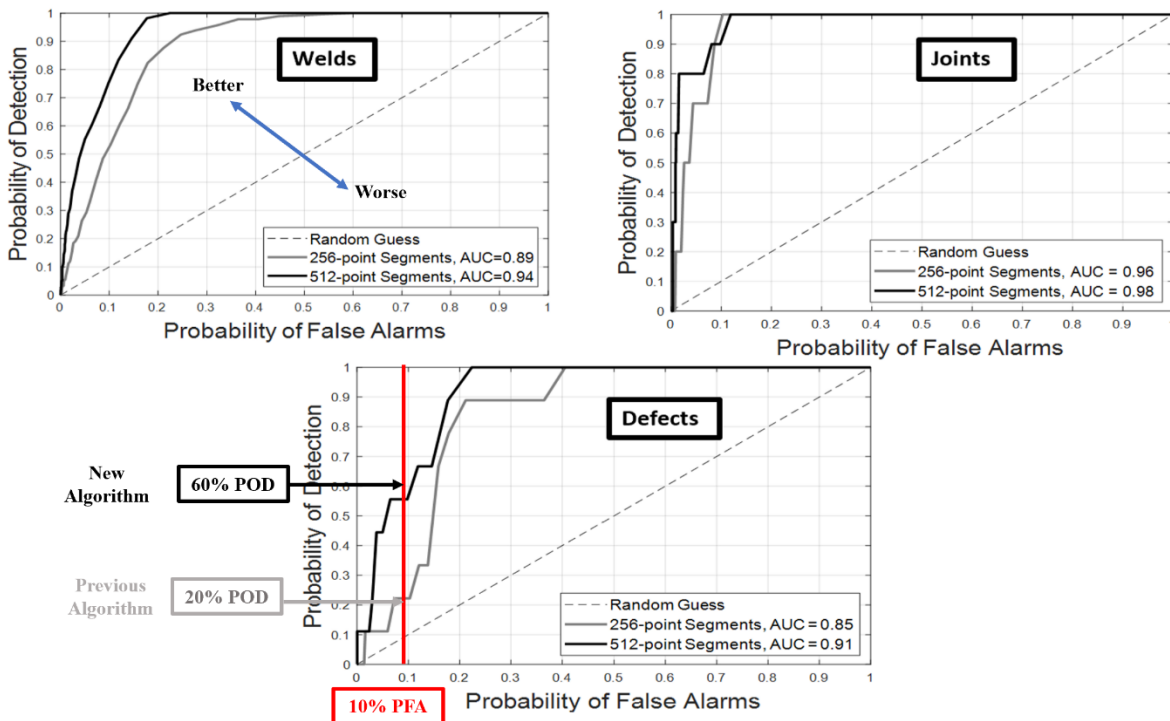


Figure 4.22 ROC curves for different segment lengths at 40 mph (Group-1 CAP-2) with source on

source turned on. Note that performance improves with 512-point segments when compared to 256-point segments. For example, with 10% PFA, the previous algorithm detects 20% of the defects and the new algorithm detects 60% of the defects. Again, the reason for this improvement can be attributed to the more stable transfer function reconstructions and better SNR with 512-point segments. The staggered nature of the ROC curves for joints and defects is due to the fact that there are fewer number of joints and defects compared to welds. Therefore, fewer values of probability of detection are possible in case of joints and defects which leads to the staggered nature of the curves in Fig. 4.22.

4.5.3.3 ROC Curves with Controlled Acoustic Source On and Off

The controlled acoustic source was added to the inspection prototype to improve the SNR of the reconstructed transfer functions. Fig. 4.23 shows the joint, weld and defect detection

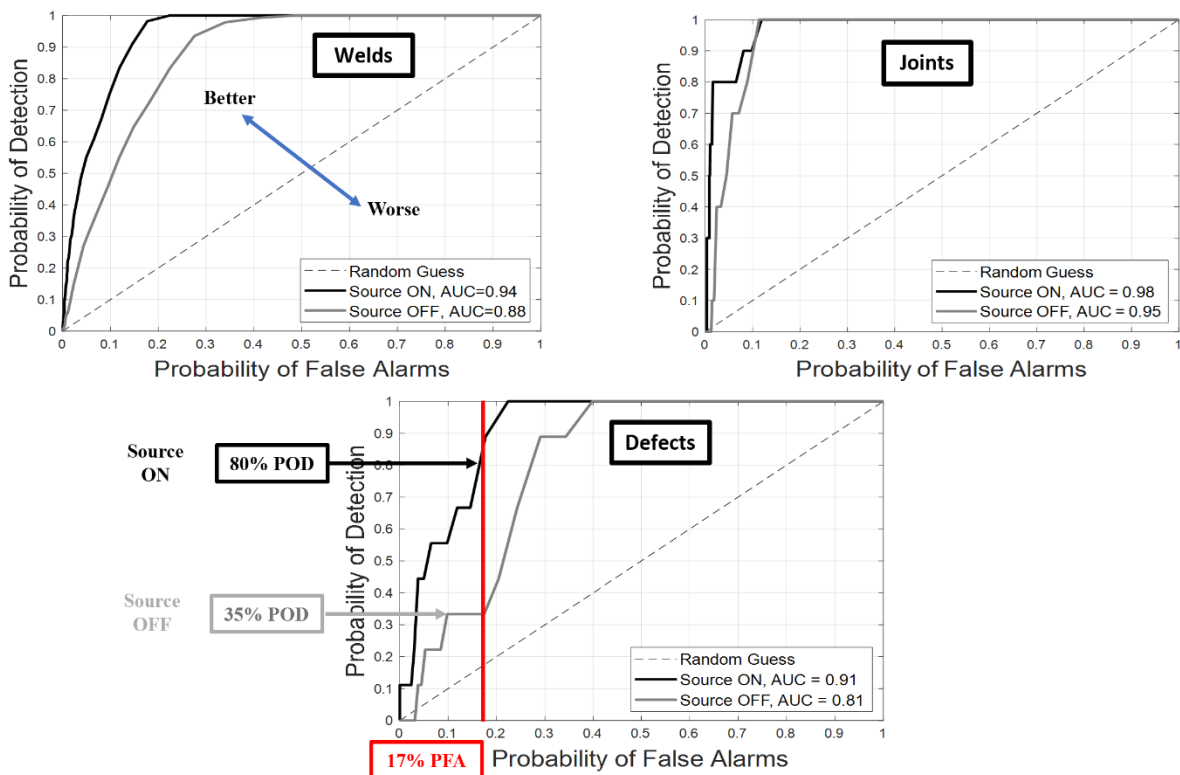


Figure 4.23 ROC curves for source on and off at 40 mph (Group-1 CAP-2)

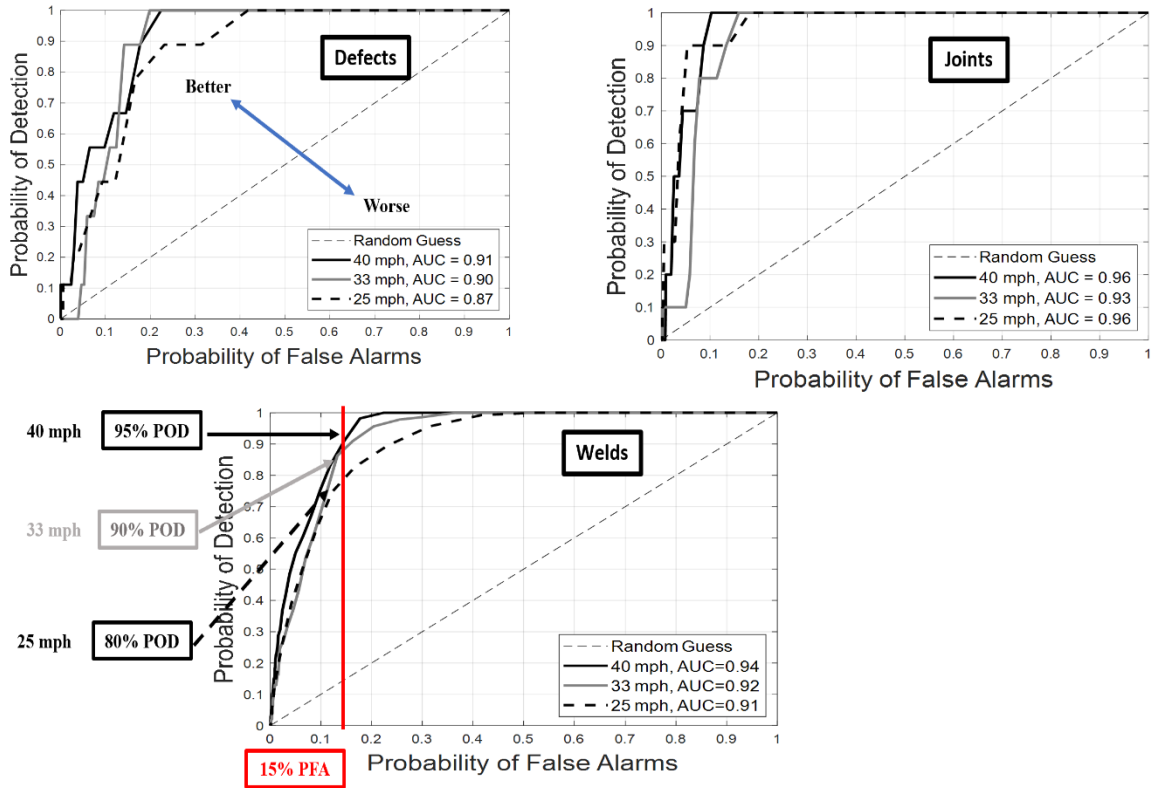


Figure 4.24 ROC curves at different speeds in the presence of acoustic source

performance for the Group-1 CAP-2 transducers at 40 mph with the source on and off. The controlled acoustic source improves the discontinuity detection performance. For example, at the expense of 17% false alarms, the defect detection rate with the source off is 35% and the defect detection rate with the source on is 80%.

4.5.3.4 ROC Curves for Different Speeds

Fig. 4.24 shows the ROC curves for joints, welds and internal defects at different testing speeds in the presence of the controlled acoustic source. Slightly improved discontinuity detection performance is still observed at higher speeds. This difference in detection performance could be attributed to the fact that the wheels generate stronger acoustic signals at higher speeds and the acoustic source doesn't compensate enough for this loss of excitation at lower testing speeds.

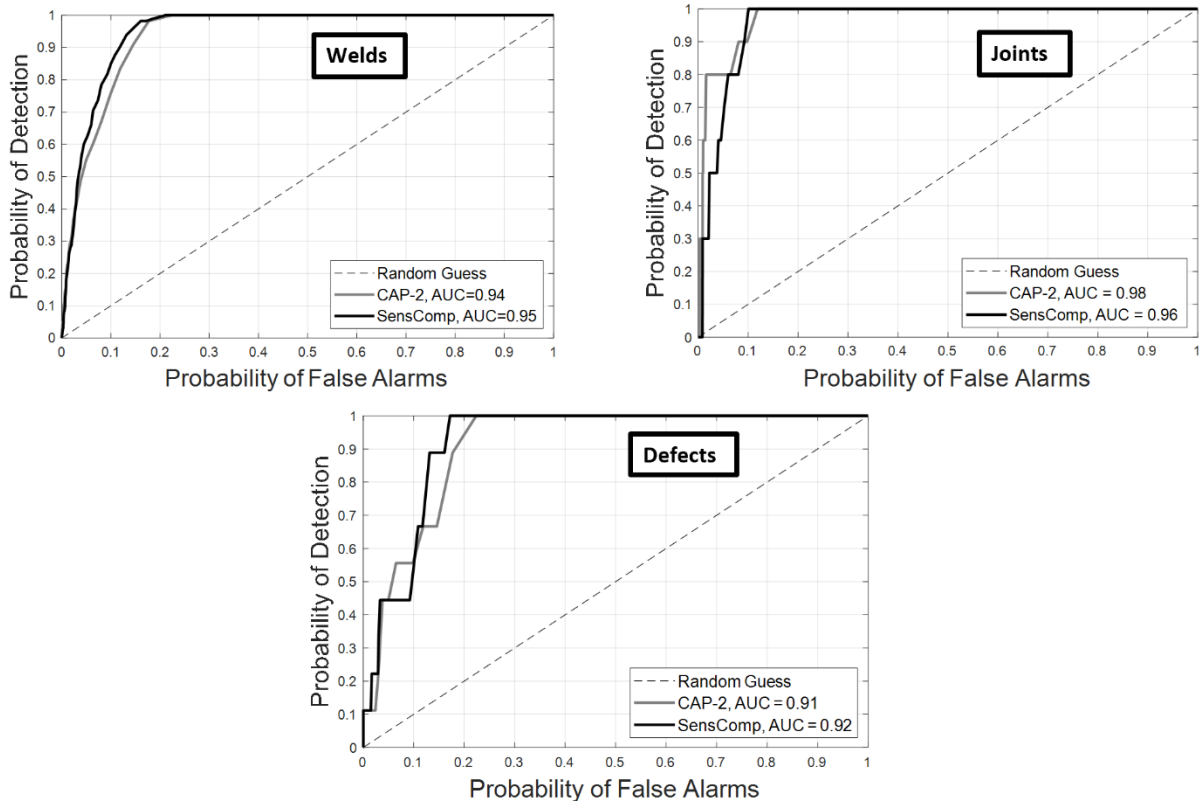


Figure 4.25 ROC curves for different transducer type (CAP-2 vs SensComp) at 40 mph with source on

4.5.3.5 ROC Curves for Different Transducers

To compare the performance of the CAP-2 capacitive transducers and the SensComp electrostatic transducers, ROC curves were computed. Fig. 4.25 shows the ROC curves at 40 mph with the source on for the CAP-2 and SensComp transducers. Similar performance in terms of detecting welds, joints and defects is observed using the two different types of transducers. This suggests that for future tests, the SensComp transducers can be used with a potentially smaller size and lighter weight of the prototype.

4.5.3.6 ROC Curves Using Compounded Data from Multiple Speeds

Two test runs each were performed at speeds of 25 mph, 33 mph and 40 mph with the active controlled source. Therefore, a total of 6 test runs were performed at different speeds. Using

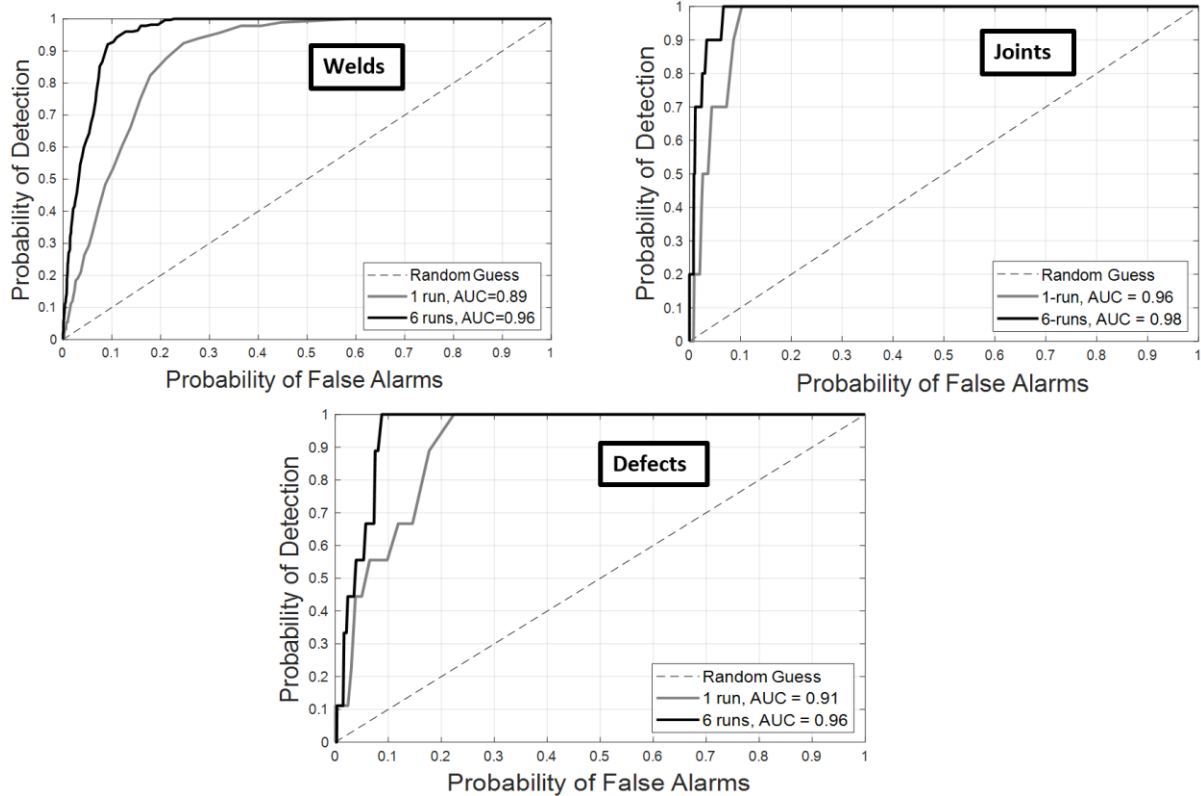


Figure 4.26 ROC curves *compounding data from multiple test runs (6 runs) at different speeds compared to data from 1 test run at 40 mph*

the concept of redundancy introduced in section 3.4.5, data from these 6 test runs are compounded to obtain ROC curves. Fig. 4.26 shows the ROC curve comparison of 1-run at 40 mph and 6 runs at different speeds (2 test runs each at 25 mph, 33 mph, 40 mph) compounded. The performance improves significantly when data from multiple train passes are compounded. For example, in Fig. 4.26, when 6 runs are compounded 100% defects are detected at the expense of 8% false alarms.

4.6. Conclusions

This chapter outlines the improvements made in the passive rail inspection system. Specifically, introduction of a controlled acoustic source, utilization of miniature electrostatic transducers, and improvements in the transfer function reconstruction algorithm are discussed. After testing numerous different alternatives, the CAP2 capacitive transducers were selected as the

controlled source of excitation. The selection criterion was primarily based on the stability of the reconstructed transfer functions and the frequency spectra of the source. The transfer functions are still extracted passively, however, the presence of the controlled acoustic source improves the damage detection performance by increasing the probability of detection (POD) and reducing the probability of false alarms (PFA). The electrostatic transducers were investigated as a possible alternative to the CAP-2 transducers used in previous generations of the prototype. Advantages of using the electrostatic transducers include: 1) smaller size, 2) lower weight, 3) in-built ruggedized design and 4) lower cost. Laboratory tests indicated that the electrostatic transducers were able to pick up the acoustic signals generated using a controlled acoustic source with minimal baseline noise floor. Results from the TTCI field tests at different testing speeds also indicate a similar performance of the electrostatic transducers when compared to the CAP-2. Changes made to the inspection prototype were the addition of the mounting system for the controlled source acoustic transducers, and the addition of the holder assembly in group-2 for the electrostatic transducers. Finally, increasing the segment length in the transfer function reconstruction algorithm resulted in improved discontinuity detection performance. This chapter, therefore, lays the foundations for developing an improved rail inspection system that will have a prototype which is potentially smaller in size, lighter in weight and has improved performance.

4.7. Acknowledgements

This work was funded by the US Federal Railroad Administration under contract 693JJ620C000024 with Dr. Robert Wilson as the Program Manager.

Chapter 4, in part, is currently being prepared for submission for publication of the material as it may appear in the following paper: **Datta, D.**, Hosseinzadeh, A. Z., Lanza di Scalea, F.

Development of an Improved High-Speed Passive Rail Inspection System. The dissertation author was the primary investigator and author of this paper.

4.8. References

- [1] Datta, D., & di Scalea, F. L. (2022). High-speed inspection of rails by passive ultrasonic monitoring. *Journal of Nondestructive Evaluation, Diagnostics and Prognostics of Engineering Systems*, 5(4). <https://doi.org/10.1115/1.4055382>
- [2] Datta, D., Cui, R., di Scalea, F. L., & Wilson, R. (2021). High-speed rail inspection by a non-contact passive ultrasonic technique. Transportation Research Board 100th Annual Meeting.
- [3] Datta, D., Liang, A., Cui, R., & Scalea, F. L. di. (2020). Defect detection performance of a high-speed rail inspection system from passive acoustic identification. *SPIE*, 11379, 196–204. <https://doi.org/10.1117/12.2558205>
- [4] Mariani, S., Nguyen, T., Zhu, X., & Scalea, F. L. di. (2017). Field test performance of noncontact ultrasonic rail inspection system. *Journal of Transportation Engineering, Part A: Systems*, 143(5), 04017007. <https://doi.org/10.1061/JTEPBS.0000026>
- [5] Mariani, S., & di Scalea, F. L. (2017). Predictions of defect detection performance of air-coupled ultrasonic rail inspection system. *Structural Health Monitoring*, 17(3), 684–705. <https://doi.org/10.1177/1475921717715429>
- [6] Brown, M. G., Godin, O. A., Williams, N. J., Zobotin, N. A., Zobotina, L., & Banker, G. J. (2014). Acoustic Green's function extraction from ambient noise in a coastal ocean environment. *Geophysical Research Letters*, 41(15), 5555–5562. <https://doi.org/10.1002/2014GL060926>
- [7] Goncharov, V. V., Chepurin, Y. A., & Godin, O. A. (2013). Passive acoustic tomography of the ocean using arrays of unknown shape. *Acoustical Physics*, 59(2), 170–178. <https://doi.org/10.1134/S1063771013020048>
- [8] Deavenport, R. L. (1966). A normal mode theory of an underwater acoustic duct by means of Green's function. *Radio Science*, 1(6), 709–724. <https://doi.org/10.1002/RDS196616709>
- [9] Santiago, J. A. F., & Wrobel, L. C. (2004). Modified Green's functions for shallow water acoustic wave propagation. *Engineering Analysis with Boundary Elements*, 28(11), 1375–1385. <https://doi.org/10.1016/J.ENGANABOUND.2004.04.004>
- [10] Sabra, K. G., Roux, P., & Kuperman, W. A. (2005). Emergence rate of the time-domain Green's function from the ambient noise cross-correlation function. *The Journal of the Acoustical Society of America*, 118(6), 3524. <https://doi.org/10.1121/1.2109059>

- [11] Welch, P. D. (1967). The use of Fast Fourier Transform for the estimation of power spectra: a method based on time averaging over short, modified periodograms. *IEEE Transactions on Audio and Electroacoustics*, 15(2), 70–73. <https://doi.org/10.1109/TAU.1967.1161901>
- [12] Martínez, D. M., & Andrade, Á. G. (2013). Performance evaluation of Welch's periodogram-based energy detection for spectrum sensing. *IET Communications*, 7(11), 1117–1125. <https://doi.org/10.1049/IET-COM.2012.0640>

Chapter 5. Ultrasonic Sonar-Based Ranging Technique for Railroad Tie Deflection Measurements (Proof of Concept)

5.1. Abstract

This chapter presents an ultrasonic technique for non-contact surface deflection mapping of railroad ties using concepts of sonar-based ranging. The technique utilizes an array of capacitive ultrasonic transducers arranged along the length of the railroad tie at a lift-off distance of 3 inches from the rail surface to ensure contactless measurements. The transducer array is used in pulse-echo mode and distances from the transducers to the tie surface are measured by tracking the time-of-flight of the waves reflected from the tie surface. A reference-based cross-correlation operation is introduced to compute the time-of-flight, wherein one of the transducers is used as a reference for the distance measurements. The reference-based cross-correlation ensures accurate peak-detection for time-of-flight based differential distance measurements and ensures robustness against variabilities of wave speed in air, elevations of different tie surfaces, etc. An acoustic signal strength-based technique is also introduced to differentiate between signals reflected from ties and ballast based on wave scattering phenomenon. Lab scale tests were performed as a proof-of-concept on a slender wooden beam to measure deflections in loaded and unloaded conditions.

5.2. Introduction

Concrete or wooden tie beams are used in railroad tracks for transferring loads from the rails to the ballast and subgrade. They also hold the rails upright and help maintain the correct

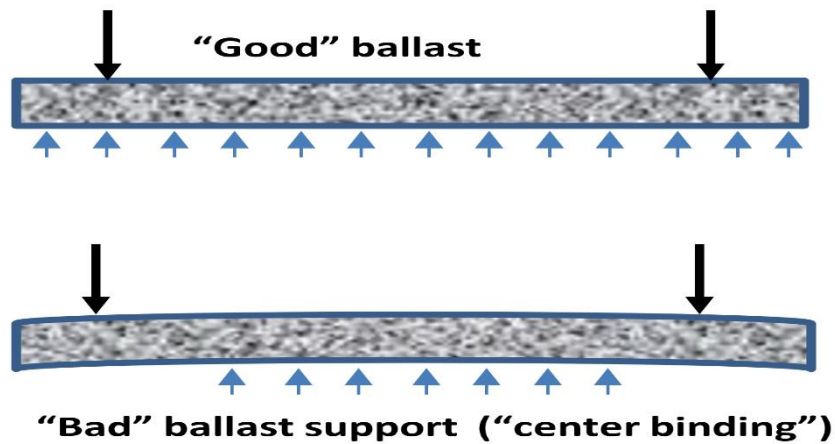


Figure 5.1 Different deflected shape profiles for good and bad ballast support conditions

gauge distance between the two rails. Concrete ties are often preferred over wooden ties for improved durability and longer service lives especially for heavy haul routes. Failure modes for railroad concrete ties [1-10] include central negative flexural cracking and abrasion along the tie-ballast interface. Reinforced concrete railroad ties are predominantly designed for positive bending with tension on the bottom surface where steel reinforcement bars are located (for singly reinforced beams). Since concrete is weak in tension, negative flexural bending (tension on top surface) can lead to flexural cracks on the top surface which is undesirable. In another failure mode, the interface between the bottom surface of the tie and the ballast can deteriorate and result in tie bottom abrasion, ballast pulverization or voids in tie-ballast interfaces. This can result in premature failure of the tie beams and potentially cause train derailments. Voids in the tie-ballast interface near the ends of the tie can lead to center-binding support conditions [11] as shown in Fig. 5.1. A study conducted at the Volpe Center in Boston, USA indicates that deteriorated support conditions such as center-binding or negative flexural bending can be detected through measurements of vertical deflection profiles of the ties [12].

Researchers have tried to come up with techniques for measuring tie deflections which can be used as a metric to flag defective ties. A possible technique for measuring tie deflections uses a linear variable differential transformer (LVDT) [13]. LVDTs, however, require a fixed reference point with respect to which the displacement can be measured. It is difficult to find a fixed reference point near a track because when a train passes, the ballast and ground nearby undergo a variable displacement [14]. Even if fixed reference points are found (for example, a bridge abutment), they are generally far away such that mounting the transducers rigidly on a mounting beam becomes impractical. Another technique for measuring tie deflections is based on a laser beam fired on a photosensitive receptor placed on the tie surface [14-15]. This system requires precise calibration and suffers from a lack of robustness in the presence of environmental elements such as fog or mist. Priest et al. [16] used geophones mounted on the ends of a railroad tie to measure vertical velocities when a train passed over the tie. A single step integration was performed on the velocity data to obtain the tie displacements. The use of accelerometers mounted on the tie with double integration signal processing techniques to compute tie deflections has been employed by many researchers [14, 17]. The challenge of double integrating acceleration responses lies in accurately modelling the boundary conditions to evaluate the integration constants. Moreover, accelerometer-based deflection measurement techniques are mostly sensitive to high frequency deflections and fail to pick up the low frequency deflections. Joh et al. [18] proposed a technique for combining acceleration and strain transducer data for computing tie deflections. The use of strain transducers enabled the measurement of low frequency deflections. Several researchers [19-20] have used digital image correlation (DIC) based techniques for evaluating tie deflections and ballast support conditions. Image-based techniques allow reconstruction of a full-field deflection profile of the ties in a non-contact manner. However, these

techniques are sensitive to lighting conditions and the presence of fog, mist, dust, rain, etc might adversely affect the results. Low-light conditions might require higher exposure times for the camera, thereby reducing frame rates and speed of testing. Moreover, distortions and aberrations produced by camera lenses near the edges of the frame might also affect the results.

Although research has been conducted for evaluating railroad tie deflections, most of the techniques are contact-based and do not provide a full-field (3D) deflection profile of the ties (except DIC-based techniques). In this study, an ultrasonic ranging non-contact technique is introduced which is capable of evaluating full-field (3D) tie deflection profiles and has the potential of operating at revenue speeds. The proposed technique utilizes an array of ultrasonic transducers located parallel to the tie in a “sonar” type mode to track the spatial position of selected points at the top surface of a tie to calculate the tie’s deflection. The transducers are mounted at a distance of at least 3 inches from the rail to ensure non-contact inspection. A reference-based cross-correlation operation is used to compute time-of-flight [21] where one of the transducers was used as a reference point. Deflections at all locations along the length of the tie are computed with respect to the reference location. An adaptive reference-based deflection computation eliminates the variabilities of wave speed in the air and the differences in distances between the transducer array and tie surface for different ties. Tests were carried out in the laboratory as a proof-of-concept on a slender wooden beam with a 3-point bending test. The deflection profile of a loaded beam was accurately determined using the proposed technique. A dynamic test was also conducted where the wooden beam was allowed to vibrate freely, and its dynamic displacements were computed [22].

5.3. Theoretical Considerations

5.3.1. Sonar Based Ranging Technique

This study proposes to utilize non-contact acoustic techniques in a “sonar” type mode to track the spatial position of selected points at the top surface of a tie to calculate the tie’s deflection at revenue speeds. The proposed technology would utilize known concepts of radar and acoustic ranging, including time-of-flight tracking, signal detection and adapt them to the specific application of tie deflection measurements. An array of non-contact acoustic transducers would be mounted on a beam (schematic shown in Fig. 5.2 that is rigidly connected to the frame of a train car. The transducers would continuously excite an acoustic signal (broadband, tone-burst or chirp). The acoustic signal would be reflected from the top surface of the tie, generating a reflection that would be measured by the same transducers (pulse-echo operation). The time-of-flights (as shown in Fig. 5.2) at all transducer locations would be similar if the tie is perfectly straight, and ballast support is good. The time-of-flights would be different if the tie has a deflected shape as shown in Fig. 5.2 Therefore, by tracking the time-of-flights, the deflected shape can be obtained.

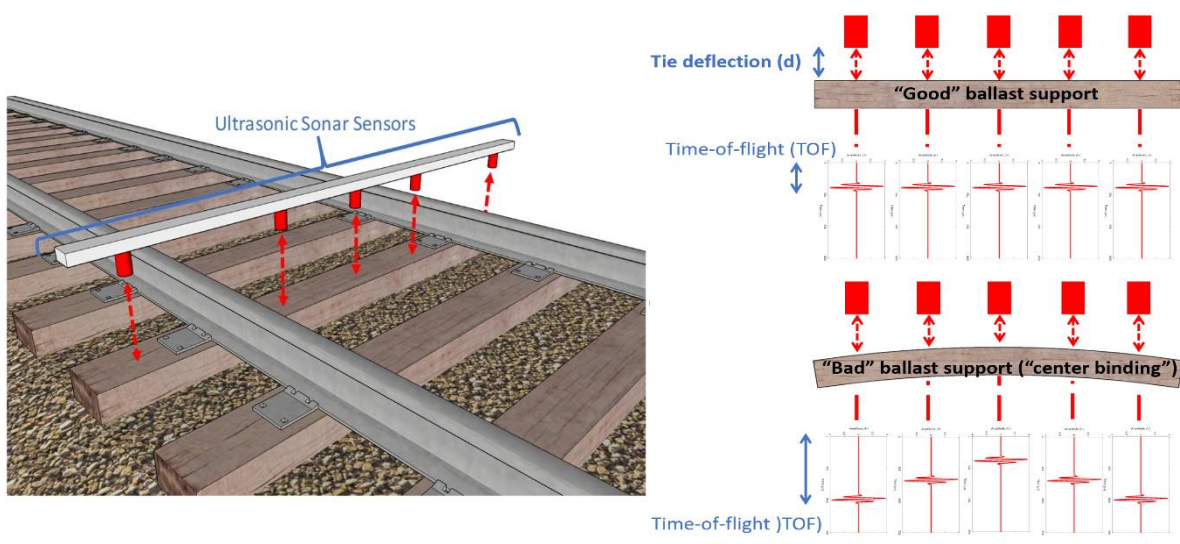


Figure 5.2 Concept of “tie sonar” for tracking the vertical deflection of a tie.

5.3.2. Reference-Based Deflection Computation

Consider an array of six non-contact acoustic transducers mounted on a beam parallel to the tie that is rigidly connected to a test vehicle (schematic shown in Fig. 5.2). The transducers are continuously excited by a pulser unit that is triggered through an encoder. The transmitted acoustic signal, upon incidence on the air-tie interface, is reflected from the top surface of the tie and received by the same transducer (pulse-echo mode). The corresponding waveforms received at each transducer are also shown. Since the speed of sound in air is known ($v = 343$ m/sec), the distance of the tie surface from the transducer face, d , can be easily calculated as:

$$d = \frac{t \times v}{2} \quad (5.1)$$

where t is the arrival time (time-of-flight) of the reflected wave from the tie surface. The factor of 2 takes into account the distance travelled by the wave from the transducer to the tie surface and back to the transducer assuming the speed of sound is the same in both directions of travel. For the assumed deflected shape (positive bending) of the tie as shown in Fig. 5.3, the distance between transducer 1 (channel 1 or *Ch1*) to the tie surface is smaller than the distance between transducer 3 (*Ch3*) to the tie surface. Therefore, the corresponding wave packet in *Ch3* arrives later than *Ch1*. The lift-off distance (distance from transducer head to the tie surface) from the tie surface at each channel can be computed by tracking the time-of-flight and using Eq. 5.1.

However, this measurement does not directly give the displacement at that transducer location. This computed lift-off distance would vary based on the difference in tie surface elevations of successive ties. A tie sitting lower on the ballast than the adjacent tie would result in a higher computed lift-off distance since the transducers are held at the same elevation. To

overcome these variabilities, one of the transducer channels is assigned as a reference (*Ch3*). The difference in time-of-flights with respect to this reference transducer is computed for all other transducer locations (1,2,4,5,6) and the distance corresponding to this difference in time-of-flight gives the actual deflection at that location with respect to the reference surface. One way to compute this reference-based deflection would be to compute the lift-off distances at each channel location through peak-detection techniques based on signal gating and thresholding and subtracting the reference transducer lift-off distance from the other transducer lift-off distances. The problem with this technique is that it relies on peak detection with thresholding and the received pulse has multiple peaks where the amplitudes depend on the tie surface (rough surfaces result in lower amplitude signals) and the lift-off distance (higher lift-off distances result in lower amplitudes due to attenuation). Wave dispersion also affects the peak detection since air is a dispersive medium and the signal pulse tends to spread out in time as it travels through space [23].

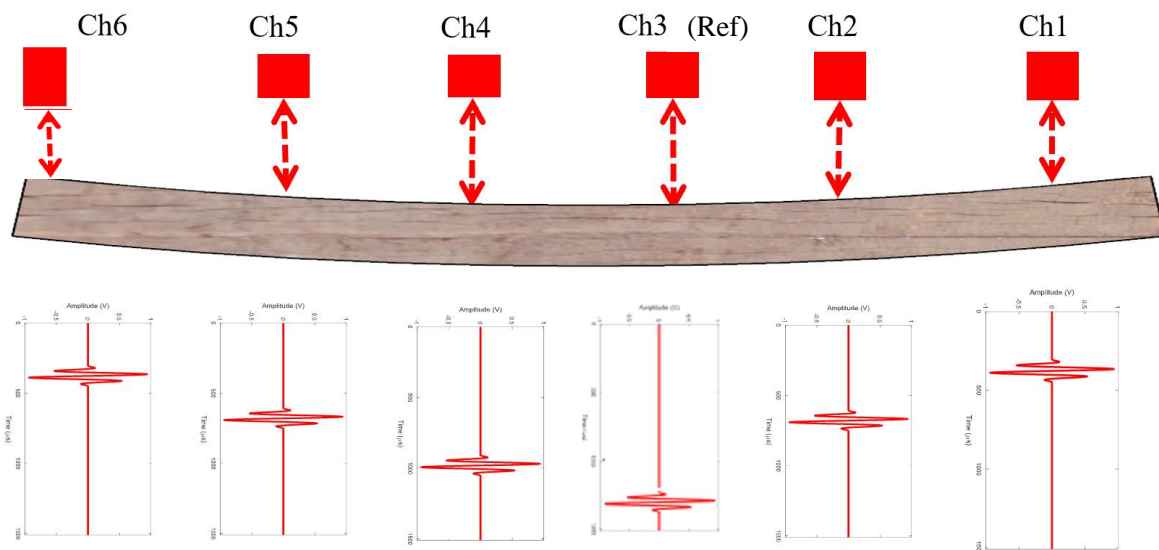


Figure 5.3 Schematic diagram of transducer array and corresponding waveforms for a tie with positive bending

To overcome these challenges, a cross-correlation based difference in time-of-flight computation technique [24-25] is used as discussed in the next section.

5.3.3. Cross-correlation Operator for Time-of-flight Computation

Consider two signals as shown in Fig. 5.4 obtained from transducer 1 (*Ch1*) and reference transducer 3 (*Ch3*) at a given location from a tie surface. The aim is to find the difference in time-of-flight (Δt) as indicated in Fig. 5.4. Δt is proportional to the deflection at *Ch1* with respect to *Ch3*. To compute Δt , a cross-correlation operation is used. Consider $x_1(t)$ be the time-series signal at transducer 1 and $x_3(t)$ be the time-series signal at transducer 3 (reference). The cross-correlation operator $R_{31}(\tau)$ is defined as:

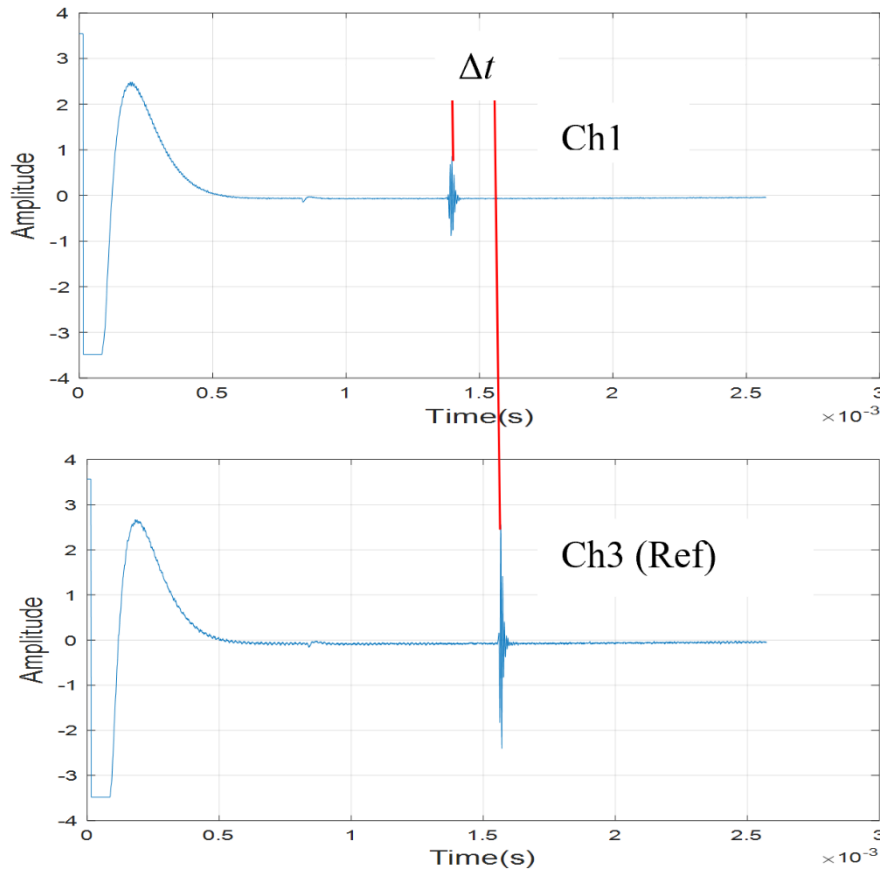


Figure 5.4 Difference in time-of-flight of two signals

$$R_{31}(\tau) = \sum_{t=-\infty}^{t=+\infty} x_3(t) x_1(t - \tau) \quad (5.2)$$

Since both $x_1(t)$ and $x_3(t)$ are finite time signals of say length (T), the expression in Eq. 5.2 can be written as:

$$R_{31}(\tau) = \sum_{t=0}^{t=T} x_3(t) x_1(t - \tau) \quad (5.3)$$

The difference in time-of-flight Δt can then be calculated as:

$$\Delta t = \operatorname{argmax} \{R_{31}(\tau)\} \quad (5.4)$$

Deflection at each transducer location is then computed as:

$$\Delta d = \frac{\Delta t \times v}{2} \quad (5.5)$$

where v is the speed of sound in air. Fig. 5.5 shows the cross-correlation series for $R_{31}(\tau)$ computed for the signals in Fig. 5.4. The cross-correlation is performed by gating both the signals between 1.25 ms and 2.25 ms which is a window within which the reflected signal is expected for a lift-off distance (distance from transducer to tie surface) of approximately 11 inches.. The gated signal is passed through a Butterworth high pass filter with a cut-off frequency of 10 kHz to eliminate low frequency noise caused by vibrations. From Fig. 5.5, it can be seen that Δt is positive. This indicates that the surface elevation of the tie at transducer location 1 (Ch1) is higher than the elevation at transducer location 3 (Ch3) which is confirmed by the deflected shape in Fig. 5.3.

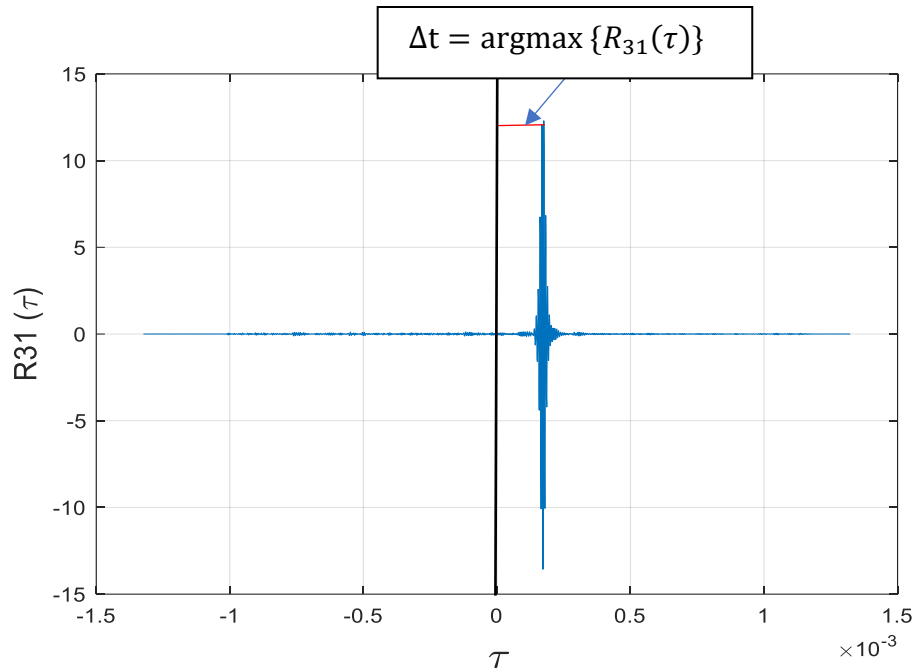


Figure 5.5 Cross-correlation operation to compute time-of-flight

5.3.4. Tie Boundary Demarcation

Since the transducers are continuously transmitting the acoustic signals while the test vehicle is traveling over the track, there is a need to differentiate a tie reflection from a ballast reflection. The differences in the morphology and in the elastic properties between tie and ballast results in a markedly different acoustic impedance mismatch that, in turn, generates specific shapes and amplitudes of the reflected signal. For example, as shown in Fig. 5.6, the signal reflected from the ballast is of significantly smaller amplitude than that reflected from the tie because of the additional scattering surfaces present in ballast. The exact differences depend on the frequency of the acoustic signal used, but, nonetheless, this drop in amplitude can be used for demarcating signals coming from ties. A peak-to-peak signal threshold level of 0.75 V was chosen to demarcate the ties. If at least four transducers had a peak-to-peak signal strength above the selected threshold (0.75 V), the signals were assigned to a tie. If this criterion was not met, the signals were assigned

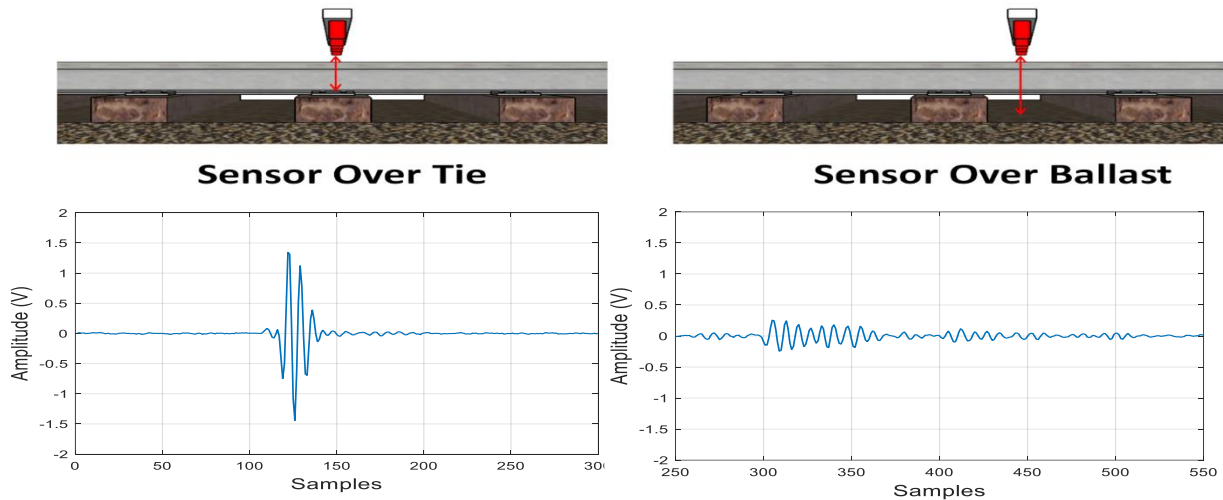


Figure 5.6 Acoustic signal strength-based tie-ballast differentiation

to ballast. Signals coming from ballast were discarded and only signals coming from ties were used for deflection computations using cross-correlations.

5.4. Selection of Optimum Transducers

One of the key aspects of designing a prototype for tie deflection measurements is selecting a suitable transducer capable of generating and receiving signals. Ideally, the transducer should be robust and fairly insensitive to external vibrations caused by the motion of the train. The transducer also needs to be sensitive enough to pick up the received signal from the tie surface such that the received signal is fairly above the electronic noise floor and can be used for time-of-flight measurements. Since the motion of the train is expected to cause some degree of misalignment and oblique angles of incidence of the generated signal on the tie surface, the transducer needs to be sensitive to received signals for allowable tilt angles caused by body roll of the moving train.

An array of air-coupled ultrasonic transducers (piezoelectric and capacitive) were tested at the Experimental Mechanics and NDE Laboratory at UCSD to select the optimum transducer to be used in the tie-sonar application. 5 piezoelectric transducers and 4 capacitive transducers were



Figure 5.7 Array of piezoelectric and capacitive transducers tested at UCSD

tested in pulse-echo mode (Fig. 5.7) for reflected signal strengths from a wood tie surface. The relative performances of these transducers are shown in Tables 5.1 – 5.2. The transducers were tested at a lift-off distance (distance between the surface of the tie to the transducer head) of 11 inches with a 59 dB gain on the receiving channel with pre-amplifiers. Parameters such as the strength of the reflected signal, effects of oblique incidence, sensitivity to external vibrations, and typical waveforms obtained are shown in Tables 5.1 – 5.2. The angles for the directivity measurements denote the oblique incident angles for which the amplitude of the received signal drops by half. Therefore, a larger angle for directivity implies greater tolerance of the transducer to misalignments. Robustness to external vibrations were tested by tapping on the sensor and the mounting system to check if these vibrations were picked up on the received signal.

Table 5.1. shows the performances of the piezoelectric transducers. The Sonoscan CF 075 manufactured by Sonoscan Inc., the Ultrason NCG 500 S-19 and the Ultrason NCG 200 S-25

manufactured by the Ultrason Group Inc. are the best performers in this group based on the strength of the reflected wave and sensitivity to vibrations. A comparison of performances of the piezoelectric transducers from Table 5.1. shows that these transducers are quite sensitive to external vibrations as compared to the capacitive transducers (Table 5.2). The strength of the received signals is also relatively low in comparison to the capacitive transducers. The piezoelectric transducers, however, have more tolerance to misalignments since the diameter of the sensor head is smaller (compared to the capacitive CAP transducers). Table 5.2. shows the performances of the capacitive transducers. The CAP-2 and CAP-3 transducers manufactured by VN Instruments Inc. are the best performers in this group based on the strength of the reflected wave and sensitivity to vibrations. The CAP-1 transducer, with a central frequency of 65 kHz is the most sensitive to external vibrations while the CAP-3 transducer centered at 300 kHz is the least sensitive to external vibrations. CAP-2 and CAP-3 have similar performance metrics with the CAP-3 being slightly less sensitive to external vibrations. The capacitive transducers, however, are more sensitive to misalignments than the piezoelectric transducers. Based on the results shown in Tables 5.1-5.2, the CAP-2 and CAP-3 sensors are the most ideal transducers which can be used for tie deflection measurements using ‘sonar’. CAP-2 transducers were chosen for the proof-of-concept tests and field tests.

Table 5.1 Performance Evaluation metrics of Piezoelectric Air-coupled Transducers in Pulse-echo Mode on Wood Tie


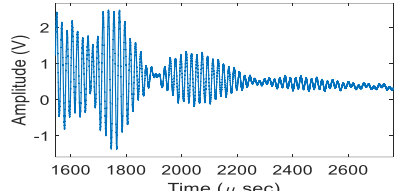

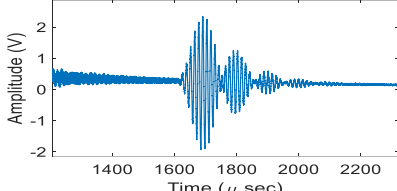
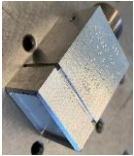
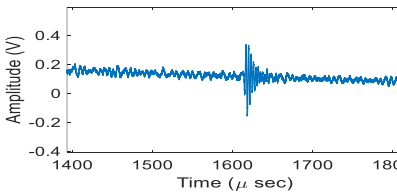

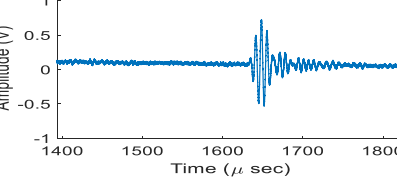

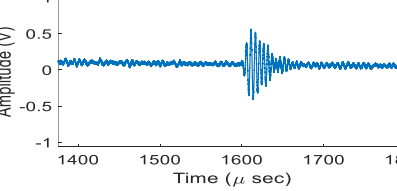

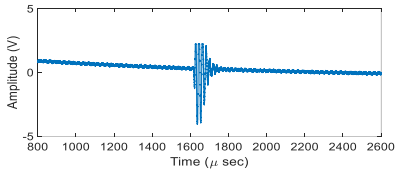

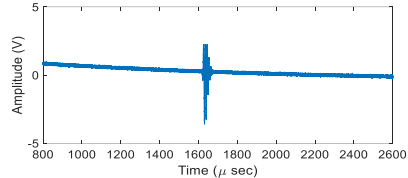

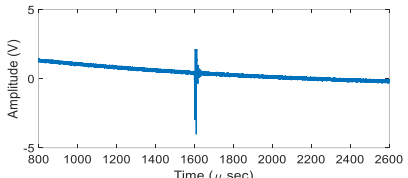

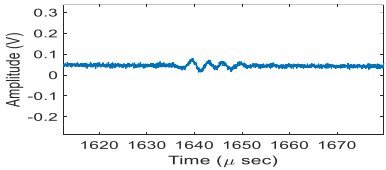
Transducer type	Reflection strength (peak-to-peak) (59dB gain) at 11 inch lift-off	Directivity (-6 dB drop)	Vibration sensitivity	Pulse-echo typical waveform from wood tie at 11 inch lift-off
 <p>Sonotec Inc. Sonoscan CF 050 (Fs= 50 kHz) (-6 dB Bandwidth = 4 kHz)</p>	3.8 V	+4°	Quite sensitive	
 <p>Sonotec Inc. Sonoscan CF 075 (Fs= 75 kHz) (-6 dB Bandwidth = 6 kHz)</p>	4.2 V	+15°	Moderately sensitive	
 <p>The Ultran Group NCG 500 S-19 (Fs= 500 kHz) (-6 dB Bandwidth = 200 kHz)</p>	550 mV	+15°	Not very sensitive	
 <p>The Ultran Group NCG 200 S-25 C-76 (Fs= 200 kHz) (-6 dB Bandwidth = 80 kHz)</p>	1.18 V	+17°	Moderately Sensitive	
 <p>The Ultran Group NCG 200 S-19 C-25 (Fs= 200 kHz) (-6 dB Bandwidth = 80 kHz)</p>	1 V	+25°	Quite sensitive	

Table 5.2 Performance Evaluation metrics of Capacitive Air-coupled Transducers in Pulse-echo Mode on Wood Tie

Transducer type	Reflection strength (peak-to-peak) (59dB gain) at 11 inch lift-off	Directivity (-6 dB drop)	Vibration sensitivity	Pulse-echo typical waveform from wood tie at 11 inch lift-off
 <p>VN Instruments Ltd. CAP-1 (Fs=65 kHz) (-6 dB Bandwidth= 55.3 kHz)</p>	6 V	+12°	Moderately sensitive	
 <p>VN Instruments Ltd. CAP-2 (Fs=135 kHz) (-6 dB Bandwidth= 112.7 kHz)</p>	6 V	+6°	Slightly sensitive	
 <p>VN Instruments Ltd. CAP-3 (Fs=300 kHz) (-6 dB Bandwidth= 344.5 kHz)</p>	6 V	+6°	Not very sensitive	
 <p>MicroAcoustic Instruments Inc. BAT-1 (Fs=1 MHz) (-6dB Bandwidth= 2.2 MHz)</p>	72 mV	+15°	Slightly sensitive	

5.5. Data Acquisition System and Signal Processing Routines on LabVIEW Real-Time

5.5.1. Data Acquisition System

A schematic diagram of the data acquisition system using capacitive air-coupled ultrasonic transducers is shown in Fig. 5.8. The setup consists of a pulser/amplifier unit which sends out excitation pulses (~ 100 V) to the transducers which triggers it to transmit the outgoing pulse to

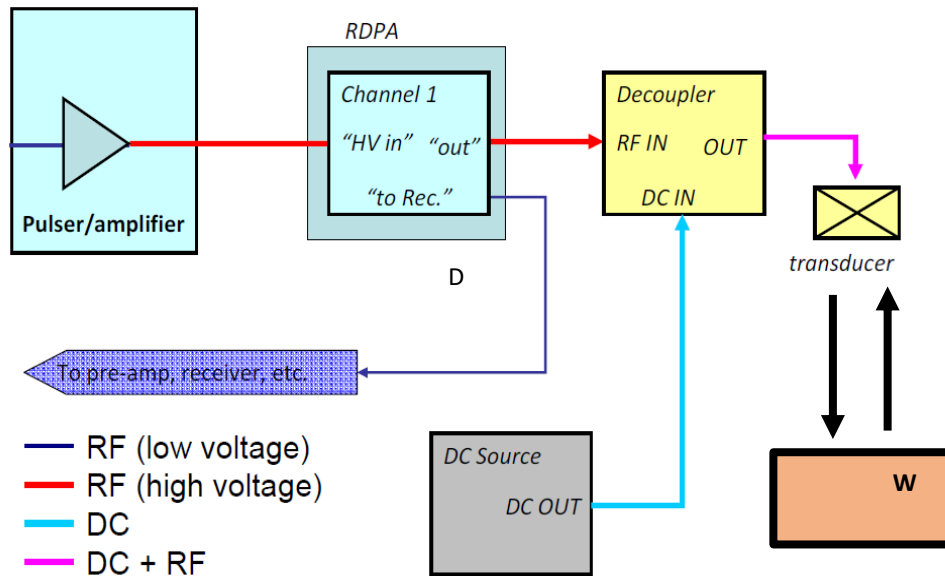


Figure 5.8 Schematic diagram of the setup for data acquisition (1-channel configuration)

the tie surface. The excitation pulses also trigger the data acquisition system programmed in LabVIEW Real-time. The high energy excitation pulse and the low energy received signal are on the same channel and the diplexer splits these two signals and prevents the high energy excitation signal from leaking into the receiving channel. The micromachined capacitive transducers require a DC bias of 200 V during operation. The AC/DC decoupler combines the excitation signal and the DC bias on the outgoing channel to the transducers and also prevents the DC bias from leaking into the receiving channel to the diplexer. The received signal from the diplexers is fed through pre-amplifiers which amplify the signals before going to the National Instruments PXI 5105 data acquisition card. The data acquisition system is programmed in LabVIEW Real-time running on a National Instruments PXIe-8135 processor. The real-time processor processes the received signals in parallel with the acquisition. The experimental setup using one transducer in pulse-echo mode is shown in Fig. 5.9. The front panel of the LabVIEW program is shown in Fig. 5.10. Controls for changing parameters such as the sampling rate, length of recorded data (samples) are embedded



Figure 5.9 Tie-sonar experimental setup using one transducer in pulse-echo mode on wood tie

on the front panel in LabVIEW. Graphs on the front panel plot the received reflected signals from the tie surface in real-time. Time-of-flight computations are performed in parallel with data acquisition and the instantaneous lift-off distance is also plotted on the front panel. Fig. 5.10 shows how the front panel of the LabVIEW VI looks during live data acquisition. The blue plot in Fig. 5.10 is the excitation pulse (5 V) which triggers the data acquisition system to start recording. The red plot is the received signal reflected from the tie surface.

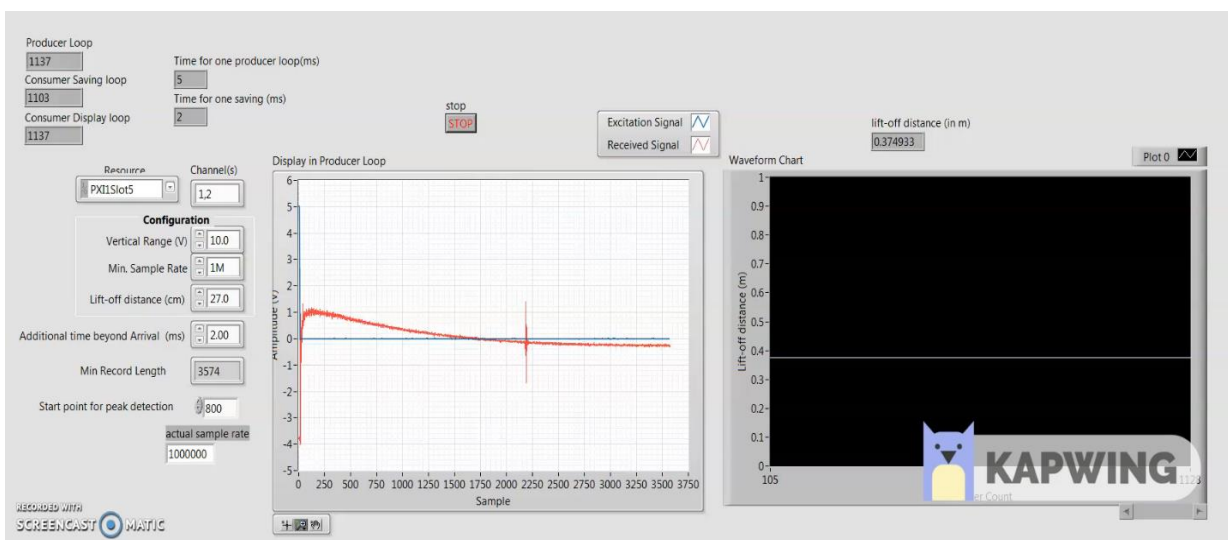


Figure 5.10 Front panel of the data acquisition program interface on LabVIEW Real-time.

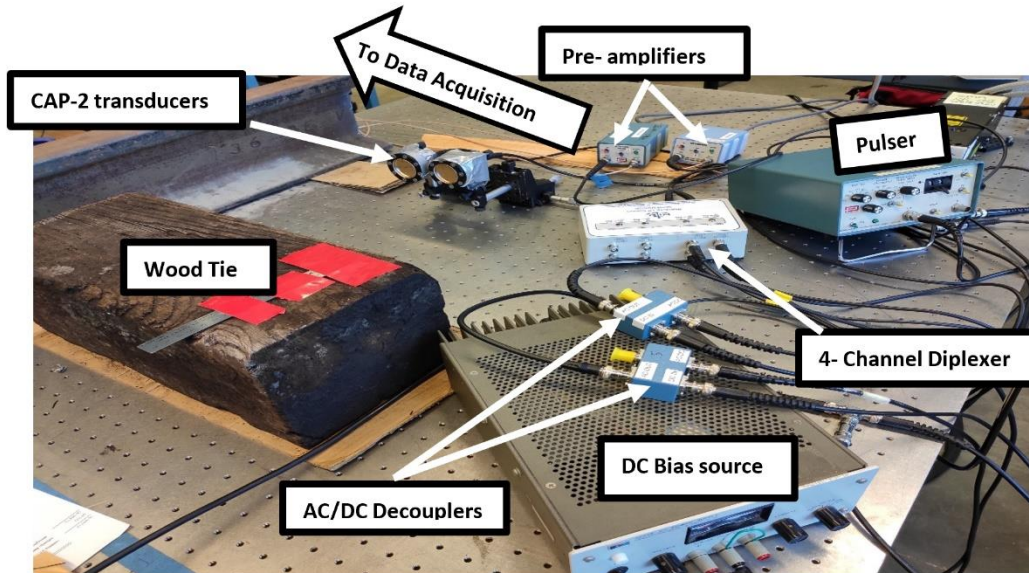


Figure 5.11 Data acquisition setup for two channel acquisition

5.5.2. Implementing Multiple Channels

To obtain the deflected profile of the rail ties, an array of 6 transducers placed along the length of the tie is proposed to be used. The LabVIEW program developed for data acquisition is capable of handling 6 channels in parallel acquisition mode. A single pulsing unit (Panametrics 5077 PR) can be used along with BNC splitters to drive all the transducers. Additional diplexers and AC/DC decouplers would need to be introduced for each separate channel. A setup for two channel acquisition is shown in Fig. 5.11. Since it is planned to drive all the transducers with the same pulsing unit, it is possible that the current to each transducer is reduced when multiple transducers are connected in parallel. To test the amount of drop in current to each transducer, 6 CAP-2 transducers were driven in parallel using the same pulsing unit and the strength of the signal transmitted from a single transducer was checked. As expected, a drop in the strength (~ 0.6 V) of the transmitted signal was observed when 6 channels were connected in parallel compared to the

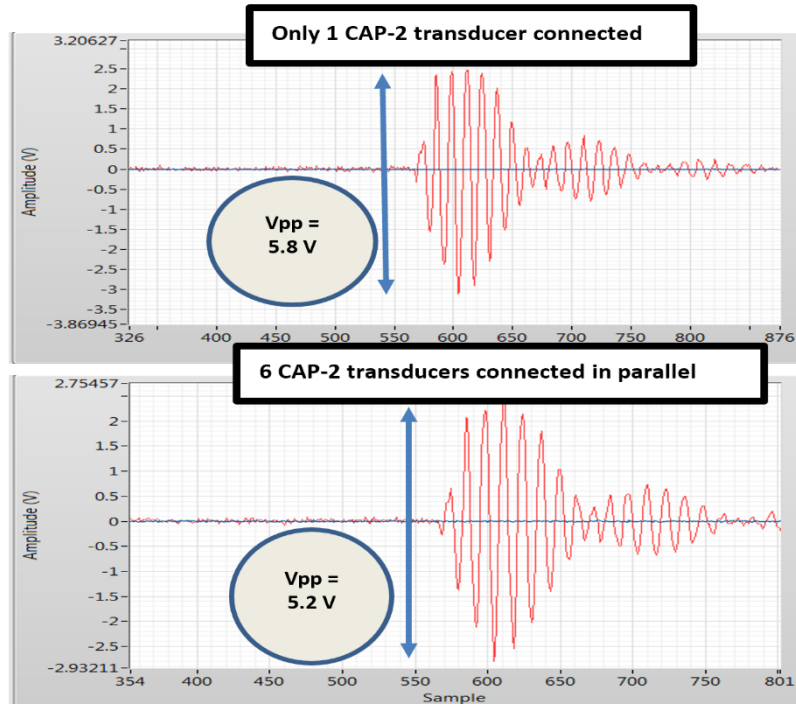


Figure 5.12 Drop in signal strength when transducers connected in parallel

strength of the transmitted signal when only one channel was connected as shown in Fig. 5.12. This drop in the signal strength of about 10% is within tolerable limits.

5.5.3. LabVIEW Real-Time Signal Processing Routines

The primary signal processing that is applied to the received signals is peak detection to compute the time-of-flight which is then used to determine the lift-off distance for an assumed speed of travel through air (343 m/s). This peak detection algorithm is implemented in LabVIEW Real-time. The program looks for peaks above a minimum set threshold value. This threshold value is set based on the expected strength of the received signal and the average noise floor of the system. An optimum value of the threshold is chosen such that it is sufficiently above the average noise floor and also below the expected strength of the reflected signal. A peak is said to occur in a sequence of numbers S when:

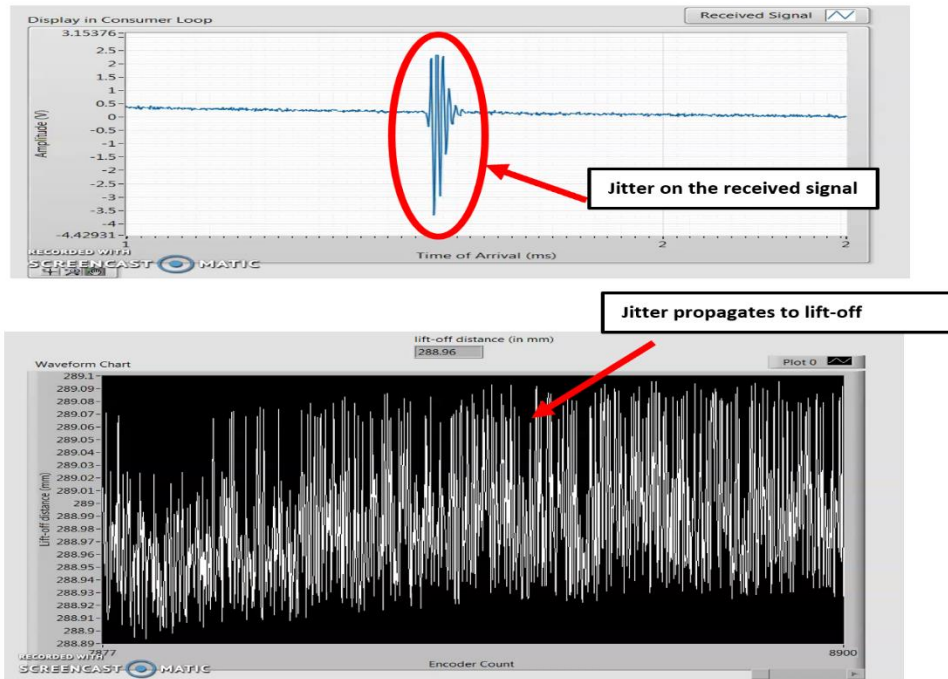


Figure 5.13 Estimating distance measurement resolution

- The elements of S begin below threshold, exceed threshold at some index, and then return to a value below threshold.
- The number of successive elements that exceed threshold is greater than or equal to a minimum width.

The peak detection algorithm implemented in LabVIEW uses a quadratic fit algorithm and returns the peak locations as floating-point numbers and not as integer index values. Therefore, the peak locations and amplitudes usually do not correspond to actual data points in the sampled input signal. This ensures that peaks locations are determined fairly accurately even if the data is not sampled adequately. Another feature of the peak detection algorithm used is that it finds peaks only in a specific window of the data. The width and location of the window is determined based on the expected time of arrival of the reflected wave for a given lift-off distance. Such a window

ensures that spurious peaks outside this expected window of arrival get eliminated. Controls for changing the location of this window is included in the LabVIEW program. The location of the window would need to be adjusted when the expected lift-off distance between the sensor and the tie surface is changed.

5.5.4. Lift-off Distance Resolution Estimation

To obtain an accurate estimate of the deflected profile of the rail ties, it is essential to get an accurate estimate of the lift-off distance in the presence of electronic jitter in the received signal. To test the precision of the estimated lift-off distance, a single transducer (CAP-2) is used in pulse-echo mode and the setup is kept stationary. Lift-off distances computed from the time-of-flight of the signal are plotted in real-time as shown in Fig. 5.13. Since the setup is kept stationary, ideally the estimated lift-off distance shouldn't change. However, a noise-like variation (jitter) is seen on the computed lift-off distance. Jitter in the received pulse causes slight shifts of the received signal along the time axis. These shifts result in slightly different time-of-flight estimates which eventually results in slightly different lift-off distances and hence the noise-like behavior. The variations in the lift-off distance due to jitter, under laboratory conditions, was found to be of the order of 0.2 mm. Since this is less than the planned minimum resolution of the system (1 mm), jitter is not expected to cause any issues.

5.6. 3-point Bending Test (Proof-of-Concept)

Various kinds of ultrasonic non-contact transducers were tested at the Experimental Mechanics & NDE Laboratory at UC San Diego to select an optimum transducer for tie deflection measurements. A wooden tie specimen was used as the target surface and a lift-off distance of 11 inches was used to evaluate the performance of the transducers in terms of parameters such as

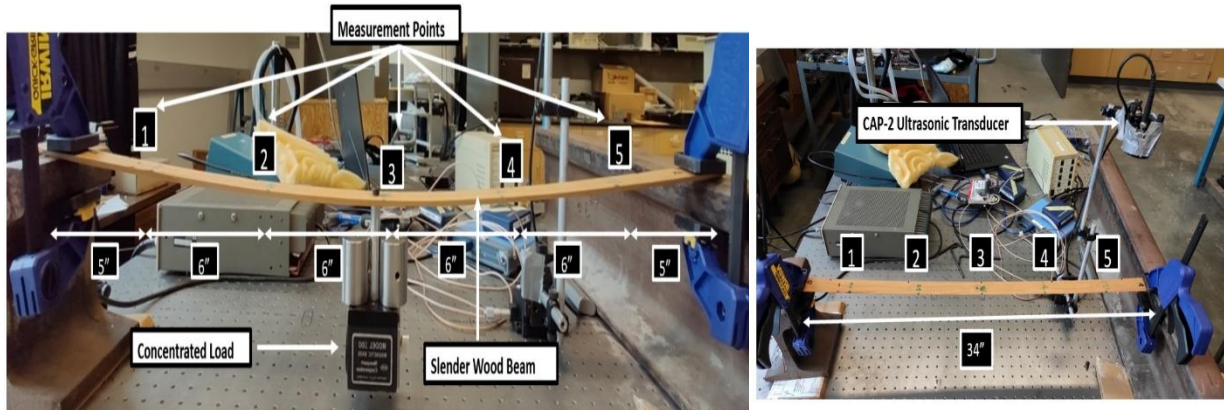


Figure 5.14 Slender wooden beam 3-point bending test setup

reflected acoustic signal strength, sensitivity to external vibrations, and drop in signal strength for oblique angles of incidence. Based on the tests, the CAP-2 capacitive micro-machined transducer by VN Instruments Inc, with a central frequency of 135 kHz, was found to be the most suitable for the given application. To demonstrate the concept of using ultrasonic transducers for tie deflection measurements, a set of tests were conducted on a slender plywood beam shown in Fig. 5.14. The 34-inch-long beam was fixed on both ends with the help of clamps and a concentrated load was fixed near the center. Deflection of the beam in the loaded condition was evaluated with respect to the unloaded condition. Dynamic deflections were also computed in continuous acquisition mode by providing an initial displacement to the beam at the center and allowing free vibration.

5.6.1. Static Test

Five equally spaced control points were setup on the plywood beam for measuring deflections. A single transducer was used in pulse-echo mode and two waveforms were recorded at each control point. The first waveform was recorded for the unloaded condition whereas the second waveform was recorded for the loaded condition with a concentrated load acting at the center of the beam (control point 3). A cross-correlation of the waveforms between the loaded and

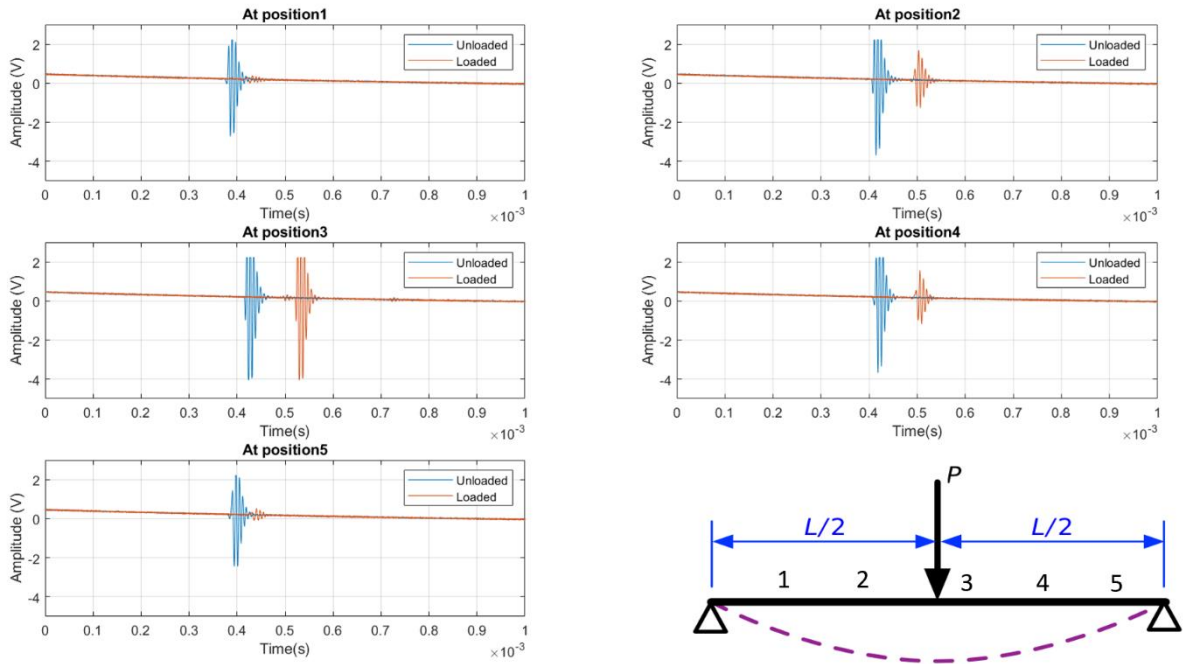


Figure 5.15 Waveforms obtained at the five control points for the loaded and unloaded conditions

unloaded waveforms at each control point was computed using Eq. 5.3 and the deflection at each point was computed using Eq. 5.5. Therefore, five discrete deflection measurements were obtained along the length of the beam. Fig. 5.15 shows the waveforms obtained at the five control points for the loaded and unloaded conditions. Note that at positions 1 and 5, which are location near the ends of the beam, the reflected signal amplitude for the loaded condition is smaller than the corresponding signals from the unloaded condition. This is because the incident angle of the outgoing excitation pulse near the ends of the beam is not perpendicular to the beam surface due to the curvature of the beam in the loaded condition. Fig. 5.16 shows the cross-correlation functions at the five control points. Fig. 5.17 shows the reconstructed deflected profile of the beam where the unloaded beam profile is assumed to be straight. Deflection measurements were also taken with a measuring tape (visual technique) at each control point and the sonar-based deflections were found to be in agreement with the visual measurements. Table 5.3 shows a

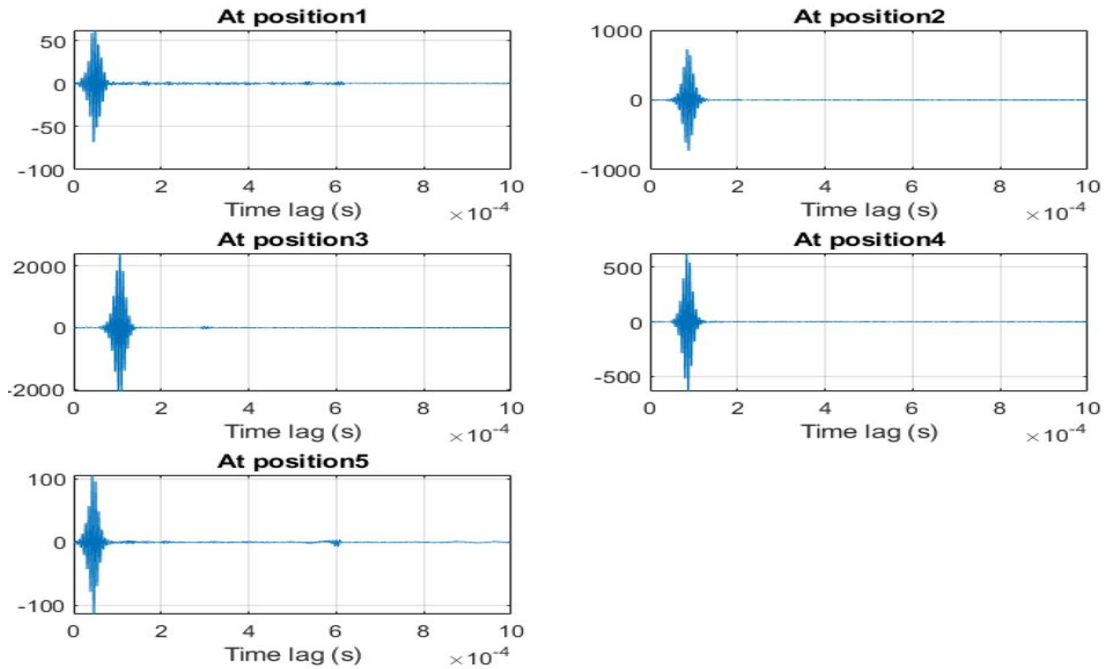


Figure 5.16 Cross-correlation between the loaded and unloaded waveforms at the five control points

comparison of the deflection measurements at the five control points for ultrasonic and visual techniques. It is worth noting that the visual-based deflections are only approximate, and the comparison is done only to show that the deflections obtained through the proposed technique are within the expected range.

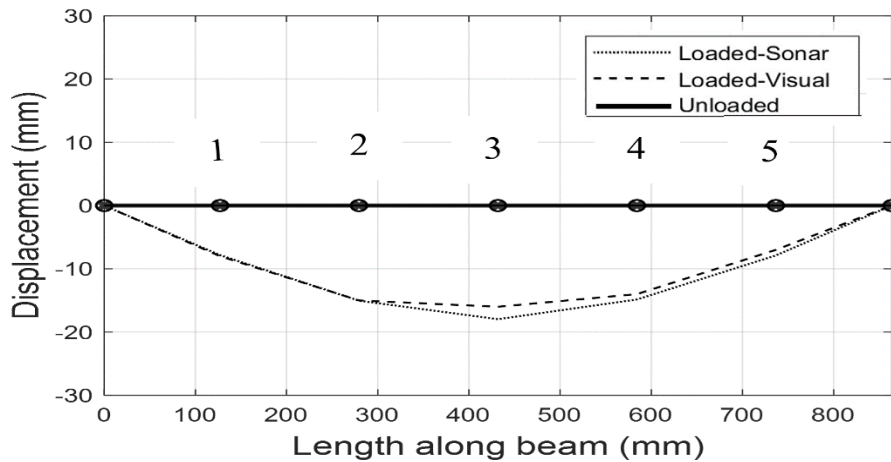


Figure 5.17 Beam deflections using ultrasonic and visual measurements

Table 5.3 Comparison of Beam deflections using ultrasonic and visual measurements at different control points

Location	1	2	3	4	5
Visual deflection (mm)	8	15	17	14	7
Ultrasonic deflection (mm)	8.42	14.42	17.97	14.22	7.23

5.6.2. Dynamic Test

Another test was done with the same setup as in Fig. 5.14, where, instead of a concentrated load, a fixed displacement of 10 mm in the downward direction was applied at the midpoint of the beam. Waveforms from the deflected beam were recorded continuously at a sampling rate of 200 Hz to build a dynamic displacement signature of the beam at different locations. Fig. 5.18 shows the dynamic displacements obtained at the five control points as a function of time. The

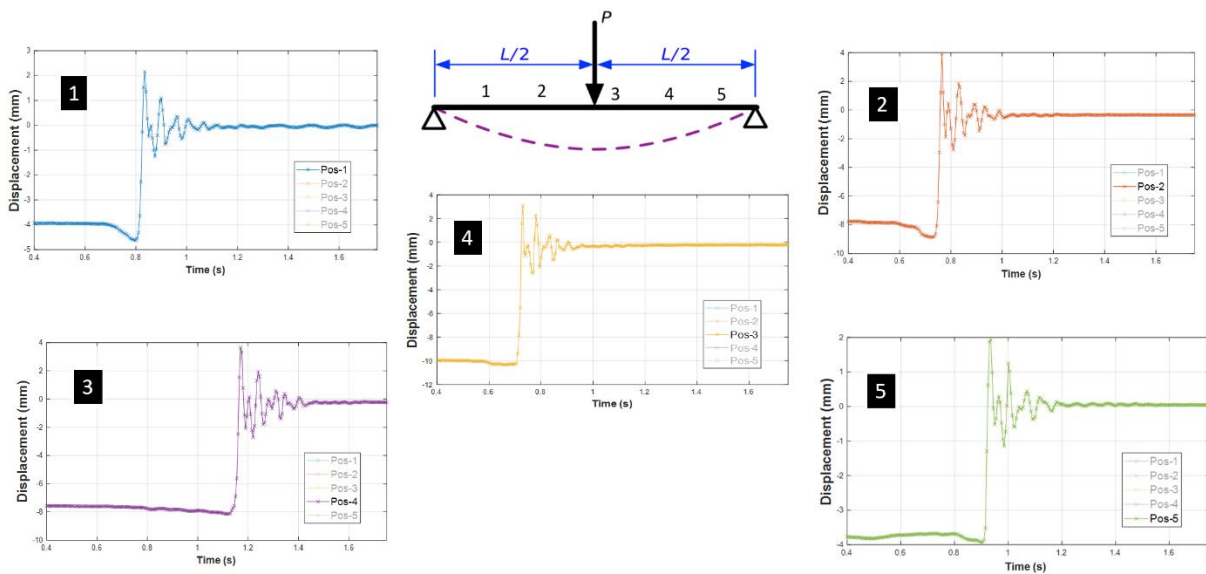


Figure 5.18 dynamic displacements obtained at the five control points as a function of time

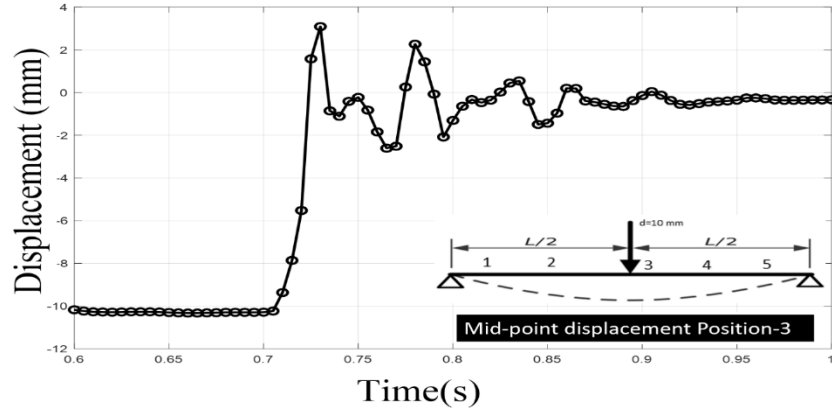


Figure 5.19 Dynamic displacement profile at mid-point of the beam

displacement at the mid-point of the beam (control point 3) shows an initial displacement of 10 mm in the downward direction and a subsequent oscillation when the beam is released. The oscillations eventually die out due to damping and the displacements at all the control points go to zero. Fig. 5.19 shows the displacement as a function of time for the mid-point of the beam. Each small circle in the plot (Fig. 5.19) indicates a measurement taken using the proposed ultrasonic technique and consecutive displacements were connected through a linear interpolation. From Fig. 5.19, it is observed that successive measurements with less than 1 mm resolution are obtained. Therefore, sub-millimetre resolution in displacement estimation can be achieved with the proposed technique.

5.7. Conclusions

This chapter discusses the various aspects of utilizing air-coupled ultrasonic transducers in pulse-echo mode for measuring tie deflections at discrete points. Key factors governing the selection of optimum air-coupled ultrasonic transducers for “airborne sonar” were discussed. An array of piezoelectric and capacitive transducers were tested, and a comparison of their performances were presented in terms of reflection strength, robustness to tilt angles and

sensitivity to external vibrations. Piezoelectric transducers were found to be more sensitive to vibrations when compared to the capacitive transducers. Based on the results obtained in the laboratory, VN Instruments Inc. manufactured CAP-2 transducers were found to be the most optimum. The different components of the data acquisition system coupled with a LabVIEW real-time processor were also discussed. Implementing the data acquisition system in LabVIEW real-time allows for processing of the data in parallel to acquisition. Such an acquisition architecture would ensure that defective tie-ballast support conditions could be detected instantaneously in the field when full-blown tests are performed. The possibility of driving six transducers in parallel acquisition mode using the same pulsing unit was also investigated. A tolerable drop in the signal strength of about 10% was observed when six transducers were driven in parallel. This drop is not expected to cause any issues since the received signal strength at the expected lift-off distance was well above the noise floor of the system. Signal processing routines for measuring the time-of-flight using a peak detection algorithm were also discussed. The use of minimum threshold levels and appropriate data windows ensures that spurious peaks in the received signal are properly eliminated. The peak detection algorithm is embedded in LabVIEW real-time facilitating the lift-off distance computation to occur in parallel with data acquisition. The effect of electronic jitter on lift-off distance measurements was also investigated. A variation of around ± 0.2 mm in the computed lift-off distance was observed as a result of jitter in the received signal. The variation is less than the target resolution for deflection measurements (1 mm) and hence is not expected to raise any issues. Proof-of-concept tests using a slender beam in a 3-point bending test confirmed the viability of the technique for measuring tie deflections. The results discussed in this chapter lay the foundations for the next phase of the project that consisted of testing a prototype system mounted on a cart moving at walking speeds.

5.8. Acknowledgements

This work was funded by the US Federal Railroad Administration under contract 693JJ619C000019 with Mr. Cameron Stuart as the Program Manager.

Chapter 5, in part, has been submitted for publication of the material as it may appear in the following paper: **Datta, D.**, Cui, R., Hosseinzadeh, A. Z., Lanza di Scalea, F. Non-contact Ultrasonic Sonar-based Ranging Technique for In-motion 3D Railroad Tie Deflection Measurements. Submitted to *Transportation Geotechnics*. The dissertation author was the primary investigator and author of this paper.

5.9. References

- [1] Abadi, T., Pen, L. Le, Zervos, A., & Powrie, W. (2019). Effect of sleeper interventions on railway track performance. *Journal of Geotechnical and Geoenvironmental Engineering*, 145(4), 04019009. [https://doi.org/10.1061/\(ASCE\)GT.1943-5606.0002022](https://doi.org/10.1061/(ASCE)GT.1943-5606.0002022)
- [2] Lutch, R. H. (2009). Capacity optimization of a prestressed concrete railroad tie. Dissertations, *Master's Theses and Master's Reports - Open*. <https://doi.org/10.37099/mtu.dc.etsds/254>
- [3] Farnam, S. M., & Rezaie, F. (2019). Simulation of crack propagation in prestressed concrete sleepers by fracture mechanics. *Engineering Failure Analysis*, 96, 109–117. <https://doi.org/10.1016/J.ENGFAILANAL.2018.09.012>
- [4] Sadeghi, J. (2008). Experimental evaluation of accuracy of current practices in analysis and design of railway track sleepers. *Canadian Journal of Civil Engineering*, 35(9), 881–893. <https://doi.org/10.1139/L08-026>
- [5] Kaewunruen, S., Gamage, E. K., & Remennikov, A. M. (2016). Structural behaviours of railway prestressed concrete sleepers (cross-ties) with hole and web openings. *Procedia Engineering*, 161, 1247–1253. <https://doi.org/10.1016/J.PROENG.2016.08.559>
- [6] Karihaloo, B. L., & Nallathambi, P. (1989). Fracture toughness of plain concrete from three-point bend specimens. *Materials and Structures*, 22(3), 185–193. <https://doi.org/10.1007/BF02472186>

- [7] Rezaie, F., & Farnam, S. M. (2015). Fracture mechanics analysis of pre-stressed concrete sleepers via investigating crack initiation length. *Engineering Failure Analysis*, 58, 267–280. <https://doi.org/10.1016/J.ENGFAILANAL.2015.09.007>
- [8] Remennikov, A. M., & Kaewunruen, S. (2014). Experimental load rating of aged railway concrete sleepers. *Engineering Structures*, 76, 147–162. <https://doi.org/10.1016/J.ENGSTRUCT.2014.06.032>
- [9] Silva, R., Silva, W. V., de Farias, J. Y., Santos, M. A. A., & Neiva, L. O. (2020). Experimental and numerical analyses of the failure of prestressed concrete railway sleepers. *Materials*, 13(7). <https://doi.org/10.3390/MA13071704>
- [10] Sadeghi, J. (2010). Field investigation on dynamics of railway track pre-stressed concrete sleepers. *Advances in Structural Engineering*, 13(1), 139–151. <https://doi.org/10.1260/1369-4332.13.1.139>
- [11] Yu, H., Marquis, B. P., & Jeong, D. Y. (2017). Failure analysis of railroad concrete crossties in the center negative flexural mode using finite element method. *Journal of Rail and Rapid Transit*, 231(5), 610–619. <https://doi.org/10.1177/0954409716685914>
- [12] Yu, H. (2016). Estimating deterioration in the concrete tie-ballast interface based on vertical tie deflection profile: a numerical study. *2016 Joint Rail Conference*. <https://doi.org/10.1115/JRC2016-5783>
- [13] Frohling, R. D. (2009). Deterioration of railway track due to dynamic vehicle loading and spatially varying track stiffness. *PhD Thesis, University of Pretoria*.
- [14] Cox, S. J. (2007). Deflection of sleeper in ballast. *Vehicle System Dynamics*, 24(1), 146–153. <https://doi.org/10.1080/00423119508969621>
- [15] Kim H, Saade L, Weston P, Roberts C. (2014). Measuring the deflection of a sequence of sleepers at a transition zone. *Railway Condition Monitoring (RCM 2014), 6th IET Conference*.
- [16] Priest, J. A., & Powrie, W. (2009). Determination of dynamic track modulus from measurement of track velocity during train passage. *Journal of Geotechnical and Geoenvironmental Engineering*, 135(11), 1732–1740. [https://doi.org/10.1061/\(ASCE\)GT.1943-5606.0000130](https://doi.org/10.1061/(ASCE)GT.1943-5606.0000130)
- [17] Askarinejad, H., Barati, P., Dhanasekar, M., & Gallage, C. (2018). Field studies on sleeper deflection and ballast pressure in heavy haul track. *Australian Journal of Structural Engineering*, 19(2), 96–104. <https://doi.org/10.1080/13287982.2018.1444335>
- [18] Joh, S. H., Magno, K., & Hwang, S. H. (2018). Dynamic deflection of a railroad sleeper from the coupled measurements of acceleration and strain. *Sensors*, 18(7). <https://doi.org/10.3390/S18072182>

- [19] Le Pen, L., Bhandari, A. R., & Powrie, W. (2014). Sleeper end resistance of ballasted railway tracks. *Journal of Geotechnical and Geoenvironmental Engineering*, 140(5), 04014004. [https://doi.org/10.1061/\(ASCE\)GT.1943-5606.0001088](https://doi.org/10.1061/(ASCE)GT.1943-5606.0001088)
- [20] Sabato, A., & Niezrecki, C. (2017). Feasibility of digital image correlation for railroad tie inspection and ballast support assessment. *Measurement*, 103, 93–105. <https://doi.org/10.1016/J.MEASUREMENT.2017.02.024>
- [21] Jackson, J. C., Summan, R., Dobie, G. I., Whiteley, S. M., Pierce, S. G., & Hayward, G. (2013). Time-of-flight measurement techniques for airborne ultrasonic ranging. *IEEE Transactions on Ultrasonics, Ferroelectrics, and Frequency Control*, 60(2), 343–355. <https://doi.org/10.1109/TUFFC.2013.2570>
- [22] Figueroa, F., & Barbieri, E. (1991). An ultrasonic ranging system for structural vibration measurements. *IEEE Transactions on Instrumentation and Measurement*, 40(4), 764–769. <https://doi.org/10.1109/19.85349>
- [23] Peter J. Shull. (2001). *Nondestructive evaluation: theory, techniques, and applications - (1st ed., Vol. 1)*. CRC Press.
- [24] Khyam, M. O., Ge, S. S., Li, X., & Pickering, M. R. (2017). Highly accurate time-of-flight measurement technique based on phase-correlation for ultrasonic ranging. *IEEE Sensors Journal*, 17(2), 434–443. <https://doi.org/10.1109/JSEN.2016.2631244>
- [25] Queiros, R., Girao, P. S., & Serra, A. C. (2007). Cross-correlation and sine-fitting techniques for high resolution ultrasonic ranging. *IEEE Instrumentation and Measurement Technology Conference Proceedings*, 552–556. <https://doi.org/10.1109/IMTC.2006.328588>

Chapter 6. In-motion Full-Field Ultrasonic Tie Deflection Measurements (Rail Defect Testing Facility Tests)

6.1. Introduction

This chapter presents an ultrasonic sonar-based ranging technique for measuring full-field railroad tie surface deflections. Tie deflection profiles can be used for flagging deteriorating tie-ballast support conditions such as center-binding. The technique utilizes an array of air-coupled capacitive ultrasonic transducers oriented parallel to the tie with a minimum clearance of 3-inches from the rail to ensure contactless inspection. The inspection prototype was designed at the Experimental Mechanics, NDE and SHM Laboratory at University of California San Diego (UCSD). The transducers are used in pulse-echo mode and the distance between the transducer to the tie surface is computed by tracking the time-of-flight of the reflected wave from the tie surface. Using one of the transducers as a reference, the deflections at all other transducer locations are computed by tracking the difference in time-of-flight with respect to the reference using a cross-correlation operator [1-2]. An adaptive reference-based cross-correlation operation ensures accurate peak-detection and results in robust measurements even in the presence of variabilities such as difference in elevations of different tie surfaces, wave dispersion, etc. Multiple measurements along the width of the tie allow the measurement of twisting deformations as well. Since the transducers are used in continuous acquisition mode while the test vehicle is traveling over the track, there is a need to differentiate a tie reflection from a ballast reflection. It is shown that wave reflections from ballast have significantly lower amplitudes and shapes than reflections

coming from ties. This enables a signal strength-based tie-ballast differentiation. Considering the distinguishable texture of the ties and ballast, an image-based classification technique is also introduced using a machine learning technique. A high-speed camera is mounted on the prototype to capture images in tandem with the reflected waveforms. Features are extracted from a set of tie and ballast images (training dataset), and Support Vector Machine (SVM) [3-7] is employed to train an identifier that can label a given image as a tie or ballast. Signals coming from the ballast can therefore be eliminated. Data acquisition and tie deflection processing is performed in real-time using a LabVIEW real-time module. Field tests on a replica test track with wood ties, at walking speeds, were performed at the Rail Defect Testing (RDTF) Facility at UCSD by mounting the prototype on a test-cart. Results from a field test conducted by mounting the prototype on an actual train car at a BNSF yard in San Diego are also presented. The initial results indicate the potential of this non-contact system to measure full-field tie deflections in 3D at high speeds.

6.2. Prototype Design

This section is devoted to introducing the prototype designed for the railroad tie inspection technique. Figs. 6.1 and Fig. 6.2 show the prototype design and components (assembled on the test cart). The prototype was designed by the Experimental Mechanics & NDE Laboratory at UCSD and fabricated by UCSD's Campus Research Machine Shop. It contains three main parts:

- (1) Transducer mounting beam: This is a 108"-long hollow aluminum beam, with a side-slit to hang 7 small aluminum tubes. This slit provides flexibility to easily adjust the location of the transducers along the beam and/or add new transducers to the beam if required.
- (2) Small aluminum tubes: The small 10"-long tubes have ten holes (spaced by 0.5") and are used to connect the transducers and camera holders to the mounting beam.

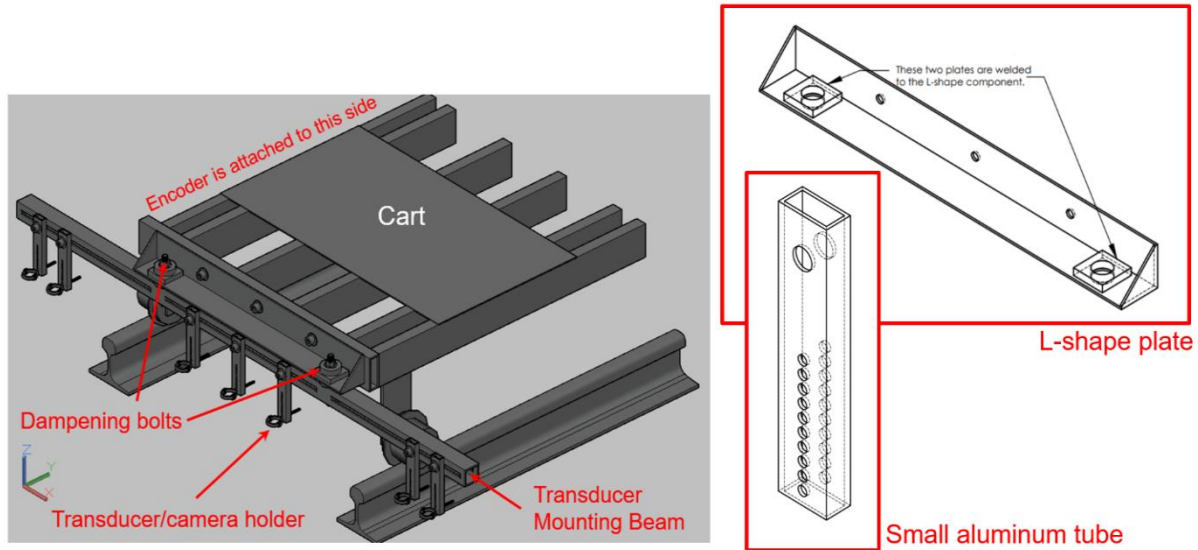


Figure 6.1 AutoCAD drawings of the designed prototype mounted on a test-cart

(3) L-shape plate: The transducer mounting beam is connected to the cart by a L-shape steel component through two dampener connections.

Stability, light weight, and flexibility in terms of smoothly adjusting the location of the transducers in both vertical and horizontal directions, are the most important factors considered in the prototype design. The clearance between the rail and prototype equipment and the average distance between the transducers and ties are 3.5" and 11.5", respectively (see Fig. 6.3). To avoid transferring the vibration of the cart to the beam (and subsequently, to the transducers), dampening bolts are used to connect the beam to the L-shape component (see Fig. 6.1). In terms of sensors, the prototype uses six CAP-2 sensors (transducers) and a high-speed camera. The camera is a Basler acA 1300-200uc (USB3.0 version), with an ON semiconductor, Python 1300 Complementary Metal-Oxide-Semiconductor (CMOS) sensor, which can deliver up to 200 frames per second (FPS) with 1.3 Megapixel resolution. The lens of the camera is a Kowa, 1/1.8" Format, Manual Iris version. The focal length of the lens is 4.4-11mm, with a zoom ratio of 2.5x. Fig. 6.4 shows the number and location of the transducers connected to the beam. The camera is connected

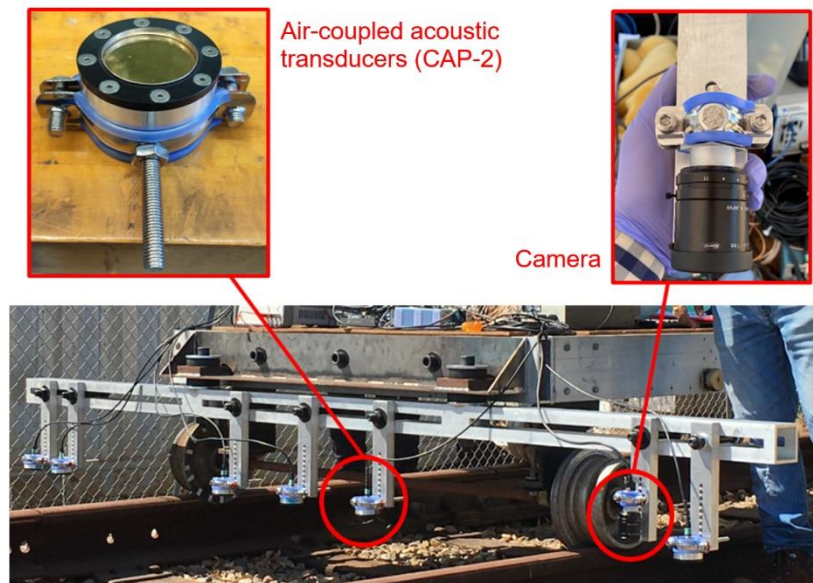


Figure 6.2 *Prototype with transducers and camera*

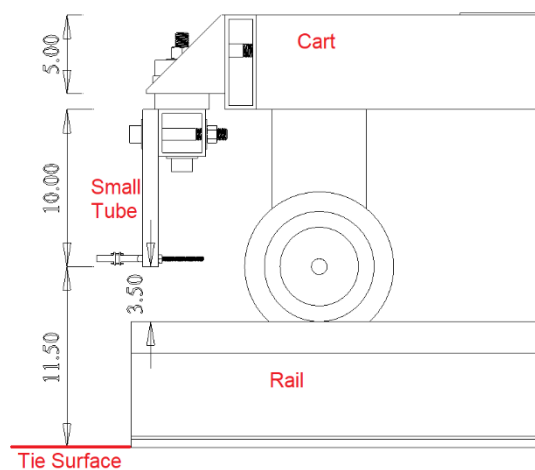


Figure 6.3 *Side view diagram of the prototype mounted on the test car*

to the holder located next to the first transducer (channel 1). The encoder is connected to the left side of the cart, and it is in contact with the front wheel (see Fig. 6.5). As the cart moves, the encoder rotates and subsequently the transducer as well as the camera data acquisition system are triggered. The data acquisition system (including the camera) is triggered by the encoder pulse with a 0.25-inch resolution.

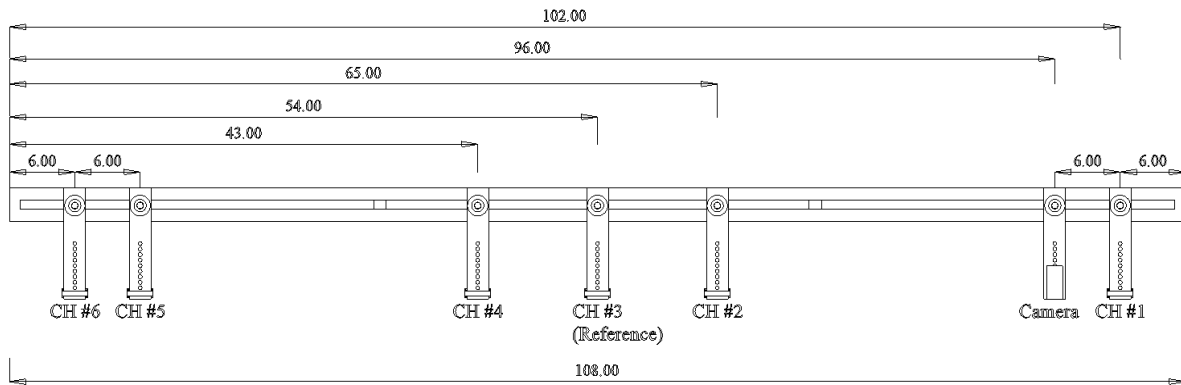


Figure 6.4 The location of the transducers and camera (unit: inch). ‘CH’ denotes the channel number assigned for the transducers.

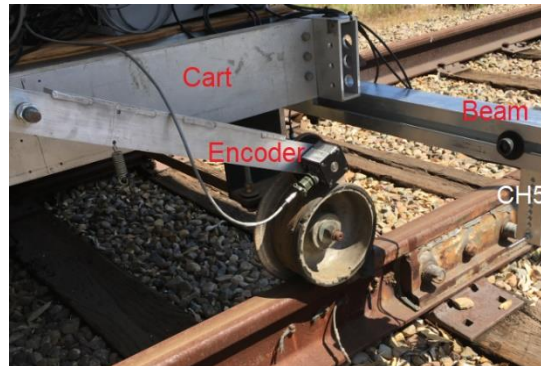


Figure 6.5 Encoder in contact with the front wheel of the cart in the left side.

6.3. Data Acquisition System

6.3.1. Hardware

A schematic diagram of the data acquisition system using capacitive air-coupled ultrasonic transducers is shown in Fig. 6.6. Six capacitive air-coupled ultrasonic transducers (VN Instruments CAP-2) with a central frequency of 135 kHz were used. The setup consists of a pulser/amplifier unit which sends out excitation pulses (~ 100 V) to the transducers which triggers it to transmit the

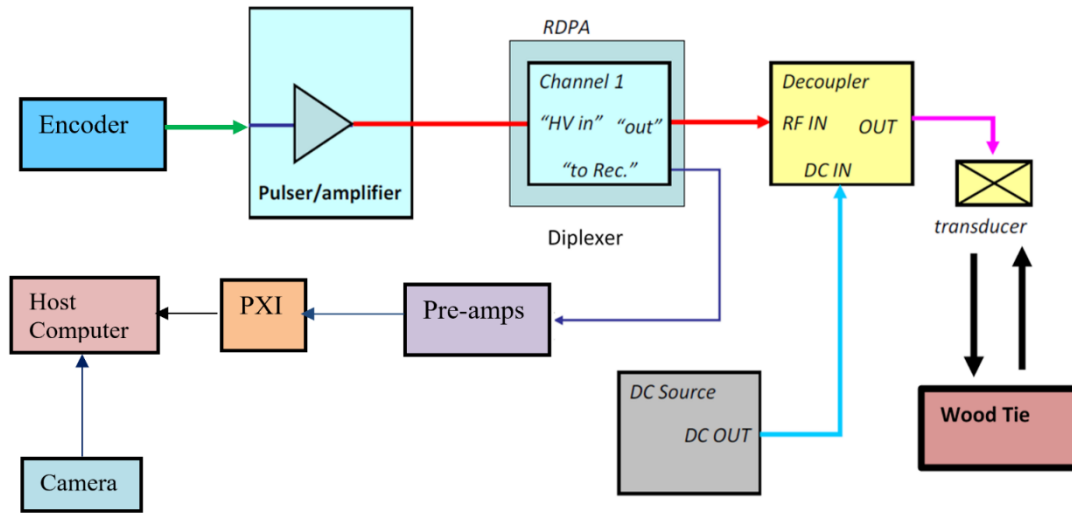


Figure 6.6 Schematic diagram of data acquisition setup (1-channel configuration)

outgoing pulse to the tie surface. The pulser unit is triggered by an encoder wheel connected to the wheel of the cart that is programmed to trigger one acquisition (deflection measurement) every 0.25 inch of length. The excitation pulse from the pulsing unit also triggers the data acquisition system programmed in NI LabVIEW Real-time. The high energy excitation pulse and the low energy received signal are on the same channel, and the diplexer (Ritec RDX-SD-2X) splits these two signals and prevents the high energy excitation signal from leaking into the receiving channel. The micromachined capacitive transducers require a DC bias of 200 V during operation. The AC/DC decoupler combines the excitation signal and the DC bias on the outgoing channel to the transducers and also prevents the DC bias from leaking into the receiving channel to the diplexer. The received signal from the diplexers is fed through pre-amplifiers (Olympus 5662) which amplify the signals before going to the National Instruments PXI 5105 data acquisition card. The data acquisition system is programmed in LabVIEW Real-time running on a National Instruments PXIe-8135 processor. The Real-Time processor analyzes the received signals in parallel with the acquisition. A host computer is used to run the LabVIEW code in the target PXI device. The

camera is connected directly to the host computer through USB 3 for high-speed data transfer and acquisition of up to 100 fps.

6.3.2. LabVIEW User Interface (Acoustic Signals)

Fig. 6.7 shows the user-interface panel of the LabVIEW Real-Time code programmed for data acquisition. The interface features controls for setting acquisition parameters such as sampling rate, length of each recording, reference channel, etc. Live signals from the six transducers are displayed and lift-off distances from the tie surfaces are also displayed next to each signal. An instantaneous deflection profile of the tie with respect to the chosen reference point is also

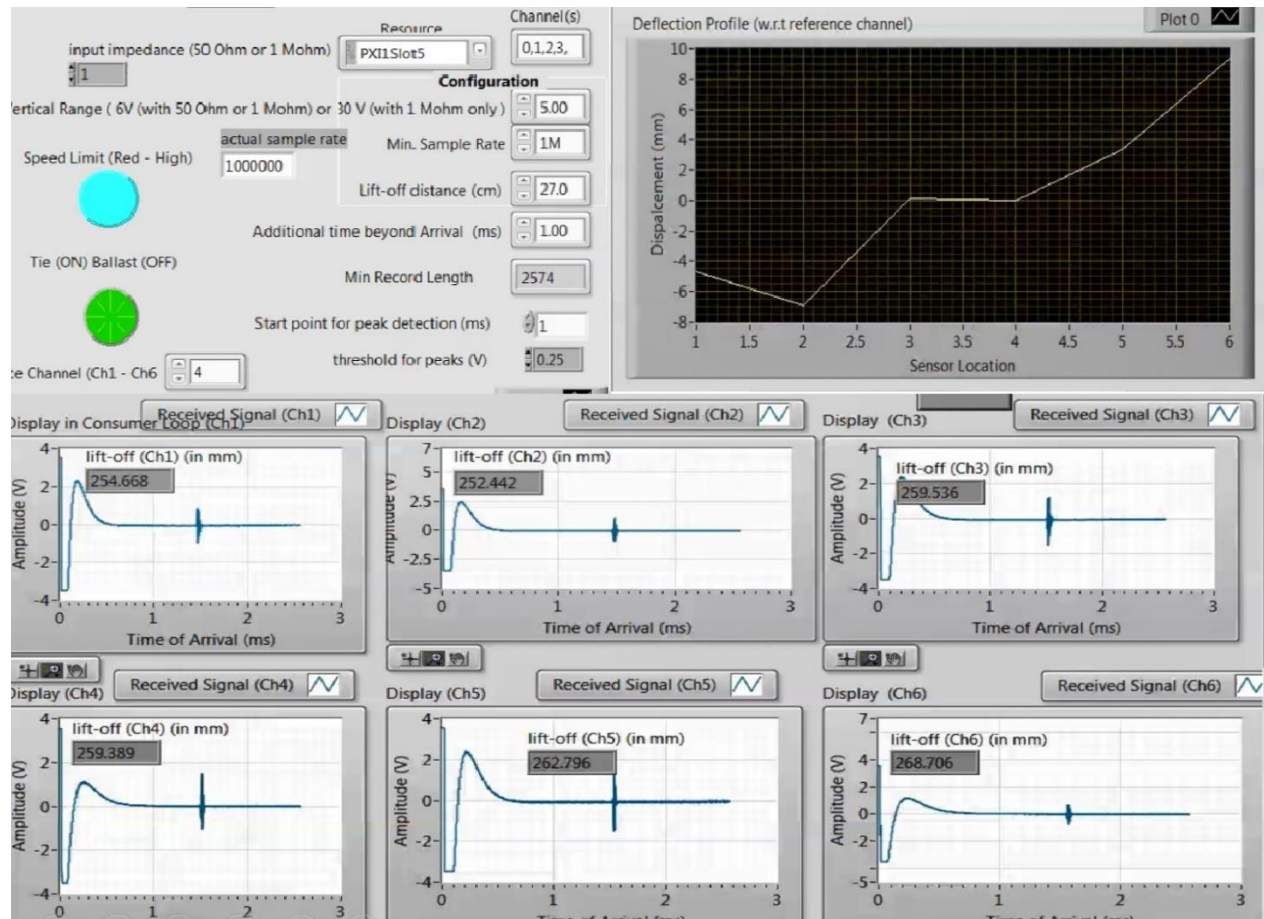


Figure 6.7 User-interface for data acquisition programmed in LabVIEW Real-Time

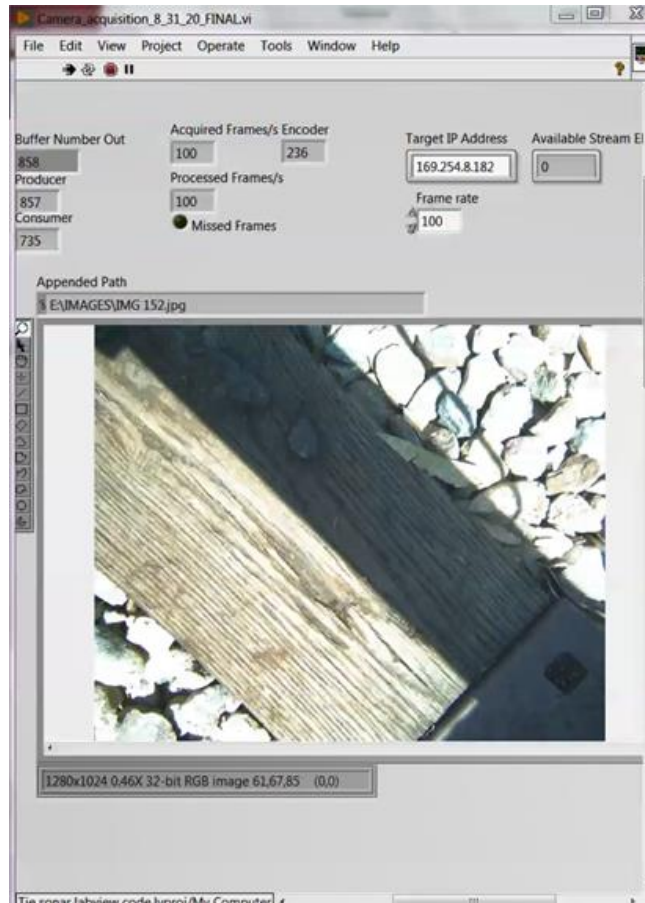


Figure 6.8 Front panel of the LabVIEW routine for the camera during a test.

displayed. An indicator (shown in green) is programmed to indicate whether the signals displayed come from a tie or ballast. The tie-ballast differentiating indicator is based on a user-controlled peak-to-peak threshold level of the signal. If the signal drops below the set threshold level, that location is assigned as a ballast. An image-based texture identification algorithm is also used for separating ties from ballast as a back-up system.

6.3.3. LabVIEW User Interface (Image Acquisition)

Fig. 6.8 shows the front panel of the LabVIEW program developed to communicate with the camera. The camera is connected to a SuperSpeed (SS) USB3.0 port on the computer, which provides the camera with both power supply and fast speed data transmission path. Running the

developed LabVIEW code, the camera turns on, and grabs images based on the encoder count number. The encoder count number comes through a network communication with the LabVIEW routine developed for the transducers (discussed in Section 6.3.2 –this routine is the host routine which manages the camera’s LabVIEW routine) and this number determines the name of the images which are saved as “jpeg” file in the computer system. If the encoder stops, the count number remains constant, and the image is overwritten with a name of that count. The camera frame rate can be controlled through the front panel of the code (see Fig. 6.8). In the field tests, the camera was set to grab 100 FPS, which is a reasonable frame rate for the walking speed test. The code is executed based on a stop command which is issued by the user through the LabVIEW routine of the signal acquisition part. Therefore, the camera’s LabVIEW routine constantly checks the comments through the network communication in terms of receiving the stop command. As soon as this command is received, the camera stops image acquisition; the code continues running until all the inline images are successfully saved in the hard drive.

6.4. Tie Boundary Demarcation

6.4.1. Signal-Based Demarcation

For this set of field tests an acoustic signal strength-based approach was used to distinguish between ties and ballast. Fig. 6.9 shows the signals acquired from the six transducers from a tie surface. It can be seen that the signals in all the six channels are clearly distinguishable above the noise floor of the data acquisition system. An initial spike in the signal can be observed before 0.2 ms in all the channels. This is because both the excitation pulse and the reflected signal are on the same channel and there is some crosstalk between the excitation pulse and received signal. This initial spike controls the minimum distance that the air-coupled ultrasonic transducer is

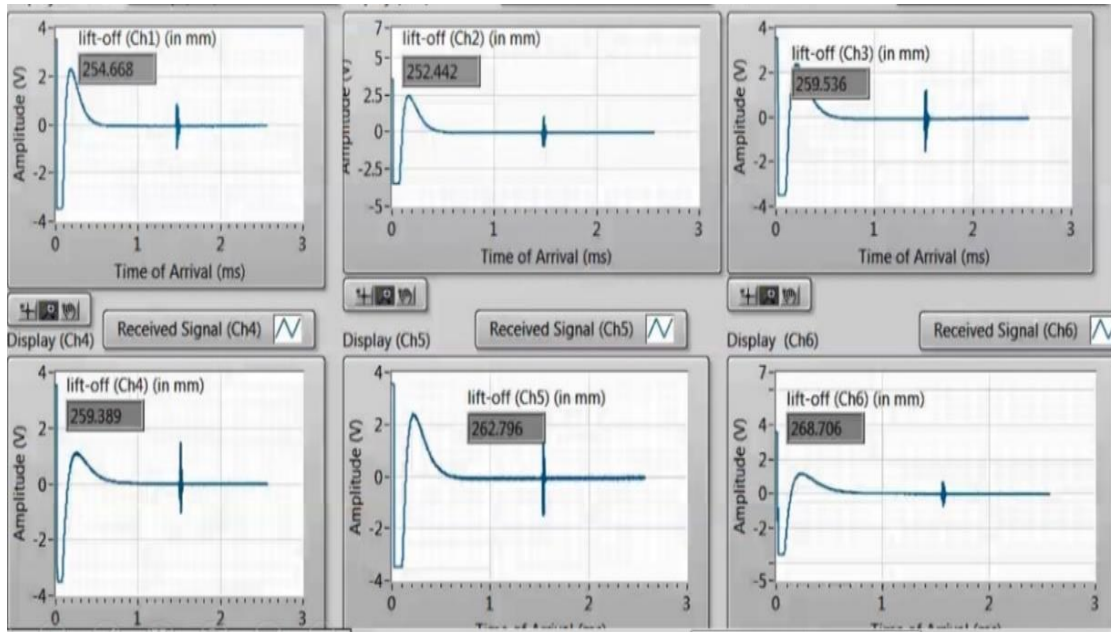


Figure 6.9 Acoustic signals at the 6 receiving channels from a tie

capable of measuring. In our case, the lift-off distance of around 11 inches ensures that our signal does not fall within the 0.2 ms window and therefore signals prior to 0.2 ms can be safely discarded.

Fig. 6.10 shows the signals received from the ballast. It is clearly observed that, as a result of wave scattering from the uneven ballast surface, the signal amplitudes drop considerably. Based

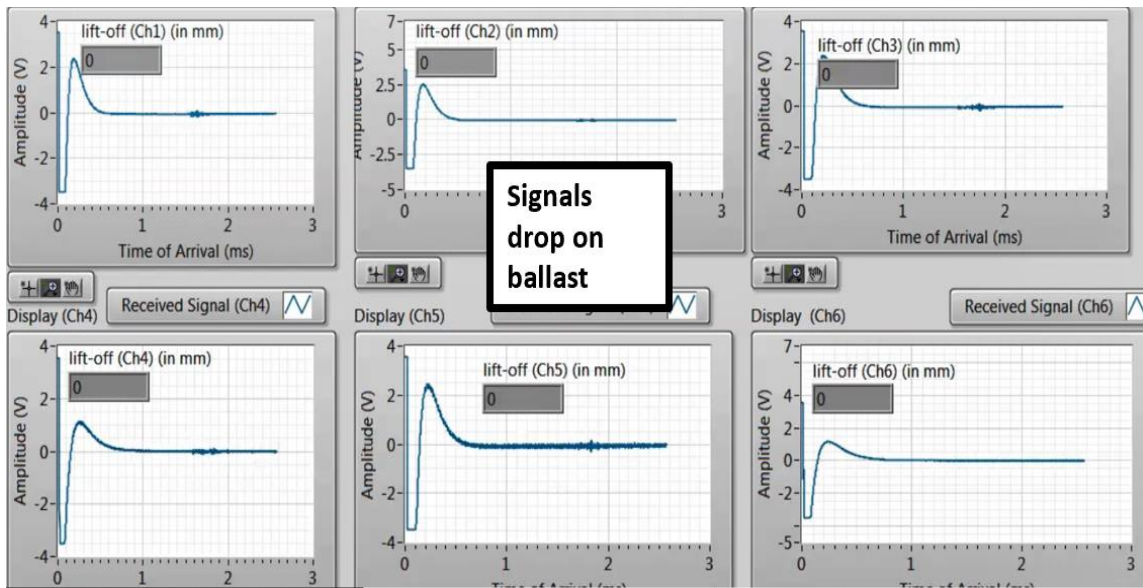


Figure 6.10 Acoustic signals at the 6 receiving channels from ballast

on these observations, a peak-to-peak signal threshold level of 0.75 V was chosen to identify the ties. If at least four transducers had a peak-to-peak signal strength above the selected threshold (0.75 V), the signals were assigned to a tie. If this criterion was not met, the signals were assigned to ballast. Signals coming from ballast were discarded from further analysis, and only signals from ties were used for the deflection computations using cross-correlations as discussed in the previous chapter.

6.4.2. Image-Based Demarcation using Machine Learning

Image-based tie/ballast classification was evaluated as a back-up method to the tie/ballast classification done by signal analysis. In this section, the details of the computer vision-based tie/ballast classification method as well as the obtained results are presented. Moreover, a comparative study is conducted between the image-based and signal-based approaches.

6.4.2.1 Preparing Images for Analysis

Fig. 6.11 shows a typical image captured by the camera. A rotation in the view field of the camera is seen because the camera was rotated by -45 deg to install in the holder. Therefore, the raw image captured by the camera was rotated back to its original configuration by the software.



Figure 6.11 Typical image showing tie and ballast captured by the camera

The image has a wide field of view; however, the Region of Interest (ROI) is a central circle equivalent to the transducer's effective area (a circle with 3.9 cm diameter). To crop the rotated image and focus on the ROI, the actual travelling distance was mapped into the pixel domain because the images are in the pixel domain. For this purpose, a couple of points in an image were selected and tracked in the next successive image. Then, pixel-domain displacement was mapped into the actual physical displacement using the frequency of the pulse generation by the encoder. The pixel-domain displacement of a given point in two successive images (which are the images captured in two successive encoder counts) was equal to 0.25". Therefore, a point tracker method was employed to extract the pixel-domain displacements. There are different point tracking algorithms in the field of computer vision. In this project, the Kanade-Lucas-Tomasi (KLT) tracker [8-12] was employed. The fundamentals of the KLT tracker are briefly explained herein.

First, the RGB image sequences are converted to grayscale format, where the hue and saturation information is eliminated and only the luminance of the images is retained. Then, an area in the image's field of view (in the first image of the sequence) is selected and the robust trackable features (points) are automatically identified. Here, the Speeded-Up Robust Features (SURF) algorithm is used to find blob features [13]. The robust trackable points are basically corner points that do not suffer from any aperture problem. In the next step, the shift (displacement) of the trackable points in the successive images are tracked. The framework of the tracking approach is based on local optimization. Generally, a squared distance criterion over a local region with respect to the transformation parameters is used to define the objective function. Then, the point displacement is approximated with a linear term using Taylor series. In the present application, the mentioned framework is used to track the 2D in-plane displacement of the robust trackable points in the successive images.



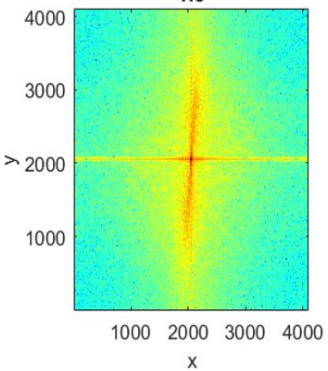
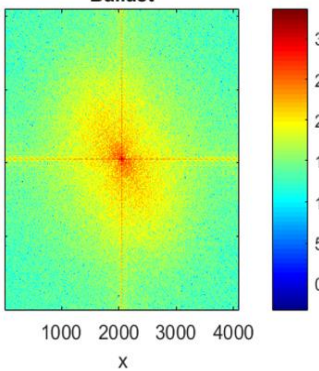
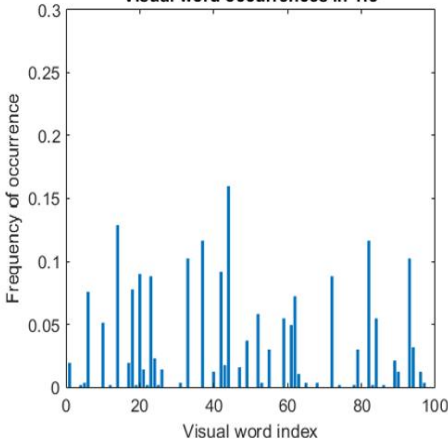
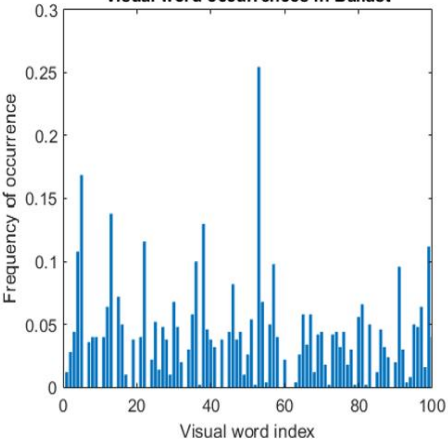
6.4.2.2 Training the Tie-Ballast Identifier Using Support Vector Machine (SVM)

The cropped images are used to train an identifier using the Support Vector Machine (SVM) method. A SVM is a discriminative classifier, which is defined by a separating hyperplane. Given a labeled training data set (supervised learning), the algorithm's output is an optimal hyperplane classifying the new examples. Here the texture of the object is used to extract the main image features for identification training. Specifically, two key texture-based features are extracted: the 2D Fast Fourier Transform (2D FFT) and the histogram of the visual words. The latter, known as Bag of Visual Words (BOVW) method in the field of computer vision, was adapted from the main concept of "Bag of Words (BOW)," in which the keywords of a text are extracted by making frequency histogram of the words and feeding into machine learning algorithms to make text search engines. To adapt this concept to the present investigation, images of the ties and ballasts were divided into small zones, and each zone was considered as a visual word. The histogram of visual words' occurrence can play the main role in classifying a given image.

In Table 6.1, the 2D FFT and histogram of 100 visual words for the ties and ballast are shown. This table shows that both 2D FFT and histogram of the visual words can be effective for classification of ties and ballast. The extracted features are fed into the SVM core to train the identifier, and the latter is used to test each image and classify it as a tie or ballast. When implementing SVM, the visual words are clustered by a K-mean approach. Each cluster contains several "words" that make a kind of visual sentence or phrase; this adds much more robustness to the trained identifier. Checking the accordance of the 2D FFT as well as the histogram of the visual phrases is the general concept used for classification. Moreover, the Kernel option of the SVM method is used to ensure that the probable outliers are removed from the samples during the training step.

In the next section, the image-based tie/ballast classification method described above is applied to the images captured from the field tests at the Rail Defect Testing Facility of UCSD during the walking speed tests on the moving cart.

Table 6.1 Typical 2D FFT and histogram of visual word occurrence for a typical tie and ballast.

Object	<p style="text-align: center;">Tie</p> 	<p style="text-align: center;">Ballast</p> 
2D-TTF	<p style="text-align: center;">Tie</p> 	<p style="text-align: center;">Ballast</p> 
Histogram of visual words	<p style="text-align: center;">Visual word occurrences in Tie</p> 	<p style="text-align: center;">Visual word occurrences in Ballast</p> 

6.4.3. Results

This section discusses the results obtained for tie/ballast classification using the vision-based method discussed. At first step, the KLT tracker was used to map the actual travelling distance to the pixel domain. Fig. 6.12 shows the selected zone as well as the automatically selected robust points (shown by numbers 1 to 4). These points were tracked in 8 successive images and the results are shown in Fig. 6.12. The tracked points reveal straight traveling lines as it is expected (there is no lateral movement). The displacement of any of the tracked points in two successive images should be equal to 0.25". Using this criterion, it is concluded that every 20 pixels on the images is equivalent with 0.25". Therefore, the ROI in the pixel domain will be a circle (at the center of the rotated images) with a diameter of 122.84 pixels. Using this information, the images were prepared for the analysis. Fig. 6.13 shows the details of this step for a typical test: the image is rotated and then, only the ROI is cropped and is saved as a new image. Note that all the procedure is done in MATLAB by using functions of the Computer Vision toolbox.

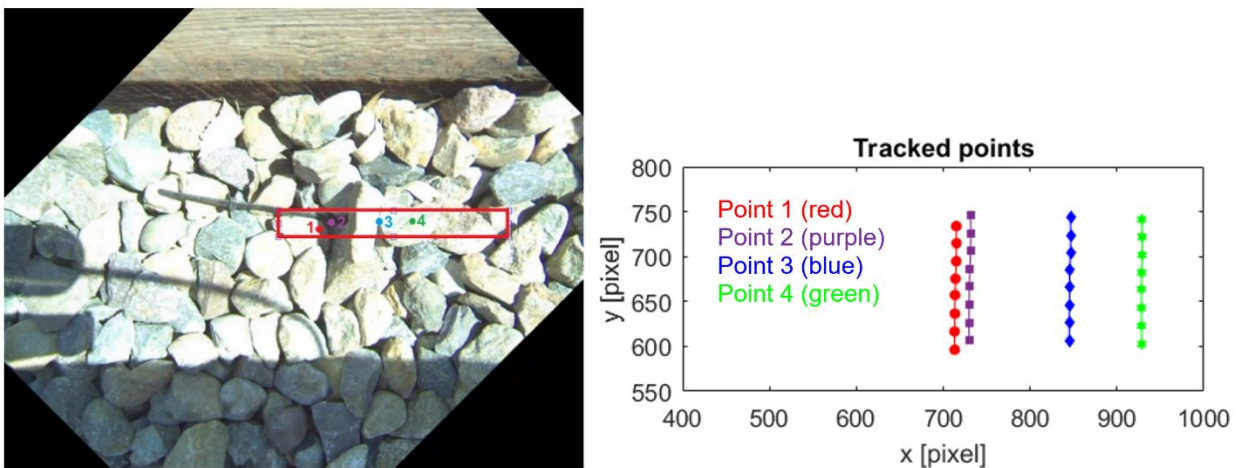


Figure 6.12 KLT tracker to map real displacement to pixel domain.

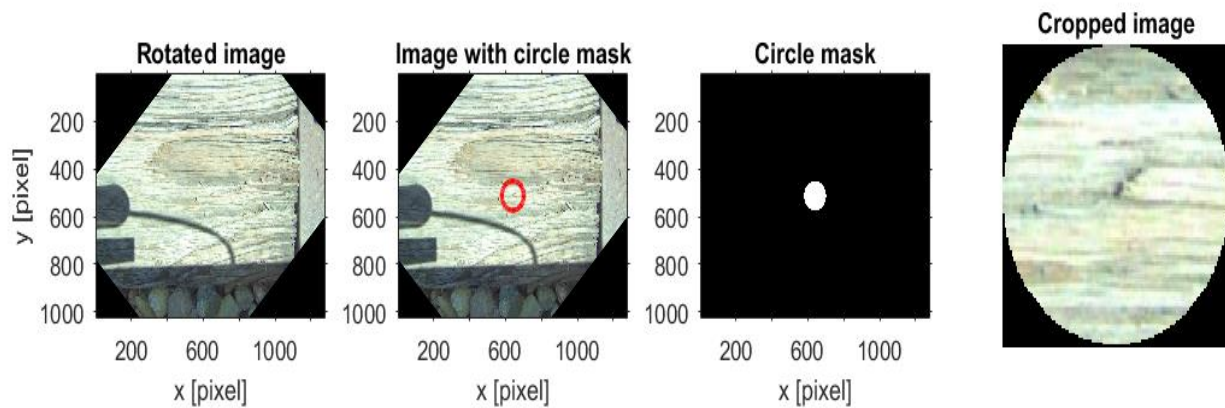


Figure 6.13 Preparing images for analysis.

In the next step, sample images of the ties and ballasts (cropped images, focused on the ROI) are randomly selected among all the images and the identifier is trained using SVM method. The initial evaluations indicated that using 2D FFT and histogram of the visual words creates an effective set of features to train the classifier. However, detailed investigations revealed that 2D FFT not only decreases the speed of the image evaluation because of the required side computations, but also cannot add much more distinguishable details in some cases. Because of the relatively small ROI, in some cases the edges of the ballasts produce locally aligned textures and the 2D FFT is almost like the 2D FFT of the ties. On the other hand, the machine learning toolbox of MATLAB has accelerated functions for BOVW computer vision algorithms which include the SVM method. This can considerably increase the speed of the training part if only the histogram of the visual words is employed as the main feature. Therefore, the optimal training system was programmed using only the histogram of the visual words to extract the object's features.

About 2% of all the images (i.e., 20 images of the ties and 20 images of the ballasts) were used for this purpose. In total, 24576 features were extracted for each category (i.e., ties and

ballasts) and 80% of the strongest features for each category was selected to make 500 visual phrases using K-means clustering approach. The confusion matrix of the evaluation process for the test set, as well as another set of 40 randomly selected images, suggested that the trained classifier has an accuracy equal to 100%.

For each run (field test), the explained procedure was repeated, and the trained classifier was used to identify tie/ballast images for the associated run. Fig. 6.14 shows the image-based tie/ballast classification results for all the five runs. Ties and ballasts are plotted with black and orange colors, respectively. The width of each cell in vertical direction is equal to the one count of the encoder (i.e., 0.25"). The results indicate that the method can properly classify ties and ballasts in different runs. Moreover, the number of the identified ties (9 ties) and their width match the ground truth.

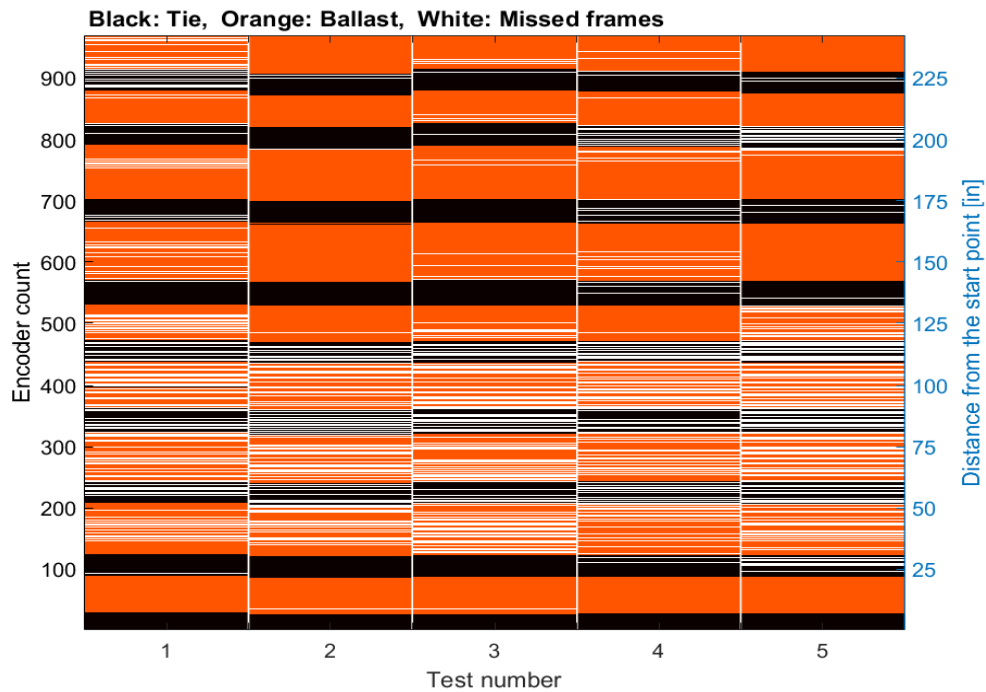


Figure 6.14 Tie-ballast classification using image-based approach

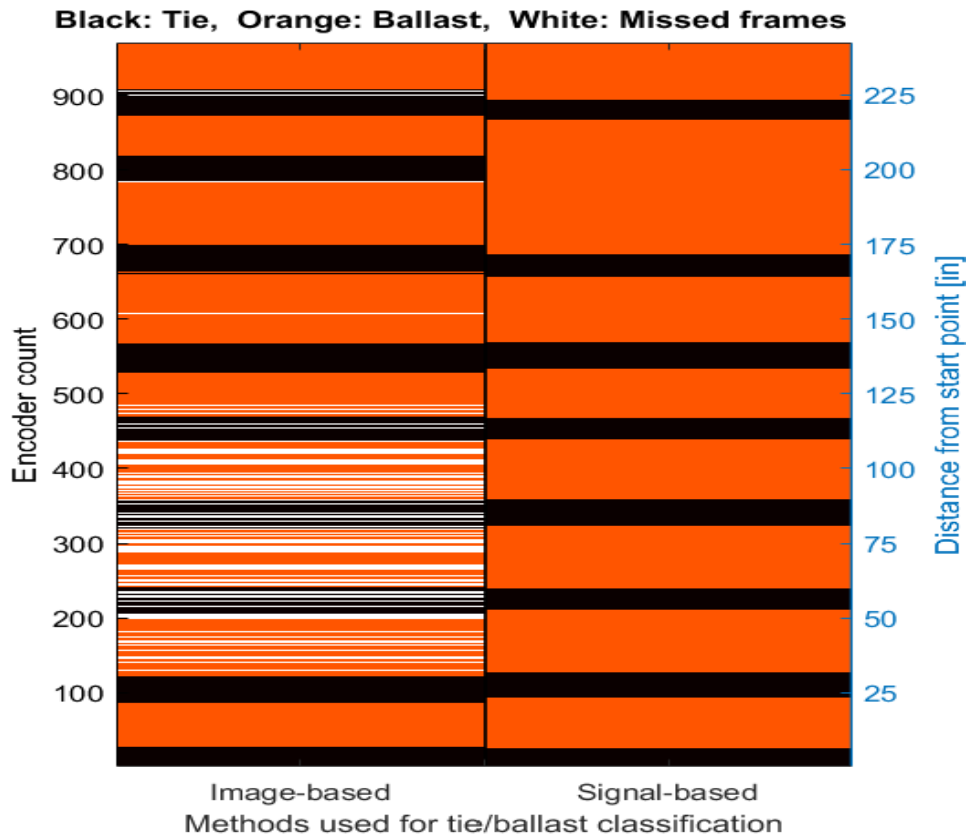


Figure 6.15 Comparison between image-based and signal-based approaches for tie/ballast classification in run #2.

In the results shown in Fig. 6.14, white cells represent the “missed” frames. That is because of the current buffer size limitation that limited the effective frame rate. In a future version, a GigE camera compatible with Real-Time Performing Systems (RTPS) can be used to eliminate missed frames.

This section ends with a study to compare the tie/ballast classification results obtained by the signal-based method and the image-based method. Fig. 6.15 shows the results obtained by these methods in the second run (test #2). In general, there is a good agreement between the two methods. In the signal-based method, however, tie-8 is not identified. The field observations revealed that this tie is not aligned with the array of the transducers. As a result, the acoustic

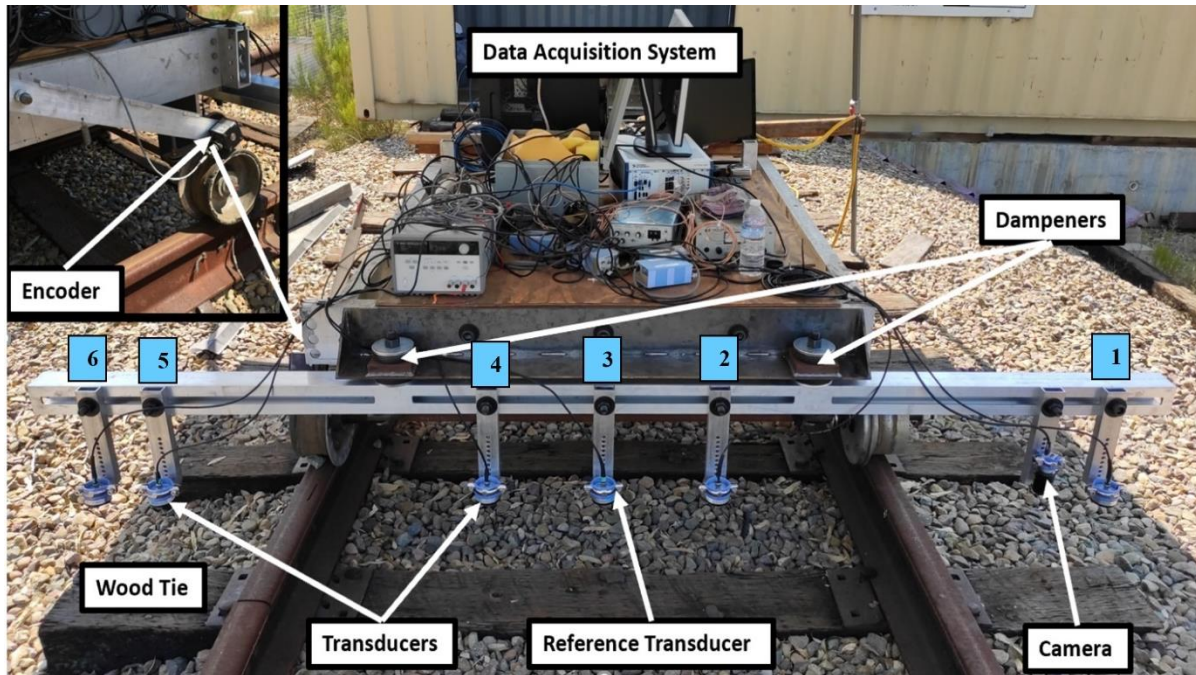


Figure 6.16 Test setup with the prototype mounted on a test cart at RDTF

reflections from the tie do not reach multiple transducers simultaneously, and hence fail the control strategy used for tie identification from the signal-based approach. Hence at this stage the vision-based method can be considered a useful back-up to the signal-based method for tie and ballast discrimination.

6.5. Field Tests (Rail Defect Testing Facility)

Fig. 6.16 shows the mounted and ready-to-go system. The various components of the prototype were discussed in Section 6.2 of this chapter. The data acquisition system (discussed in section 6.2) consisting of the computer, PXI, transducers, etc. were placed on the cart.

6.5.1. Test Methodology

Tests were conducted at walking speeds (~3 mph) at the Rail Defect Testing Facility of the University of California San Diego. The test cart was hand-pushed to scan a total of 9 ties starting

from the center of the 1st tie and ending at the center of the 9th tie. During each test run a total of 20 ft distance was covered. Five test runs were conducted over the same set of ties. Since tests were conducted at very low speeds, the encoder was programmed for a resolution of 0.25 inch along the direction of the run. The average width of each tie beam was 7 inches; a 0.25-inch resolution resulted in 28 possible surface deflection probes along the tie width. Multiple samplings along the width of the tie allowed the system to not only measure deflections along the tie length but also twisting deformations along the tie width (3D tie deflection measurements). Sampling of the signals was done at 1 MHz to adequately satisfy the Nyquist sampling frequency for the 135 kHz transducers. The acquired data was saved and later processed by MATLAB, in addition to Real-Time LabVIEW.

6.5.2. Test Results

6.5.2.1 Tie Deflection Profiles

Fig. 6.17 shows the 3D surface deflection profile of the same tie (tie-3) for two different runs. The length of the tie is divided into 6 different zones (for the 6 transducers). The zones are divided in such a manner such that each transducer position is at the center of each zone. Along the tie width, each cell has a dimension of 0.25-inch which is the resolution programmed for the encoder. During each run, the encoder values are tagged to the respective signals which makes it possible to determine the spatial coordinates of the displacement across the tie. Spatial coordinates along the tie are determined from the known locations of the transducers on the mounting beam. As discussed earlier, all deflections are calculated with respect to the reference channel 3 transducer and therefore the deflections at this position are all zero. This referencing allows to extract the absolute tie deflection.

Fig. 6.17 shows that the 3D deflection profiles for two different runs over the same tie yield consistent results. The waviness of the surface along the tie width is seen by transducer 1 and 6 in both the runs. Also, the region near transducer 6 is ~ 10 mm below reference surface, while the region near transducer 1 is ~ 10 mm above the reference surface. This indicates a possible rigid body rotation of the tie in anticlockwise direction along the length.

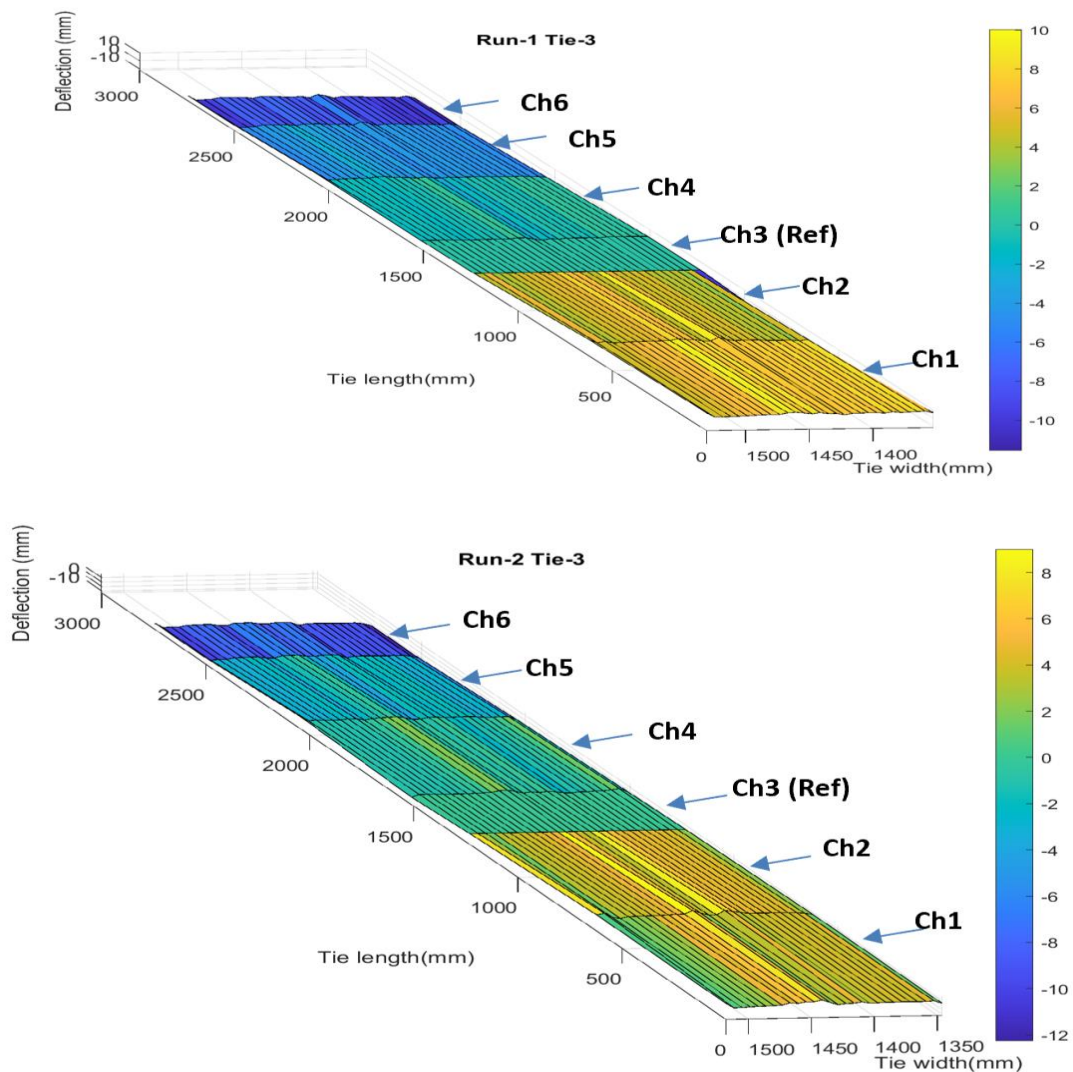


Figure 6.17 3D surface deflection profiles for same tie (tie-3) in two different test runs

Fig. 6.18 shows the 3D deflection profiles of all the eight ties scanned during one test run. The first tie profile is narrower in width compared to the other ties because the test runs started from the center of the first tie and only half the width was scanned. The white regions as seen on tie-2 and tie-4 indicate that the signals in the regions were unreliable, and these regions were classified as ballast based on acoustic signal strengths. These regions possibly had a rough tie surface or hollow cracks that resulted in a drop in signal strength. An adaptive baseline threshold for signal strengths to classify ties and ballast is under investigation to make the classification more robust and independent of random drops in signal strength. One of the ties (tie-8) was missed based

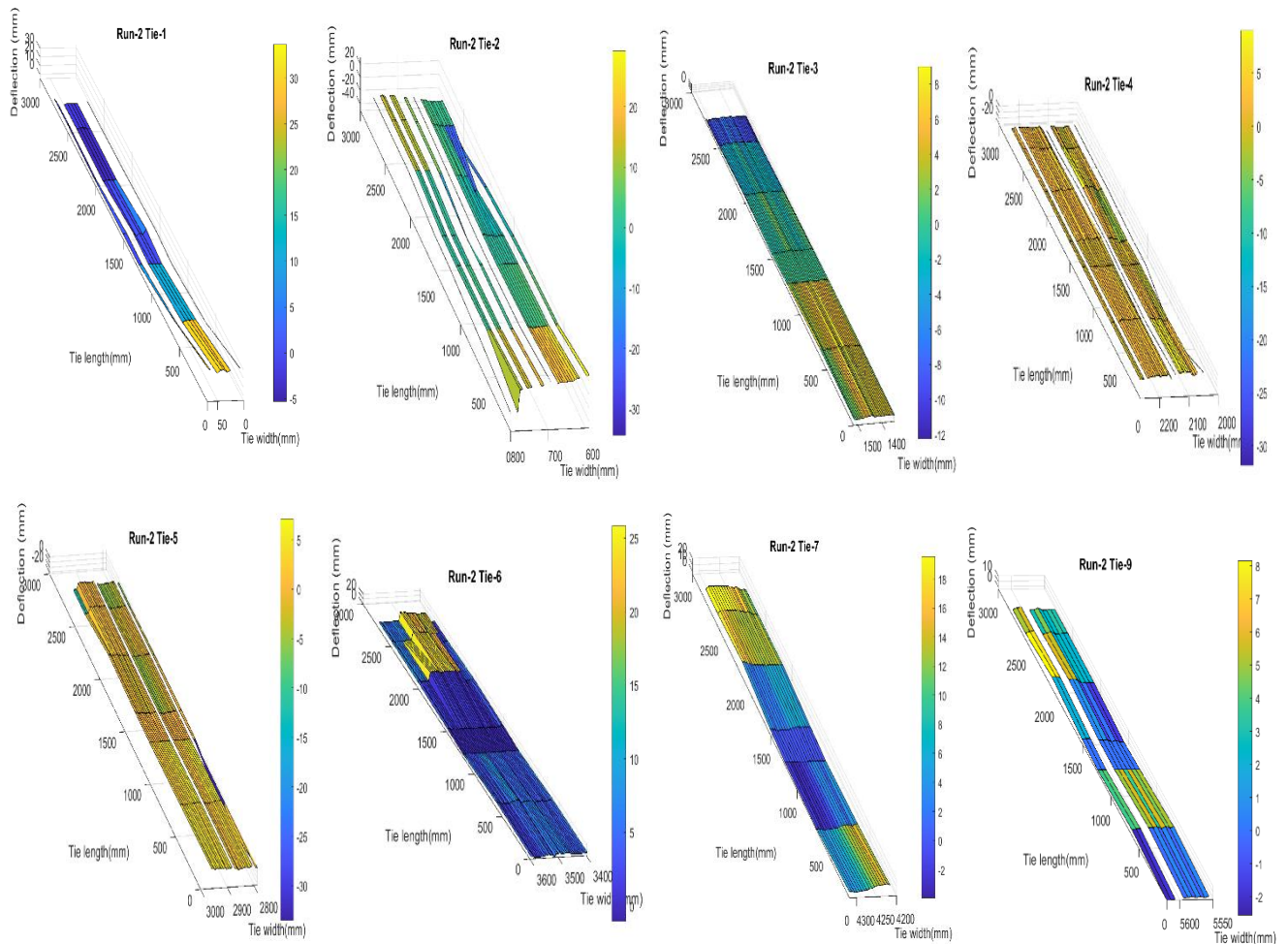


Figure 6.18 3D tie deflection profiles for all 8 ties scanned in one test run

on signal-based detection. This was because tie-8 was improperly aligned with the transducer array and signal strengths at any four channels did not cross the pre-set threshold (0.75 V). An increased elevation near transducers 5 and 6 can be seen on tie-6, which was a control point for validation the measurements. Details of this control point are discussed in the next section.

6.5.2.2 Displacement Accuracy Verification (Control Tie-6)

A control wooden plank of known thickness (19 mm) was placed on the edge of tie-6 in a way that only transducers 5 and 6 could ‘see’ the plank. Fig. 6.19 shows the control wood plank and the 3D surface displacement profile obtained for tie-6. The wood plank can clearly be seen on the surface profile as an increase in elevation at locations 5 and 6. A surface elevation profile along the tie width is shown in Fig. 6.20 for transducer locations 4, 5 and 6. Transducers 5 and 6

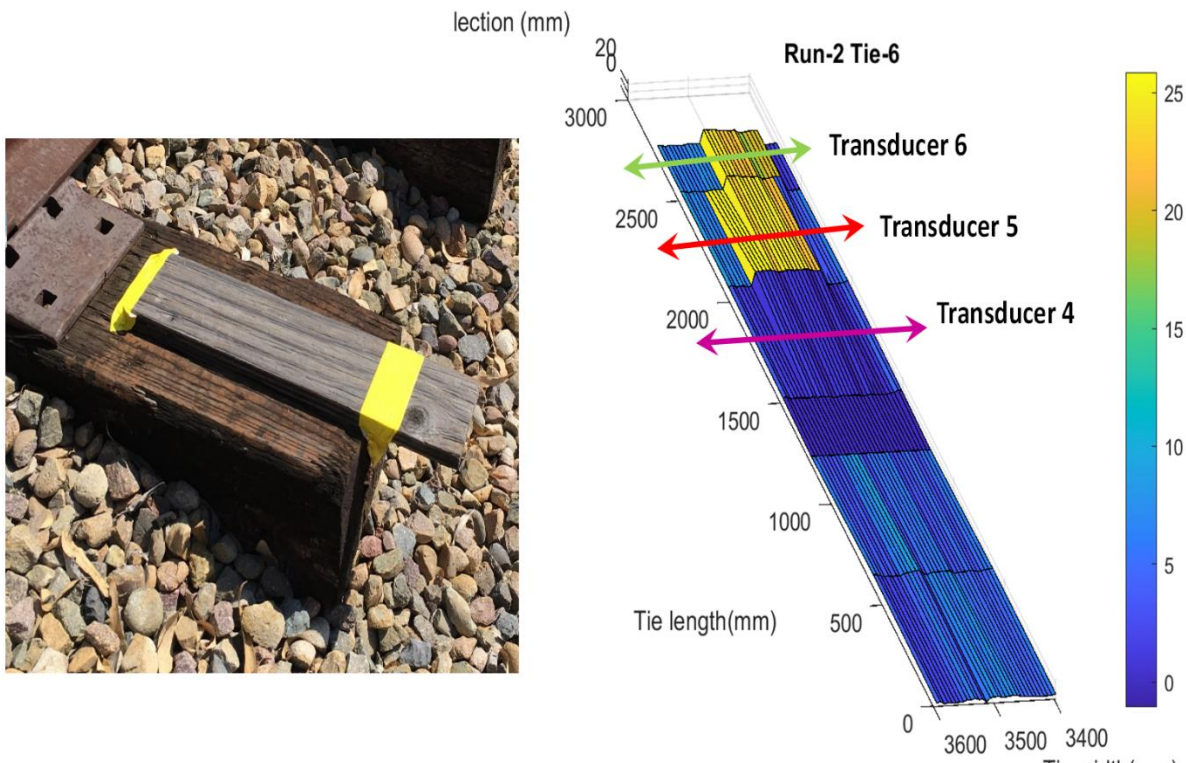


Figure 6.19 “Control” wood plank for displacement accuracy verification at tie-6

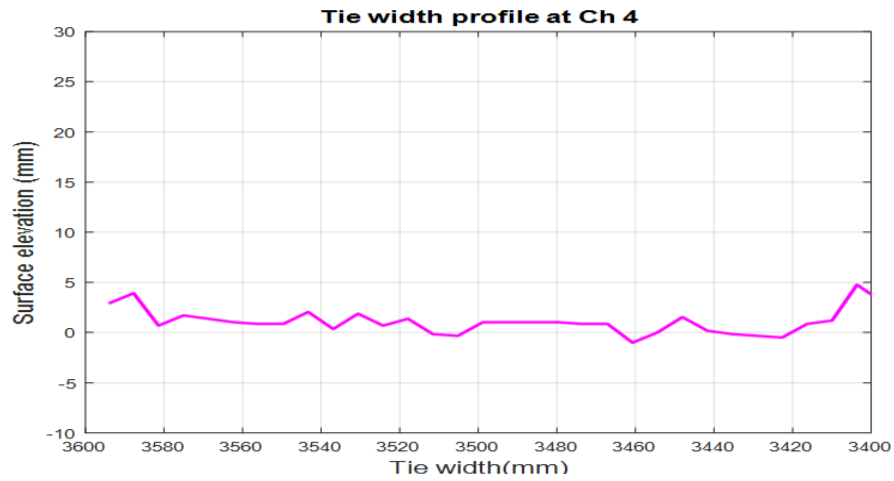
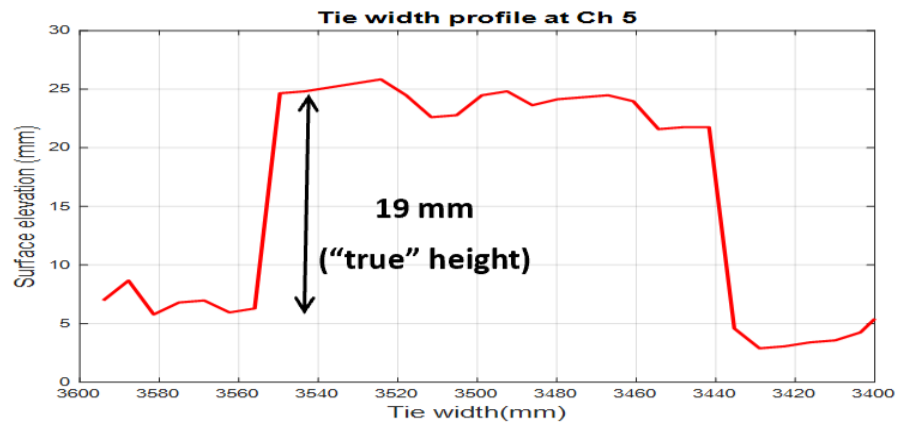
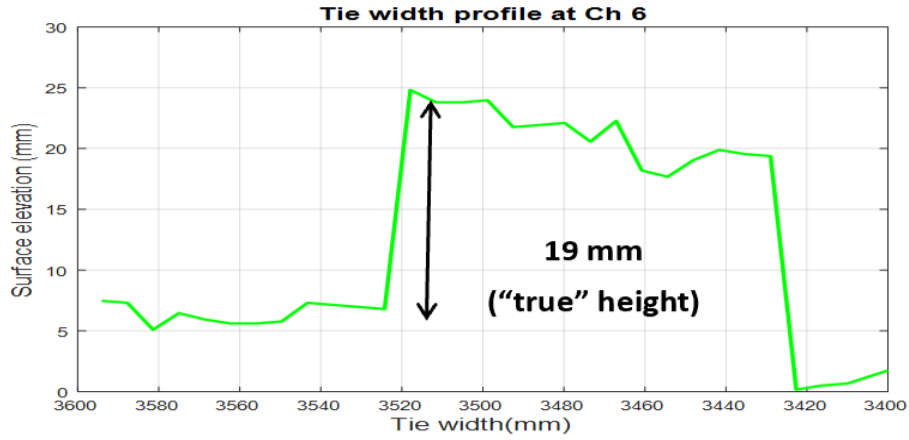


Figure 6.20 Tie-width profile at transducer locations 4, 5 & 6

clearly show the increase in elevation over the plank width. The ‘true’ height can be calculated the subtracting the baseline tie surface elevation from the elevation of the wood plank. This value was found to be equal to the thickness of the wood plank as expected. These results verify the accuracy

of deflection measurements from the tie-sonar system. Since transducer 4 did not scan the wood plank, it does not show an increase in the elevation as expected.

6.6. Vibration Tolerance Tests

6.6.1. Vibration Tolerance Test Setup

One of the concerns for the sonar-based tie deflection measurements are the vibrations induced by the moving test-car on the sensor mounting beam. These vibrations are expected to increase when the speed of the test car is increased. Rigid body translational motion of the sensor mounting beam in the vertical direction is not expected to affect the deflection measurements since that will affect the measurements at all the sensor locations equally and the reference-based deflection measurement will eliminate such variations (bias). However, the elastic deformations caused by the beam vibrations will affect each sensor differently (the magnitude of the deformation will vary at each sensor location) and this will propagate into the final reconstructed 3D deflection profile of the ties. To reduce these dynamic elastic deformations, dampening bolts were used to connect the prototype beam to the cart. The dampening bolts are expected to absorb a significant amount of the energy transferred by the moving cart on the prototype beam. Foam padding material

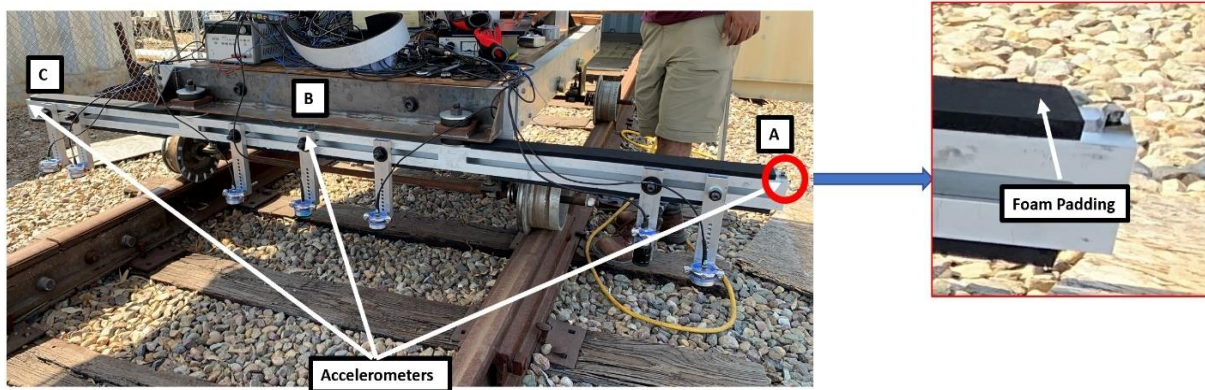


Figure 6.21 Prototype beam with accelerometers and foam padding

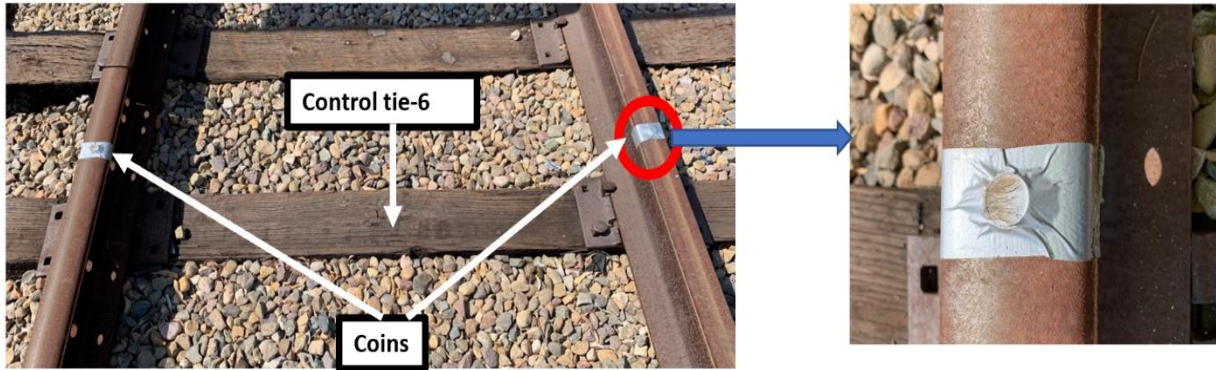


Figure 6.22 Coins placed on both rails at the beginning of control tie-6

was also added on the top and bottom surfaces of the beam (shown in Fig. 6.21) to further absorb the energy of the elastic stress waves propagating through the beam. Three uniaxial accelerometers were placed on the prototype beam to measure vertical acceleration at different locations (shown in Fig. 6.21). Coins were placed on both rails at the beginning of control tie-6 (shown in Fig. 6.22) to induce sudden vertical vibrations. Tests similar to the previous runs were conducted, and acceleration data from all the three accelerometers were recorded during each of the test runs.

6.6.2. 3D Tie Surface Deflection Profiles (With Coin-Induced Vibrations)

6.6.2.1 Control Tie-6

Fig. 6.23 shows the 3D deflection surface profiles of control tie-6 which had the wooden plank of known thickness placed near sensor locations 5 & 6 (discussed previously in Section 6.5.2.2) obtained with and without the coin-induced vibrations. This figure shows that consistent 3D surface deflection profiles were extracted in both cases, indicating that the system is quite robust against the coin-induced vibrations, at least at the walking speed employed for this run. Fig. 6.24 shows the surface profiles along the tie width at sensor locations 5 and 6, again for tests conducted with and without the coin-induced vibrations. Sensor locations 5 & 6 both ‘see’ the

wooden plank of known thickness, showing a rise in surface elevation matching the “true” thickness of the plank (~19 mm). Fig. 6.24 confirms that the coin-induced vibrations do not adversely affect the tie deflection measurements, since the thickness of the wooden plank is still identified accurately.

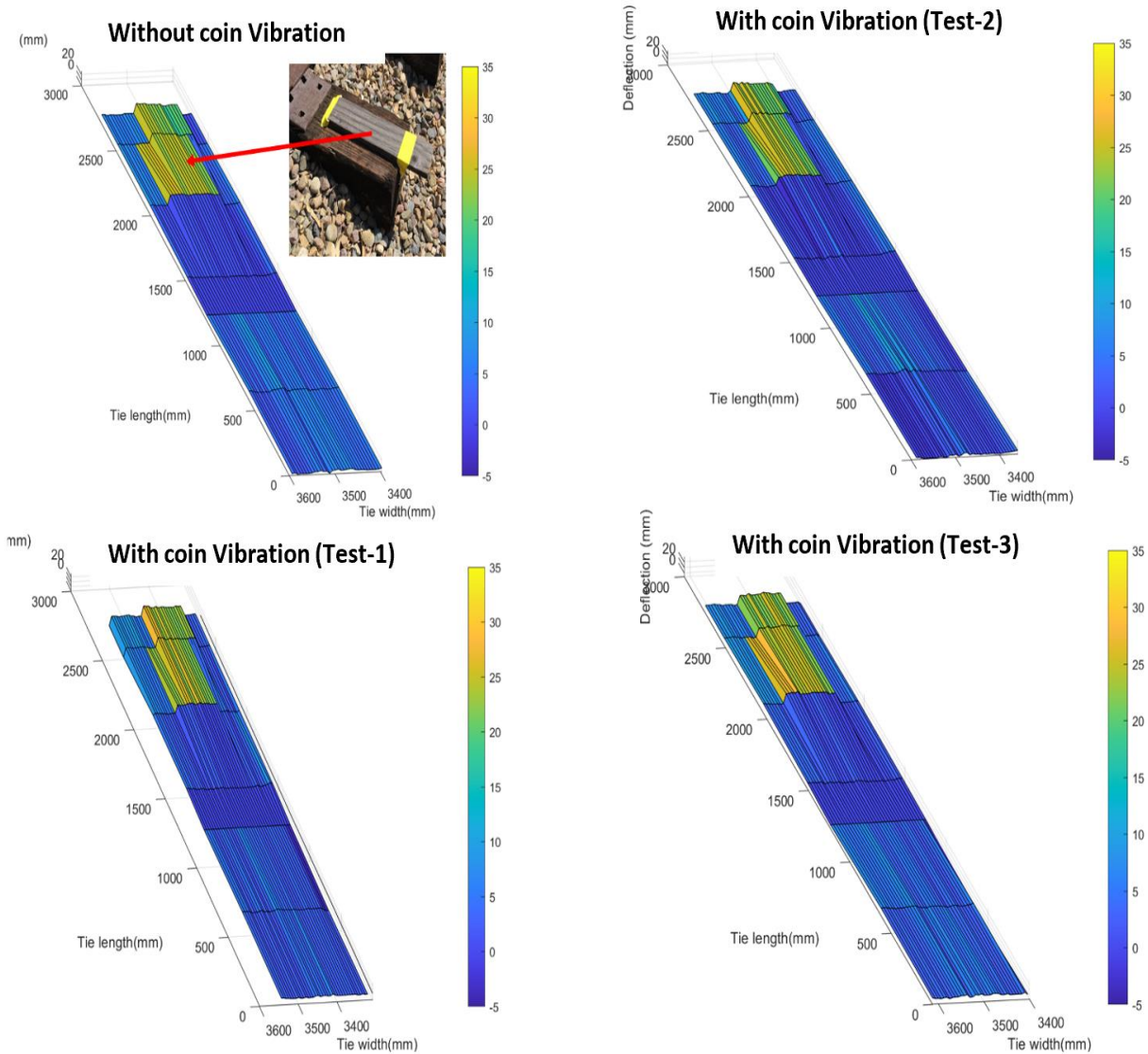


Figure 6.23 3D surface deflection profiles of control tie-6 with and without the coin-induced vibrations

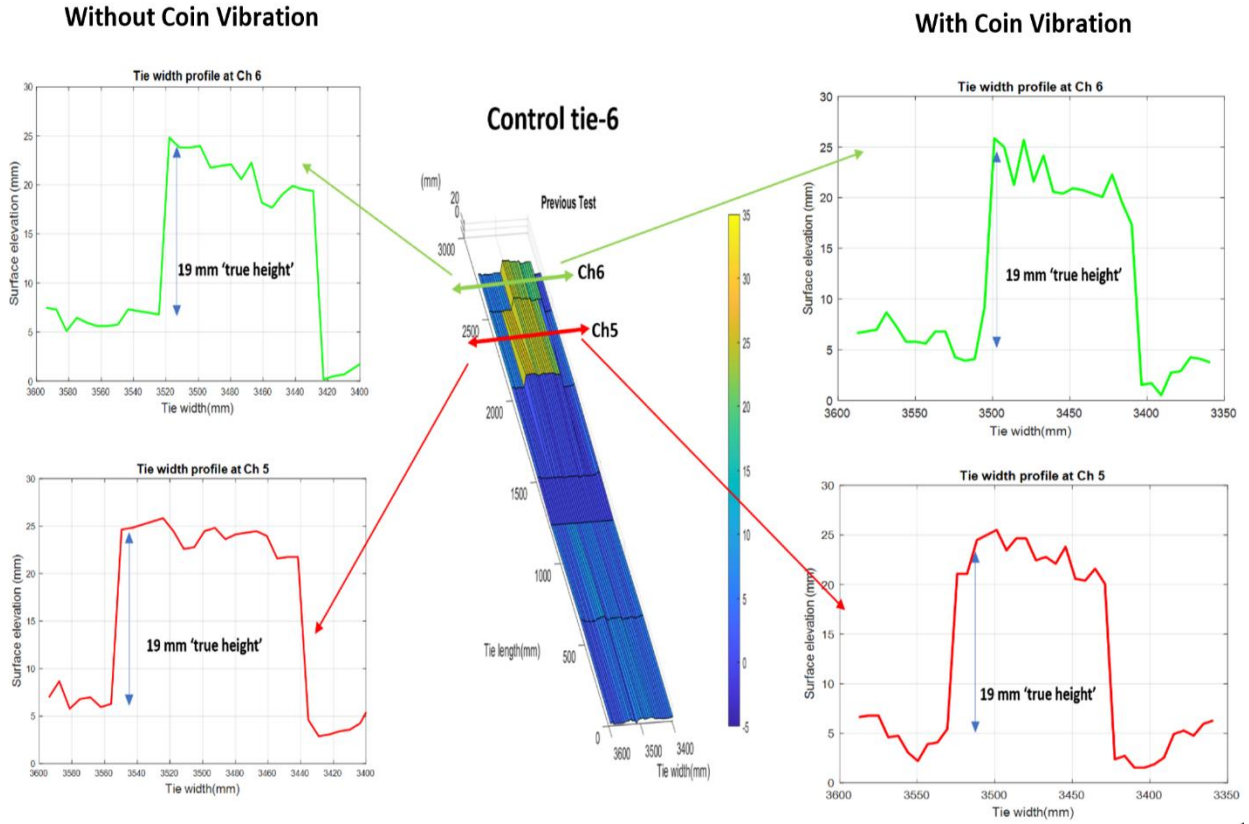


Figure 6.24 Surface elevation profiles along the width at sensor locations 5 & 6 with and without the coin-induced vibrations

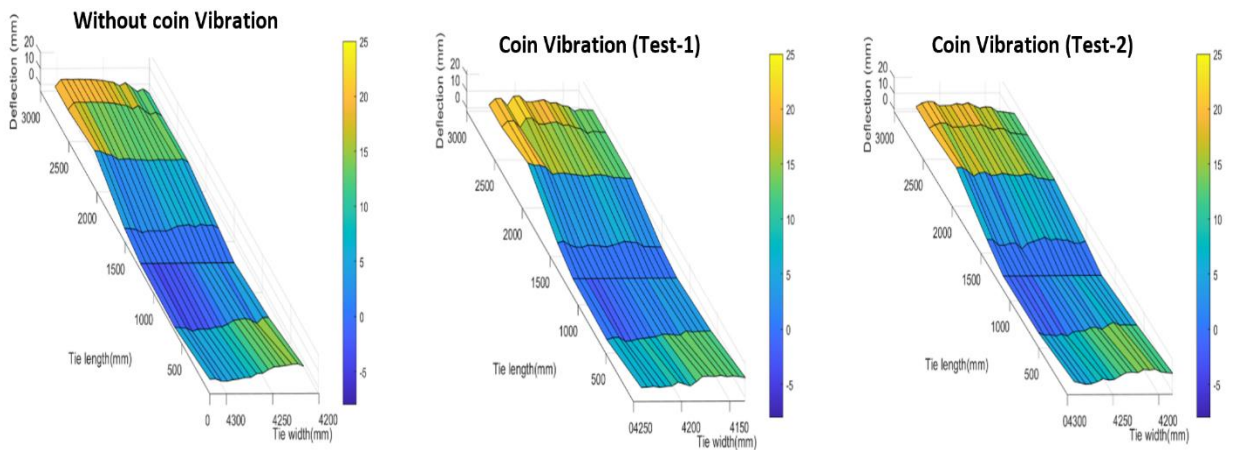


Figure 6.25 3D surface deflection profiles of tie-7 with and without the coin-induced vibrations (Top View)

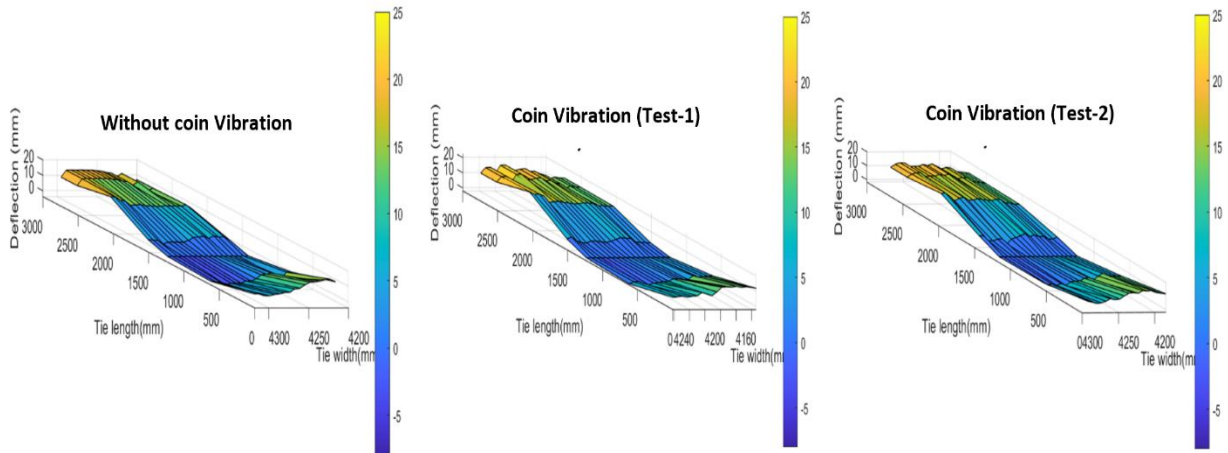


Figure 6.26 3D surface deflection profiles of tie-7 with and without the coin-induced vibrations (Elevation View)

6.6.2.2 Tie-7

To verify if the results of another tie were affected by the coin-induced vibrations, 3D surface profiles of tie-7 are presented here. Fig. 6.25 shows the 3D surface deflection profiles of tie-7 with and without the vibrations. Again, compared to the baseline measurement without

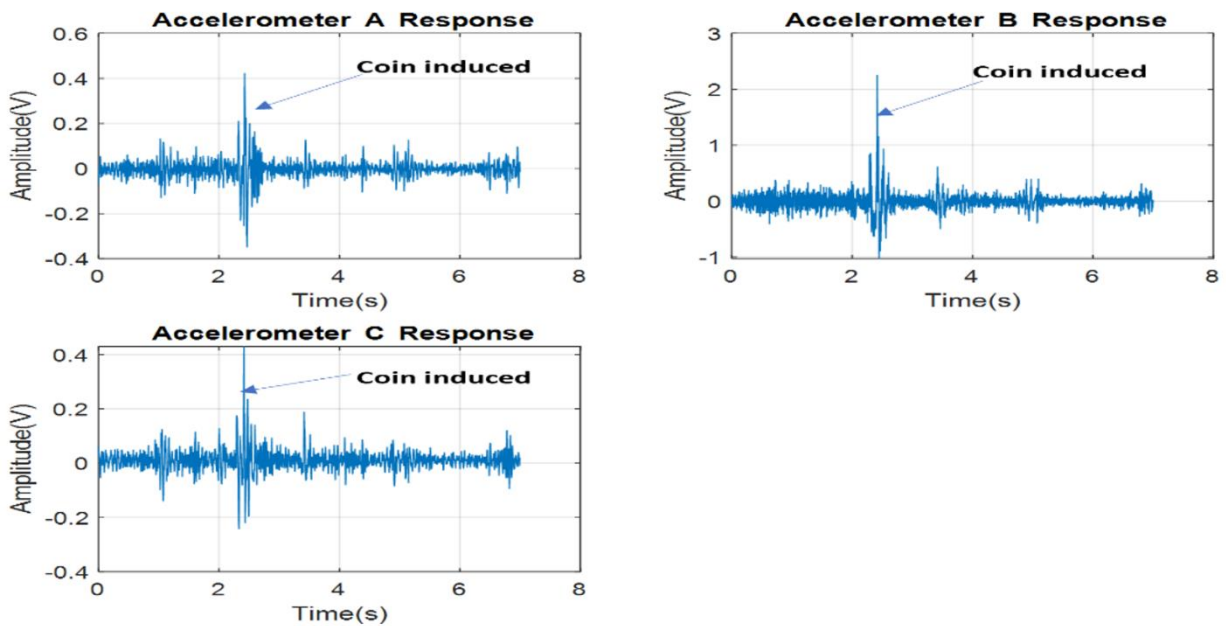


Figure 6.27 Acceleration time-histories from test-run 1 truncated to 8s

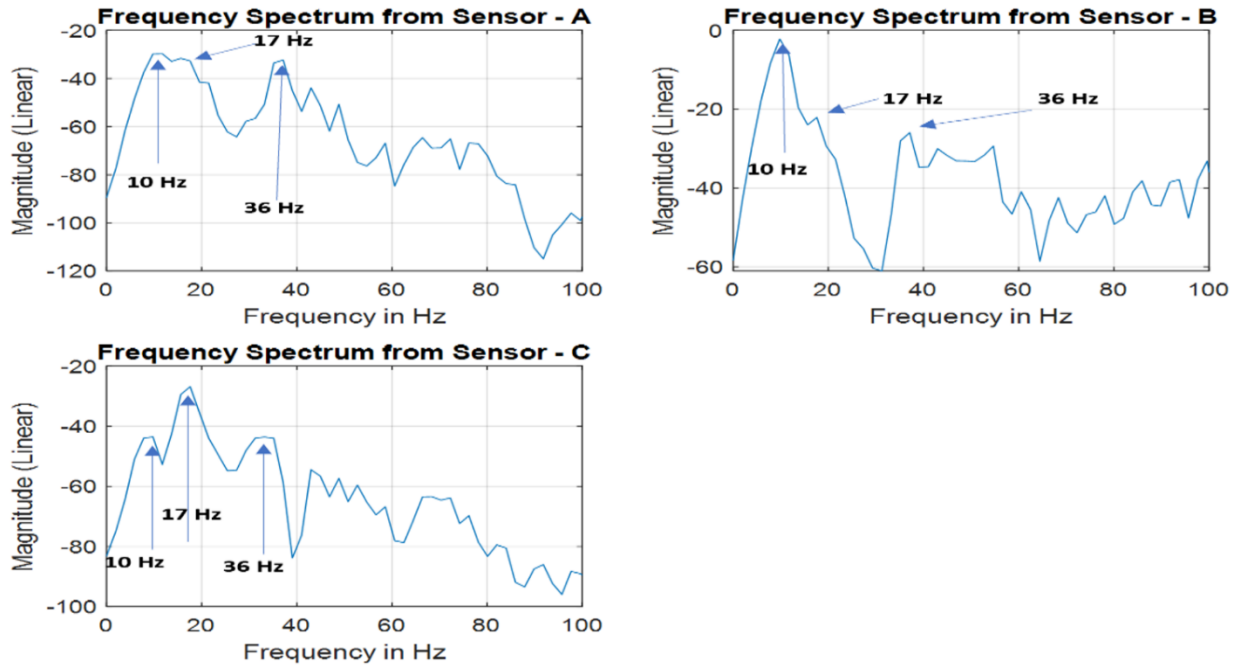


Figure 6.28 Frequency spectrum of acceleration responses

vibrations, the 3D profiles with vibrations are found to closely match. Fig. 6.26 shows another view of the tie-7 deflections showing the consistency in deflected shapes for all 3 tests (with and without the vibrations).

6.6.3. Resonance Frequency Identification

Fig. 6.27 shows the acceleration time-histories of all three accelerometers truncated to 8s of recording length. The instant the test-cart goes over the coins can be seen as a spike in the acceleration amplitude. Fig. 6.28 shows the respective frequency spectrums of the time-histories obtained by Welch's periodogram method [14-15] along with a Hamming window on each snapshot. Signal processing routines such as mean-subtraction, down-sampling with anti-aliasing Chebyshev filters, low-pass Butterworth 6th order filtering with a cut-off frequency of 250 Hz were used. Resonant frequencies appear as peaks in the frequency spectrum plots at frequency values

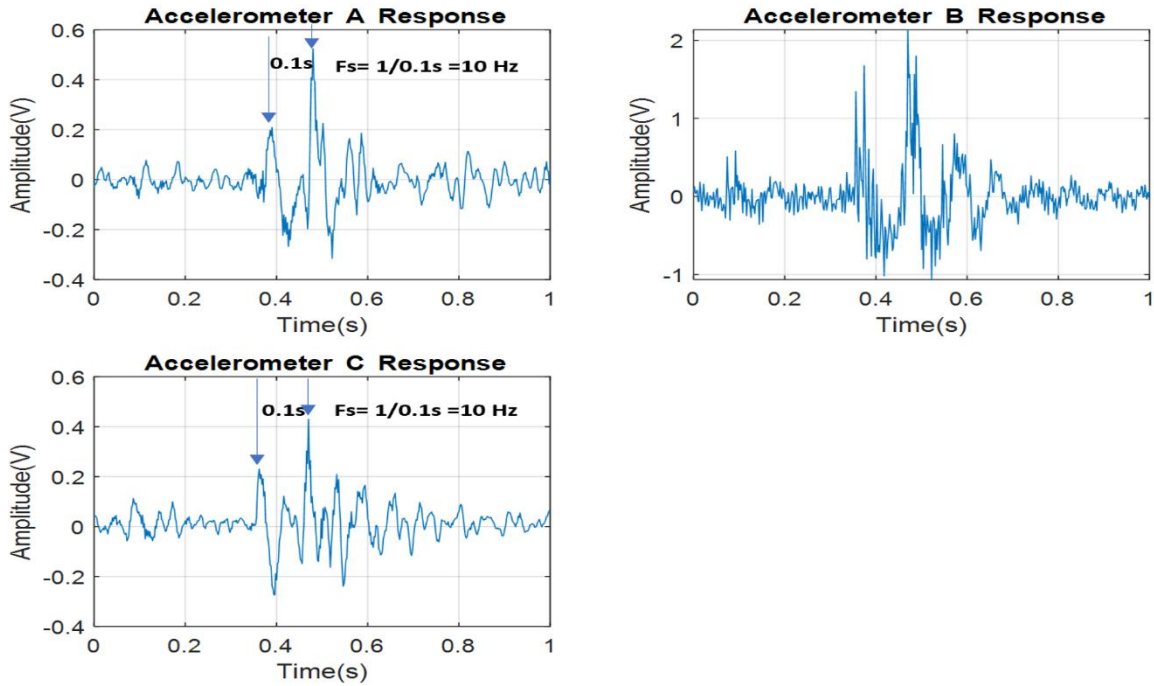


Figure 6.29 Acceleration time-histories from test-run 2 truncated to 1s

of 10 Hz, 17 Hz and 36 Hz. Fig. 6.29 shows the acceleration time-histories from another test run truncated at 1s recording length. An output-only stochastic subspace identification [16-19] technique with different model orders was used to determine the natural frequencies of the prototype beam. A stabilization plot was constructed, using stochastic subspace identification to

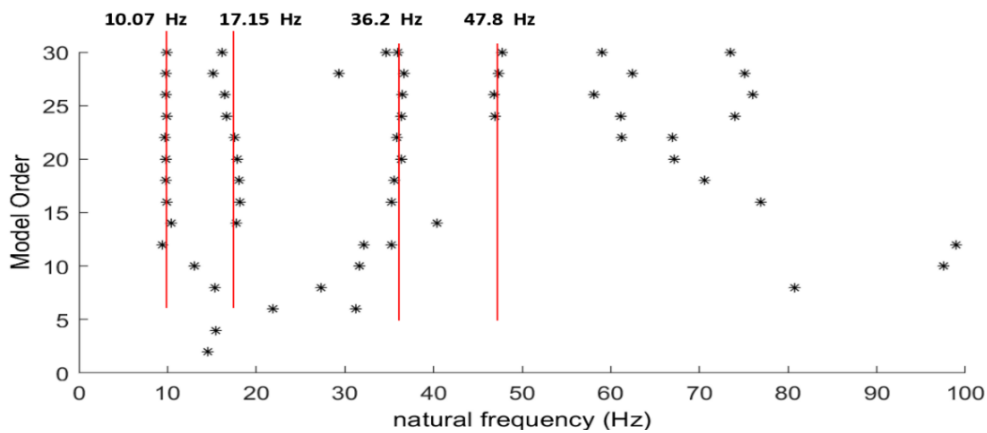


Figure 6.30 Stabilization plot from stochastic subspace system identification

identify frequencies repeating for different model orders as shown in Fig. 6.30. Table 6.2 shows the natural frequencies and the damping ratios for the first three modes. This method confirmed the resonant frequencies of 10 Hz, 17 Hz and 36 Hz for the mounting beam.

Table 6.2 Identified natural frequencies and damping ratios

Mode	1	2	3
Natural Frequency	10.07 Hz	17.15 Hz	36.2 Hz
Damping Ratio	0.18	0.07	0.12

6.7. Conclusions

This chapter discusses the tie-sonar prototype designed for testing on a moving cart at UCSD’s Rail Defect Testing Facility. The various components of the prototype are first described, along with key signal processing routines utilized to extract the time-of-flight measurements from the airborne acoustic signals. It is explained how the system is able to compute 3D tie deflection measurements (i.e. vertical deflections and twisting of the ties) in a completely non-contact manner (the recommended 3in sensor clearance envelope from the top of the rail is amply satisfied). The ability to extract 3D tie deflections is expected to greatly improve the identification of adverse rail support conditions (e.g., tie center binding), hence improving rail safety.

In the first set of tests at the Rail Testing Facility, five independent runs were conducted at sustained walking speed for a total of nine ties scanned during each run. The tie deflections were computed using a time-of-flight tracking algorithm using a cross-correlation operator. Acoustic

signal strength and an artificial intelligence-based image classification were used as two independent methods to distinguish between ties and ballast.

The results from these tests seem to confirm the ability for the system to compute 3D tie deflection profiles at walking speeds. The use of a reference transducer provided an adaptive baseline which made deflection measurements independent of variabilities in lift-off distances from the tie surface (absolute tie deflections). The speed of testing allowed for approximately 28 measurement locations with a resolution of 0.25-inch along the width of each tie. At higher revenue speeds (~ 60 mph) this resolution is of course expected be coarser, with approximately five measurements (resolution of 1.4-inch) expected across each tie width. This resolution should still give useful information on tie twisting (besides the tie vertical deflections, whose resolution is only controlled by the number of transducers used along the mounting beam). One of the 9 ties could not be detected based on signal-based classification, possibly because of a misalignment of the specific tie with respect to the transducer array that prevented the reflected signals from this tie to reach multiple transducers simultaneously. Different signal controls, including an adaptive signal strength threshold, could be considered in the future to further improve the tie identification process. The image-based classification was able to detect this tie. Hence the image-based tie vs. ballast classification could be used in the future to complement the signal-based classification method.

The tests also included a validation process for the precision of the tie distance positions extracted from the airborne signals. For this purpose, a wood plank of known height (“control” point) was positioned on one of the ties. The airborne signals were able to correctly “see” this control point with a distance measurement that closely matched the “true” distance. This test gave

great confidence on the ability of this system to extract accurate 3D deflection information for the ties.

One of the potential challenges of any non-contact rail sensing system is the tolerance to vibrations. To address this aspect, dynamic tests were conducted on the test platform. Specifically, coins were installed on both rails prior to the “control” point tie to induce a sudden “jump” of the cart (impulse vibration). Accelerometers placed on the mounting beam and two different dynamic characterization algorithms identified resonance frequencies of this beam to be 10 Hz, 17 Hz and 36 Hz. This information will be useful for any future installation of this beam on a train moving at higher speed. More importantly, the tie deflection measurements extracted at the “control” tie with the coin-induced vibrations matched closely with those extracted previously without the coin-induced vibration. This result confirmed the good tolerance of the designed prototype to vibrations, at least at the walking speeds utilized for this set of tests.

6.8. Acknowledgements

This work was funded by the US Federal Railroad Administration under contract 693JJ619C000019 with Mr. Cameron Stuart as the Program Manager.

Chapter 6, in part, has been published in the following paper: **Datta, D.**, Hosseinzadeh, A. Z., Cui, R., & Lanza di Scalea, F. (2023). High-Speed 3D Railroad Tie Deflection Mapping in Real-Time Using an Array of Air-Coupled Non-contact Transducers. *Lecture Notes in Civil Engineering*, 254 LNCE, 895–904. The dissertation author was the primary investigator and author of this paper.

6.9. References

- [1] Yoo, J. C., & Han, T. H. (2009). Fast normalized cross-correlation. *Circuits, Systems and Signal Processing*, 28(6), 819–843. <https://doi.org/10.1007/S00034-009-9130-7>
- [2] Tsai, D. M., & Lin, C. T. (2003). Fast normalized cross correlation for defect detection. *Pattern Recognit. Lett.*, 24(15), 2625–2631. [https://doi.org/10.1016/s0167-8655\(03\)00106-5](https://doi.org/10.1016/s0167-8655(03)00106-5)
- [3] Chapelle, O., Haffner, P., & Vapnik, V. N. (1999). Support vector machines for histogram-based image classification. *IEEE Transactions on Neural Networks*, 10(5), 1055–1064. <https://doi.org/10.1109/72.788646>
- [4] Foody, G. M., & Mathur, A. (2004). A relative evaluation of multiclass image classification by support vector machines. *IEEE Transactions on Geoscience and Remote Sensing*, 42(6), 1335–1343. <https://doi.org/10.1109/TGRS.2004.827257>
- [5] Okwuashi, O., & Ndehedehe, C. E. (2020). Deep support vector machine for hyperspectral image classification. *Pattern Recognition*, 103, 107298. <https://doi.org/10.1016/J.PATCOG.2020.107298>
- [6] Cervantes, J., Garcia-Lamont, F., Rodríguez-Mazahua, L., & Lopez, A. (2020). A comprehensive survey on support vector machine classification: applications, challenges and trends. *Neurocomputing*, 408, 189–215. <https://doi.org/10.1016/J.NEUCOM.2019.10.118>
- [7] Negri, R. G., Dutra, L. V., & Sant’Anna, S. J. S. (2014). An innovative support vector machine based method for contextual image classification. *ISPRS Journal of Photogrammetry and Remote Sensing*, 87, 241–248. <https://doi.org/10.1016/J.ISPRSJPRS.2013.11.004>
- [8] Tomasi, C., Kanade, T. (1991). Detection and tracking of point features, *Technical Report Carnegie Mellon University*, CMU-CS-91-132.
- [9] Trummer, M., Denzler, J., & Munkelt, C. (2009). Guided KLT tracking using camera parameters in consideration of uncertainty. *Communications in Computer and Information Science*, 24, 252–261. https://doi.org/10.1007/978-3-642-10226-4_20/COVER
- [10] Kim, H., Cho, J., Jung, Y., Lee, S., & Jung, Y. (2020). Area-efficient vision-based feature tracker for autonomous hovering of unmanned aerial vehicle. *Electronics*, 9(10), 1591. <https://doi.org/10.3390/ELECTRONICS9101591>
- [11] Trummer, M., Denzler, J., & Munkelt, C. (2009). Guided KLT tracking using camera parameters in consideration of uncertainty. *Communications in Computer and Information Science*, 24, 252–261. https://doi.org/10.1007/978-3-642-10226-4_20/COVER
- [12] Baker, S., & Matthews, I. (2004). Lucas-Kanade 20 years on: A unifying framework. *International Journal of Computer Vision*, 56(3), 221–255. <https://doi.org/10.1023/B:VISI.0000011205.11775.FD>

- [13] Bay, H., Ess, A., Tuytelaars, T., & Van Gool, L. (2008). Speeded-Up Robust Features (SURF). *Computer Vision and Image Understanding*, 110(3), 346–359. <https://doi.org/10.1016/J.CVIU.2007.09.014>
- [14] Same, M. H., Gandubert, G., Gleeton, G., Ivanov, P., & Landry, R. (2020). Simplified welch algorithm for spectrum monitoring. *Applied Sciences*, 11(1), 86. <https://doi.org/10.3390/APP11010086>
- [15] Jin, X., Wang, Y., & Hong, W. (2019). Power Spectrum Estimation Method Based on Matlab. *ACM International Conference Proceeding Series*. <https://doi.org/10.1145/3387168.3387223>
- [16] Datta, D., & Dutta, A. (2017). Comparison of black and gray box models of subspace identification under support excitations. *Structural Monitoring and Maintenance*, 4(4), 365–379. <https://doi.org/10.12989/SMM.2017.4.4.365>
- [17] Kim, J., & Lynch, J. P. (2012). Subspace system identification of support-excited structures-part I: Theory and black-box system identification. *Earthquake Engineering and Structural Dynamics*, 41(15), 2235–2251. <https://doi.org/10.1002/EQE.2184>
- [18] Kim, J., & Lynch, J. P. (2012). Subspace system identification of support excited structures-part II: Gray-box interpretations and damage detection. *Earthquake Engineering and Structural Dynamics*, 41(15), 2253–2271. <https://doi.org/10.1002/EQE.2185>
- [19] Van Overschee, P., & De Moor, B. (1994). N4SID: Subspace algorithms for the identification of combined deterministic-stochastic systems. *Automatica*, 30(1), 75–93. [https://doi.org/10.1016/0005-1098\(94\)90230-5](https://doi.org/10.1016/0005-1098(94)90230-5)

Chapter 7. In-Motion Full-Field Railroad Crosstie Deflection Measurements (Full-Scale Field Tests)

7.1. Introduction

This chapter discusses the field tests that were performed at a BNSF yard in San Diego by mounting the sonar-based deflection measurement prototype [1-5] on a loaded gas tank train car at walking test speeds. The data-acquisition system used for this test was similar to the tests conducted at the Rail Defect Testing Facility (RDTF) (discussed in Chapter 6) with three changes. First, a gasoline-operated electric generator was used to power the instrumentation. Second, the encoder was eliminated and to track the spatial locations along the tie-width, camera images were

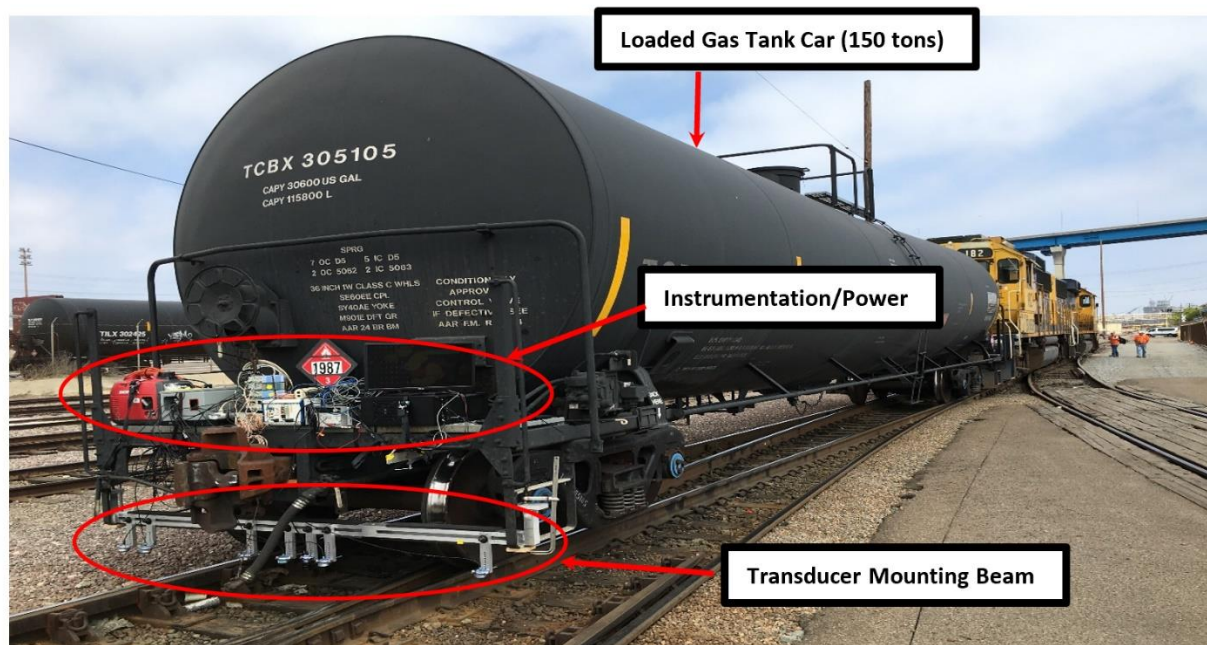


Figure 7.1 Test setup at the BNSF test yard in San Diego

used and is discussed in section 7.4 of this chapter. Third, the location of the camera was shifted near the center of the prototype beam. The data-acquisition system was programmed to trigger deflection measurements at a constant pulse repetition rate of 100 Hz. The mounted system is shown in Fig. 7.1. The system was mounted on a loaded gas tank car with a total load of 150 tons and 75 tons on each axle.

7.2. Test Procedure

Test runs were performed at walking speeds (~ 5 mph) over a tangent section of track with wood ties. For each test run, scanning of ties started from the center of the first tie until the center of the last tie. A total of 150 ties were scanned during each test run. Data acquisition was stopped after the last tie was scanned, and the train was brought back to the first tie to begin the next test run. A total of 4 test runs were performed and the same ties were scanned during each test run. Due to different mounting conditions, the average distance between the transducer to the tie surface (lift-off distance) for these tests was around 15 inches which was higher than the average distance

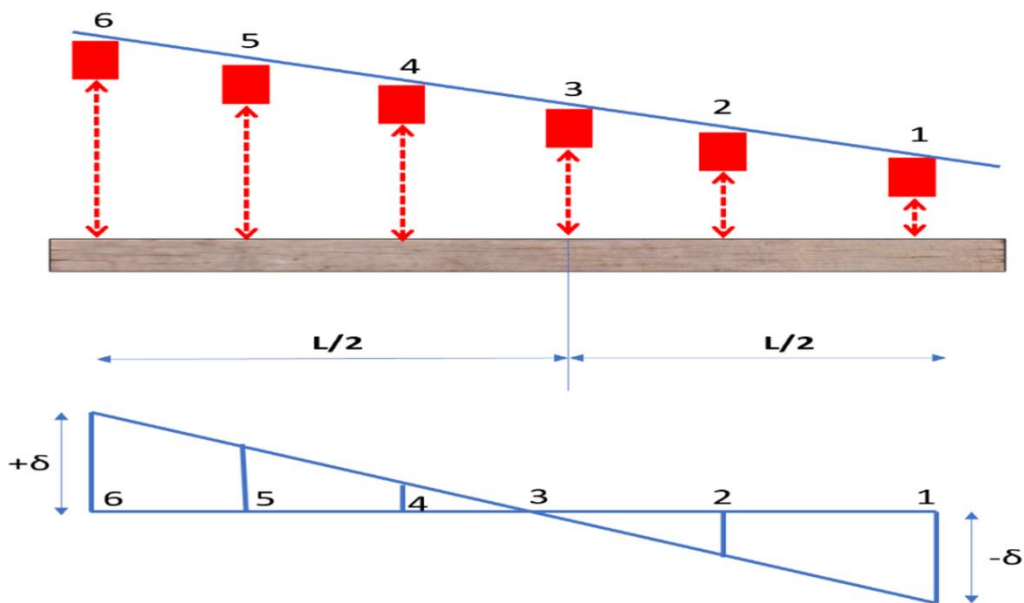


Figure 7.2 Bias removal from tie deflection measurements

for the RDTF tests (11 inches). Despite the higher lift-off distance, the strength of the reflected waveform was still found to be high enough for stable deflection measurements.

7.3. Bias Removal from Computed Deflections

One concern that was observed during the BNSF tests was some misalignment of the transducer beam that introduced some bias in the deflection measurements. This type of misalignment occurred because the transducer on one end of the beam was sitting lower than the transducer at the other end of the beam. Fig. 7.2 the schematic of the issue. Fig. 7.2 shows that transducer 1 on one end of the beam sits lower than transducer 6 on the other end because the transducer mounting beam is not perfectly horizontal. Such an arrangement produces some spurious deflections even if the tie is perfectly straight as shown in Fig. 7.2 with transducer 1 measuring a deflection in the downward direction ($-\delta$) and transducer 6 measuring a deflection in the upward direction ($+\delta$). Similarly, the deflections at transducer locations 2, 4, 5 are also off and a linear variation of spurious deflections is observed. The magnitude of bias (δ) at transducer locations 1 and 6 is the same because they are equidistant from the center of the mounting beam where the reference transducer is located (location 3). To remove the bias, the average difference in deflections at transducer locations 1 and 6 was computed over several different ties and this computed value in the average sense would converge to 2δ (assuming the two ends of the tie would be at the same level in an averaged sense over a number of ties). Once the magnitude of the bias is determined at the two ends of the beam (δ), a bias negating value is added to each transducer deflection measurement to effectively remove the bias. For example, the bias negative value at locations 1 and 6 would be $+\delta$ and $-\delta$ respectively. The bias negating values at locations 2, 4, 5 can be determined from similarity of triangles since the distances between transducer locations is

known. All results presented in the subsequent sections include the bias removal technique discussed here.

7.4. Image Processing for Spatial Location Along Tie Width and Tie Boundary Demarcation

A high frame-rate camera was used to capture images during the test run. By processing the captured images, two main goals were achieved. First, the travel distance was extracted to determine the spatial resolution required in visualizing the obtained results from signal-based tie condition assessment. Second, a machine learning-based object classification was performed to supplement the signal-based tie-ballast discrimination.

7.4.1. Extracting the Travel Distance by Image Analysis

7.4.1.1 Converting Pixel Domain to Physical Domain

Since the measurements extracted by image inspection are in the pixel domain, a mapping factor is required to convert the measurements into the physical length domain. The mapping factor is calculated through a calibration study. For this purpose, the width of the first four ties were measured in the field. Next, inspecting the images captured by the camera, one which covers end-to-end edges of the corresponding tie was selected and using thresholding techniques, a purified and polished grey-scale version of the image was reproduced, in which the edges of the ties can be clearly identified (see Fig. 7.3). Note that since the camera was rotated by 45° to put in the holder, the images were rotated back by -45° before analysis to have the ties in an orientation parallel to the local horizontal axis of the field of view. Selecting one point on the lower edge and one point on the upper edge of the given tie, a straight line (parallel to the local horizontal axis of the image) was fitted through, and the distance between the two lines was computed to represent

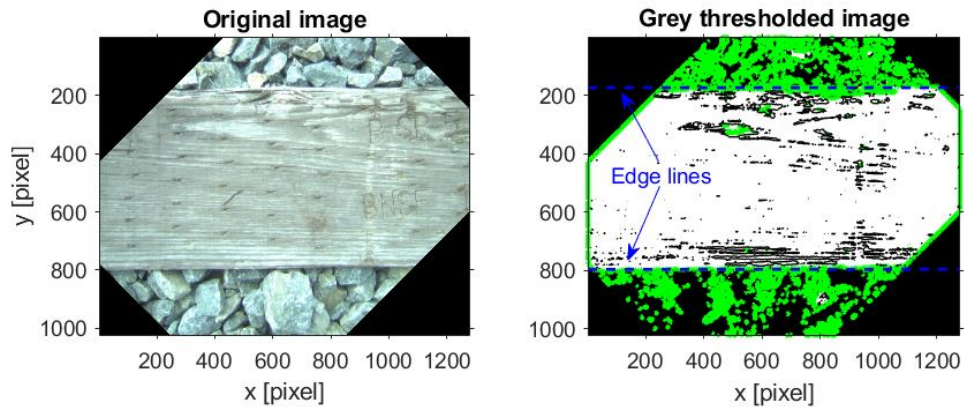


Figure 7.3 Estimation of the tie's width in the pixel domain

the width of the tie in the pixel domain (see Fig. 7.3). The procedure was repeated three times for each tie by selecting different sets of points on the edges and the average of the pixel-domain widths was used to calculate the mapping factor. Equivalency between the in-situ measurements and pixel-domain estimations of the ties' width revealed that each pixel is equal to 0.0130 inch.

7.4.1.2 Estimating Travel Distance Between Two Consecutive Images

The travel distance between two successive images can reveal the spatial resolution of the probing system. The details of the technique used to estimate the travel distance are explained herein. In a laboratory-scale preliminary investigation, it was revealed that by setting the camera's specifications to capture and save images with a steady rate of 100 frames per second, a considerable number of the frames are missed because of buffer size issues. In such a condition, although the repurposed footage can be smooth enough due to the overlap between the saved frames, lowering the number of the missed frames is preferred to maximize the details extracted from the images. By optimizing the camera's specifications to reach the optimal and timely buffer release, missed frames were observed in a one-in-between (i.e., alternate) scheme. This configuration was used in the present study, which is beneficial in terms of retrieving the missing

frames, which is discussed in the next subsection. To estimate the travel distance between two successive saved images, a relatively wide inspection region was selected in each frame and the Speeded-Up Robust Features (SURF) algorithm [6] was used to find blob features in each frame. The robust trackable points were automatically selected and tracked by Kanade-Lucas-Tomasi (KLT) tracker algorithm [7] through the next available frame. Because of the relatively wide inspection region, many robust features were selected and tracked; however, some of them are recognized as invalid points in meeting the track reliability criteria. Missing of the tracked point in the successive frame due to its new position somewhere out of the defined inspection region is one of the main reasons that makes a track invalid. Such points were automatically detected and removed from the analyses. Moreover, an outlier analysis was performed on the reported pixel-domain relative travel distances to reach a set of homogeneous data. Note that dislocating the robust features because of local oscillation and sudden change in either the natural light or lens's focus can add outliers to the data. Eventually, the average of the pixel-domain travel distances

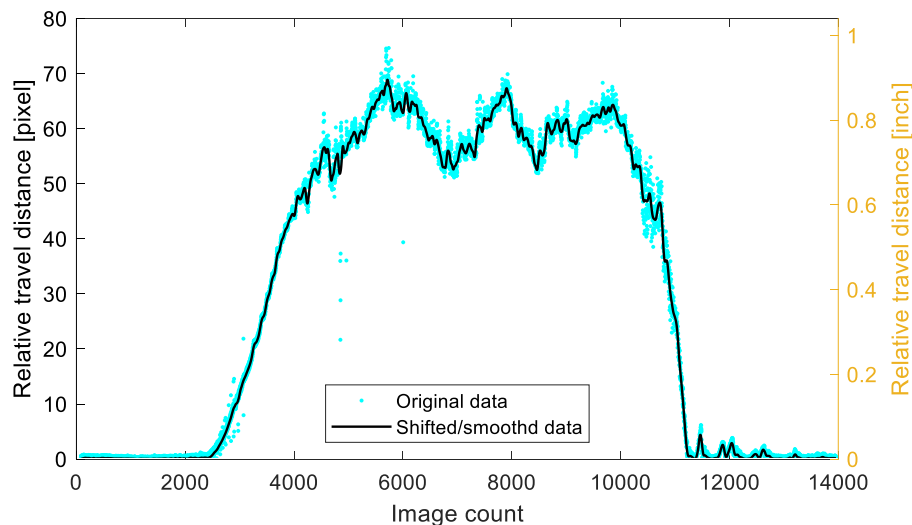


Figure 7.4 Relative travel distance for test #2. Each data point represents the relative travel distance of the corresponding image count with respect to the previous image count.

reported by the tracked features was computed as the travel distance between two successive saved frames. Repeating this procedure for all the existing frames, the “relative” displacement between two saved images was achieved, as shown in Fig. 7.4 for test #2. Some local oscillations in the reported relative displacements are observed, which are because of the camera’s “ego-motion” induced by the rigid body-type vibration of the prototype beam. To mitigate this issue, a data-smoothing technique based on local regression (using weighted linear least squares and a 2nd degree polynomial model) was employed and a curve was fitted to the data. Moreover, a baseline shift was applied to the fitted curve to decline the low-level oscillations during initial waiting time, before the train starts to move.

7.4.1.3 Retrieving Region of Interest for Missed Frames

The Region of Interest (ROI) is defined as a circle with a diameter of 3.9 cm, which is equivalent to the effective area probed by the transducer. In the saved images, the ROI is isolated by placing a circle with an equivalent diameter of 118.11 pixels at the center of the images. Considerable overlap between the successive saved images as well as the one-in-between scheme of the missed frames gives insights to retrieve the ROI of the missed frames from the saved images. For this purpose, a “forward/backward inspection” technique was proposed to find the center of the circle representing the ROIs associated with the missed frames. A linear interpolation was applied to the pixel-domain relative travel distances to find the point on the last saved image (i.e., the image right before the missed image) that the center of the missed ROI should be placed there. The accuracy of the retrieved ROI is doublechecked through a backward inspection approach: On the first saved image next to the missed frame, a template ROI was gradually slipped back in a direction against the train movement direction to make the candidates for the missed ROIs. Then, the Structural Similarity Index (SSIM) [8] between the retrieved and candidate ROIs was

computed. If SSIM is greater than 90% for a candidate ROI, a complete similarity between the retrieved ROI and the candidate ROI is reported. A further calculation was also carried out to check if the estimated relative travel distance between the centers of the retrieved and the next available ROIs matches with the corresponding portion of the travel distance adapted from linear interpolation-based analysis. Employing the mentioned forward/backward inspection, all the missed ROIs were retrieved. The backward inspection-based analysis revealed that the linear interpolation employed in the forward inspection-based is an acceptable assumption to retrieve the missed ROIs.

7.4.2. Machine Learning-Based Tie-Ballast Classification

The machine learning-based image classification approach to tie/ballast image discrimination was introduced in Chapter 6. Herein, this approach is used for image classification in the tests conducted at BNSF yard. The classification is based on texture analysis of the objects observed in the ROIs. Sample images of the ROIs (containing ties and ballasts) are randomly selected among all the images and the identifier is trained using Support Vector Machine (SVM) method. In the present study, 65 images of the ties and 65 images of the ballasts were used to train and test the identifier. In total, 106560 features were extracted for each category (i.e., ties and ballasts) using the Bag-of-Words (BoW) texture analysis technique, and 80% of the strongest features for each category was selected to make 500 visual words using K-Means clustering approach. Feeding the histogram of the visual words into the SVM core, the identifier was trained. The kernel option of the SVM was enabled to ensure that the outliers are removed from the samples sorted for the training step. The confusion matrix of the evaluation process for the test set of the randomly selected images returned an accuracy of 95% for the trained identifier. In the next step, the identifier was used to classify tie/ballast images. A complete set of ROIs, (17966 and 13879

images for tests #1 and 4, respectively (including the retrieved ROIs)), were recalled and the identified class was reported as the output of the system. Fig. 7.5 shows the obtained tie/ballast classification results (plotted on the image processing-based reconstructed travel distance) for test run 1. There were ~150 ties in the tested path and all were correctly identified by the trained system. Note that in Fig. 7.5, the travel distance has been plotted as a function of image count. Therefore, for a given image count, the cumulative travel distance (with respect to the start point) can be extracted by checking the corresponding point on the vertical axes and accordingly, the object observed in that location is identified. The white strips between the identified ties represent the segments classified as ballast.

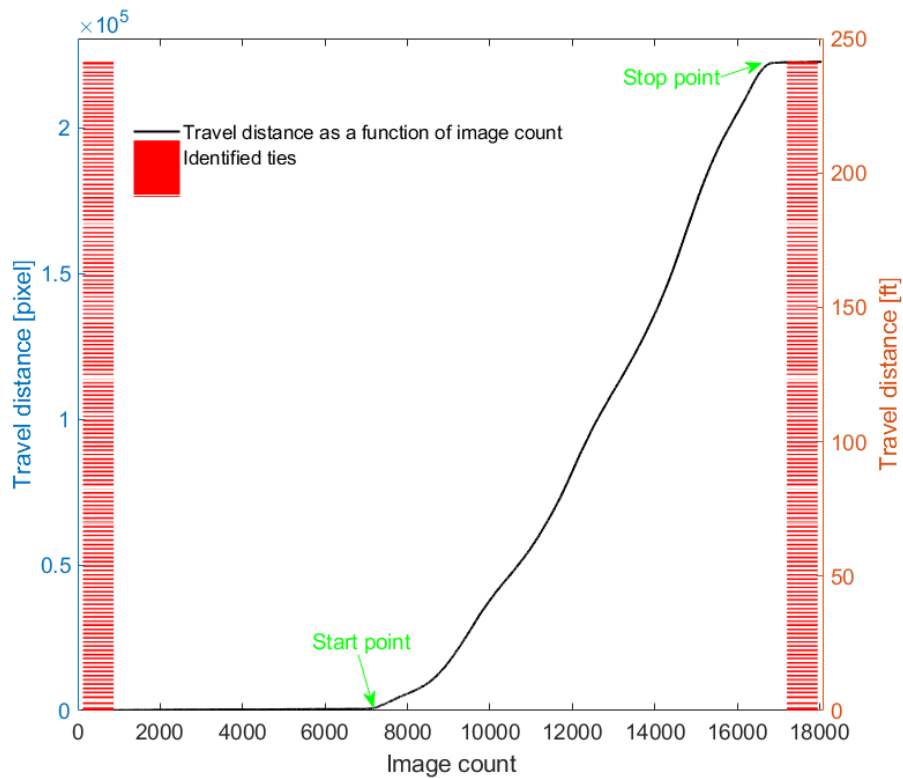


Figure 7.5 Image-based reconstructed travel distance and the obtained tie/ballast image classification results for test #1.

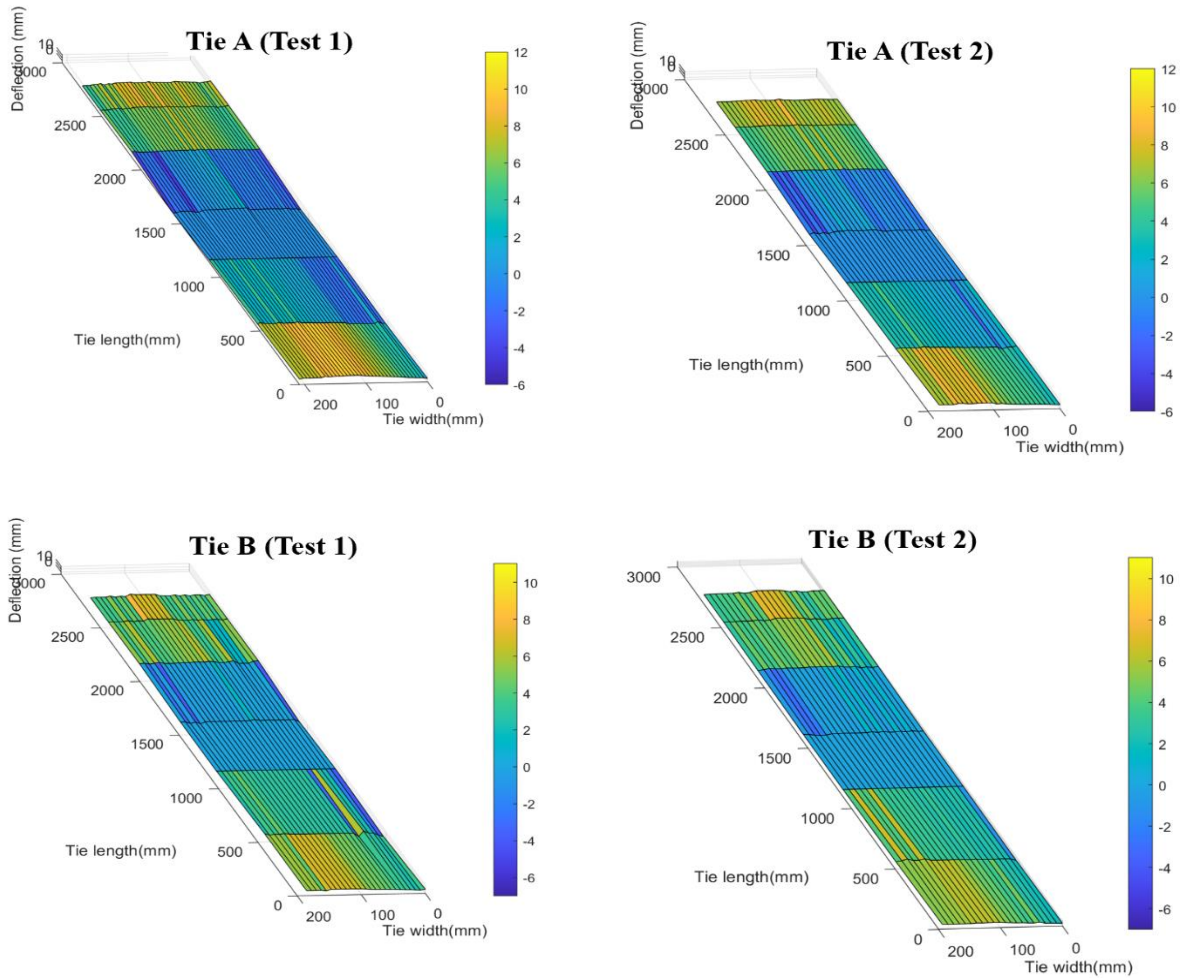


Figure 7.6 3D deflection profiles for two different ties in two independent test runs

7.5. Results

7.5.1. 3D Tie Deflection Profiles

Signal processing routines as outlined in Chapter 5 were used to compute the tie surface deflection profiles. Fig. 7.6 shows the 3D tie deflection profile for two ties (A & B) for two different independent test runs.

Fig. 7.7 shows the 3D tie deflection profiles of 9 ties scanned during one of the test runs. The white regions in some of the ties indicate missed points where sufficient signal strength was

not achieved at all six transducers and therefore reliable measurements could not be obtained. The consistency in the reconstructed 3D profiles of the same tie for two different runs can be observed indicating that the deflection measurements are reasonably precise.

Fig. 7.8 shows the longitudinal and transverse (twisting) deflections for three ties in one test run with the deflections scaled by 20x for better visualization. From Fig. 7.8 it is clear that both longitudinal deflections and tie cross-sectional twisting deformations can be obtained due to multiple measurements from different areas of the tie. It must be noted that walking test speeds allows a larger number of measurements along the tie width and fewer locations might be probed at higher testing speeds.

7.5.2. Displacement Accuracy Verification

A wooden block of known thickness was placed on one of the ties (control tie) in a way such that only transducer-1 would scan the plank. Fig. 7.9 shows the block placed on the tie. Fig. 7.10 shows the 3D tie surface deflection for the control tie with the wood block. The wood block can be seen in the influence region of transducer-1 as an increase in surface elevation. Fig. 7.11 shows the tie width profile at transducer-1 with the block appearing as a rise in the surface elevation over the width with respect to the baseline and again falling to baseline after transducer-1 completes scanning the block. The apparent tapering of the wood block across the influence zone of transducer-1 (Ch1) in Fig. 7.10 is an artefact produced by the linear interpolation performed between two transducer deflections to ensure continuity of the longitudinal deflection profile.

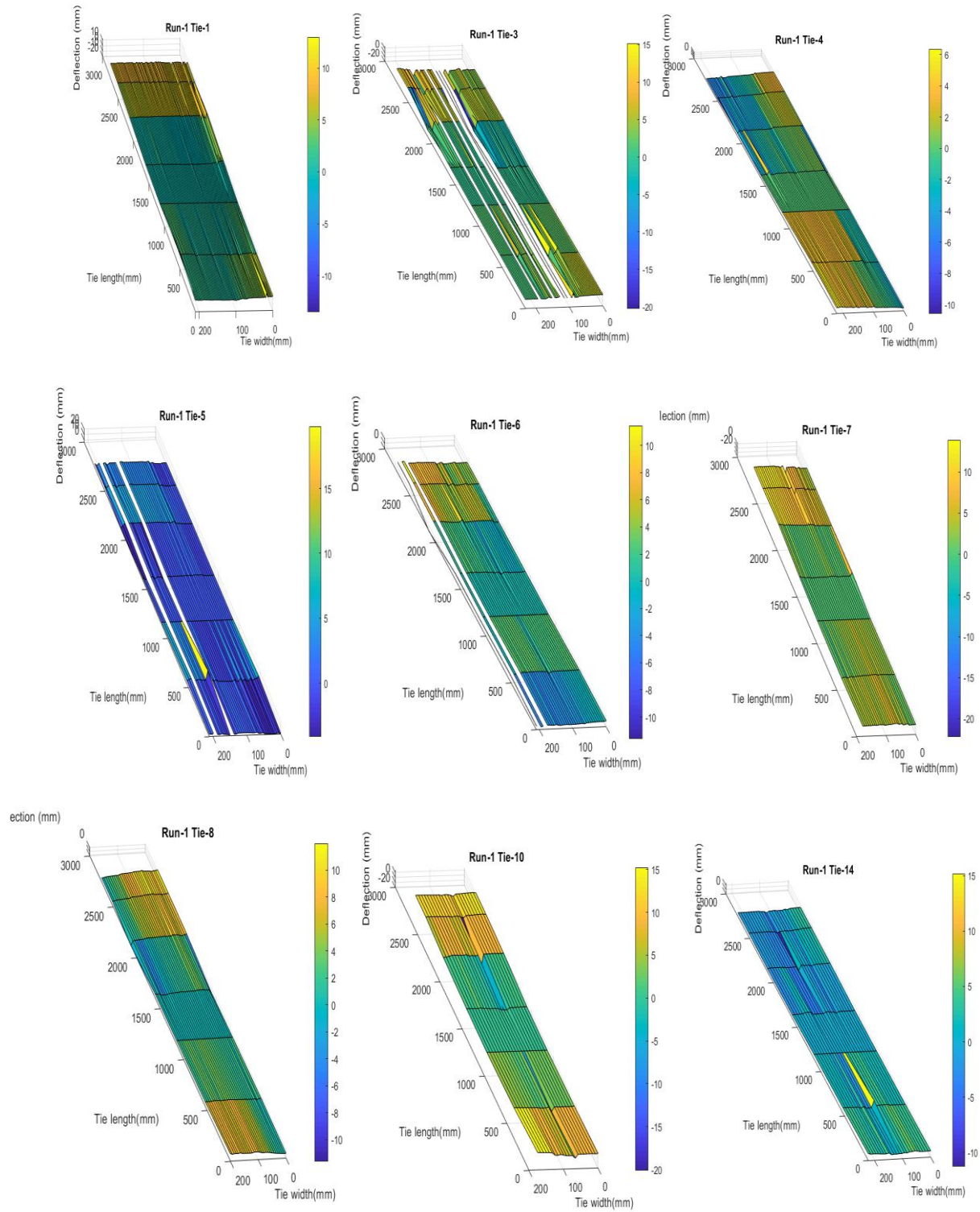


Figure 7.7 3D deflection profiles of 9 ties scanned in a test run

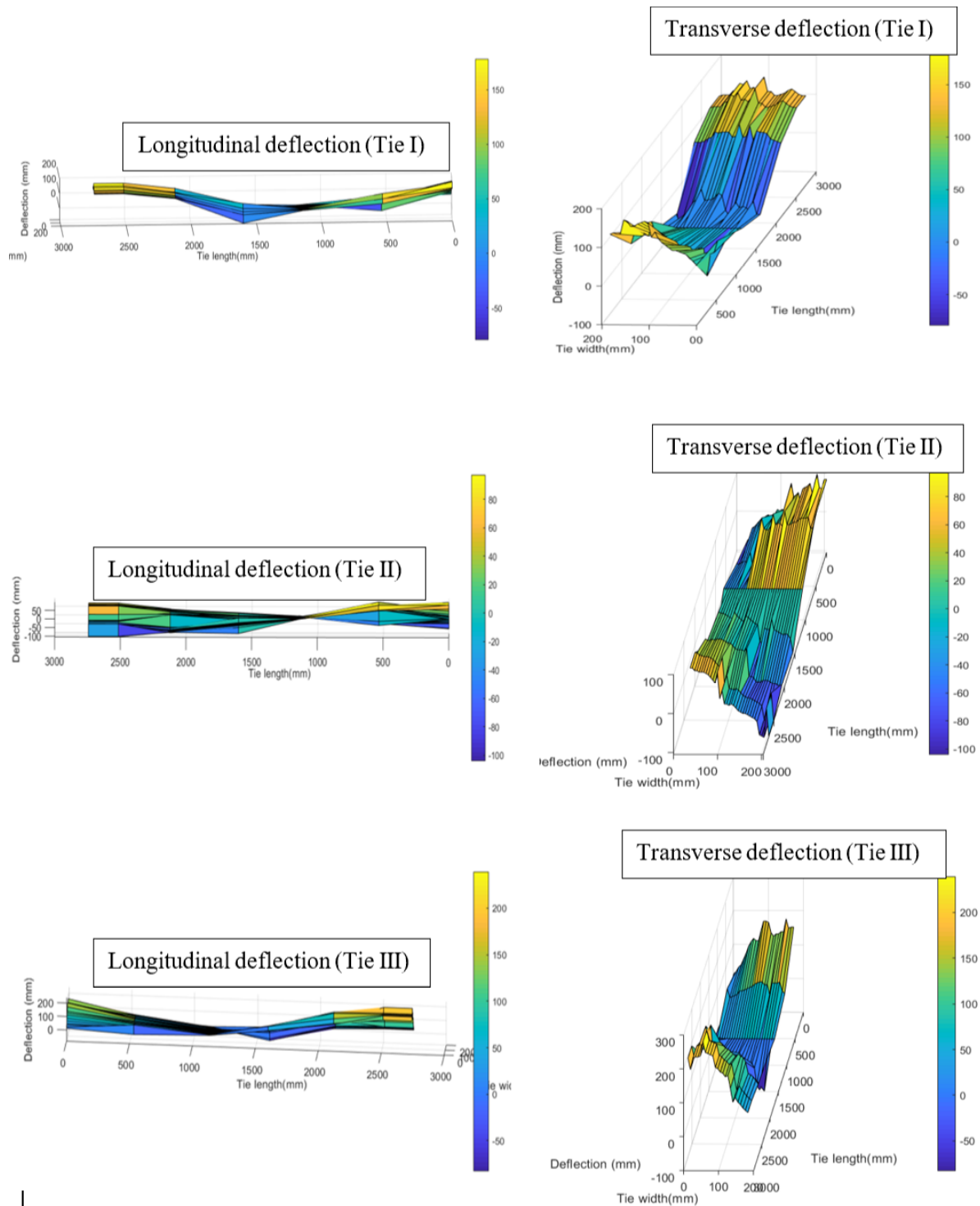


Figure 7.8 Longitudinal and transverse deflection profiles of 3 different ties with deflections scaled by 20x



Figure 7.9 Wood block placed on one of the ties

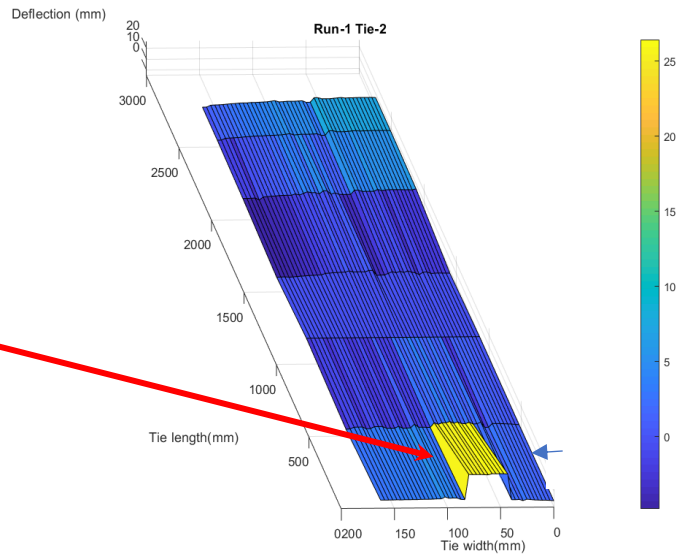


Figure 7.10 3D tie deflection profile with wood block near transducer 1

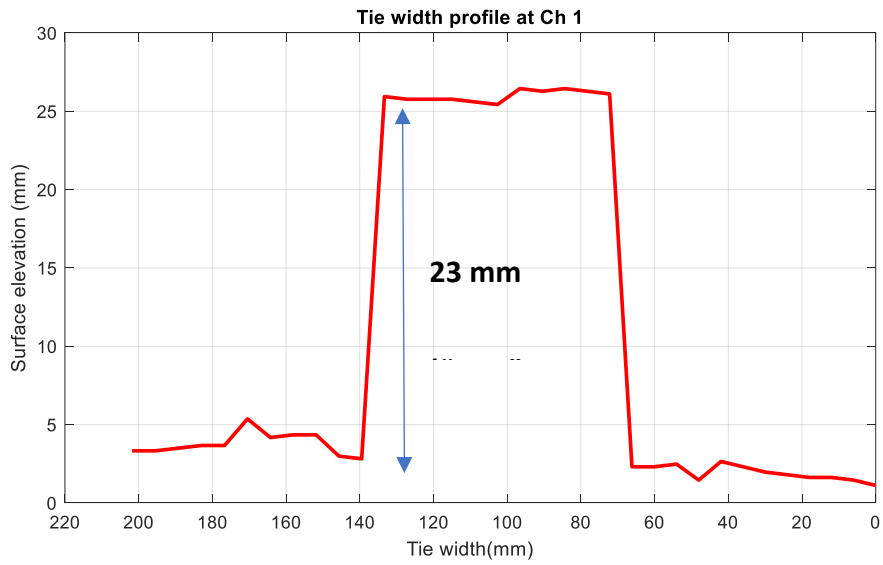


Figure 7.11 Tie width profile at transducer location-1 for control tie with wood block

7.6. Statistical Analysis

A statistical analysis was performed to evaluate the repeatability of the deflection measurements of the ties for different runs. The tie deflections at the two ends were tracked with respect to the central deflection for different ties and a mean and standard deviation of the deflections was computed over 4 different test runs. Fig. 7.12 shows the mean tie deflections for the first 20 ties. Fig. 7.13 shows the standard deviation for the first 20 ties. Standard deviations for most ties are less than 0.5 mm indicating good precision when tests are repeated.

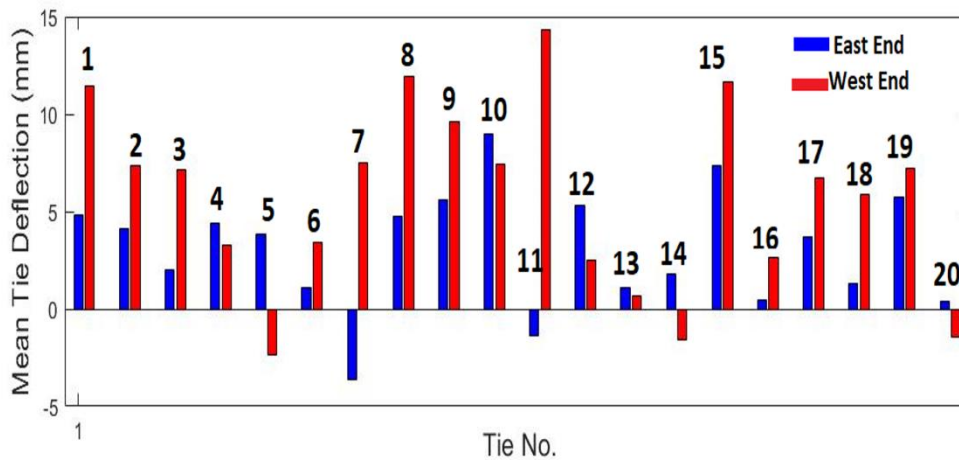


Figure 7.12 Mean tie end deflections of the first 20 ties computed over 4 test runs

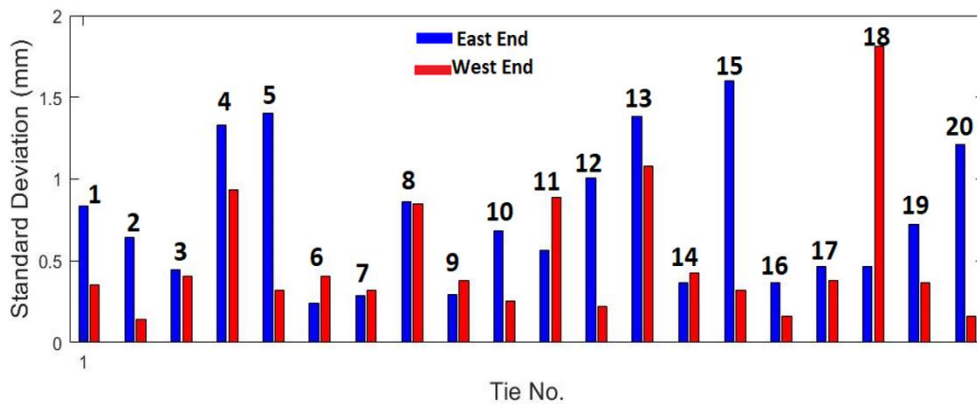


Figure 7.13 Standard deviation of tie end deflections of the first 20 ties computed over 4 test runs

7.7. Conclusions

This chapter discusses the tests conducted at the BNSF rail yard in San Diego with the sonar-based prototype mounted on a loaded gas tank train car. Testing parameters included validating the precision and accuracy of tie deflection measurements with the ultrasonic system at walking test speeds. Results obtained in these tests closely reflect those obtained during the tests conducted at the RDTF discussed in chapter 6. The use of camera acquired images to track spatial locations along the tie width was introduced as a convenient alternative to using an encoder. The reconstructed 3D tie surface profiles indicate that both longitudinal and transverse (twisting) deflections could be reasonably estimated using the proposed technique. The tests were conducted on a relatively new section of tangent track where the old ties had been reportedly replaced with new ties about three years ago. Since most of the ties were new and pristine, the system was not able to identify any ties with center-binding support conditions during these tests. Preliminary results, however, suggest that such defective support conditions can possibly be identified.

7.8. Acknowledgements

This work was funded by the US Federal Railroad Administration under contract 693JJ619C000019 with Mr. Cameron Stuart as the Program Manager.

Chapter 7, in part, is currently being prepared for submission for publication of the material as it may appear in the following paper: **Datta, D.,** Hosseinzadeh, A. Z., Cui, R., Lanza di Scalea, F. In-Motion Ultrasonic Non-contact Full-Field Railroad Crosstie Deflection Measurements During Full-Scale Field Tests. The dissertation author was the primary investigator and author of this paper.

7.9. References

- [1] Datta, D., Hosseinzadeh, A. Z., Cui, R., & di Scalea, F. L. (2023). High-speed 3D railroad tie deflection mapping in real-time using an array of air-coupled non-contact transducers. *Lecture Notes in Civil Engineering*, 254, 895–904. https://doi.org/10.1007/978-3-031-07258-1_90/FIGURES/9
- [2] Hosseinzadeh, A. Z., Datta, D., & Scalea, F. L. di. (2022). In-motion railroad tie deflection measurement via ultrasonic airborne sonar and computer vision techniques. *Research in Nondestructive Evaluation*, 1–21. <https://doi.org/10.1080/09349847.2022.2136808>
- [3] Hosseinzadeh, A. Z., Datta, D., & di Scalea, F. L. (2022). Railroad crosstie deflection measurement via ultrasonic airborne sonar and computer vision techniques. *ASNT Research Symposium*. <https://doi.org/10.32548/RS.2022.011>
- [4] Stuart, C., Lanza di Scalea, F. (2022). Air-borne tie sonar for loaded tie deflection measurements. Department of Transportation. Federal Railroad Administration. Office of Research. <https://doi.org/10.21949/1503647>
- [5] Hosseinzadeh, A. Z., Datta, D., & Scalea, F. L. di. (2022). Artificial intelligence-based approach to estimate relative deflection of railroad ties using airborne ultrasonic testing. *SPIE*, 12048, 300–308. <https://doi.org/10.1117/12.2617558>
- [6] Bay, H., Ess, A., Tuytelaars, T., & Van Gool, L. (2008). Speeded-Up Robust Features (SURF). *Computer Vision and Image Understanding*, 110(3), 346–359. <https://doi.org/10.1016/J.CVIU.2007.09.014>
- [7] Baker, S., & Matthews, I. (2004). Lucas-Kanade 20 years on: A unifying framework. *International Journal of Computer Vision*, 56(3), 221–255. <https://doi.org/10.1023/B:VISI.0000011205.11775.FD>
- [8] Wang, Z., Bovik, A. C., Sheikh, H. R., & Simoncelli, E. P. (2004). Image quality assessment: from error visibility to structural similarity. *IEEE Transactions on Image Processing*, 13(4), 600–612. <https://doi.org/10.1109/TIP.2003.819861>

Chapter 8. Conclusions and Future Work

This study presented novel inspection techniques utilizing advanced digital signal processing routines for non-contact high-speed ultrasonic monitoring of railroad tracks using air-coupled transducers. The proposed technologies could help make the railroad industry safer and more reliable by detecting defects in rails and degraded ballast support conditions at early stages and preventing accidents. The concluding remarks and future avenues for each inspection technique is discussed in this chapter.

8.1. Passive Rail Inspection Technique

Chapters 2, 3, 4 on the passive rail inspection technique presented the analysis of a high-speed non-contact ultrasonic approach that utilized the rolling train wheels as the excitation. The transfer function of the rail between two points was extracted passively from a normalized cross correlation operation on the signals recorded by two transducers. The attraction of this idea is the possibility to install it in trains running at revenue speed, therefore with no or minimal disruption of normal train traffic operations and a great opportunity for test redundancy. Data from a prototype tested in the field at TTCI were analyzed in terms of ROC curves to evaluate its detection performance for joints, welds, and internal defects. In particular, the performance was evaluated as a function of various relevant operational parameters, including different excitation strengths, defect position margins, test speed, length of statistical baseline distribution, and multiple runs. The results generally show expected trends, such as improved performance with higher speeds, larger defect position margins, smaller baseline lengths, and multiple runs. Results from tests conducted with an improved inspection prototype with a controlled acoustic source were also discussed. Possible future avenues of research could include the following:

1. Additional signal metrics could be considered in the feature vector of the outlier analysis to further enhance the robustness of the discontinuity detection.
2. An interesting exercise that could be carried out is to process the data in the opposite direction of the running train, i.e., by comparing a “current” location with a baseline collected “ahead” of the train. This analysis should theoretically provide the same ROC results, although there may be ways to exploit the double directions for improved detection performance.
3. The effect of train loads on the defect detection performance could be investigated. It can be reasonably assumed that test cars with higher payloads would generate higher energies into the rail and possibly improve the detection performance.

8.2. Tie Inspection Technique

Chapters 5, 6, 7 discussed a technique and prototype under development for the measurement of 3D deflections of railroad ties in motion. The various components of the system along with key signal processing routines utilized to extract the time-of-flight measurements from the airborne acoustic signals were discussed. The proposed technique is capable of measuring full-field 3D tie deflections (i.e., vertical deflections and twisting) in a completely non-contact manner conforming with the 3-inch clearance requirement from the rail surface for non-contact inspections. The ability to extract 3D tie deflections is expected to greatly improve the identification of adverse rail support conditions (e.g., tie center-binding), hence improving rail safety. Acoustic signal strength-based demarcation of tie boundaries was utilized to differentiate between signals coming from the ties and ballast to ensure continuous and smooth operation eliminating the requirement of stop and go measurements. The results from the tests conducted at the RDTF and BNSF facilities confirm the ability for the system to compute 3D tie deflection profiles at walking speeds. The use of a reference transducer provided an adaptive baseline which made deflection

measurements independent of variabilities in lift-off distances from the tie surface (absolute tie deflections). While the low speeds of the testing allowed a spatial resolution of 0.25-inch along the width of each tie, at higher speeds (e.g., revenue speed) this resolution is of course expected to be coarser, with approximately five measurements (resolution of 1.4-inch) expected across each tie width at 60 mph. This resolution should still give useful information on tie twisting (besides the tie vertical deflections, whose resolution is only controlled by the number of transducers used along the mounting beam). The tie deflection measurements extracted at the “control” tie with the coin-induced vibrations matched closely with those extracted without the coin-induced vibrations. This result confirmed the good tolerance of the designed prototype to vibrations, at least at the walking speeds utilized for the set of tests in the current phase of the project. Possible future avenues of research could include the following:

1. Ties that are misaligned with respect to the transducer array present a challenge for measuring deflections and demarcating tie boundaries. For misaligned ties, drifted measurements could be utilized such that deflection measurements from different transducers at different positions along the width of the tie could be used computing the deflection profile in the longitudinal direction of the misaligned tie.
2. Different signal controls, including an adaptive signal strength threshold, could be considered in the future to further improve the tie boundary demarcation process.
3. Since, measurements of deflections are made only on the tie surface, pre-existing surface undulations may erroneously appear as tie deflections. Moreover, surface measurements alone may not fully indicate the extent of deformations on the bottom surface of the tie which is in contact with the ballast. To evaluate “true deflections”, two transducer arrays (one placed near the axles that produce higher loads on the ties and one placed away from the axles producing lower loads

on the ties) could be utilized. The difference in load factors for the different locations of the arrays could be utilized to compute differential deflections to extract the “true deflections”. For example, the measurements from the array placed away from the axles could be used as a baseline and the measurements from the array located closer to the axle could be compared to the baseline measurements to obtain the “true deflections”.

4. The LabVIEW user interface could be updated with controls for autonomously identifying ties with center-binding. Moreover, tests need to be conducted at higher speeds to study the effects of vibrations on the deflection measurements.